Technische Universität München

Department of Chemistry and Catalysis Research Center
Chair of Technical Electrochemistry

Electrochemical Impedance Spectroscopy (EIS) and Surface Analysis of High-Energy Cathodes for Lithium-Ion Batteries

Daniel J. Pritzl

Vollständiger Abdruck der von der Fakultät für Chemie der
Technischen Universität München zur Erlangung des akademischen Grades eines

Doktors der Naturwissenschaften (Dr. rer. nat.)

genehmigten Dissertation.

Vorsitzender:	Prof. Dr. Tom Nilges
Prüfer der Dissertation:	1. Prof. Dr. Hubert A. Gasteiger
	2. Prof. Dr. Andreas Jossen
	3. Prof. Dr. Jürgen Janek

Diese Dissertation wurde am 22.11.2018 bei der Technischen Universität München eingereicht und durch die Fakultät für Chemie am 16.01.2019 angenommen.

Abstract

Many processes occurring on the cell chemistry level in lithium-ion batteries are not fully understood yet and need to be investigated in detail with advanced characterization tools. The first part of this thesis deals with the development of a new reference electrode and a novel measurement procedure for electrochemical impedance spectroscopy (EIS) and its application to analyze the failure mechanism of graphite/$LiNi_{0.5}Mn_{1.5}O_4$ lithium-ion cells. First, a micro-reference electrode consisting of a polyimide insulated gold wire was developed which fulfills all requirements for producing valid impedance spectra of anode and cathode versus the reference electrode. With the reference electrode at hand, the impedance of graphite/$LiNi_{0.5}Mn_{1.5}O_4$ cells cycling at 40 °C were analyzed over extended charge/discharge cycling by using a novel impedance procedure. The procedure records impedance spectra in blocking condition (no charge transfer reaction possible) and in non-blocking condition (charge transfer possible), by which the impedance of the $LiNi_{0.5}Mn_{1.5}O_4$ electrode could be deconvoluted into its resistance contributions. The cathode impedance was then further studied in detail, and electrolyte oxidation and cathode impedance response could be correlated for the first time. Last, the anode of a graphite/$LiNi_{0.5}Mn_{1.5}O_4$ cell was analyzed with the same blocking/non-blocking approach and the impedance response could be deconvoluted in its contributions and related to manganese dissolution from the $LiNi_{0.5}Mn_{1.5}O_4$ electrode.

The second part of this thesis deals with the mechanistic understanding of the washing process of nickel-rich layered oxide based cathode materials ($LiNi_{0.85}Co_{0.10}Mn_{0.05}O_2$) for lithium-ion batteries. It could be shown by OEMS that upon washing of a nickel-rich cathode material with water, a strongly reduced O_2 release at high degrees of delithiation is observed. By analyzing the wash solution, performing impedance spectroscopy and on-line electrochemical mass spectrometry on the washed cathodes, a detailed, conclusive mechanism for the washing of nickel-rich materials could be provided.

Kurzfassung

Viele Prozesse die sich auf Zellchemie-Ebene in Lithium-Ionen Batterien abspielen sind bis jetzt nicht gut verstanden und es bedarf einer detaillierten Untersuchung dieser Prozesse mittels besserer Charakterisierungsmethoden. Der erste Teil dieser Doktorarbeit befasst sich mit der Entwicklung einer neuen Referenzelektrode und einer neuartigen Messprozedur für Elektrochemische Impedanz Spektroskopie (EIS), um die Fehler-Mechanismen für Graphit/$LiNi_{0.5}Mn_{1.5}O_4$ Lithium-Ionen Zellen zu untersuchen. Zuerst wurde eine Mikro-Referenz Elektrode entwickelt, die aus einem Polyimid-beschichten Golddraht besteht und die alle Anforderungen erfüllt, korrekte Impedanz Spektren von Anode und Kathode bezogen auf die Mikro-Referenz Elektrode zu generieren. Mit der nun entwickelten Referenzelektrode wurde die Impedanz von Graphit/$LiNi_{0.5}Mn_{1.5}O_4$ Zellen bei 40 °C über mehrere Zyklen hinweg mit Hilfe einer neuartigen Impedanz Prozedur analysiert. Mittels der Prozedur wurden Spektren in *blocking* Bedingungen (kein Ladungsübergang möglich) und in *non-blocking* Bedingungen (Ladungsübergang möglich) aufgenommen und die Impedanz der $LiNi_{0.5}Mn_{1.5}O_4$ Elektrode in die einzelnen Widerstandsbeiträge aufgetrennt. Die Impedanz der Kathode wurde tiefergehend untersucht und Elektrolytoxidation konnte zum ersten Mal mit der Impedanz der $LiNi_{0.5}Mn_{1.5}O_4$ Elektrode korreliert werden. Als letztes wurde die Anode in einer Graphit/$LiNi_{0.5}Mn_{1.5}O_4$ Zelle mit der gleichen Prozedur untersucht, womit die Impedanz der Anode in die einzelnen Widerstandsbeiträge aufgespalten werden konnte und mit der Manganauflösung der $LiNi_{0.5}Mn_{1.5}O_4$ Elektrode korreliert werden konnte.

Der zweite Teil der Doktorarbeit beschäftig sich mit dem Mechanismus des Waschungsprozesses von Nickel-reichen Schichtoxid-basierten Kathoden ($LiNi_{0.85}Co_{0.10}Mn_{0.05}O_2$). Es konnte gezeigt werden, dass nach dem Waschen der Materialien mit Wasser, ein drastisch reduzierter Sauerstoffaustritt bei hohen Delithierungsgraden vorliegt. Mittels Untersuchung der Waschlösung, Impedanz Spektroskopie und Gasanalyse der Kathoden wurde ein detaillierter Mechanismus zum Waschen von Nickel-reichen Kathodenmaterialien erstellt.

Contents

List of Acronyms

Abbreviation	**Description**
BET	Brunauer-Emmett-Teller
CC	constant current
CCCV	constant current constant voltage
CE	coulombic efficiency
CEI	cathode electrolyte interface
CV	constant voltage
EC	ethylene carbonate
EIS	electrochemical impedance spectroscopy
EMC	ethyl methyl carbonate
EV	electrical vehicle
FEC	fluoroethylene carbonate
GWRE	gold wire reference electrode
LEDC	lithium ethylene dicarbonate
LNMO	high-voltage spinel ($LiNi_{0.5}Mn_{1.5}O_4$)
LP57	EC/EMC solvent (3:7, v:v) with 1M $LiPF_6$
LSV	linear sweep voltammetry
NMC	lithium nickel manganese cobalt oxide ($LiNi_xMn_yCo_zO_2$)
NMR	nuclear magnetic resonance
NMP	N-methyl pyrrolidone
OCV	open-circuit voltage
OEMS	on-line electrochemical mass spectrometry
OER	oxygen evolution reaction
PVdF	polyvinylene difluoride
SEI	solid electrolyte interface
SOC	state of charge
TGA	thermogravimetric analysis
VC	vinylene carbonate
XPS	x-ray photoelectron spectroscopy

List of Symbols

Symbol	Name	Unit
α	constant phase factor	-
ε	porosity	-
κ	conductivity	S/m
η	overpotential	V
Φ	phase shift	rad
ρ	density	kg/m^3
τ	tortuoisty	-
ω	angular frequency	rad/s
A	surface area	m^2
C	capcaitance	F/m^2
d	length	m
f	frequency	1/s
i	Imaginary number	-
I	current	A
n	mol	mol
M	molar mass	g/mol
Q	charge/capacity	As
Q	constant phase element	$F \cdot s^{(\alpha-1)}$
R	resistance	Ω
$R_{Cont.}$	contact resistance	Ω
R_{CT}	charge transfer resistance	Ω
$R_{El.}$	electrical resistance	Ω
R_{Pore}	pore resistance	Ω
U	voltage	V
Z	complex impedance	Ω

1 Introduction

Today's batteries for consumer electronics as well as for electrical vehicles (EV's) are based on the lithium-ion battery technology. This technology had its breakthrough in 1991[1] when Sony commercialized the first lithium-ion battery, which was developed for portable electronics. The cell chemistry consisted of a hard carbon anode and a $LiCoO_2$ (LCO) cathode and the cathode is still in use today. The layered transition metal oxide cathode material was invented by John B. Goodenough[2] and coworkers and was in principle a further development of the sulfide cathode TiS_2 which was developed by M. Stanley Whittingham[3] in 1976. The invention of TiS_2 was groundbreaking as it was the first material where lithium ions could be deintercalted and reintercalated reversibly to yield $LiTiS_2$. The drawback of the sulfide cathode material was the very low average voltage of 1.9 V vs. metallic lithium at a reversible capacity of 210 mAh/g which results in low energy density of ≈400 Wh/kg_{LiTiS2}.[4,5] In addition, it required the use of a metallic lithium anode as the TiS_2 cathode could not be produced in the lithiated form. The LCO cathode instead (producible in the lithiated state), could be used with lithium-free anodes like graphite, providing a specific energy density of ≈560 Wh/kg_{LCO} due to a mean voltage of 3.8 V vs. metallic lithium and a reversible capacity of 148 mAh/g.[4] This cathode shows good cycle life (in graphite/LCO cells) and good energy density, but has the drawback of the high cobalt content that makes it a very expensive material. In August 2017, one ton of cobalt was ≈60.000 $[6]. Another frequently used metal for cathode materials is nickel where one ton costs only ≈10.000 $[7]. A second drawback is the fact that most of the cobalt is mined in the Democratic Republic of Congo under questionable ethical conditions such as child labor.[8] Thus, both cost and supply constraints require to minimize or eliminate the use of cobalt in electrical vehicles, where high amounts of cathode materials are needed.

Very soon, the cobalt in the LCO cathode was substituted by other transition metals in order to lower the cobalt amount and increase the energy density. One material found by the group of Naoki Yabucchi is NMC111 with a chemical formula of $LiNi_{0.33}Mn_{0.33}Co_{0.33}O_2$.[9] Here the cobalt content is reduced to 33% and due to nickel in the structure, which is redox active at higher potentials (compared to cobalt), the energy density of layered oxides could be increased. The value for the NMC111 is ≈590 Wh/kg_{NMC111} calculated with an average voltage of 3.7 V vs. metallic lithium and a reversible capacity of 160 mAh/g.[4] Still, the energy density of this material is not a strong improvement compared to LCO. Due to this, some electrical vehicles (e.g. Tesla Model S)[10] contain a layered oxide cathode with the chemical formula $LiNi_{0.8}Co_{0.15}Al_{0.05}O_2$ (NCA), which provides a specific energy density of ≈740 Wh/kg_{NCA} (calculated with a mean voltage of 3.7 V vs. Li^+/Li and a reversible capacity of 199 mAh/g)[4,11]; it thereby more closely meets the requirements of high energy density, high rate capability, long cycle life and a reduced amount of cobalt in the structure.

As the target of the automotive manufacturers in 2025 is an energy density of ≈250 Wh/kg at the battery level, the cathode active material must have an energy density of close to ≈800 Wh/kg.[12] In order to reach the required high energy density, the industry and academia have been working on Ni-rich NMC materials with nickel amounts equal to 80% – e.g. NMC811 ($LiNi_{0.8}Mn_{0.1}Co_{0.1}O_2$) - and higher, heading towards a pure layered nickel oxide $LiNiO_2$ (LNO). The issues with such high nickel contents are thermal and structural instability at high degrees of delithiation[13,14] and a tremendous reactivity of the surface towards ambient air.[15] The stabilization of this material is object of current research on cathode materials. The development of an LNO cathode appears as a continuous approached target in world-wide battery R&D, however the material has already been found by Jeff Dahn and coworkers in 1991.[16] The understanding of the surface chemistry of nickel-rich layered oxide based cathode active materials constitutes one part of this PhD Thesis and is theoretically highlighted in the next section.

A cathode material which is cobalt free, and therefor cheap, is the so-called "manganese spinel" with the chemical formula of $LiMn_2O_4$ (LMO) found by Thackeray, Bruce, David and Goodenough in 1983.[17] The energy density of this

cathode material is low (≈490 Wh/kg_{LMO}) due to the poor reversible capacity of 120 mAh/g at an average voltage of 4.1 V vs. Li^+/Li.[4] In order to increase the energy density of LMO, part of the manganese was replaced with nickel to yield the so-called "high-voltage spinel" with the chemical formula $LiNi_{0.5}Mn_{1.5}O_4$ (LNMO)[18,19].This material has an operating voltage of ≈4.75 V vs. Li^+/Li at a reversible capacity of 140 mAh/g, resulting in a high energy density of ≈670 Wh/kg_{LNMO}.[12,20] This material has the advantage of a high energy density, good rate capability, and decent cycling stability at moderate temperatures (e.g. 25 °C). Unfortunately, when the temperature is increased to over 40 °C, drastic cell fading occurs.[21] The focus of this PhD thesis is the analysis of the graphite/LNMO system at elevated temperatures (40 °C) concerning stability of the solid electrolyte interface (SEI) on the anode, and the impedance increase on anode and cathode side.

1.1 Theoretical Background on Li-Ion Batteries

Working principle

A conventional lithium-ion battery consists of two intercalation electrodes coated on metal current collectors, a separator, and a lithium ion conducting electrolyte, composed of a lithium salt, which is dissolved in liquid alkyl carbonate-based solvents. The typical anode consists of graphite (C_6) into which lithium (Li) can be intercalated. In battery research, the negative electrode is commonly referred to as anode, independent of whether the discharge or charge reaction is considered. The reaction for a graphite anode is summarized in equation 1.

$$C_6 + Li^+ + e^- \leftrightarrows LiC_6 \quad (1)$$

During the charge of a battery, lithium is intercalated into graphite (C_6) up to a stoichiometry of LiC_6, which corresponds to a specific capacity of 372 mAh/g_{C6}.[22] During discharge, the reaction is reversed. The lithium source in a today's lithium ion batteries is the cathode, where layered transition metal oxides, manganese spinels, and olivine materials are frequently used.[23] These materials are described later, and the cathode reaction is exemplarily shown for the high-voltage spinel LNMO ($LiNi_{0.5}Mn_{1.5}O_4$) cathode in equation 2.

$$LiNi_{0.5}Mn_{1.5}O_4 \leftrightarrows Ni_{0.5}Mn_{1.5}O_4 + Li^+ + e^- \quad (2)$$

During the charge of a battery, the transition metals are oxidized, resulting in a deintercaltion of Li^+. In the case of the LNMO cathode material almost entirely nickel is the redox active metal.[19] In the pristine material, lithium is in the oxidation state +1 (Li^+) and nickel is in +2 (Ni^{2+}). Upon charge, the oxidation state of nickel goes to +4 (Ni^{4+}), resulting in a specific capacity of 146 mAh/g_{LNMO}. Upon discharge, lithium ions can be reintercalated into the delithiated spinel structure changing the oxidation state of nickel back to +2 (Ni^{2+}).

The ionic current in the battery is balanced by an electronic current, meaning that during charge lithium ions are transported from the cathode to the anode and reduced there by the electrons flowing from the cathode to the anode current collector. During discharge, lithium ions move from the anode to the cathode and

the electrons are used to reduce the transition metals. Ion transport between anode and cathode is enabled by a liquid electrolyte (a mixture of cyclic and linear carbonates) which contains a dissolved lithium salt (mostly $LiPF_6$). The electrolyte fills the pores of anode, cathode and the separator (a polyolefin-based porous membrane in commercial lithium-ion batteries). The separator divides anode and cathode electronically to avoid a short-circuit of the cell. In order to visualize the above-described battery setup, Figure 1.1 shows a single-layer configuration of a battery test cell used in this work.

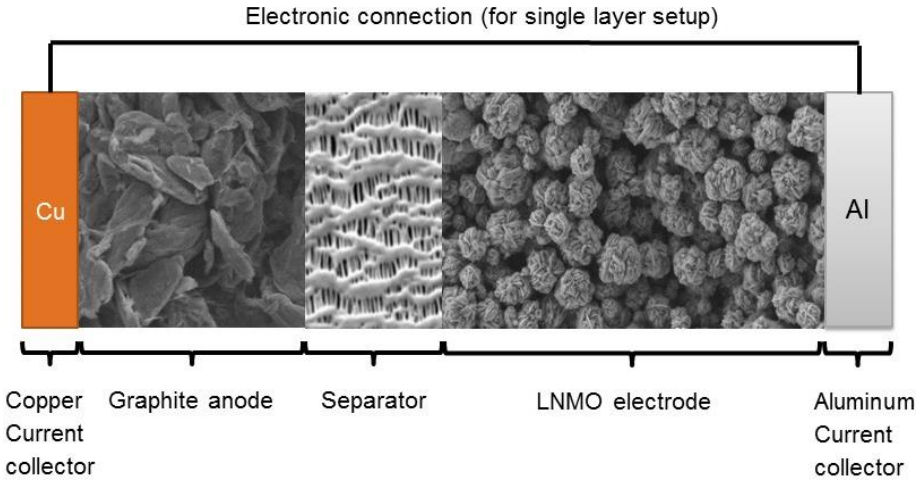

Figure 1.1: Schematic drawing of a lithium-ion battery with a graphite anode coated on a copper current collector, a separator, and an LNMO cathode coated on an aluminum current collector.

A typical graphite anode contains low weight percentages (up to 5%) of a binder which enables adhesion to the current collector and cohesion inside the coating to ensure mechanical stability. Common binders are polyvinylene difluoride (PVdF) when anodes are processed with N-methyl pyrrolidone (NMP). However, state-of-the art anodes are processed in water[24] and the choice of binder is a combination of sodium carboxymethyl cellulose (CMC) and styrene butadiene rubber (SBR).[25] Anodes are coated on a copper current collector as it does not form alloys with lithium and has a high electronic conductivity.[26]

Cathodes are composite electrodes which consist of high active material contents (> 92%)[27] in order to achieve high energy densities, and of a PVdF binder for adhesion to the current collector and cohesion of the coating and carbon black to ensure good electronic conductivity. The carbon additive is mandatory, as typical

cathode materials are poor electronic conductors, with electronic conductivities of ≈10^{-6} S/cm (exemplarily for a $LiMn_2O_4$ material).[28] As current collector, aluminum foil is used. Intrinsically, no metal is stable at potentials where typical cathodes are being operated (≈4.3 V vs. Li^+/Li). However, aluminum has a native oxide (Al_2O_3) on the surface which is transformed to an AlF_3 layer in organic electrolytes with a $LiPF_6$ salt, and hence is chemically stable towards oxidation/corrosion at high potentials.[29]

Anodes & solid electrolyte interphase (SEI)

The first lithium batteries were based on pure lithium metal as anode material.[23] The reason for this is the fact, that the first cathode materials could not be produced in the lithiated state. Besides that, lithium metal is now very attractive due to the high specific capacity of 3862 mAh/g_{Li}, and the low potential of -3.04 V (versus the standard hydrogen electrode).[30] The first commercialized cells by Moli Energy had an oversized lithium metal anode and a MoS_2 cathode.[31] These cells could be cycled reversibly, but as many cells caught fire during operation, they had to be recalled from the market.[32] The reason for the fire incident are lithium dendrites which form during the plating of metallic lithium.[31,33] Metal dendrites can grow through the separator and build up an electrical contact between anode and cathode, and thereby short-circuiting the cell.

At the operating potential of lithium metal and lithiated graphite, no organic solvent is stable and gets reduced when it comes into contact with the metal surface.[31] This fact would lead to a continuous consumption of lithium during operation, however the so-called solid electrolyte interphase (SEI)[34] prevents the decomposition of the organic electrolyte. The SEI is a layer of several nanometers and consists of reduction products of the electrolyte such as lithium carbonate (Li_2CO_3), lithium fluoride (LiF), lithium alkyl carbonates, poly-olefins and further reduction products which are dependent on the used solvents and salt.[35,36] The SEI allows ion transport through the layer (Li^+ - conduction) but inhibits electron transport (e^- - conduction) and does so prevent further electrolyte reduction. However, on a lithium metal anode the ratio between discharge capacity (Q_D) and charge capacity (Q_C) – the ratio of Q_D/ Q_C is called coulombic efficiency (CE) – ranges around ~99.0%,[32] which

suggests that the SEI on lithium metal anodes is not stable during battery operating conditions and lithium is lost in the SEI continuously. This observation can be explained by the fact that lithium has an infinite volume change upon its complete dissolution during charge. This volume change leads to cracks in the SEI which results in new available surface area for further electrolyte reduction. Up to now, many efforts are made to suppress dendrite formation and achieve high coulombic efficiencies with lithium metal anodes. [37]

The first safe lithium-ion batteries (commercialized by Sony in 1991) replaced the lithium metal by a graphitic anode.[1,32] Very soon, graphite was discovered as stable and safe anode for lithium-ion batteries. Graphite has a specific capacity of 372 mAh/g (based on a LiC_6 phase) and operates at an equilibrium potential of ≈0.1 V vs. Li^+/Li.[4] This material was first used with an ethylene carbonate (EC) based electrolyte for lithium-ion battery research by Dahn and coworkers[22] and showed only irreversible reactions during the first charge/discharge cycle which are associated with SEI formation on the surface of the graphite particles. However, after the first cycle, the graphite anode can be cycled reversibly almost without active lithium loss.[22] The amount of lost lithium in the SEI was found to be proportional to the graphite surface area, and the coulombic efficiency of the first cycle ranges between 80 – 95%. After the first cycle, the graphite anode can be cycled close to a coulombic efficiencies of 100%.[38] Graphite electrodes can be cycled at high coulombic efficiencies, as the volume expansion is very low with ≈10%.[4] One important factor which influences the SEI on graphite anodes is the dissolution of transition metals from the cathode and their deposition on the anode. Transition metals like manganese or nickel dissolve from the cathode and are reduced on the graphite anode. The reduction of the transition metals leads to the oxidation of lithium in the graphite anode and hence to an active lithium loss. Furthermore, the transition metals are catalytically active, meaning they can continuously consume active lithium once they are deposited on the graphite anode.[39,40] A special charge characteristic of graphite is the so-called "*stage formation*"[38] what means that first in every 4th graphene layer (C_6) lithium is intercalated corresponding to an LiC_{24} phase. Afterwards, every second graphene layer is occupied (LiC_{12}) and last lithium is intercalated in every graphene layer a lithium atom is inserted. The existence of

plateaus during charge/discharge cycling of graphite are caused by the simultaneous existence of two phases (often called two-phase material).[38]

A so-called "zero-strain" anode material is LTO ($Li_4Ti_5O_{12}$), which has a volume expansion during lithiation and delithiation of only 0.20%, leading to excellent reversible cycling of this anode active material.[4] The specific capacity of LTO is 175 mAh/g_{LTO} at an operating voltage plateau of ≈1.5 V vs. Li^+/Li.[41] The advantage of this high reversible potential is that no SEI is formed at such high potentials, so that the first cycle coulombic efficiency is ~100%. The drawback of this material is the low energy density when paired with conventional cathodes due to the high operating potential of LTO and the resulting low cell voltage. A further unsolved issue is the formation of gaseous products such as H_2 caused by the pristine LTO surface in contact with the carbonate electrolyte.[42]

An intensively studied anode material is silicon, with a specific capacity of 3579 $mAh/g_{silicon}$ (based on the $Li_{15}Si_4$ phase) at an average potential of ≈0.2 V vs. Li^+/Li.[4,43] Silicon does electrochemically form alloys with lithium. A drawback of alloy materials such as silicon is the high volume expansion during each charge/discharge cycle of ≈270%.[4,44] This compromises the integrity of the SEI and leads to a continuous consumption of the lithium inventory. Another challenge is the electronic isolation of lithiated silicon particles under a thick SEI layer.[45] Many efforts have been undertaken by researchers in order to stabilize the SEI on silicon and to mitigate the isolation of silicon particles.[46]

Electrolyte

The liquid electrolyte for lithium-ion batteries consists mainly of three components: (i) the lithium salt $LiPF_6$ which is responsible for the ionic conductivity and is commonly added at concentrations of roughly one molar (1 mol/L)[47], (ii) a cyclic carbonate like ethylene carbonate (EC) which leads to the SEI formation[48] as it is reduced below 0.8 V vs. Li^+/Li[49] forming lithium ethylene dicarbonate (LEDC), a major component of an EC derived SEI.[50] The high polarity of EC is important in order to dissolve the lithium salt. The last component (iii) is a linear carbonate like ethyl methyl carbonate (EMC) or diethyl carbonate (DEC), which keeps the viscosity

of the electrolyte low to ensure good ionic conductivity.[51] The $LiPF_6$ salt fulfills the requirements of a good ionic conductivity with ≈10.7 S/cm in a mixture of EC/DEC at 25 °C, [51] and the ability to passivate the current collector[52]. A drawback of $LiPF_6$ is the fact that the following equilibrium reaction occurs: $LiPF_6 \leftrightarrows PF_5 + LiF$. The equilibrium is shifted to the right-hand-side with increasing temperature and since PF_5 is a strong Lewis acid, unwanted side reactions are triggered, like the formation of HF which is known to decrease the cycle life of lithium-ion batteries.[51]

Another very important component of the electrolyte are additives which are commonly added up to amounts of 5% to the electrolyte solution. The most important function of additives is the modification of the SEI, and thus the improvement of the long-term cycling stability of lithium-ion cells.[48] The additive which is widely used in commercial lithium-ion batteries is vinylene carbonate (VC) which was introduced by Aurbach et al.[53] Vinylene Carbonate is reduced at potentials higher than 1.0 V vs. Li^+/Li and hence leads to the suppression of EC reduction.[50,54] The major component of the VC derived SEI is poly(VC), a polymeric species which is attributed to create a more temperature stable SEI on graphite anodes.[55] Burns et al.[56] investigated different amounts of VC in commercial graphite/LCO cells and found that 2% VC (in commercial scale cells) show the best performance based on coulombic efficiency and cycle life measurements. A remaining challenge is still the use in lithium-ion cells that exceed a cathode voltage of 4.4 V vs. Li/Li^+. Under these conditions, VC decreases cell performance drastically.[57] This Thesis examines the use of VC in graphite/LNMO cells which operate up to cathode potentials of 4.9 V vs. Li^+/Li, using gas- and impedance analysis and showing the boundaries within VC can still be employed successfully in graphite/LNMO cells.

Cathode

The currently used cathode materials in lithium-ion batteries can be divided into three groups: (i) spinel oxides with the general formula unit LiM_2O_4, (ii) phospho-olivines with the structure $LiMPO_4$ and (iii) layered metal oxides with the general formula unit $LiMO_2$ (or its overlithiated version $Li_{1+x}M_{1-x}O_2$).

The spinel oxide $LiMn_2O_4$ is of special interest as it is a very cheap material, non-toxic, and with manganese as redox active metal very abundant. A further positive criterion especially regarding the safety of lithium-ion cells is the high thermal stability of $LiMn_2O_4$.[4,17] These materials are typically cycled to an upper cut-off voltage of 4.2 V vs. Li/Li^+ and the resulting capacity is 120 mAh/g_{LMO}.[4,58] However, lithium-ion cells with $LiMn_2O_4$ as cathode material do generally not possess a long-term cycling stability. Their capacity fading is associated with two phenomena: (i) the spinel phase tends to form a tetragonal phase during cycling, especially at high charge/discharge currents and (ii) transition metal dissolution and hence a degradation of the graphite anode SEI.[40,59] Furthermore, to improve energy density by increasing capacity and voltage, parts of the manganese were substituted with nickel. The resulting material is the so-called high-voltage spinel $LiNi_{0.5}Mn_{1.5}O_4$ (LNMO) which will be discussed in more detail in section 1.2.

The use of phospho-olivines as cathode material for lithium-ion batteries was discovered by the group of John B. Goodenough in 1997.[60] The commercially most successful material is lithium iron phosphate (LFP) with a chemical composition of $LiFePO_4$. LFP has the advantage – compared to other cathode materials – of being based on abundant and inexpensive materials with no environmental hazards.[4] The olivine type structure offers several advantages, as for example high structural and thermal stability which makes it a safe battery material.[4] LFP is a two-phase material and has a voltage plateau at 3.45 V vs. Li^+/Li over the entire SOC range. The theoretical capacity of this material is 170 $mAh/g_{LFP,}$ however this capacity is not gained practically. Micrometer-sized LFP particles are known to have a low rate capability and the reason for this is the low electronic conductivity and low solid state lithium diffusion. [61] In order to approach the theoretical capacity of LFP, two strategies were applied: (i) the synthesis of this material as nanoparticles where the conduction path length of both electrons and lithium-ions in the material (solid state diffusion) is shortened and so that the associated transport resistance is increased, [62] or (ii) a carbon coating of the LFP particles in order to overcome the high electronic contact resistance across the LFP/conductive carbon interface.[63] A drawback of LFP is the low voltage plateau leading to a low energy density of the

cathode. Current research focuses therefore on other olivine type materials as for example $LiCoPO_4$ (LCP) which has a higher operating voltage plateau.[4]

The materials which have attracted most attention in current lithium-ion battery research are layered transition metal oxides. The nickel manganese cobalt layered oxides with the chemical formula $LiNi_xMn_yCo_ZO_2$ (x+y+z = 1) abbreviated as stoichiometric NMC. In contrast to spinel oxides or phospho-olivines, NMC materials cannot be completely delithiated during charge of a battery. A general restriction criteria for stoichiometric NMC materials is the upper cut-off voltage of 4.3 V vs. Li/Li^+. The specific capacity of NMC materials (at the same cut-off voltage) correlates with the amount of nickel in the structure. In general a NMC111 ($LiNi_{0.33}Mn_{0.33}Co_{0.33}O_2$) material delivers a capacity of 163 mAh/g, a NMC622 ($LiNi_{0.60}Mn_{0.20}Co_{0.20}O_2$) has a capacity of 187 mAh/g and NMC811 ($LiNi_{0.80}Mn_{0.10}Co_{0.10}O_2$) has a capacity of 203 mAh/g (charge until a cut-off potential of 4.3 V vs. Li^+/Li and values based on a discharge versus metallic lithium at C/10).[64] Stoichiometric NMC materials cannot be cycled with full capacity (delithiated completely) as the impedance of the cathode increases tremendously whereas the bulk structure is maintained.[65] However, Streich et al.[66] and Jung et al.[67] both could show that impedance increases due to O_2 release from the near-surface region leading to a high impedance and O_2-deficient surface layer. Further they correlated the onset of oxygen release from stoichiometric NMC materials with the oxidation of the electrolyte leading to a deterioration of the cycling performance. When oxygen evolution from the stoichiometric NMC lattice happens, the evolution of CO and CO_2 were observed at the same time. The general opinion in the battery field was, that the high cut-off potential by itself causes electrolyte oxidation. When Jung et al.[67] measured the gas evolution of a high-voltage spinel (which operates at 4.7 V vs. Li^+/Li) no oxygen evolution and also no CO and CO_2 evolution were observed. From this, the authors concluded that the gaseous oxygen leads to the oxidation of the electrolyte and not the high potential.[68] Wandt et al.[69] further showed that the released oxygen from the surface is singlet oxygen which can react with the carbonate-based electrolyte. A further failure mechanism from NMC materials is associated with the cracking of the agglomerated NMC crytallites upon lithiation and delithiation due to the volume change of the crystal structure.[14] As the volume

contraction correlates with the nickel content – NMC111 shows a volume contraction of 0.5%, while NMC811 has a volume contraction of 5% when the materials are both cycled to 4.3 V vs. Li^+/Li – the cracking and subsequent isolation of particles is seen as a challenge for nickel-rich NMC materials.[70] A third challenge is the detrimental effect of moisture on nickel-rich NCM materials, which will be discussed in section 1.3.

In order to achieve higher energy densities for the NMC materials, the so-called Li-rich NMC's were introduced.[71] For regular NMC materials (Li^+ with the stoichiometry of ~1) the lithium layer and the transition metal layer are occupied ideally by only lithium and transition metals, respectively. Contrary to that, Li-rich NMC materials can also incorporate lithium-ions in the transition metal layer leading to more accessible lithium. The general formula of these materials can be written as: x Li_2MnO_3 • (1-x) $LiMeO_2$ when regarding the material as a two-phase material[72] (nano-domains of NMC and Li_2MnO_3 existing next to each other) or as a one-phase material written as $Li_{1+x}Me_{1-x}O_2$. The Li-rich NCM's (also called HE-NMC) need an activation charge to 4.7 V vs. Li^+/Li (characterized by a charge plateau only present during the first charge) in order to access the total specific capacity which is higher than 300 mAh/g in the first charge cycle. Reversibly, 250 mAh/g can be used from the HE-NMC materials, as these materials can be completely delithiated.[73] The material is not yet commercialized mostly for two reasons: (i) Due to the high operating potential (up to 4.7 V vs. Li^+/Li) and the loss of reactive oxygen from the surface of the lattice[74] both electrochemical electrolyte oxidation (especially at elevated temperatures) and chemical electrolyte oxidation affects the long-term cycling performance and (ii) voltage fading occurs which means that the voltage during discharge decreases and hence leads to an energy fade.[75]

Battery Testing

In the following, important terms and protocols are defined which are central to lithium-ion battery research. The specific capacity of a battery material (e.g. a graphite anode or a LNMO cathode) is calculated with equation 3:

$$Q_{spec.} = \frac{n \cdot F}{M} \tag{3}$$

where $Q_{spec.}$ is the specific capacity (in units of As/g, generally converted to mAh/g), n is the number of exchanged lithium ions per unit formula, F the Faraday constant (96485 As/mol) and M is the molar mass (in g/mol). When lithium ion batteries are assembled, the capacities of anode and cathode are balanced such that the anode could take up slightly more lithium than the cathode can provide upon its delithiation to a fixed upper cutoff potential. This is done for safety reasons because if the cathode capacity exceeds the anode capacity already during the first cycle, lithium plating occurs which not only compromises the long-term durability but also may lead to safety hazards. A typical balancing factor of cathode to anode total capacity is 1 : 1.1 (cathode to anode ratio, used in this work), however commercial cells are balanced more closely to 1 : 1 in order to increase their energy density. This balancing factor does not cause lithium plating as during the first charge lithium-ions from the cathode are also used for building up the SEI.

A further important term is the so called C-Rate. The C-rate (equation 4) defines the relationship between the current (I) which is drawn from a battery and the total capacity (Q):

$$C - Rate = \frac{I\ [A]}{Q\ [Ah]} = 1/h \tag{4}$$

A C-Rate of one is defined as charging or discharging the total capacity of the battery in one hour. After matching the capacities of anode and cathode and building a lithium-ion cell, generally two formation cycles at C/10 (i.e., one charge takes 10 h) are carried out. The slow cycles at the beginning ensure enough time so that the solid electrolyte interphase (SEI) can form on the graphite anode. In Figure 1.2, a typical formation protocol is shown for graphite/LNMO cells at 25 °C with a cathode loading of 1.9 mAh/cm^2 and a respective anode loading of 2.1 mAh/cm^2. The typical charging protocol consists of a constant current charge (CC) followed by a constant voltage (CV) phase. The constant current charge is carried out with C/10 (=0.19 mA) followed by a CV phase which has a cut-off criterion for the current of C/20. After this, a constant current discharge at C/10 is applied. The cell cut-off

voltages for graphite LNMO cells are 4.8 V as upper cut-off and 3.5 V as lower cut-off. Figure 1.2 further shows the half-cell voltages vs. Li^+/Li determined with a lithium reference electrode of graphite vs. Li^+/Li (in blue) and of LNMO vs. Li^+/Li (in red).

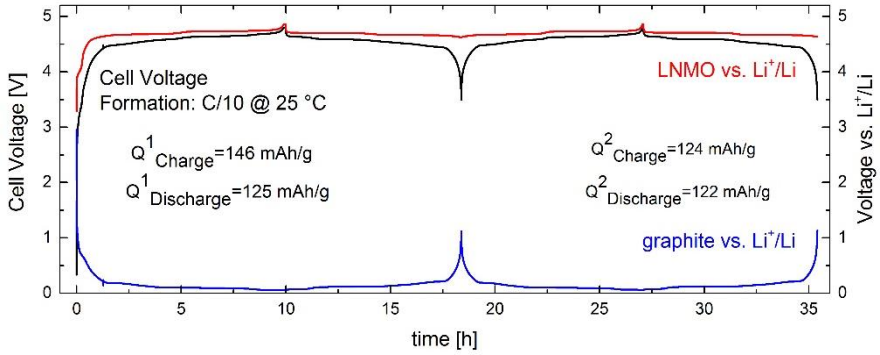

Figure 1.2: Formation protocol of a graphite/LNMO cell with a loading of 1.9 mAh/cm^2, a balancing factor of 1:1.1 (cathode:anode), two glass fiber separators and 60 µL of an EC/EMC electrolyte with 1M $LiPF_6$ with a lithium reference electrode. The full-cell voltage is shown in black, the cathode half-cell voltage in red and the anode half-cell voltage in blue. The full-cell voltage is plotted on the left y-axis and the half-cell voltages are plotted on the right y-axis.

The cell voltage V_{Cell} corresponds to the difference between the half-cell voltages: $V_{Cathode} - V_{Anode}$. The cell cut-off of 4.8 V ensures that the total capacity of LNMO can be used, as up to the end of charge the cathode voltage (in red) turns vertically, meaning that the cathode does no longer contain lithium-ions. The first charge capacity is 146 mAh/g_{LNMO} which corresponds to the theoretical capacity of LNMO. The first discharge capacity is 125 mAh/g resulting in a first-cycle coulombic efficiency ($Q_{Discharge}$ / Q_{Charge}) of ≈86% due to the SEI formation of the graphite anode. The second cycle has a coulombic efficiency of ≈98.3% based on a charge capacity of 124 mAh/g and a discharge capacity of 122 mAh/g, indicating that the SEI formation is almost finished. The lower cut-off of 3.5 V is chosen in order to empty the graphite anode completely (anode voltage is above 1 V and here the graphite contains no more lithium) and hence ensure the total utilization of the active lithium. The LNMO voltage stays always on the plateau as the cathode cannot be lithiated (cell discharge) completely due the lithium loss from SEI formation. A further important term is the state-of-charge (SOC). The SOC of a standard lithium-ion battery (full-cell configuration and limiting cathode, equation 5) defines the position of the active lithium in the cell:

$$SOC = 100 \cdot \frac{Q_{Cell} - Q_{Cathode}}{Q_{Cell}} \% \quad (5)$$

If all active lithium is stored in the cathode (discharged state) then the SOC is defined as 0%; all active lithium is stored in the anode (charged sate) then the SOC is 100%.

1.2 Challenges of $LiNi_{0.5}Mn_{1.5}O_4$ (LNMO) cathodes

LNMO is an interesting cathode material for lithium-ion batteries as it is cobalt-free and provides a high energy density. However, the high operating potential of ≈4.75 V vs. Li/Li^+ causes some severe challenges. One challenge is the capacity retention of graphite/LNMO cells at elevated temperatures. Lu et al.[21] carried out charge/discharge cycling experiments at 25 °C and at 55 °C. The capacity retention is stable when cells are cycled at 25 °C however when the temperature is switched to 55 °C drastic capacity fading occurs. As 55 °C are very harsh conditions for lithium-ion batteries – as the equilibrium of $LiPF_6$ is shifted to the gaseous and reactive lewis acid PF_5 which triggers side reactions leading to active lithium loss – a more reasonable condition is 40 °C. Figure 1.3 shows graphite/LNMO T-cells with a loading of 1.9 mAh/cm^2 (cells used in this thesis) cycled at 1C CCCV charge and a 1C CC discharge at 25 °C or at 40 °C. For the cells cycled at 40°C, each 22nd two 1 C charge and 3 C discharge cycles are carried out in order to probe the resistance/C-rate dependence of the full-cells.

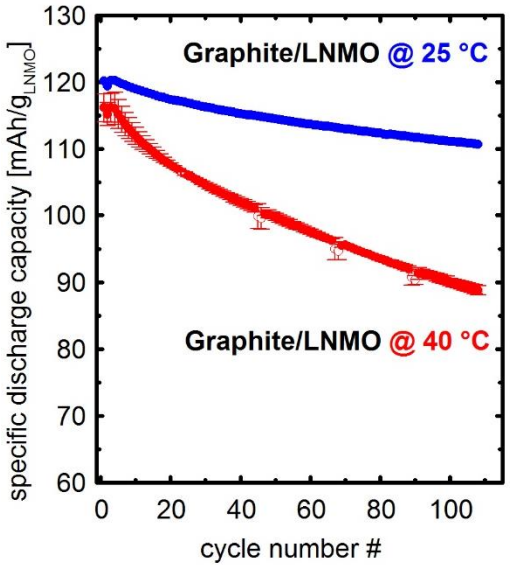

Figure 1.3: graphite/LNMO cells with a loading of 1.9 mAh/cm^2 with two glass fiber separators, a gold-wire reference electrode (GWRE) and 60 µL of LP57 electrolyte. Before the cells are cycled in the 1C/1C at 40 °C charge/discharge procedure, two formation cycles at 25 °C are carried out.

The cells cycled at 25 °C (blue curve) show a specific discharge capacity of ≈120 mAh/g after formation and a capacity loss of ≈10 mAh/g over the course of 108 charge/discharge cycles. When nominally identical cells are cycled at 40 °C, the

specific discharge capacity after formation is ≈118 mAh/g and the capacity loss after 108 charge/discharge cycles is almost ≈30 mAh/g. These data sets already point out that an increased temperature is a severe problem for this cell chemistry. The phenomenon of the strong capacity fade at elevated temperatures is seen in the transition metal dissolution – both nickel and manganese – from the high-voltage spinel cathode[20] followed by a subsequent damage of the SEI on the graphite anode.[76]

Pieczonka et al.[77] have analyzed the transition metal dissolution of LNMO half-cells by harvesting the electrolyte of half-cells stored at a 100% SOC for 60 days at different temperatures. They could show that already increasing the storage temperature from 30 °C to 45 °C increases the amount of dissolved nickel by a factor of 1.5 and the dissolved manganese by a factor of 2.5. The reason of transition metal dissolution is seen in the formation of protic species, e.g. HF at high voltages, which was already stated for the LNMO cell chemistry by Aurbach et al.[78] HF corrodes the high-voltage spinel cathode, leading to a surface composition of MnF, MnO_2 and a loss of transition metals. Indeed, Metzger et al.[79] could indirectly proof that protic species are formed at high potentials (> 4.5 V vs. Li^+/Li). This was examined by operando gas analysis of graphite/NMC cells. When regular cells are charged to high potential, increased amounts of H_2 were found; however when a sealed Ohara-glass is placed between anode and cathode and the cell is charged to high potential, no H_2 formation was observed. This result suggests that protic species, e.g. HF are formed at high potentials which are than reduced on the graphite anode in order to form hydrogen gas.

The detrimental effect of protons leading to transition metal dissolution has been investigated by Leitner et al.[80] They performed cycling experiments with a graphite/LNMO pouch cells utilizing three different separators: (i) a conventional separator (polyolefin based), (ii) a separator consisting of an LTO coated PET non-woven sandwiched between two polyolefin separators and (iii) an electroactive separator consisting of an LTO coated PET non-woven sandwiched between two polyolefin separators where the LTO has been lithiated prior to cell assembly. Both cases (i) and (ii) show the expected capacity fading during cycling at 45 °C. However in case (iii) the separator contains lithiated LTO which has a potential of ~1.55 V vs.

Li^+/Li and can hence reduce protons to hydrogen and also reduce the dissolved metals, e.g. Mn^{2+} and Ni^{2+} and act as a scavenger. By using an electroactive separator, 500 cycles at 45 °C can be reached without almost any loss in discharge capacity. This further underlines that transition metal dissolution is the main ageing mechanism of graphite/LNMO cells at elevated temperatures.

1.3 Challenges of Ni-rich NMC cathodes

Ni-rich cathode materials tend to have an increased reactivity of the surface towards moisture and CO_2 with increasing nickel content. These reactions cause a high basicity of the materials and lead to a gelation of the ink during slurry preparation, resulting in cathode coatings with very bad mechanical and electrochemical properties. Zhao et al.[81] investigated different cathode materials like lithium nickel oxide (LNO) and the high-voltage spinel (LNMO) via CO_2 adsorption micro calorimetry. With this technique, the adsorption of CO_2 on the cathode material allows for the quantification of the basic sites via measuring the differential heat and coverage of CO_2 on the surface. They found that LNO reacts heavily with CO_2 and shows the largest coverage of it on the surface, whereas the LNMO cathode does not react with CO_2. This study implies that Ni-rich NCM surfaces are highly reactive compared to other generally used cathode materials. Next, it is interesting what species can be found on nickel-rich cathode materials and how they affect the cycle life.

In this context, Jung et al.[15] compared the storage properties of NMC111 and NMC811 regarding the surface composition and the electrochemical performance. By storing electrodes for up to 1 year in ambient air, NMC111 cathodes showed no capacity loss nor an increase in cell polarization after 1 year storage and the Raman spectra of the pristine NMC111 and 1-year stored NMC111 were almost identical. This picture changes tremendously when performing the identical experiments with NMC811. Here a loss in specific capacity and an increased polarization is observed for the 1 year stored sample. Also, the Raman spectra develop a novel feature and do not match the pristine NMC811 spectra. By analyzing numerous different compounds, the authors found that the dominant species on this material is $(NiCO_3)_2*(Ni(OH)_2)_3*4H_2O$ in the following referred to as “nickel basic carbonate hydroxide” (NBCH). The accumulation of this surface species over one year of ambient storage of NMC811 was paralleled by a strong capacity fading (compared to the pristine sample) and an increasing cell polarization stemming from the cathode.

A further frequently observed surface species on the surface is lithium carbonate, which was investigated in literature for LNO cathodes. Liu et al.[82] stored $LiNiO_2$ powder up to 1 year in air and reported a decrease of specific capacity and an increase in the polarization of these materials, which increases with storage time. By using XRD analysis, they found that the sample stored in air for one year shows an Li_2CO_3 content of up to 13.3%. Interestingly, they have also observed a reduction of Ni^{3+} to Ni^{2+} by measuring XPS in the Ni 2p region. They claim that the reduction of the nickel occurs spontaneously and can next to the formation of Li_2CO_3 be the source for the drop of capacity and increase of the polarization of LNO cathodes. Similar results have been reported by the same group[83] on the cathode material $LiNi_{0.8}Co_{0.2}O_2$. They found Li_2CO_3, and LiOH on the surface of the cathode material. Summing up, nickel-rich cathode materials show a strong reactivity of the surface towards moisture and CO_2, which strongly affects the electrochemical performance of these materials.

In the literature, some methods to remove surface impurities have already been proposed. Kim et al.[84] removed LiOH and Li_2CO_3 surface contaminants on NCA material by washing the cathode material in water. Here, they stirred 20g of NCA in 50 mL of water for 30 minutes. After heating the material, they determined the moisture and carbon content on the NCA material and could show that both were reduced by an order of magnitude. Further, they showed that after washing, the materials are much more resistant towards the uptake of moisture or Li_2CO_3. Lastly, they could also show an increase in cycling performance of the NCA electrodes when washing is carried out. They attribute this to the removal of surface impurities on the cathode material upon washing.

In this PhD thesis, the last section will deal with the washing process of nickel-rich cathode materials, as this process is not well described in the literature and could be a path in order to stabilize the surface of nickel-rich materials. The aim of chapter 3.2 is a detailed understanding how nickel-rich materials react with moisture and how the surface changes after washing the cathode materials.

2 Experimental Methods

2.1 Electrochemical Impedance Spectroscopy (EIS)

The literature of this part is based on Lvovich[85], Lasia[86] and Gasteiger.[87] Electrochemical Impedance Spectroscopy (EIS) is a non-destructive technique, which allows for the analysis of interfaces in electrochemical systems. The general principle of impedance spectroscopy is based on applying an AC voltage U with an amplitude U_A (V) at a certain frequency f (Hz). The voltage can be written time-dependent with the following expression:

$$U(t) = U_A \sin(2\pi f t) = U_A \sin(\omega t) \tag{6}$$

The frequency term is expressed as "radial frequency" which is defined as: $\omega = 2\pi f$. As a sinusoidal voltage is applied to an electrochemical system and the requirements of an EIS measurement are linearity, also the measured current will be a sinusoidal signal. This signal however is shifted in phase, which depends on the resistive, capacitive, and inductive properties of the system. The response current to the voltage signal can also be written in a time-dependent form I(t) which is shifted in phase (Φ) and has an amplitude I_A:

$$I(t) = I_A \sin(\omega t + \Phi) \tag{7}$$

By using Euler's formula, the impedance can be converted in a complex form:

$$e^{i\Phi} = \cos\Phi + i\sin\Phi \tag{8}$$

With Ohm's Law – dividing the voltage U(t) by the current I(t) - the impedance can be expressed in a complex form by rewriting the time-dependent voltage as $U(t) = U_A e^{i\omega t}$ and the time-dependent current as $I(t) = I_A e^{i\omega t - i\Phi}$:

$$Z^* = \frac{U(t)}{I(t)} = \frac{U_A e^{i\omega t}}{I_A e^{i\omega t - i\Phi}} = Z_A e^{i\Phi} = Z_A(\cos\Phi + i\sin\Phi) = Z_{real} + iZ_{im} \quad (9)$$

Z_{real} is the real part of the impedance and Z_{im} is the imaginary part of the impedance. A very common representation of impedance spectra is the so-called Nyquist Plot where the negative imaginary part of the impedance is plotted on the y-axis and the real part of the impedance is plotted on the x-axis. The imaginary axis is flipped and shows negative values in positive y-direction, as most electrochemical systems show capacitive behavior.

In general, an impedance spectrum allows for the quantification of the resistance and capacitance contributions of an electrochemical system. In order to understand the impedance response of an electrochemical system (e.g. a lithium-ion battery) the impedance of a resistor and a capacitor must be defined. The impedance of a resistor R is independent of frequency, has no phase-shift, and can be written as $Z_{R(\omega)} = R$. The imaginary part of the impedance is zero for all measured frequencies and the real part is the resistance R. In Nyquist representation, a resistor is a point on the real axis.

The impedance of a capacitor is phase-shifted by $\pi/2$ and shows a dependency on the measured frequency. The impedance of an ideal capacitor can be written as $Z_{C(\omega)} = \frac{1}{i\omega C}$. The imaginary part of a capacitor goes towards zero with the frequency going to infinitely high values. The real part of a capacitor is zero for all measured frequencies. In order to understand an electrochemical interface, electrical equivalent circuits with a parallel connection of a resistor R and a capacitor C are commonly used. The first representing charge transfer reactions and the second represents double-layer charging/discharging.

Figure 2.4 shows a simple equivalent circuit which helps to understand the impedance spectrum of a lithium-ion battery. However, this equivalent circuit oversimplifies the impedance of a lithium-ion cell and is only shown in order to explain the most basic features of the impedance spectrum of an electrochemical system. The equivalent circuit consists of the high frequency resistance R_{HFR}, which describes the separator resistance, a parallel R_{CT}/C_{CT} element describing the charge transfer resistance and capacitance of anode and cathode with the electrolyte phase, and last a Warburg element reflecting diffusion.

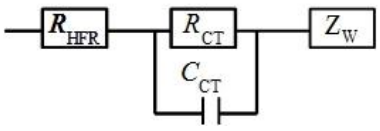

Figure 2.4: Simple equivalent circuit consisting of a high frequency resistance R_{HFR} serially connected to a parallel connection of a R_{CT}/C_{CT} element, and last a Warburg element Z_W.

Generally, the impedance is measured from highest frequencies (100 kHz, typical for a small lithium-ion test cell) to the lowest frequencies (typically 100 mHz or less) by applying a voltage amplitude (around 10 mV) between working- and counter electrode. At the highest frequencies (~100 kHz), the current during the impedance flows mostly through the high frequency resistance R_{HFR} and through the capacitor C_{CT}, as at high frequencies the impedance of the capacitor approaches zero. Therefore, the impedance consists only of the R_{HFR} element at the highest frequencies and allows for the assessment of the separator resistance if the impedance goes towards zero for highest frequencies. Once the frequency is lowered, the impedance of the capacitor grows and the current now flows both through R_{CT} and C_{CT}. As the impedance of a capacitor goes towards infinity for low frequencies, the current then flows only through the resistor (R_{CT}). Due to this, a semi-circle is observed in impedance spectra for a parallel connection of a resistor and a capacitor. At very low frequencies, the Warburg element Z_W becomes dominant which results in a 45° line.

Figure 2.5 shows a typical Nyquist plot of a lithium-ion battery (graphite/LNMO full cell, 100 kHz – 100 mHz) in order to explain the features of an impedance spectrum. Every point in an impedance spectrum is determined by the length of the vector |Z| (ratio of the voltage and current amplitude) and the phase shift Φ between voltage and current signal. This is illustrated for the 900 Hz point in Figure 2.5. A very important frequency in impedance spectroscopy is the apex frequency of a semi-circle (marked with f_{apex} in Figure 2.5). If this feature is a true R_{CT}/Q_{CT} element semi-circle, f_{apex} is defined as:

$$f_{apex} = \frac{1}{2\pi RC} \tag{10}$$

By the frequency of the semi-circle maximum and the diameter of the semi-circle (generally called low frequency resistance (LFR)) the capacitance of the lithium-ion battery (sum of anode & cathode) can be assessed according to equation 10. The

capacitance probes the double-layer of an electrochemical system and is therefore proportional to the surface area of the electrodes.

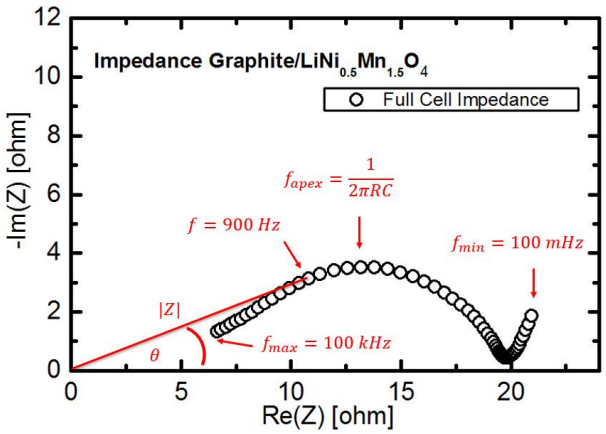

Figure 2.5: Full-cell impedance spectrum of a graphite/LNMO cell (7.0 $mg_{graphite}/cm^2$ and 13.6 mg_{LNMO}/cm^2) after formation (2 cycles at C/10) at 50% SOC. The impedance is measured from 100 kHz – 100 mHz with a voltage perturbation of 15 mV at 25 °C.

As the impedance is measured at different frequencies, processes with different time constants are probed at a different location in the Nyquist plot. The time constant τ is defined as:

$$\tau = RC \tag{11}$$

In Figure 2.5, the impedance is measured between cathode and anode and only one semi-circle appears for both electrodes. This results out of the consequence that both the capacitance C (~surface area) and the resistance R (charge transfer reaction) are very similar and have hence a very similar time constant. In order to understand the complex interactions in a lithium ion battery the anode and cathode impedance must be separated. The complex interplay of cathode and anode and a method in order to deconvolute the impedance of both is described in the next section.

2.2 Deconvolution of the full-cell impedance into its contributions of anode & cathode

In order to illustrate the amount of parameters which are measured with one full-cell impedance, Figure 2.6 shows a schematic overview of a graphite/LNMO cell with all the resistance, capacitance and diffusion contributions. Note that the before explained ideal capacitance C is replaced by a constant phase element Q. The impedance of a constant phase element is defined as: $Z_{\mathrm{Q}(\omega)} = \frac{1}{(i\omega)^{\alpha}Q}$. The only difference to the capacitance C is the exponent α accounting for the existence of depressed semi-circles and not perfect semi-circles in most of the impedance spectra. This phenomenon is related to the surface roughness/porosity of electrodes.[88]

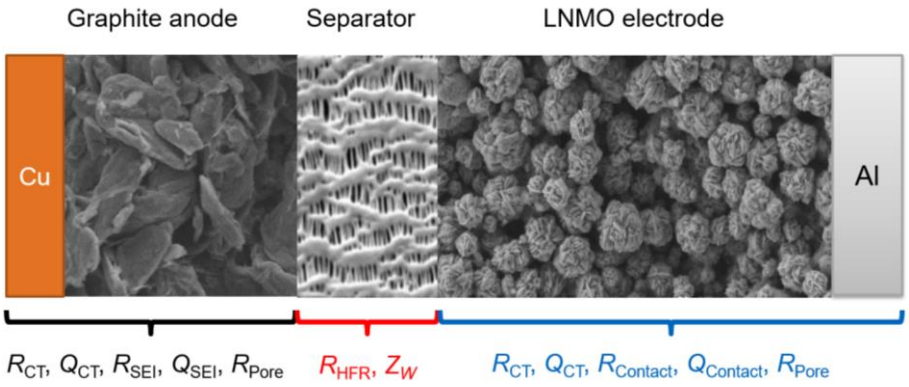

Figure 2.6: Schematic representation of a graphite/LNMO lithium-ion battery with different contributions from resistances and capacitances which contribute to the full-cell impedance spectrum.

Figure 2.6 illustrates the different contributions to the full-cell impedance spectrum shown in Figure 2.5. Starting from the left, the anode shows a contribution from the charge transfer reaction (R_{CT} and Q_{CT}) and a contribution from the solid electrolyte interface (R_{SEI} and Q_{SEI}) which covers the graphite particles. Further, as lithium-ion batteries consist of porous electrodes, the ionic resistance within the electrolyte phase (R_{Pore}) of the porous graphite particles has to be taken into account. Ogihara et al.[89] showed that the ionic resistance has a huge contribution to the overall impedance response of a porous electrode. The separator phase contributes at highest frequencies with the ionic resistance of the electrolyte soaked separator (R_{HFR}) and at lowest frequencies to the diffusion of lithium-ions in the electrolyte

phase (Z_W). Lastly, the cathode contributes also with the charge transfer reaction (R_{CT} and Q_{CT}) and the pore resistance (R_{Pore}) to the full cell impedance. A further impedance characteristic stemming from the cathode is the contact resistance ($R_{Contact}$ and $Q_{Contact}$) between aluminum current collector and cathode coating. The existence and appearance of the contact resistance to the impedance of the cathode was first shown by Gaberscek et al.[90] In this publication they showed that the impedance of the cathode is dominated by a high-frequency semi-circle stemming from the electrode/current collector interface by coating an LFP electrode on an aluminum current collector and an aluminum foil with conductive silver paste. On the standard aluminum current collector the high-frequency semi-circle was observable, whereas it was not observed for electrodes coated on the silver paste coated current collector. This high-frequency semi-circle has been interpreted incorrectly as the so-called cathode electrolyte interface (CEI) by many publications in the literature.[78,91] The presence of numerous resistance and capacitance contributions from anode and cathode in one full-cell impedance spectrum make it very clear that in order to understand the impedance of a lithium-ion cell one must use a method to separate the half-cell impedances (of anode and cathode) separate from the full cell impedance.

One "ex-situ" technique is the symmetrical cell approach. Chen et al.[92] introduced this approach to the battery community by charging an 18650 cell to 50% SOC and then punching out two anodes and two cathodes from the large cell and assembling coin cells in symmetrical configuration. Petibon et al.[93] used this approach for the evaluation of electrolyte additives. They showed that some commonly used additives – dependent on their concentration and combination – react both on the anode and cathode. With this approach, a much better understanding of the way additives work in a lithium-ion cell could be provided.

As the symmetrical cell approach is an ex-situ method, in order to monitor the half-cell impedances over cycling or at different states-of-charge many cells have to be assembled and afterwards disassembled. A technique where anode and cathode impedance can be measured "in-situ" during cycling is based on the use of a reference electrode. Ender et al.[94] carried out simulations of reference electrode setups with a centered reference electrode located at the outer perimeter of the

separators. Here they could show that such a setup is very sensitive towards geometrical misalignment. A small shift of anode and cathode towards each other in a real lithium-ion battery setup (high electrolyte conductivity) leads to an asymmetric field distribution at the edges of the electrodes. This has as a consequence that the half-cell impedances have a different high frequency resistance (HFR) and a different magnitude of the impedance, even if identical electrodes are used as anode and cathode. Another type of misalignment is seen when electrodes are used which differ largely in their kinetics as for example LFP (porous intercalation electrode with high surface area) and lithium metal. Here the time constants of both electrodes are very different and have hence overpotentials at different frequencies which affects the potential of the reference electrode. This kind of misalignment leads to the existence of high and low frequency inductive loops in the impedance spectra of the half-cells. The authors recommend to insert a reference electrode between anode and cathode in order to minimize artefacts. Reference electrodes which are inserted between two separators have to be very small and are hence called "micro-reference electrodes" or "µ-reference electrodes".

Dees et al.[95] showed in their simulations that the alignment of an external reference electrode significantly impacts the impedance of the half-cells. They further analyzed the use of an internal reference electrode with a diameter of 25 µm. The wire itself distorts the potential field of the electrolyte but this has an insignificant impact on the accuracy of the impedance measurement. In order to record meaningful impedance data with a micro-reference electrode the authors state that the diameter of the wire should be on the order or less than the thickness of the separators used.

Besides the geometry, it is important that the potential of the micro-reference electrode only shifts little within the time scale of the impedance measurement. Victoria et al.[96] show both the effect of the amplitude and of potential drifts on the quality of impedance spectra. Regarding the amplitude, a small perturbation (< 2 mV) gives a poor signal-to-noise ratio for the impedance spectra whereas a large amplitude leads to a non-linearity of the impedance response. A frequently used amplitude for recording impedance spectra is 10 mV. Lastly, also potential

drifts during the impedance measurement results in unreliable impedance data. Therefore, a stable potential of the micro-reference is necessary in order to get true information from the impedance measurement. Most micro-reference electrodes consist therefore of lithium alloys or lithium metal plated on the tip of the wire.

Zhou et al.[97] developed a micro-reference electrode consisting of a 40 µm thick insulated copper wire where lithium metal is plated in-situ on the tip of the wire. Lithium metal plated up to a layer thickness of 4 µm showed a very good long-term potential stability of more than 1500 h. Abraham et al.[98] used a tin-wire with a diameter of 25 µm which was in-situ lithiated to form a lithium-tin alloy (Li-Sn_x). The potential of this RE was stable for more than one week at 25 °C but was unstable at 55 °C. The data measured with this micro-reference electrode was self-consistent and produced reliable impedance data.

In this PhD thesis a micro-reference electrode – the so-called gold wire reference electrode (GWRE)[99] - was developed and used in all further studies and marks also the first part of the Results chapter (3.1). The GWRE fulfills all the above listed requirements such as: (i) placement of the wire between two separators, (ii) insulation of the wire with polyimide so that only the tip of the wire is in contact with the electrolyte, (iii) a small diameter of the wire (50 µm gold wire + 7 µm polyimide insulation) compared to the thickness of the separators (2 x 200 µm, glassfiber separator), and (iv) a stable potential versus metallic lithium ensured by an in-situ lithiation. Figure 2.7 shows the application of the GWRE in a graphite/LNMO cell chemistry measured at 10% SOC at 40 °C. The plot is used in order to show that meaningful impedance spectra can be achieved with this technique. The full-cell impedance spectrum is shown in black, the anode impedance is shown in red and the cathode impedance in blue. The anode impedance shows the largest impedance (diameter of the semi-circle) contributing to the full-cell impedance.

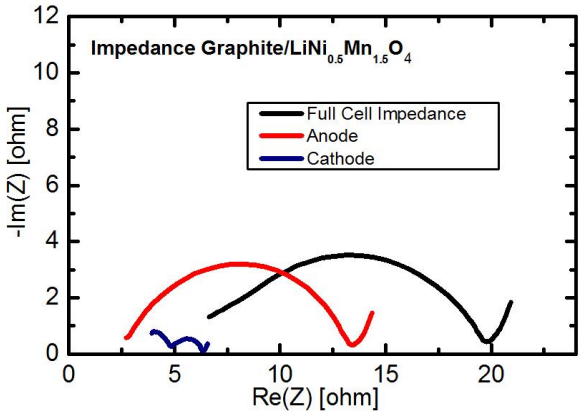

Figure 2.7: Impedance response of a graphite/LNMO cell equipped with a gold wire reference electrode (GWRE). The impedance was recorded at 10% SOC and at 40 °C. The full-cell impedance is shown in black, the anode impedance in red, the cathode impedance in blue.

The cathode impedance is small compared to the anode impedance and shows two semi-circles. In Figure 2.6 all the listed parameters are hidden beneath one full-cell impedance. By using a micro-reference electrode, anode and cathode contribution to the full cell impedance can be separated and so a much better understanding of the impedance can be generated. Based on this technique, this PhD Thesis tries to provide a better understanding of the half-cell impedance of anode and cathode in a full-cell configuration during operation of a lithium-ion battery.

2.3 Further Experimental Techniques

X-ray photoelectron spectroscopy (XPS)

X-ray photoelectron spectroscopy was used in order to characterize the surface of samples for the last chapter of this thesis (Washing of Ni-rich cathode materials). The experiments were carried out on an Axis Supra spectrometer from Kratos with an automated sample handling. For sample preparation, an air-tight sample loading device from Kratos was used, avoiding any air or moisture contamination of the samples. All samples were pressed to a pellet (diameter of 3 mm) inside an argon-filled glovebox. The samples were mounted on a conductive copper foil which was placed on a sample holder where the metallic surface was covered by an adhesive paper in order to ensure electronic insulation. After the preparation, the sample was connected to the flexi-lock of the XPS without any exposure to air. The sample was kept in the flexi-lock antechamber until a pressure of $\approx 10^{-8}$ torr was reached and was then transferred to the sample analysis chamber (SAC) where the pressure was always kept below $\approx 10^{-9}$ torr during the whole measurement period. Sample irradiation was carried out with monochromatic Al K_α radiation (1486.6 eV) with an emission current of 15 mA. Survey spectra were recorded for all samples with a stepsize of 0.5 eV and at a pass energy (PE) 160 eV. Elemental spectra were recorded with a step size of 0.2 eV, and an emission current of 15 mA and a pass energy of 20 eV. For all measurements a charge neutralizer was used and the spectra were calibrated to the adventitious carbon peak with a binding energy (BE) of 284.8 eV. In order to ensure high data quality, several spectra were recorded and averaged by the Escape software from Kratos.

On-line Electrochemical Mass Spectrometry (OEMS)

In order to assess the anodic stability of the additive VC (chapter 3.1.2) or analyze the effect of washing on the gassing of NCM cathodes (chapter 3.2), a custom-made gas analysis system with a closed battery cell was used according to Tsiouvaras et al.[100] The battery test cell was coupled to a mass spectrometer via a crimped capillary with a calibrated leak of 1 µl/min what allows measurement times around 30 h. The analyzed cathodes were coated on a stainless steel mesh (SS316, aperature 26 µm, wire diameter 25 µm, The Mesh Company Ltd., UK) in order to record the evolved gases. OEMS cells were always assembled in an argon-filled glove box with a lithium metal counter electrode, one glassfiber separator and a carbon black or NCM851005 working electrode. As electrolyte, 1.5 M $LiPF_6$ dissolved in ethylene carbonate (EC) was used. The cells were connected to the mass spectrometer system after assembly and then a 4 h OCV (open circuit voltage) period was carried out. Afterwards either linear sweep voltammetry (LSV) to 5.5 V vs. Li^+/Li or a constant current charge (CC) to 5.0 V vs. Li^+/Li was carried out. The mass spectrometer currents were quantified by a calibration gas containing 2000 ppm of each H_2, CO_2, O_2 and C_2H_4 in argon. In order to account for pressure or temperature effects on the evolved gases all mass currents were normalized to the mass current of argon (m/z = 36).

3 Results

This section contains the published work and the manuscripts which are currently under review or will be submitted soon. Section 3.1 presents the results of the studies on electrochemical impedance spectroscopy with a µ-reference electrode. In section 3.1.1 the development of the gold wire reference electrode (GWRE) is presented. Here the lithiated gold-wire is benchmarked and validated that it produces correct half-cell impedance spectra. The reference electrode is then applied in the analysis of the prominent additive Vinylene carbonate in a graphite/LNMO cell system (section 3.1.2). In this chapter impedance spectra of the graphite anode and the LNMO cathode were recorded. In order to more precisely deconvolute the various contributions to anode and cathode impedances, a novel impedance procedure was developed and demonstrated with graphite/LNMO full cells (section 3.1.3). It is based on the concept of driving a given electrode into blocking conditions by holding the cell potential such that the respective electrode is fully delithiated, in which case its charge transfer resistance becomes very large. With the novel procedure the LNMO impedance could be deconvoluted in its resistance contributions. Subsequently, this novel procedure was applied to analyze the graphite anode (section 3.1.4) and here the resistance contribution could be deconvoluted as well as manganese dissolution from the LNMO cathode was correlated with a new feature of the anode impedance. After analyzing the anode and cathode impedance in a full-cell, the most interesting feature of the cathode impedance (high-frequency semi-circle) is investigated in detail (section 3.1.5) and electrochemical electrolyte oxidation could be correlated with the cathode impedance response.

In section 3.2, the washing process of Ni-rich materials is investigated and a detailed mechanism about the washing process is presented.

3.1 Electrochemical impedance spectroscopy with a micro-reference electrode

3.1.1 Development of a micro-reference electrode

This section presents the article *"A Gold-Micro Reference Electrode for Impedance and Potential Measurements in Lithium Ion Batteries"*.[99] The paper was submitted to the peer-reviewed Journal of the Electrochemical Society in June 2016 and published in August 2016. The article is published open access and distributed under the terms of the Creative Commons Attribution 4.0 License. The permanent web link is available under: http://jes.ecsdl.org/content/163/10/A2265. The article was presented by Sophie Solchenbach at the PRiME meeting 2016 in Honolulu (USA) in October 2016 (Paper 211).

Most of the impedance measurements in the literature are carried out in a full-cell configuration,[65,101] however as the impedance contribution from anode and cathode have a similar time constant, they cannot be separated from the full-cell impedance spectrum. This means that a rigorous quantitative interpretation of these impedance spectra is almost impossible. Methods to separate the impedance of anode and cathode are either the assembly of symmetrical cells (pair of anodes and pair of cathodes)[92] or the use of a micro-reference electrode.[95,97,102–104] The symmetric cell approach requires a large number of experiments and to the disassembly of the original cell that can easily introduce errors. Regarding reference electrodes, different designs are used in the literature, such as ring electrodes arranged concentrically around the reference electrode[102] which are very sensitive towards misalignment. A better choice are reference electrodes inserted between the separators which minimize the risk of geometric misalignment.[94]

In this study we developed a micro-reference electrode which takes all the advantageous designs from the literature and combines them together in order to get an artefact free impedance response. Important criteria are: (i) small diameter of the reference electrode compared to the thickness of the separators,[95] which is realized by a polyimide coated gold wire with a diameter of 57 µm (ii) positioned

between the separators in order to mitigate any edge effects leading to inductive loops and cross contamination of the half-cell impedance spectra.[94] This is ensured by a new reference stamp design and (iii) a stable potential of the RE.[98] A stable reference electrode potential is achieved by an in-situ lithiation of the gold wire reference electrode (GWRE) from the cathode. This leads to the formation of a gold-lithium alloy with a stable potential of 311 mV versus metallic lithium with a long-term stability of more than 500 h (even at elevated temperatures). Its very long potential stability makes the GWRE not only feasible for impedance measurements, but also for half-cell potential measurements of anode and cathode versus the GWRE. We validated the half-cell impedance response with a symmetrical cell approach and showed that impedance spectra obtained from GWRE measurements are identical to the impedance spectra from symmetric cells. Lastly, we tried to reproduce impedance data from the literature by investigating the reduction of vinylene carbonate (VC) on graphite anodes. Here we could show that by using a similar VC to active material ratio of the additives (and not simply the additive concentration) we could reproduce the data from Burns et al.[105]

Author contributions

D.P. and J.L. developed the three-electrode design in order to host the gold wire. D.P. and S.S worked on the alloying process of the gold wire in order to obtain a stable potential. D.P., S.S., and E.K., performed the electrochemical measurements. The data was analyzed by S.S., D.P. and J.L. and the manuscript was written by S.S. and H.A.G. All authors discussed the data and commented on the results.

A Gold Micro-Reference Electrode for Impedance and Potential Measurements in Lithium Ion Batteries

Sophie Solchenbach,[a,*,z] Daniel Pritzl,[a,*] Edmund Jia Yi Kong,[a,b] Johannes Landesfeind,[a,*] and Hubert A. Gasteiger[a,]**

[a]*Chair of Technical Electrochemistry, Department of Chemistry and Catalysis Research Center, Technische Universität München, D-85748 Garching, Germany*
[b]*Singapore Institute of Technology, Singapore*

Impedance measurements of lithium-ion batteries are a powerful tool to investigate the electrolyte/electrode interface. To separate the contributions of anode and cathode to the full-cell impedance, a reference electrode is required. However, if the reference electrode is placed inappropriately, the impedance response can easily be biased and lead to erroneous conclusions. In this study, we present a novel micro-reference electrode for Swagelok-type T-cells which is suitable for long-term impedance and reference potential measurements. The reference electrode consists of a thin insulated gold wire, which is placed centrally between cathode and anode and is in-situ electrochemically alloyed with lithium. The resulting lithium-gold alloy reference electrode shows remarkable stability (>500 h) even during cycling or at elevated temperatures (40°C). The accuracy of impedance measurements with this novel reference electrode is carefully validated. Further, we investigate the effect of different vinylene carbonate (VC) contents in the electrolyte on the charge transfer resistance of LFP/graphite full cells and demonstrate that the ratio of VC to active material, rather than the VC concentration, determines the impedance of the anode SEI.
 [DOI: 10.1149/2.0581610jes]

Manuscript submitted June 7, 2016; revised manuscript received July 26, 2016. Published August 19, 2016. This article is a version of Paper 211 from the Honolulu, Hawaii, Meeting of the Society, October 2–7, 2016.

The lifetime of lithium-ion batteries strongly depends on the properties of the interfaces between each electrode and the electrolyte. Electrochemical impedance spectroscopy (EIS) is a simple and non-destructive method to investigate the kinetics of active materials, the resistance of electrode/electrolyte interfaces, and the effect of electrolyte additives.[1,2] As impedance measurements of full-cells always reflect the sum of both electrodes, it is difficult to deconvolute the individual contributions by the cathode and the anode. To gain insight into the impedance of individual electrodes, measurements on symmetric cells have been proposed, where two cathodes or two anodes from nominally identical cells are reassembled to symmetric cells.[3,4] While this method leads to reliable results, it requires the disassembly and destruction of the original cells. Hence, for the impedance investigation of cells at different state-of-charge (SOC) values or at different points in their cycle life, a large number of nominally identical cells operated or aged at identical conditions is required.

An alternative approach is the use of a reference electrode, where the AC potential perturbation is measured between working and reference electrode, while the current is applied between working and counter electrode. A number of cell designs for impedance measurements with a reference electrode have been suggested, with the reference electrode either placed between anode and cathode,[5–9] or placed in-plane with anode or cathode through a central hole (also referred to as co-axial arrangement).[10–12] The more commonly used design, however, is a Swagelok T-cell design with the reference electrode (typically consisting of a lithium metal disc) being placed perpendicularly to the anode and cathode, outside the active area.[13] Yet, experiments and numerical simulations by Ender et al.[14] showed that the impedance measurements with the latter reference electrode placement can display significant distortions caused by small in-plane offsets between anode and cathode (referred to as geometrical asymmetry) and/or by large differences in the impedance response of anode and cathode (referred to as electrical asymmetry), consistent with earlier work by Dees et al.[15] This is also the case for coaxially located reference electrodes, for which the measured anode or cathode impedance is shown to be highly sensitive toward misplacements of the electrodes.[10,12,16] The impedance artefacts in both of these designs stem from the location of the reference electrode being *at the edge* of the working and the counter electrodes, where the current density is not homogeneous. If one electrode is now shifted slightly toward the reference electrode, the potential field around the reference electrode is dominated by this electrode, which leads to a biased impedance response. In contrast, if the reference electrode is placed *centrally between* the electrodes far away from their edges, small relative shifts of the electrodes do not affect the impedance response.[15] This geometry is typically realized by using a thin wire with an electronic insulator around its perimeter, being exposed only at its end, which is placed well inside the active area.[6–8] Yet, this location of the reference electrode can block parts of the working electrodes and thus alter the potential field between them. In order to minimize this effect, the reference electrode needs to be small compared to the size of the electrodes and the distance between them. Dees et al.[15] showed that a 25 μm thick reference electrode, between two electrodes separated by 100 μm, delivered sufficiently accurate potential and impedance measurements.

Unfortunately, the design of a micro-reference electrode, i.e., an insulated wire with small diameter (25–50 μm) imposes difficult requirements on the choice of material. Lithium metal, which is typically used as reference electrode in lithium ion cells, is difficult to accurately produce and handle in micron-sized dimensions. On the other hand, the potential of the reference electrode should be well-defined and stable in a lithium-ion electrolyte, as the reference electrode should (ideally) also be able to record the absolute potential of both electrodes during cycling. Additionally, potential drifts during impedance measurements can lead to a biased impedance response.[17] Zhou et al.[7] successfully plated lithium in-situ onto a thin, insulated copper wire as reference electrode. As the wire insulation was only removed at the very tip of the wire, the reference electrode active area was small and located far away from the electrode edges. However, they also showed that the potential stability of the reference electrode depends strongly on the plating parameters, as thin films of high surface area lithium can be completely dissolved or disconnected due to continuous SEI growth.

A similar approach has been followed by Abraham et al.[6] using an insulated tin-coated copper wire. Yet, instead of plating metallic lithium on a non-alloying copper wire like Zhou et al.,[7] lithium was in-situ electrochemically alloyed with the tin coating at the wire tip, where the insulation had been removed. While the long-term potential stability of this reference electrode is also limited, it can

*Electrochemical Society Student Member.
**Electrochemical Society Fellow.
[z]E-mail: sophie.solchenbach@tum.de

nevertheless be used for impedance measurements of individual electrodes during long-term cycling studies by short re-lithiation prior to the measurement.[8,18] The use of lithium alloys as reference electrode brings – in theory – a number of advantages: i) lithium forms alloys with a large number of metals, which are readily available as thin wires and at high purity;[19,20] and ii) the volume expansion and thus the specific surface area of lithium alloys is smaller compared to in-situ plated lithium, which means that the alloy should be less prone to self-delithiation surface reactions. Yet, only few lithium alloys have been employed as reference electrodes apart from Li-Sn:[6,8,18] a lithiated aluminum wire has been used as reference electrode by Verbrugge et al.;[9] and Gómez-Cámer and Novák[21] recently demonstrated the use of a lithium-bismuth alloy as reference electrode in their specifically designed impedance cell with a coaxial reference electrode.

So far, the viability of lithium-gold alloys as reference electrodes has not yet been examined. Studies on the electrochemical lithiation of gold are limited, as its poor capacity retention, high cost and low specific capacity compared to other alloys disqualify gold as a potential anode material. The Li_3Au phase is the most lithium-rich composition which can be obtained electrochemically, corresponding to a specific capacity of 408 mAh/g_{Au}.[19,22–26] The lithiation of gold proceeds in two main potential plateaus, with the first stage having an OCV potential of ∼0.3 V vs. Li/Li^+, and the second ∼0.2 V vs. Li/Li^+.[25] Surprisingly, the intermediate phases detected between α-Au and Li_3Au during electrochemical alloying could not be assigned to any of the known thermodynamic Li-Au phases.[27–30] Bach et al.[30] recently identified the metastable Li_3Au_2, Li_5Au_3, Li_3Au_5 and $LiAu_2$ phases by in-situ high energy X-ray diffraction during the electrochemical lithiation and delithiation of gold thin film electrodes.

Despite its drawbacks as an anode, several properties of the lithium-gold alloy make it an interesting reference electrode material: i) the potentials of both stages are very flat, and already low degrees of lithiation will result in an OCV of around 0.31 V vs. Li/Li^+; ii) it is difficult to completely delithiate a lithium-gold alloy by electrochemical or chemical means;[24,26] iii) gold is chemically resistant against HF and does not form any substantial surface oxide films;[31] and, iv) the high electrical conductivity of gold means that the potential drop along the length of the reference electrode wire is negligible.

In this study, we developed a novel micro-reference electrode based on a 50 μm thick, insulated gold wire, which we integrated into a conventional T-cell design. This gold wire reference electrode (GWRE) is placed centrally between both electrodes and two 200 μm thick glass fiber separators. Analogous to the approach used by Abraham et al.[6] for a tin-based reference electrode, we achieve a stable potential of the gold wire by in-cell electrochemical alloying with lithium. We show that the potential of the lithiated GWRE is stable for several weeks, even under elevated temperatures (40°C). With this lithiated GWRE, we are able to record the potential of both electrodes in LFP/graphite full-cells for more than 200 cycles. Further, we evaluate the capabilities of the lithiated GWRE to accurately measure the impedance of individual electrodes in full-cells, which we verify by symmetric cell measurements. As a proof of concept, we conduct a similar study as Burns et al.[32] on the impedance growth of anode and cathode in the presence of different concentrations of vinylene carbonate (VC) in LFP/graphite full-cells, using however our lithiated GWRE instead of a symmetric cell approach. We can reproduce the findings by Burns et al.[32] and further demonstrate that the total amount of VC per active material, rather than its concentration, is the key parameter for the electrolyte/anode interface resistance. This result is important when electrolyte additives are tested in laboratory cells, as these cells typically have a higher electrolyte to active material ratio than commercial lithium-ion cells.

Experimental

Electrode preparation.—Lithium iron phosphate ($LiFePO_4$, LFP) electrodes were prepared by mixing LFP (BASF SE, Germany), carbon black (Super C65, Timcal), and polyvinylene diflouride (PVDF, Kynar) in a mass ratio of 93:3:4 with NMP (N-methyl pyrrolidone, anhydrous, Sigma-Aldrich, Germany) in a planetary mixer (Thinky Corp.) for 15 min. The resulting ink was coated on carbon-coated aluminum foil (MTI) with a doctor blade mounted on an automatic coater and dried at 50°C in a convection oven for at least 3 h. The final LFP coating had a loading of 11.7 mg_{LFP}/cm^2 (≡ 2.0 mAh/cm^2 based on 170 mAh/g_{LFP}). Electrodes with a diameter of 11 mm were punched out and pressed to 35% porosity (2 × 60 s at 260 MPa) with a KBr press (Mauthe, PE-011). Graphite electrodes were prepared by mixing graphite (T311, SGL Carbon GmbH) and PVDF in a mass ratio of 95:5 with NMP, following the same procedure. The graphite ink was doctor-blade coated on copper foil (MTI) and dried in a convection oven at 50°C for at least 3 h. The final loading of the graphite coating was 5.9 $mg_{graphite}/cm^2$ (≡ 2.2 mAh/cm^2 based on 372 $mAh/g_{graphite}$) at a porosity of 40%. Both types of electrodes were dried under dynamic vacuum at 120°C overnight and transferred to an Argon-filled glove box (MBraun, Germany) without exposure to air.

Cell design and assembly.—The reference electrode current collector of a 3-electrode Swagelok T-cell (see Figure 1a) was modified to be able to host the GWRE. To this purpose, a small hole (1 mm diameter, 2.5 mm depth) was drilled into the flat front side of the reference current collector. To fix the GWRE wire, a thread was cut into the side of the reference current collector at approximately 2 mm distance from the front edge. For the actual reference electrode, a gold wire with a core diameter of 50 μm, coated with a 7 μm thick polyimide insulation (Goodfellow Cambridge Ltd., United Kingdom), was cut into pieces of ∼1.5 cm. The last 3 mm of one end of the wire was slightly scratched with a scalpel to allow good electrical contact of the wire to the reference electrode current collector. The scratched end of the wire was then inserted into the hole of the reference current collector and fixed with a small set screw. During cell assembly, the GWRE was inserted through a hole in the polymer lining of the T-cell (green lines in Fig. 1) and cushioned between two glassfiber separators (see Figure 1b); note that the insulation at the wire perimeter was not removed and that the only segment of the wire accessible to the electrolyte is the cut cross-section at the tip of the wire (see Figure 1c). The SEM image of the wire tip in Figure 1c shows that the polyimide insulation is almost completely intact around the edge of the cut cross-section, and that the exposed gold surface is relatively smooth. As the sealing and all other cell components are left unchanged compared to the conventional T-cell design, we could omit any benchmarking and air permeation tests that are normally required when developing a new electrochemical cell for the lithium ion chemistry. T-cells with GWRE were assembled with graphite as anode, LFP as cathode, and 2 glassfiber sheets (Whatman) as separator soaked with 60 μL electrolyte.

As standard electrolyte, 1 M lithium hexafluorophosphate ($LiPF_6$) in a mixture of ethylene carbonate (EC) and ethyl methyl carbonate (EMC) at a weight ratio of 3:7 was used (LP57, BASF SE, Germany). The water content of this electrolyte was determined via Karl-Fischer-Titration to be <10 ppm. Vinylene carbonate (VC, BASF SE, Germany) was added in weight ratios of 0.17% and 0.52% to the standard electrolyte. These concentrations were chosen as they yielded g_{VC}/Ah_{Cell} ratios equal to 2% and 6% VC additive (same solvent/salt) in 225 mAh full-cells used in a study on the anode and cathode impedance growth in the presence and absence of VC by Burns et al.[32] For stability measurements of the gold wire electrode, symmetrical lithium/lithium cells with a GWRE were built using 11 mm lithium discs (450 μm thickness, Rockwood, USA) as both cathode and anode.

Cell cycling and impedance measurements.—The gold wire reference was lithiated by applying a current of 150 nA between the working electrode (LFP or lithium) and the gold wire reference electrode using a potentiostat (VMP300, BioLogic, France). Please note that the selected current range of 10 μA has an accuracy of 0.1%, which leads to an error of ∼10 nA. LFP/graphite cells were cycled

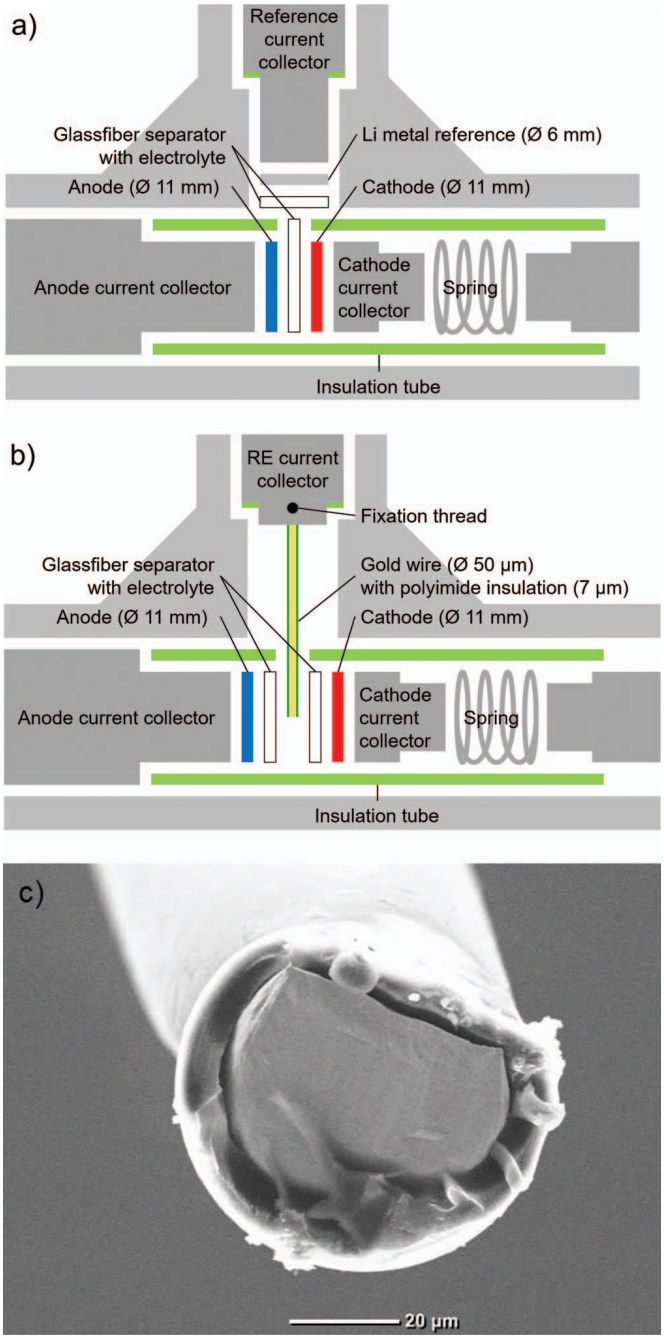

Figure 1. a) Conventional Swagelok T-cell design, b) modified T-cell design with gold wire reference electrode (GWRE), c) SEM image of the cut cross-section of gold wire tip prior to lithiation.

between cell voltages of 2 and 4 V using a BioLogic potentiostat and a CCCV charge/CC discharge procedure with a C/20 current cutoff to end the CV phase. During cycling, the cells were placed inside a climatic chamber with a constant temperature of 25°C or 40°C. Electrochemical impedance spectroscopy (EIS) measurements were conducted either potential controlled with a perturbation of 5 mV at OCV (referred to as PEIS, with the AC voltage perturbation applied between working and reference electrode) or current controlled with a perturbation of 0.5 mA (referred to as GEIS), both in a frequency range of 100 kHz–0.1 Hz. The impedance measurements were conducted at 50% SOC and 25°C or 10°C. Prior to the measurement, the cells were allowed to rest at OCV and thermally equilibrate for 15 min.

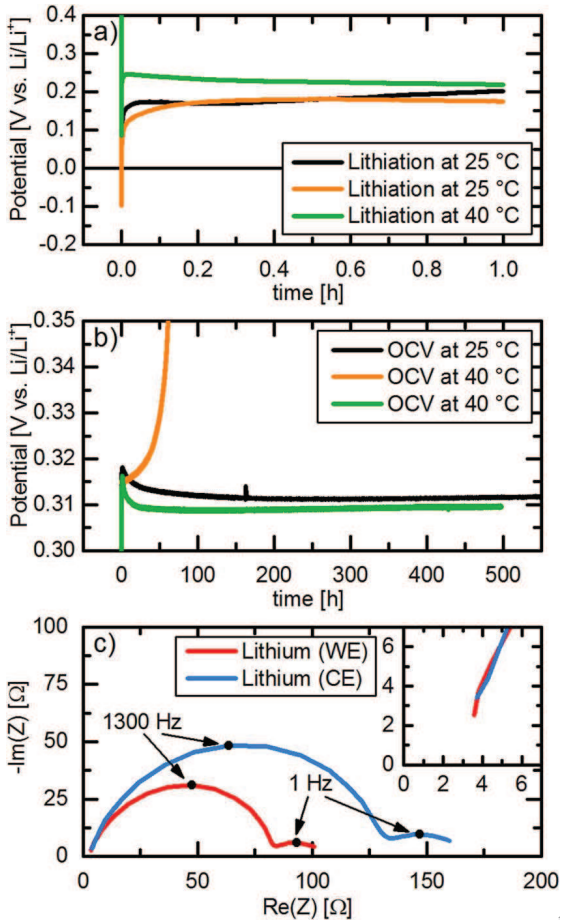

Figure 2. a) Potential of two GWREs during lithiation at 25°C (black and orange lines) and of one GWRE during lithiation at 40°C (green line) with 150 nA for 1 h. b) Potential of GWREs lithiated at 25°C during subsequent OCV at 25°C (black line) or at 40°C (orange line) as well as of the GWRE lithiated at 40°C during subsequent OCV at 40°C (green line). c) Nyquist plot of the lithium electrodes in a lithium/lithium cell at OCV at 25°C after lithiation of the GWRE at 25°C (PEIS, 100 kHz to 0.1 Hz, 5 mV AC perturbation). All potentials are given vs. Li/Li^+ and experiments were conducted in LP57 electrolyte.

Results and Discussion

Suitability of the GWRE to quantify individual electrode impedance in full-cells.—As a first step, the potential stability of a lithiated GWRE was investigated in symmetric lithium-lithium T-cells with our modified design (see Fig. 1b). The GWRE was lithiated by applying a current of 150 nA for 1 h between one of the lithium electrodes and the GWRE. The black curve in Figure 2a shows the potential of the GWRE vs. Li/Li^+ during galvanostatic lithiation at 25°C. The potential drops briefly below 0 V vs. Li/Li^+ and then stays constant at ~0.2 V vs. Li/Li^+ during the entire lithiation procedure, which is similar to the first potential plateau observed during the electrochemical lithiation of gold thin films.[25] The overpotential at the first moments of lithiation have been attributed to the reduction of surface oxides[19] or the nucleation of the lithium-gold alloy phase.[25] During the subsequent OCV at 25°C (see black curve in Figure 2b), the potential of the GWRE shoots up to 0.318 V and then quickly relaxes to ~0.311 V vs. Li/Li^+, which corresponds to the OCV potential of a Li_xAu alloy with $0 < x < \sim 1.2$.[25] The lithiated GWRE potential remains stable for more than 500 h, varying by less than 2 mV after the initial 20 h of the OCV period. This means that the lithiated GWRE might not be suitable for highly accurate potential measurements during initial cycles, but is sufficient for tracking electrode potentials during prolonged cycling. Further, no morphological

changes of the wire could be observed visually after disassembly of the cells.

As many battery cycling tests are performed at higher temperatures to accelerate aging and to reflect more realistic operating conditions, it is desirable that the GWRE also functions at higher temperatures. However, if the GWRE is lithiated at 25°C and the cell temperature is then increased to 40°C for OCV measurements, the gold wire potential starts to drift to more positive values after less than 10 hours (see orange curve in Figures 2a and 2b). This is in accordance with Abraham et al.,[6] who reported that the potential of a lithiated tin wire is substantially less stable at elevated temperatures, where the rate of SEI growth and the concomitant self-delithiation is generally enhanced. Once the cell is heated to 40°C, this effect must lead to a rather rapid depletion of lithium at the wire's tip, resulting in the observed potential drift. Interestingly, a re-lithiation of the wire with the same procedure at 25°C restored a stable GWRE potential of 0.311 V vs. Li/Li^+, as long as the cell was kept at 25°C. We also observed that the GWRE potential stability over long time was limited in combination with high voltage cathodes (>4.7 V vs. Li/Li^+), and also here the GWRE could be relithiated.[33]

After further investigations, we found that if the gold wire lithiation is conducted at 40°C (see green curve in Figures 2a and 2b), the GWRE shows the same stability during OCV at 40°C as was observed at 25°C, only shifted downwards by 1–2 mV. It is reported that an SEI formed at higher temperatures contains more inorganic species,[34] which we hypothesize might form a more effective surface film on the lithium-gold alloy. While high temperature SEI formation was shown to lead to inferior capacity retention on graphite anodes during cycling,[34] the more inorganic SEI could be advantageous in the absence of cycling-induced volume changes, i.e., for reference electrodes. However, the exact mechanism behind this enhanced stability by lithiation at higher temperatures is not clear at this point. We further believe that the stable potential of the GWRE for over hundreds of hours at up to 40°C is partly due to the fact that, contrary to previous micro-electrode designs,[6,7] the reference electrode area exposed to the electrolyte is limited to the cross-sectional area of the tip (see Figure 1c), minimizing side reactions with the electrolyte. The stable potential over 500 h indicates that the lithium diffusion along the wire (i.e., away from the tip) must be sufficiently slow to prevent a significant depletion of lithium at the tip.

To evaluate if the GWRE in the modified T-cell design is suitable for impedance measurements of individual electrodes, we also measured the impedance of a symmetrical lithium/lithium cell with a GWRE (see Figure 2c). Arbitrarily, one of the lithium electrodes was designated as working electrode (WE), while the other was designated as counter electrode (CE). Prior to the impedance measurement in the lithium/lithium cell, the GWRE was lithiated at 25°C as described above from the lithium electrode designated as WE. The high frequency resistance (see inset) is identical for both lithium electrodes, which indicates that the GWRE is located centrally between the electrodes. Hence, a first precondition for an artefact-free measurement is fulfilled.[14] Both lithium electrodes show a large semicircle in the high-frequency region (100 kHz–20 Hz, with the apex at ≈1.3 kHz), followed by a smaller semicircle at frequencies between 20 and 0.1 Hz (with the apex at ≈1 Hz), as reported previously for lithium metal electrodes.[35,36] While the high-frequency semicircle has been ascribed to the SEI resistance, the semicircle in the low-frequency region is thought to represent the charge transfer resistance.[36] Interestingly, both semicircles of the electrode used for the lithiation of the GWRE (designated as WE, see red line in Figure 2c) are about 35% smaller compared to the other electrode (≡ CE, s. blue line). We believe that this originates from the stripping of lithium from the WE electrode during lithiation of the GWRE, as this would cause a roughening of the lithium surface, leading to higher surface area and thus smaller impedance.

As a next step, the use of the GWRE in a LFP/graphite full-cell is tested and evaluated. Here, we also want to assess whether lithiation of the reference electrode is necessary for impedance measurements, i.e., whether the non-lithiated Au wire can be used as pseudo-GWRE.

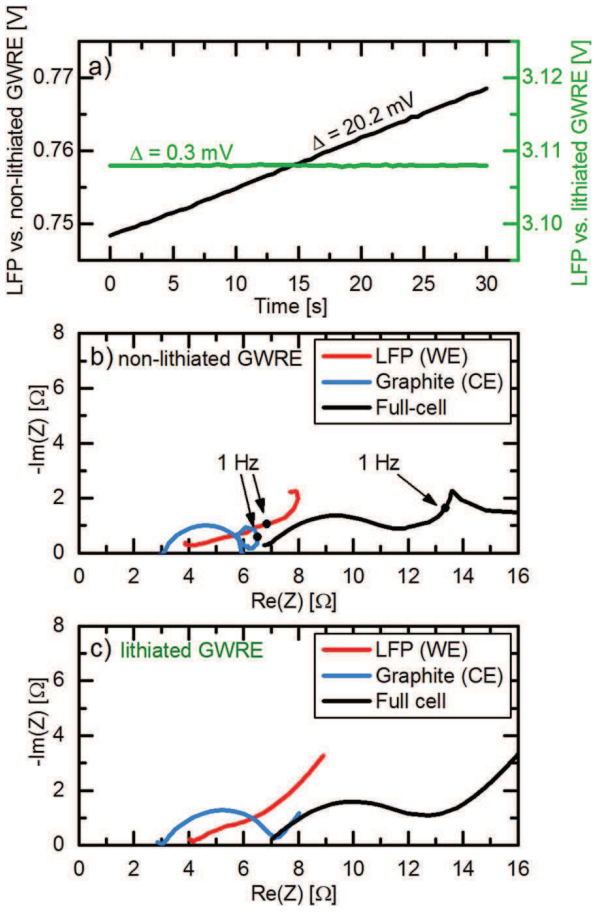

Figure 3. Comparison of voltage drift and impedance quality for a lithiated GWRE and a non-litiated pseudo-GWRE in LFP/graphite full-cells. a) Measured potential between the LFP working electrode (WE) and either the non-lithiated pseudo-GWRE (black line) or the lithiated GWRE (green line). b) Nyquist plot of an LFP/graphite full-cell obtained with a non-lithiated pseudo-GWRE before lithiation. c) Nyquist plot of an LFP/graphite full-cell obtained with a lithiated GWRE. Conditions: 25°C, LP57 electrolyte, PEIS with 5 mV amplitude at OCV (100 kHz–0.1 Hz).

To this purpose, we built identical LFP/graphite cells with GWRE: in one case, we lithiated the GWRE with 150 nA for 1 h at 25°C from the LFP electrode (note that the 150 nAh needed for lithiation of the GWRE are negligible compared to the LFP cathode capacity of 1.95 mAh); in the other case, we did not lithiate the GWRE. Subsequently, both cells underwent one formation cycle (at a rate of C/10) at 25°C and then were charged to 50% SOC. Figure 3a shows the potential of the LFP cathodes vs. the non-lithiated pseudo-GWRE and vs. the lithiated GWRE during 30 seconds of OCV prior to the impedance measurement. As the potential of the LFP electrode does not change significantly during the measurement, all potential changes can be ascribed to changes in the GWRE potential. While the LFP potential vs. the non-lithiated GWRE drifts about 20 mV during 30 seconds (black curve in Figure 3a), the LFP potential vs. lithiated GWRE remains stable within 0.3 mV (green curve in Figure 3a). In the subsequent potential-controlled impedance measurement (PEIS; 5 mV amplitude, 100 kHz–0.1 Hz) at OCV, the cell with the non-lithiated GWRE (see Figure 3b) shows significant distortions at frequencies near/below 1 Hz: i) the graphite impedance (blue line) displays an inductive loop; ii) the LFP impedance (red line) bends toward lower Re(Z) values; and, iii) even the full-cell impedance (black line) shows an irregular sharp peak. These distortions appear at frequencies near or below 1 Hz, where the average potential drift of 0.67 mV/s of the non-lithiated pseudo-GWRE (see black line in Figure 3a) is no longer significantly lower than the change of the AC voltage amplitude of

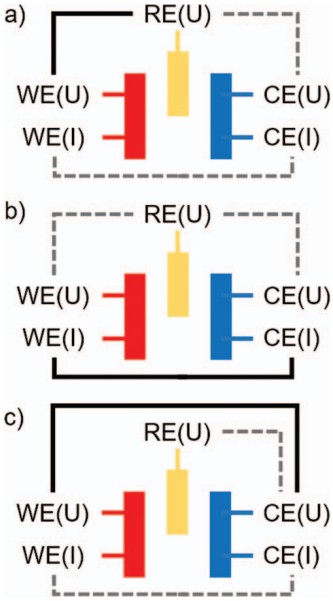

Figure 4. Systematic scheme of impedance measurements modes. a) Potential-controlled impedance spectroscopy (PEIS): The potential perturbation is controlled between WE and RE (black solid line), while current and potential between WE - CE are measured (gray dotted lines). A drift of the RE will lead to bias current between WE and CE. b) Current-controlled impedance spectroscopy (GEIS): The current perturbation is applied between WE and CE (black solid line), while potentials between WE - RE and CE - RE are measured. c) Modified potential-controlled impedance spectroscopy (PEIS): The potential perturbation is controlled between WE and CE (black solid line), while current between WE - CE and potential between RE - CE are measured (gray dotted lines).

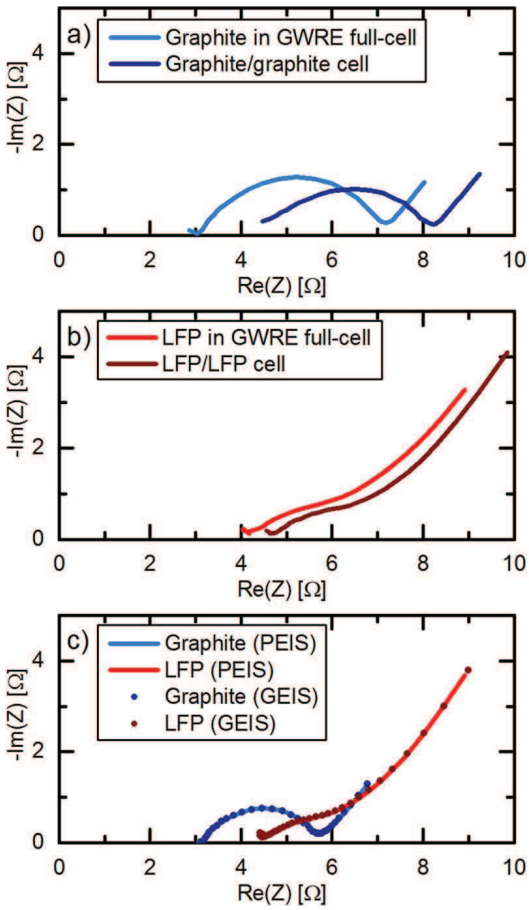

Figure 5. Impedance measurements on LFP and graphite electrodes after one C/10 formation cycle at 25°C and subsequent charge to 50% SOC. a) Nyquist plot of the graphite electrode of an LFP/graphite full-cell with lithiated GWRE (blue line) and of a symmetrical graphite/graphite cell divided by 2 (dark blue). b) Nyquist plot of the LFP electrode of an LFP/graphite full-cell with lithiated GWRE (red line) and of a symmetrical LFP/LFP cell divided by 2 (dark red). c) Comparison of the impedance response (100 kHz–0.1 Hz) of graphite and LFP electrodes under potential-controlled (PEIS at 5 mV amplitude, straight lines) and current-controlled (GEIS at 0.5 mA amplitude, dotted lines) conditions. All impedance measurements were conducted at 25°C.

5 mV. In contrast, the impedance spectra of the cell with the lithiated GWRE (Figure 3c) do not show these distortions, as the reference potential drift is almost two orders of magnitude lower in this case (0.01 mV/s). Our measurements are in agreement with simulations by Victoria et al.,[17] who showed that linear potential drifts on the order of 0.1 mV/s during impedance measurements can lead to these types of artefacts below 1 to 0.1 Hz, depending on the excitation amplitude. The potentiostatic impedance measurement mode used here (see Figure 4a), where the potential between WE and RE is controlled, leads to a particularly detrimental effect: As the base potential between RE and WE is fixed, the WE potential has to drift in the same way as the RE, which leads to a bias current between WE and CE. This continuously increasing current renders the full system nonlinear and time-variant, leading to the full cell impedance artefacts observed at low frequencies. While normally the full cell impedance should be unaffected by artefacts related to the reference electrode,[14] this comparison shows that it is crucial to use a reference electrode with a stable and defined potential for WE - RE potential controlled impedance measurements at low frequencies. To avoid the effects of a drifting pseudo-reference electrodes on the full cell impedance, one could either use a current-controlled measurement mode (GEIS, see Figure 4b), or control the potential between WE and CE during the impedance measurement (Figure 4c). Yet, artefacts of a non-stable RE will still be visible in the half cell impedance in these measurement setups.

Next, we take a closer look at the impedance spectra of the LFP and graphite electrodes recorded with a lithiated GWRE (Figure 3c). In contrast to the previous setup with two lithium electrodes, the HFR of both electrodes is not identical here. Gaberscek et al.[37] showed that the contact resistance between an aluminum current collector and an LFP electrode composite can be on the order of several Ωcm^2. Our own measurements confirm that the through-plane resistance of the used LFP electrodes is about 1 Ωcm^2 higher compared to the graphite electrodes (data not shown). Thus, the $\approx 1\ \Omega$ difference in HFR originates from the higher contact resistance between the LFP coating and the current collector (1 Ωcm^2 corresponds to $\approx 1\ \Omega$ for our electrode area of 0.95 cm^2). The charge transfer semicircle of the LFP electrode is small and almost invisible, which suggests the lack of a resistive cathode film.[38,39] At the same time, the graphite anode shows a clearly distinguishable semicircle. As this semicircle is not visible in graphite electrodes prior to cycling, we attribute it to a combined SEI/charge transfer resistance on the graphite surface.

To further validate the impedance data measured in a full-cell with a lithiated GWRE, we compare its impedance response with that of symmetric cells, which are commonly used for accurate impedance measurements.[4] Figures 5a and 5b show the comparison of the impedance spectra of a graphite and a LFP electrode measured in a full-cell with lithiated GWRE and in reassembled symmetric LFP/LFP and graphite/graphite cells, all after one C/10 formation cycle at 25°C and subsequent charge to 50% SOC. Note that the impedances of the symmetric cells have been divided by 2 in order to account for the two nominally identical electrodes in the symmetric cells. Apart from a slight shift in HFR, the impedance response of the symmetric cells and the full-cell with the lithiated GWRE are essentially identical for both graphite (Figure 5a) and LFP (Figure 5b) electrodes. The HFR shift is probably introduced by a weaker compression of the glassfiber seperators in the symmetric cells, caused by the slightly different assembly

procedure for cells with and without GWRE. The additional high frequency contact resistance feature visible in the impedance spectra of symmetric cells by Dahn's group,[4] which results from the contact resistance between the cell housing and the electrode coating on the back side, does not appear in our symmetric cell impedance spectra (see Figures 5a and 5b), as we use single-side coated electrodes for both symmetric cells and full cells.

As a final consistency check, we performed a potential-controlled impedance measurement (PEIS) followed by a current-controlled impedance measurement (GEIS) on the same LFP/graphite full-cell with a lithiated GWRE (see Figure 5c). Mathematically speaking, both measurements should give identical results in a Nyquist plot; hence any differences between them would indicate a biased impedance response.[21] However, Figure 5c shows that the two methods deliver completely identical impedance spectra. These results confirm that the presented cell setup with the lithiated GWRE is free of measurement artefacts and is suitable for the impedance investigation of individual electrodes in full-cells. In summary, our modified T-cell design with a lithiated GWRE is able to provide accurate impedance measurements of individual electrodes in full-cells in a wide frequency range (100 kHz–0.1 Hz). A stable potential of the GWRE is especially crucial for measurements at low frequencies. If lithiated at elevated temperature, the potential of the GWRE is stable for several weeks at up to 40°C, which we partially attribute to the small area exposed to the electrolyte.

Anode & cathode impedances during cycling in full-cells with GWRE.—In the following, we want to demonstrate the suitability of the lithiated GWRE to investigate the evolution of anode and cathode impedances during extended charge/discharge cycle tests in full-cells. To this purpose, LFP/graphite full-cells with lithiated GWRE were cycled at 25°C for 200 cycles at a rate of 1C after two initial formation cycles at C/10. Impedance measurements were performed at 50% SOC after 5, 10, and each subsequent 10th cycle at 25°C. Figures 6a and 6b show the potential of the cathode and anode vs. the lithiated GWRE potential (left y-axis) during cycles 10, 50, 100 and 200 (for the sake of clarity, cycles in between were omitted), which can easily be converted into the Li/Li$^+$ scale by adding 0.311 V (right y-axis). The LFP charge and discharge plateaus are centered around 3.11 V vs. the lithiated GWRE (see Figure 6a and also Figure 3a), corresponding to a calculated value of 3.42 V vs. Li/Li$^+$, which matches well with the true LFP equilibrium potential.[40] The LFP potential center vs. lithiated GWRE remains constant during cycling, meaning that the lithiated GWRE maintains its stable potential of 0.311 V vs. Li/Li$^+$. Throughout cycling, the overpotentials of both electrodes do not change, yet the maximum potential of the graphite anode at the discharge end point moves upwards (see dark blue to light blue lines in Figure 6b). At the same time, the minimum potential of the cathode also moves upwards (see dark red to light red lines in Figure 6a), which indicates that the SOC of both electrodes slip against each other. Figure 6c shows the impedance spectra of both cathode and anode after 10, 50, 100 and 200 cycles. Note that both the cathode and anode impedance decrease slightly from cycle 5 (data not shown) to cycle 10, which could be related to the dissolution of gasses evolved during formation and/or improved wetting over the first cycles. Between cycle 10 and 200, the high frequency resistance of both electrodes increases slightly by about 0.1–0.2 Ω. This could be due to an increased electrical resistance between the electrode coatings and the current collectors, implying a very slow delamination of the composite electrodes, or a higher ionic resistance within the bulk electrolyte. While the cathode impedance shows no further changes during cycling, the anode semicircle increases slightly from ~1.9 Ω after cycle 10 to ~2.2 Ω after cycle 200, which indicates a very slow SEI growth. Overall, the potential changes of both electrodes during cycling and the small but measureable impedance growth of the anode can be related to the loss of active lithium due to a slow but steady SEI growth, which has been identified as the dominant aging mechanism in LFP/graphite cells.[41–45]

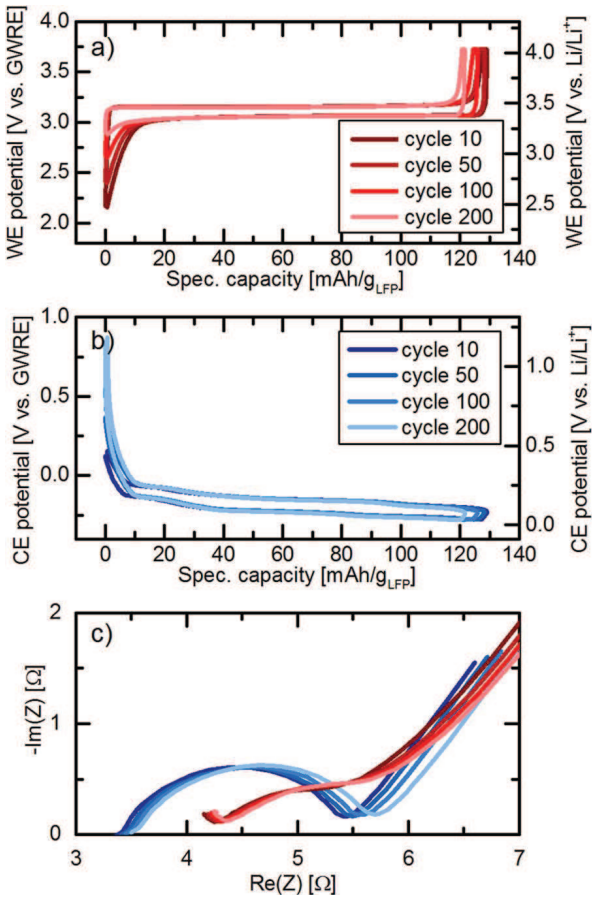

Figure 6. Charge/discharge of an LFP/graphite full-cell with a lithiated GWRE at a rate of 1C after two initial formation cycles at C/10 (LP57 electrolyte, 25°C). a) Cathode potential vs. the lithiated GWRE of cycles 10, 50, 100 and 200. b) Anode potential vs. the lithiated GWRE of cycles 10, 50, 100 and 200. The conversion to the Li/Li$^+$ scale (right axis in a and b) was done by adding 0.311 V to the GWRE potential. c) Nyquist plot of the PEIS (5 mV amplitude, 25°C) at 50% SOC of both the graphite anode (shown in the range from 100 kHz to 0.1 Hz) and the LFP cathode (shown in the range from 100 kHz to 0.3 Hz) after cycle number 10, 50, 100 and 200.

Application of the GWRE to anode & cathode impedance growth during full-cell formation.—Vinylene carbonate (VC) is one of the most commonly used electrolyte additives, as it leads to improved SEI stability at elevated temperatures and thus enhanced cycle life of lithium ion cells.[46,47] However, high concentrations of VC have shown to increase the impedance of both anode and cathode,[32] which in turn leads to higher overpotentials and heat generation during cycling. Freiberg et al.[48] recently indicated that the absolute amount of an additive per active material, instead of its concentration, is the crucial parameter when comparing larger cells (e.g. commercial cells) and small lab-scale cells (e.g. coin cells). Therefore, we want to compare the effect of different amounts of VC in LP57 electrolyte on both anode and cathode impedance in LFP/graphite full-cells obtained with a lithiated GWRE to the study by Burns et al.,[32] who used 225 mAh LCO/graphite pouch cells with the same electrolyte and examined the effect of VC on the impedance of the individual electrodes via symmetric cell measurements. In Burns' study, it was shown that the charge transfer resistance of a graphite anode decreases slightly from 0% to 0.5% VC in the electrolyte and increases roughly linearly with VC concentration between 1% and 6% VC (see Figure 9b in Ref. 32). At the same time, the impedance of the LCO cathode from Burns' study (see Figure 9a in Ref. 32) decreases about 50% from 0% to 2% VC and then gradually increases again up to VC concentrations of 6% to a value which is still below the 0% VC case. Unfortunately, the exact amount of active material in the cells used by Burns et al. was not

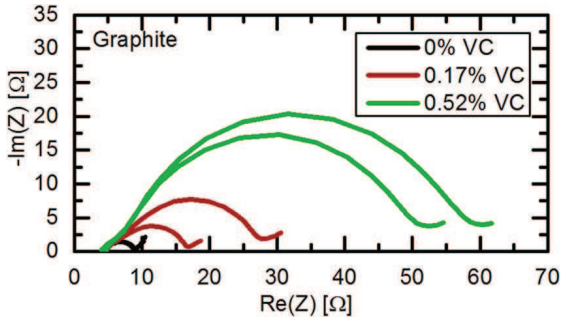

Figure 7. Nyquist plot of the graphite anode impedance after one formation cycle and recharge to 50% SOC at 40°C of LFP/graphite full-cells with a lithiated GWRE in LP57 electrolyte containing 0%, 0.17%, and 0.52% VC in the electrolyte. PEIS was measured at 10°C between 100 kHz–0.1 Hz with an amplitude of 5 mV.

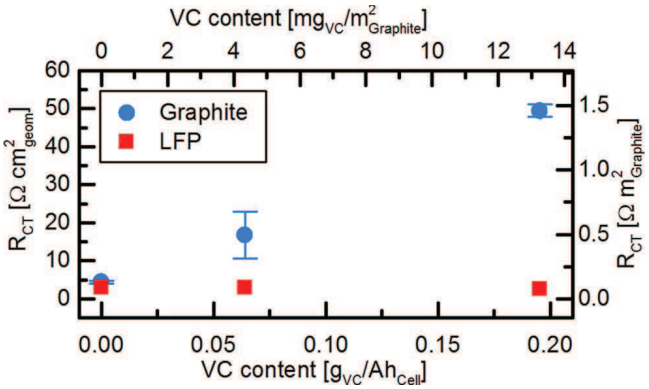

Figure 8. R_{ct} of the graphite anode and the LFP cathode after formation in LFP/graphite full-cells with different VC amounts added to LP57 electrolyte. Impedance data were obtained with a lithiated GWRE (PEIS at 5 mV amplitude and 10°C between 100 kHz and 0.1 Hz) and fitted by an equivalent circuit consisting of a resistor for the electrolyte, an RQ-element for the electrolyte/electrode interface resistance, and a Warburg element for solid-state diffusion. Note that the upper x-axis and the right y-axis display the VC content and charge transfer resistance normalized to the graphite BET surface area.

given. However, the specific capacities of LCO and LFP are similar, and our anode to cathode capacity ratio of 1.1 is close to a commercial balancing. Hence, we think it is reasonable to assume that the masses of both anode and cathode active materials are proportional to the respective cell capacity. As the ratio of electrolyte to cell capacity (and thus active material) in our lab-scale T-cell design is 11.6 times higher compared to Burns et al.[32] (38 $g_{electrolyte}/Ah_{Cell}$ vs. 3.3 $g_{electrolyte}/Ah_{Cell}$), we adjusted the amount of VC in the electrolyte accordingly. Thus, our chosen concentrations of 0.17% and 0.52% VC represent the same g_{VC}/Ah_{Cell} ratio, namely 0.06 g_{VC}/Ah_{Cell} and 0.2 g_{VC}/Ah_{Cell}, as cells with 2% and 6% VC in the study by Burns et al.[32] After lithiation of the GWRE and one formation cycle at 40°C, the LFP/graphite cells were charged to 50% SOC and the impedance measurements were then conducted at 10°C, i.e., under the same conditions as reported by Burns et al.[32]

Figure 7 shows the Nyquist plot of graphite electrodes after formation with different concentrations of VC. For each concentration, two cells are shown to assess the cell to cell variation. Quite clearly, the cells with 0.17% and 0.52% VC show an increased charge transfer resistance of the graphite anodes. These results already indicate that electrolytes cannot be compared without considering the amount of active material, as the anode charge transfer resistance decreases up to a VC concentration of 0.5% in the study by Burns et al.,[32] while Figure 7 shows that the anode charge transfer resistance increases substantially within the same VC concentration range.

To quantify the charge transfer resistances, the impedance spectra of cathode and anode of each cell were fitted using a simple electrochemical equivalent circuit composed of: i) a resistor for the electrolyte, ii) a resistor and a constant phase element in parallel to describe the electrolyte/electrode interface resistance, and, iii) a Warburg-type diffusion element in series representing solid state diffusion. This circuit is a simplified version of a model used by Illig et al.[35] for LFP electrodes; we omitted the electrode contact resistance and the low frequency capacitor, as both are not visible within our measurement range. Figure 8 shows the average fitted charge transfer resistances (left y-axis), normalized to the geometrical electrode area, of both electrodes at different g_{VC}/Ah_{Cell} ratios (lower x-axis). The anode charge transfer resistance is ~5 Ωcm^2 for cells without VC and increases to ~16 Ωcm^2 and ~47 Ωcm^2 for cells with 0.06 g_{VC}/Ah_{Cell} (≡0.17% VC) and 0.2 g_{VC}/Ah_{Cell} (≡0.52% VC), respectively. In comparison, Burns et al.[32] showed an anode charge transfer resistance of ~30 Ωcm^2, ~60 Ωcm^2 and ~150 Ωcm^2 for cells with identical g_{VC}/Ah_{Cell} ratios (0%, 2% and 6% VC in their study). The linear increase in charge transfer resistance from 0.033 to 0.2 g_{VC}/Ah_{Cell} that has been observed by Burns et al.[32] (corresponding to 1%-6% VC in their study) is also found in our results within the same g_{VC}/Ah_{Cell} range, although our absolute VC concentrations are completely different (0–0.52% VC). This further proves that the amount of additive per active material (here corresponding to the g_{VC}/Ah_{Cell} ratio) determines the effect of an additive on the surface of an electrode, and not its concentration. The differences in absolute resistance values between Burns' study[32] and ours could be explained by differences in active material loading and BET surface area of the used electrodes: As the impedance of an electrode is inversely proportional to the electrochemical active area, a higher roughness factor (i.e., electrode surface area per geometric area) will result in an overall lower impedance, even if the surface chemistry is identical. While our electrodes are loaded with 5.9 mg/cm^2 graphite having a BET surface area of ~5 m^2/g, we can estimate the anodes investigated by Burns et al.[32] to have a loading of ~10 mg/cm^2 graphite[49] with a BET surface area of ~0.7 m^2/g.[50,51] In total, this would give a ~5-fold higher roughness factor in our study, which would fit with the measured ~4 times lower absolute charge transfer resistance values. However, it is to note that the assumed values for loading and BET were taken from other publications by the Dahn group and not directly from Burns et al.,[32] and hence this is only an estimate. A different BET surface area would also affect the amount of additive per unit surface, and thus result in a different charge transfer resistance. To make our data more comparable to future studies, we therefore included the amount of VC per graphite BET surface area ($mg_{VC}/m^2_{Graphite}$, upper x-axis) and the charge transfer resistance normalized to the graphite BET surface area (Ω $m^2_{Graphite}$, right y-axis) in Figure 8. An additional difference between our cells and the study by Burns et al.[32] is the different cycling protocol: Our impedance data was recorded after one formation cycle, whereas the cells by Burns et al.[32] were disassembled for impedance measurements of symmetric cells after 23 cycles. However, further cycling and impedance measurements of our LFP/graphite cells showed that the impedances of both electrodes does not change significantly with cycle number once the formation cycle is completed.

The charge transfer resistance of the LFP cathode in our study does not show any dependency on the VC content (see Figure 8). In contrast, Burns et al.[32] found that the impedance of an LCO cathode decreases about half by the addition of low concentrations of VC (0.5–2%) and increases again slightly at higher VC concentrations (4–6%). This discrepancy can be understood considering the studies by El Ouatani et al.,[52,53] which showed that LCO cathodes form a surface film of poly(VC) in VC-containing electrolytes, while this film is lacking on LFP cathodes. Thus, the cathode charge transfer resistance remains constant and independent from the VC content in LFP/graphite cells. As VC reacts on the LCO surface,[52,53] one can imagine that slightly less VC is available for SEI formation in LCO/graphite than in LFP/graphite cells. This could in turn also partially explain the deviations of the absolute values for the anode charge

transfer resistance at points of equal g_{VC}/Ah_{Cell} in our study compared to Burns et al.[32] Hence, we can conclude that not only the ratio of additive to active material, but also the cell chemistry of cathode and anode and their reactivity toward the additive is an important aspect to consider when comparing additives across different cell types.

Conclusions

In this study, we introduce a novel micro-reference electrode in a Swagelok T-cell design, which is suitable for impedance and potential measurements of both working and counter electrode individually. The reference electrode consists of a thin, insulated gold wire and is placed centrally between both electrodes and two 200 µm thick glass fiber separators. By electrochemical alloying with lithium, we achieve a defined potential of 0.311 V vs. Li/Li^+ of the gold wire reference electrode (GWRE), which is stable for several weeks during cycling and even under elevated temperatures (40°C). In contrast to previous micro-reference designs, only the cut cross-section of the wire's tip is the electrochemically active area, which supposedly minimizes side reactions with the electrolyte and contributes to the long-term stable potential of the GWRE. The cell setup with GWRE was validated by impedance measurements of the corresponding symmetrical cells. Further, we demonstrated the suitability of the lithiated GWRE for impedance and potential measurements in LFP/graphite full-cells for up to 200 cycles. Based on these measurements, we could identify lithium inventory loss due to SEI growth as the dominant aging mechanism in LFP/graphite cells at room temperature, in agreement with literature.

As a proof of concept, we investigated LFP/graphite full-cells with a lithiated GWRE and different VC contents in the electrolyte. Using symmetrical cells, Burns et al.[32] showed that the charge transfer of a graphite anode depends almost linearly on the concentration of vinylene carbonate (VC) in the electrolyte. We can reproduce the findings by Burns et al.[32] using a lithiated GWRE, and further demonstrate that the ratio of mass VC to active material, rather than the VC concentration, is the key parameter for the electrolyte/anode interface resistance. This result needs to be considered when electrolyte additives are tested in laboratory cells, as these cells typically have a higher electrolyte to active material ratio than commercial lithium-ion cells.

Acknowledgment

This work is financially supported by the BASF SE Battery Research Network. J. L. gratefully acknowledges the funding by the Bavarian Ministry of Economic Affairs and Media, Energy, and Technology for its financial support under the auspices of the EEBatt project.

References

1. M. Klett, J. A. Gibson, S. E. Trask, B. J. Polzin, A. N. Jansen, D. W. Dees, and D. P. Abraham, *J. Electrochem. Soc.*, **163**, A875 (2016).
2. N. Ogihara, S. Kawauchi, C. Okuda, Y. Itou, Y. Takeuchi, and Y. Ukyo, *J. Electrochem. Soc.*, **159**, A1034 (2012).
3. C. H. Chen, J. Liu, and K. Amine, *J. Power Sources*, **96**, 321 (2001).
4. R. Petibon, C. P. Aiken, N. N. Sinha, J. C. Burns, H. Ye, C. M. VanElzen, G. Jain, S. Trussler, and J. R. Dahn, *J. Electrochem. Soc.*, **160**, A117 (2013).
5. T. S. Ong and H. Yang, *J. Electrochem. Soc.*, **149**, A1 (2002).
6. D. P. Abraham, S. D. Poppen, A. N. Jansen, J. Liu, and D. W. Dees, *Electrochim. Acta*, **49**, 4763 (2004).
7. J. Zhou and P. H. L. Notten, *J. Electrochem. Soc.*, **151**, A2173 (2004).
8. A. N. Jansen, D. W. Dees, D. P. Abraham, K. Amine, and G. L. Henriksen, *J. Power Sources*, **174**, 373 (2007).
9. M. W. Verbrugge, D. R. Baker, and B. J. Koch, *J. Power Sources*, **110**, 295 (2002).
10. S. Klink, E. Madej, E. Ventosa, A. Lindner, W. Schuhmann, and F. La Mantia, *Electrochem. commun.*, **22**, 120 (2012).
11. C. Bünzli, H. Kaiser, and P. Novák, *J. Electrochem. Soc.*, **162**, A218 (2015).
12. C. Delacourt, P. Ridgway, V. Srinivasan, and V. S. Battaglia, *J. Electrochem. Soc.*, **161**, A1253 (2014).
13. V. R. Koch, C. Nanjundiah, G. B. Appetecchi, and B. Scrosati, *J. Electrochem. Soc.*, **142**, L116 (1995).
14. M. Ender, A. Weber, and E. Ivers-Tiffée, *J. Electrochem. Soc.*, **159**, A128 (2012).
15. D. W. Dees, A. N. Jansen, and D. P. Abraham, *J. Power Sources*, **174**, 1001 (2007).
16. S. Klink, D. Höche, F. La Mantia, and W. Schuhmann, *J. Power Sources*, **240**, 273 (2013).
17. S. N. Victoria and S. Ramanathan, *Electrochim. Acta*, **56**, 2606 (2011).
18. D. P. Abraham, M. M. Furczon, S.-H. Kang, D. W. Dees, and A. N. Jansen, *J. Power Sources*, **180**, 612 (2008).
19. A. N. Dey, *J. Electrochem. Soc.*, **118**, 1547 (1971).
20. J. Wang, I. D. Raistrick, and R. A. Huggins, *J. Electrochem. Soc.*, **133**, 457 (1986).
21. J. L. Gómez-Cámer and P. Novák, *Electrochem. commun.*, **34**, 208 (2013).
22. T. L. Kulova, A. M. Skundin, V. M. Kozhevin, D. A. Yavsin, and S. A. Gurevich, *Russ. J. Electrochem.*, **46**, 877 (2010).
23. Y. J. Lee, Y. Lee, D. Oh, T. Chen, G. Ceder, and A. M. Belcher, *Nano Lett.*, **10**, 2433 (2010).
24. K. Nishio, K. Yuda, and H. Masuda, *ECS Electrochem. Lett.*, **2**, C1 (2012).
25. P. Bach, M. Stratmann, I. Valencia-Jaime, A. H. Romero, and F. U. Renner, *Electrochim. Acta*, **164**, 81 (2015).
26. G. Taillades, N. Benjelloun, J. Sarradin, and M. Ribes, *Solid State Ionics*, **152-153**, 119 (2002).
27. G. Kienast and J. Verma, *Zeitschrift für Anorg. und Allg. Chemie*, **310**, 143 (1961).
28. A. D. Pelton, *Bull. Alloy Phase Diagrams*, **7**, 228 (1986).
29. S. Misra, N. Liu, J. Nelson, S. S. Hong, Y. Cui, and M. F. Toney, *ACS Nano*, **6**, 5465 (2012).
30. P. Bach, I. Valencia-Jaime, U. Rütt, O. Gutowski, A. H. Romero, and F. U. Renner, *Chem. Mater.*, **28**, 2941 (2016).
31. B. D. Craig and D. S. Anderson, *Handbook of Corrosion Data*, p. 439, (1994).
32. J. C. Burns, R. Petibon, K. J. Nelson, N. N. Sinha, A. Kassam, B. M. Way, and J. R. Dahn, *J. Electrochem. Soc.*, **160**, A1668 (2013).
33. D. Pritzl, S. Solchenbach, and H. A. Gasteiger, Manuscript in preparation.
34. S. B. Lee and S. Il Pyun, *Carbon N. Y.*, **40**, 2333 (2002).
35. J. Illig, M. Ender, T. Chrobak, J. P. Schmidt, D. Klotz, and E. Ivers-Tiffée, *J. Electrochem. Soc.*, **159**, A952 (2012).
36. R. Mogi, M. Inaba, S.-K. Jeong, Y. Iriyama, A. Abouimrane, and Z. Ogumi, *J. Electrochem. Soc.*, **149**, A1578 (2002).
37. M. Gaberscek, J. Moskon, B. Erjavec, R. Dominko, and J. Jamnik, *Electrochem. Solid-State Lett.*, **11**, A170 (2008).
38. N. Dupré, J.-F. Martin, J. Degryse, V. Fernandez, P. Soudan, and D. Guyomard, *J. Power Sources*, **195**, 7415 (2010).
39. M. Cuisinier, N. Dupré, J.-F. Martin, R. Kanno, and D. Guyomard, *J. Power Sources*, **224**, 50 (2013).
40. A. Yamada, H. Koizumi, S.-I. Nishimura, N. Sonoyama, R. Kanno, M. Yonemura, T. Nakamura, and Y. Kobayashi, *Nat. Mater.*, **5**, 357 (2006).
41. L. Castro, R. Dedryvère, J.-B. Ledeuil, J. Bréger, C. Tessier, and D. Gonbeau, *J. Electrochem. Soc.*, **159**, A357 (2012).
42. M. Dubarry, C. Truchot, and B. Y. Liaw, *J. Power Sources*, **258**, 408 (2014).
43. M. Kassem, J. Bernard, R. Revel, S. Pélissier, F. Duclaud, and C. Delacourt, *J. Power Sources*, **208**, 296 (2012).
44. T. G. Zavalis, M. Klett, M. H. Kjell, M. Behm, R. W. Lindström, and G. Lindbergh, *Electrochim. Acta*, **110**, 335 (2013).
45. H. Zheng, L. Chai, X. Song, and V. S. Battaglia, *Electrochim. Acta*, **62**, 256 (2012).
46. D. Aurbach, K. Gamolsky, B. Markovsky, Y. Gofer, M. A. Schmidt, and U. Heider, *Electrochim. Acta*, **47**, 1423 (2002).
47. B. Zhang, M. Metzger, S. Solchenbach, M. Payne, S. Meini, H. A. Gasteiger, A. Garsuch, and B. L. Lucht, *J. Phys. Chem. C*, **119**, 11337 (2015).
48. A. Freiberg, M. Metzger, D. Haering, S. Bretzke, S. Puravankara, T. Nilges, C. Stinner, C. Marino, and H. A. Gasteiger, *J. Electrochem. Soc.*, **161**, A2255 (2014).
49. R. Petibon, E. C. Henry, J. C. Burns, N. N. Sinha, and J. R. Dahn, *J. Electrochem. Soc.*, **161**, A66 (2013).
50. A. J. Smith, J. C. Burns, X. Zhao, D. Xiong, and J. R. Dahn, *J. Electrochem. Soc.*, **158**, A447 (2011).
51. X. Xia, P. Ping, and J. R. Dahn, *J. Electrochem. Soc.*, **159**, A1834 (2012).
52. L. El Ouatani, R. Dedryvère, C. Siret, P. Biensan, and D. Gonbeau, *J. Electrochem. Soc.*, **156**, A468 (2009).
53. L. El Ouatani, R. Dedryvère, C. Siret, P. Biensan, S. Reynaud, P. Iratçabal, and D. Gonbeau, *J. Electrochem. Soc.*, **156**, A103 (2009).

3.1.2 Application of a micro-reference electrode in a high-voltage cell chemistry

This section presents the article *"Analysis of Vinylene Carbonate (VC) as Additive in Graphite/$LiNi_{0.5}Mn_{1.5}O_4$ Cells"*.[106] The paper was submitted to the peer-reviewed Journal of the Electrochemical Society in June 2017 and published in August 2017. The article is published open access and distributed under the terms of the Creative Commons Attribution Non-Commercial No Derivatives 4.0 License. The permanent web link is available under: http://jes.ecsdl.org/content/164/12/A2625. The article was presented by Daniel Pritzl at the PRiME meeting 2016 in Honolulu (USA) in October 2016 (Paper 567).

Vinylene carbonate (VC) is one of the most efficient anode additives regarding the stability of the SEI on graphite anodes. The additive was discovered by Aurbach et al.[53] and is frequently reported to increase coulombic efficiency[55] of the graphite anode (over charge/discharge cycling) and increase the cycle life of lithium-ion batteries.[105] Furthermore, it is reported that VC is reduced on the graphite anode,[50] leading to a linear increase in the anode charge transfer resistance with concentration.[105] The positive electrode's impedance decreases at low concentrations (until 1% in a commercial cell) and stays then constant. El Ouatani et al.[107] found surface films consisting of poly(VC) both on anode and cathode explaining the impedance change on both electrodes with different amounts of VC.

However, all these cell chemistries used cathodes which operate up to a voltage of maximum 4.3 V vs. Li^+/Li, and here the dominant interaction of VC proceeds with the graphite anode. In contrast, when cells are charged to 4.45 V vs. Li^+/Li and then stored at elevated temperatures, the cell voltage decays very rapidly in the presence of VC.[108] This implies that the additive is oxidized on the cathode and the products can then consume active lithium from the anode, explaining the cell voltage drop. When VC is used in a graphite/LNMO cell chemistry at elevated temperatures (45 °C), a drastic decrease in the capacity retention and a lower coulombic efficiency with VC is observed compared to cells without VC.[57] The authors also

write that the origin of performance decrease with VC is yet unknown, hindering the successful use of the VC additive in this cell chemistry.

In this study we first investigate the oxidative stability of VC via OEMS and find that oxidation occurs already starting from 4.3 V vs. Li^+/Li, by the release of gaseous CO_2. Next, different concentrations of the oxidatively instable additive are investigated in the graphite/LNMO cell chemistry and adjusted such that 1% VC in our lab test cells correspond to roughly 10% in a commercial scale cell. Via impedance measurements with the µ-reference electrode we can show that VC at concentrations above 0.17% (in a lab test cell) is both reduced on the anode and oxidized on the cathode, leading to a strong impedance increase, especially on the cathode and a decrease in cell performance. If the VC concentration is adjusted to 0.09%, only the impedance of the anode increases while the capacity retention and the coulombic efficiency of the cells is improved. By keeping the concentration as low as 0.09%, the additive is only consumed on the graphite anode, leaving no VC behind which could be oxidized at the cathode, releasing oxidation products which decrease the cell performance. With the help of the µ-reference electrode, a concentration level of the additive was detected where the additive VC could be used in graphite/LNMO cells leading to a performance increase at elevated temperatures. These finding lead to new strategies and guidelines how to incorporate anode additives in this kind of cell chemistries.

Author contributions

S.S performed the OEMS measurement. D.P performed all cycling and impedance measurements. D.P. and M.W. performed the calculations on the mono-layer coverage of the additive. The data was analyzed by D.P. and S.S. The manuscript was written by D.P., S.S. and H.A.G. All authors discussed the data and commented on the results.

Analysis of Vinylene Carbonate (VC) as Additive in Graphite/$LiNi_{0.5}Mn_{1.5}O_4$ Cells

Daniel Pritzl,*,z Sophie Solchenbach,* Morten Wetjen, and Hubert A. Gasteiger**

Chair for Technical Electrochemistry, Department of Chemistry and Catalysis Research Center, Technical University of Munich, Munich, Germany

Vinylene Carbonate (VC) is an effective electrolyte additive to produce a stable solid electrolyte interphase (SEI) on graphite anodes, increasing the capacity retention of lithium-ion cells. However, in combination with $LiNi_{0.5}Mn_{1.5}O_4$ (LNMO) cathodes, VC drastically decreases cell performance. In this study we use on-line electrochemical mass spectrometry (OEMS) and electrochemical impedance spectroscopy (EIS) with a micro-reference electrode to understand the oxidative (in-)stability of VC and its effect on the interfacial resistances of both anode and cathode. We herein compare different VC concentrations corresponding to VC to graphite surface area ratios typically used in commercial-scale cells. At low VC concentrations (0.09 wt%, corresponding to 1 wt% in commercial-scale cells), an impedance increase exclusively on the anode and an improved capacity retention is observed, whereas higher VC concentrations (0.17 wt – 2 wt%, corresponding to 2 wt - 23 wt% in commercial-scale cells) show an increase in both cathode and anode impedance as well as worse cycling performance and overcharge capacity during the first cycle. By considering the onset potentials for VC reduction and oxidation in graphite/LNMO cells, we demonstrate that low amounts of VC can be reduced before VC oxidation occurs, which is sufficient to effectively passivate the graphite anode.

Manuscript submitted June 26, 2017; revised manuscript received August 16, 2017. Published August 31, 2017. This was Paper 567 presented at the Honolulu, Hawaii, Meeting of the Society, October 2–7, 2016.

During the first charge of a lithium ion battery (LiB), the so called solid electrolyte interphase (SEI)[1] is formed on the surface of the negative electrode. The standard electrolyte for LiBs consists of a mixture of cyclic and linear carbonates, e.g., ethylene carbonate (EC) and ethyl methyl carbonate (EMC), typically with lithium hexafluorophosphate ($LiPF_6$) as salt. Starting from a potential of ~0.8 V vs. Li/Li^+, EC is reduced electrochemically into ethylene gas and lithium ethylene dicarbonate (LEDC), which is a key component of the SEI.[2,3] Vinylene carbonate (VC) is one of the most effective additives to modify the SEI on graphite anodes, as it is reduced at potentials more positive than 1.0 V vs. Li/Li^+ and hence suppresses the reduction of EC.[4,5] Aurbach et al. have used VC as electrolyte additive in an EC/DMC (dimethyl carbonate) based electrolyte and that time reported a reduction of the irreversible capacity in the first cycles and an improved cycling stability at elevated temperatures for graphite anodes. The SEI resulting from the reduction of VC consists mainly of poly (vinylene carbonate) (poly(VC)).[4,6]

Important studies on the impact of different VC concentrations in graphite/NMC pouch cells have been carried out by the Dahn group. For example, Burns et al.[7] investigated the effect of different concentrations of VC (0, 1 and 2 wt%) on cycle life and impedance growth of full-cells with graphite anodes and either LCO ($LiCoO_2$) or NMC ($Li(Ni_{0.42}Mn_{0.42}Co_{0.16})O_2$) cathodes, employing galvanostatic cycling experiments coupled with high precision coulombic efficiency and electrochemical impedance spectroscopy (EIS) measurements. For cells with VC additive, they observed higher coulombic efficiencies and reduced capacity fading, whereby a notable increase in cell impedance was observed for cells with 2 wt% VC, which they attributed to a thicker SEI-film at the surface of the anode. However, since it is known that LCO cathodes can also form a resistive surface film in the presence of VC additive (presumably consisting of poly(VC)[8,9]), an assignment of the overall cell impedance growth to the individual contributions from anode and cathode requires more advanced techniques, like the symmetric cell approach.[10] Thus, later on, Burns et al.[10] investigated the effect of VC (0 - 6 wt%) over extended charge/discharge cycling of graphite/NMC 18650 cells on anode and cathode impedance growth via symmetric cell measurements. They showed that indeed the impedance of the negative electrode increases nearly linearly with VC concentration, whereas the impedance of the positive electrode first decreases as the VC concentration is increased to 2 wt% and then only increases gradually at higher VC concentrations. The strong anode impedance growth suggests that VC is mostly consumed at the graphite anode, leading to SEI growth. This is consistent with a study by Petibon et al.,[11] who analyzed the consumption of vinylene carbonate in graphite/NMC pouch cells and showed that the additive is mainly consumed at the anode side (both during high temperature formation (50°C) and during a potential hold at 4.2 V cell voltage). In addition, they found that nearly 2 wt% VC were consumed during formation, so that little residual VC remained after formation for VC concentrations of ≤2 wt%. In a subsequent study, Petibon et al.[12] also showed that residual VC after formation leads to a fast decay in the open-circuit voltage during storage in cells charged to 4.4 V cell voltage, caused by the poor oxidative stability of VC.

In a recent study from our group,[13] we compared the effect of different VC concentrations on the impedance of graphite anodes in graphite/LFP ($LiFePO_4$) full-cells, using a Swagelok T-cell configuration with a reference electrode which enables the deconvolution of the overall cell impedance into the individual contributions from anode and cathode. There, we showed that the VC to active material ratio (expressed as the ratio of VC mass to graphite surface area in the cell), rather than the concentration of the additive in the electrolyte, is a key parameter when comparing results using different types of battery cell hardware. Basically, the cell hardware can roughly be categorized either into lab-scale-cells with a small total capacity (<10 mAh, i.e., <5 cm^2 electrode area), which due to design constraints require a high electrolyte/active material mass ratio in order to function properly (e.g., coin or Swagelok T-cells), or into commercial-scale cells with a high total capacity (>100 mAh, i.e., >20 cm^2 electrode area), which are assembled with much lower electrolyte/active material mass ratios (e.g., multi-layer pouch or 18650 cells with low electrolyte/active material mass ratio). Consequently, the electrolyte/active material mass ratio in the latter is ~12-fold lower compared to commonly used lab-scale cells, so that a concentration of 2 wt% VC in the study from Burns et al.[10] based on 18650 cells would corresponds to ~0.17 wt% VC in a typical lab-scale cell. This scaling factor between commonly used lab-scale cells and commercial-scale cells needs to be considered when using lab-scale cells to evaluate the effect of additives.

*Electrochemical Society Member.
**Electrochemical Society Fellow.
zE-mail: daniel.pritzl@tum.de

While the above discussed studies show that the cathode impedance growth with VC additive is generally small for graphite/LCO and graphite/NMC cells operating at cell voltages up to 4.4 V, this is not the case when higher voltage cathode active materials such as high-voltage spinel $LiNi_{0.5}Mn_{1.5}O_4$ (LNMO) are used. Li et al.[14] have shown that the cell performance of graphite/LNMO cells drastically decreases when 1 or 2 wt% of VC are added to the electrolyte, consistent with studies by Lee et al.[15] and Song et al.,[16] which demonstrated that the oxidative stability of VC is insufficient for operation with an LNMO cathode. The oxidative instability of VC was examined in more detail in a recent study from the group of Brett Lucht:[17] By means of ex-situ surface analysis (XPS and FT-IR) they showed that the oxidation of VC starts at already ~4.5 V vs. Li/Li^+, leading to the formation of poly(VC) at the surface of the LNMO cathode. Even though these studies demonstrate that VC is not a suitable additive for cells with LNMO cathodes, they were all based on lab-scale cell setups with a high electrolyte/active material ratio, so that the ratio of VC mass over graphite surface area for the used VC concentrations of 1–2 wt% was roughly an order of magnitude higher than what would be present in commercial-scale cells.

The additive VC behaves very differently in high-voltage cells compared to fluorinated additives. Fluoroethylene Carbonate (FEC) is often used in this type of cells, leading to an overall increased battery performance. On the one hand both additives (VC and FEC) generate CO_2 during reduction,[5,18] thus improving the anode SEI. On the other hand, FEC is more stable towards oxidation[19] (compared to VC) and can thus be used in large concentrations/quantities even at high voltages (e.g., with LNMO or HE-NCM cathodes).

In the present study, we therefore want to investigate much lower VC concentrations in the electrolyte in lab-scale cell tests (0.09–0.52 wt% VC), which would correspond to VC concentrations of 1–6 wt% in commercial-scale cells for the same ratio of VC mass to graphite surface area. The first part of our investigation aims to understand the drastic decrease in cell performance when large amounts of VC are added to graphite/LNMO cells (i.e., at very high ratios of VC mass to graphite surface area). To this end, we will examine the anodic stability of VC via on-line electrochemical mass spectrometry (OEMS) using carbon black model electrodes and a VC-only electrolyte with 1 M $LiPF_6$. As a next step, we conduct impedance measurements in graphite/LNMO cells using a micro-reference electrode,[13] quantifying anode and cathode impedance after formation in electrolytes with different amounts of VC (0.09, 0.17, 0.52, and 2 wt%). In the second part, we examine the impact of different VC concentrations on the cycling behavior of graphite/LNMO cells and on anode/cathode impedance during cycling at 40°C. We also show that the additional capacity during the first charge correlates with the impedance of the LNMO cathode. Finally, by comparing the impedance growth of the graphite anode in cells with either an LNMO or an LFP cathode, we can clearly show that VC is consumed at the LNMO cathode, resulting in a lower impedance of the of the graphite anode in a graphite/LNMO vs. a graphite/LFP cell.

Experimental

Electrode preparation.—$LiNi_{0.5}Mn_{1.5}O_4$ (LNMO) electrodes were prepared by mixing LNMO (BASF SE, Germany), carbon black (Super C65, Timcal), and polyvinylene difluoride (PVDF, Kynar) at a mass ratio of 92/5/3 with NMP (N-methyl pyrrolidone, anhydrous, Sigma-Aldrich, Germany) in a planetary mixer (Thinky Corp.) for 15 min. The ink was coated onto aluminum foil (MTI, 18 μm) with a doctor blade coater and dried afterwards at 50°C in a convection oven for at least 3 h. The final LNMO coating had a loading of ~13.6 mg_{LNMO}/cm^2, corresponding to ~1.9 mAh/cm^2. Electrodes with a diameter of 11 mm (≡0.95 cm^2) were punched out and compressed to ~30% porosity with a KBr press. Graphite electrodes were prepared by mixing graphite (T311, SGL Carbon, Germany) and PVDF at a mass ratio of 95/5 with NMP by applying the same procedure as for the positive electrodes. The graphite ink was coated onto copper foil (MTI, ~12 μm) and dried in a convection oven at 50°C for 3 h. The loading of the graphite coating was ~7 $mg_{graphite}/cm^2$ corresponding to ~2.6 mAh/cm^2. The electrodes were punched out with a diameter of 11 mm and compressed to a porosity of ~30%. Both types of electrodes were dried under dynamic vacuum at 120°C for at least 12 h in a vacuum oven (Büchi, Switzerland) and then transferred into an Argon-filled glove box (MBraun, Germany) without exposure to air.

For OEMS measurements, isotopically labelled ^{13}C-electrodes were prepared by dispersing ^{13}C-carbon (BET ~140 m^2/g, 99% isotopic purity, Sigma-Aldrich, Germany) in NMP with an ultrasonication horn. PVDF was dissolved in NMP to yield a 10% wt solution. The PVDF solution was added to the ^{13}C-dispersion to yield a final mass ratio of 1:2 (PVDF:^{13}C), and stirred carefully. The ink was then coated onto a polyester separator (Freudenberg, Germany) with a wedge bar and dried in a convection oven at 50°C. Afterwards, electrodes with a diameter of 15 mm were punched out, dried under dynamic vacuum at 120°C over night and transferred into an argon-filled glove box. The final electrodes had a loading of ~1 mg_C/cm^2.

On-line electrochemical mass spectrometry.—The on-line electrochemical mass spectrometry (OEMS) setup has been described in more detail in a previous publication by our group.[20] For the experiments in this study, we used a recently developed sealed 2-compartment cell,[21] where working and counter electrode are separated by a sealed lithium-ion conductive glass ceramics (Ohara Corp., Japan). In this way, only gases coming directly from the working electrode are detected, and any gas evolution related to the lithium counter electrode or electrode crosstalk can be avoided. The cells were assembled with a lithium counter electrode (Ø 17 mm, 450 μm thickness, Rockwood Lithium, USA), a glassfiber separator soaked with 250 μL electrolyte in the lower compartment and a polyester separator soaked with 100 μL electrolyte in the upper compartment. The investigated electrolytes consisted only of EC or VC with 1 M $LiPF_6$ (all from BASF SE, Germany). To distinguish between electrolyte oxidation and carbon corrosion, we used isotopically labelled ^{13}C-carbon electrodes coated on a polyester separator as working electrodes (see above). The oxidative stability of the electrolytes was investigated by a linear potential sweep from OCV (~3 V vs. Li/Li^+) to 5.5 V vs. Li/Li^+ at a scan rate of 0.1 mV/s. The quantification of the OEMS signals in terms of moles of produced gas was described previously,[22] and gas evolution rates are reported in terms of μmol gas/m^2_{BET} of the ^{13}C-electrode.

Electrochemical characterization.—Swagelok T-cells with a Gold Wire Reference Electrode (GWRE)[13] were assembled in an argon filled glove box (O_2 and H_2O < 0.1 ppm, MBraun, Germany) using two glass fiber separators (11 mm diameter, 200 μm thickness, glass microfiber #691, VWR, Germany) and 60 μL of electrolyte. The electrolyte consisted of standard LP57 (1 M $LiPF_6$ in EC: EMC (3:7 wt/wt) < 10 ppm H_2O, BASF, Germany) without and with different amounts of vinylene carbonate (VC, BASF SE, Germany), which was added at concentrations of 0.09, 0.17 0.52 and 2 wt% to the electrolyte. The cells were assembled using a graphite anode, a LNMO cathode, and a gold wire reference electrode (GWRE). The detailed experimental procedure for the assembly can be found in Reference 13. For charge/discharge cycling, identical Swagelok T-cells without a reference electrode were assembled. Cell cycling was carried out in a climate chamber (25°C or 40°C, Binder, Germany) with a battery cycler (Series 400, Maccor, USA). The cycling protocol consisted of the following steps: i) two formation cycles with C/10 at 25°C, ii) charge/discharge cycling with 1C (20 cycles) at 40°C, and iii) charge/discharge cycling with 1C/3C (2 cycles) at 40°C. The steps ii) and iii) were repeated five times. All cycles were performed between 3.5 V – 4.8 V cell voltage, using a constant current constant voltage (CCCV) charge with a current limit of C/20 for the constant voltage phase and a constant current (CC) discharge. The C-rate is referenced to the theoretical capacity of the LNMO cathode (140 mAh/g_{LNMO}), i.e., 1C corresponds to 140 mA/g_{LNMO}. or ~1.9 mA/cm^2.

Electrochemical impedance spectroscopy (EIS) measurements on graphite/LNMO cells with GWRE were conducted after the first

formation cycle at 50% SOC (charged to 50% SOC with C/10) and after the 22nd, 66th and 102nd (charged to 50% SOC with 1C) using a potentiostat (VMP300, BioLogic, France). Prior to the impedance measurement, the cells were charged to 50% SOC, transferred to a climate chamber set to 10°C, and stored for 1 h in order to ensure a constant temperature of the cells. Galvanostatic electrochemical impedance spectroscopy (GEIS) was used in a frequency range from 100 kHz – 100 mHz with an amplitude of 0.6 mA.

In a previous study[13] we have demonstrated the stability of the GWRE reference potential (0.31 V vs. Li/Li^+) in graphite/LFP cells to be >500 h. By replacing the LFP electrode (upper cut off potential ~4.1 V vs. Li/Li^+) by a $LiNi_{0.5}Mn_{1.5}O_4$ electrode (upper cut off potential ~4.9 V vs. Li/Li^+), the long-term stability of the GWRE reference potential is limited. The potential drift observed in the latter case might be caused by oxidation products generated at the high-voltage positive electrode (LNMO) and their subsequent reduction at the exposed surface of the gold wire, leading to an oxidation of the lithium-gold alloy (i.e., to its gradual delithiation). To overcome this issue, relithiation of the GWRE (at 150 nA for 1 h, consuming <0.1% of the capacity of the LNMO electrode during each charge) is carried out before each impedance measurement. A similar observation is reported by Klett et al.,[23] who also relithiated their Li_xSn reference electrode prior to each impedance measurement.

Results

Anodic stability of vinylene carbonate (VC) investigated via on-line electrochemical mass spectrometry (OEMS).—Until now, the detrimental oxidation of VC is regarded as a major obstacle for the successful use of VC in LNMO cells.[14–17] In order to investigate the onset potential for VC oxidation and its products, we performed on-line electrochemical mass spectrometry on electrolytes based on only VC or EC mixed with 1 M $LiPF_6$. For these experiments, we used carbon black electrodes made from isotopically labelled ^{13}C-carbon, so that we can track the gas evolution from the unlabeled ^{12}C-electrolyte by monitoring the corresponding ^{12}C-related signals of CO_2 and CO.[22] As Jung et al.[24] recently showed that the onset and extent of electrolyte oxidation on LNMO and carbon black is identical, it is safe to transfer the results obtained from the ^{13}C-carbon model electrodes to real LNMO cathodes later on. To avoid crosstalk between oxidized species and the lithium counter electrode, we used our sealed 2-compartment cell setup.[21] In this way, only the direct oxidation of the pure electrolyte is observed. Figure 1 shows the current profile (a) and the gas evolution (b) of $^{12}CO_2$ (m/z = 44, solid lines) and ^{12}CO (m/z = 28, dotted lines) during an oxidative scan in either EC-only or VC-only electrolytes with 1 M $LiPF_6$ from OCV (~3 V vs. Li/Li^+) to 5.3 V vs. Li/Li^+. While the current signal includes processes like capacitive currents related to the electrode surface or PF_6^- intercalation into the graphitic domains of the conductive carbon, which is reported to start around 4.6 V vs. Li/Li^+,[25,26] we believe that the evolution of gaseous electrolyte oxidation products is a more meaningful indicator for the onset of electrolyte oxidation. As expected, Figure 1b shows that the oxidative CO_2-release of VC starts at significantly lower potentials (~4.3 V vs. Li/Li^+) compared to EC (~4.8 V vs. Li/Li^+). The small current starting at ~3.7 V vs. Li/Li^+ for VC is most likely related to the oxidation of the BHT stabilizer (butylated hydroxytoluene), as its integration between 3.67 V and 4.0 V yields a charge of 10.2 mAs compared to the 11.9 mAs theoretically needed for the 1-electron oxidation of the 200 ppm BHT contained in VC. Interestingly, there is no CO evolution resulting from the oxidation of VC (See red dotted line in Figure 1b); on the other hand, the electrooxidation of EC yields both CO_2 and small amounts of CO (see black dotted lines in Figure 1, bottom panel), as we had discussed previously.[27]

The lower anodic stability of VC compared to EC has already been demonstrated by previous experimental results[15,17,28] and calculations.[29,30] The CO_2 evolution from VC at potentials above ~4.3 V vs. Li/Li^+ (see Figure 1b), corresponding to ~4.2 V cell voltage in a full-cell with a graphite anode, fits well to the observation made by the Dahn group[11,31–33] that commercials cells containing VC

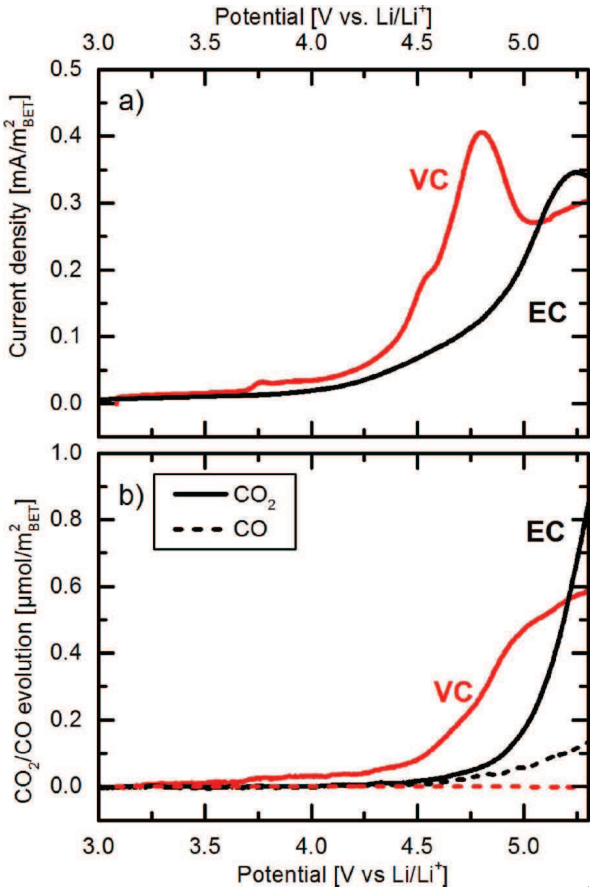

Figure 1. Anodic current (a) and evolution of $^{12}CO_2$ (b, solid lines) and ^{12}CO (b, dotted lines) from the electrolyte during a linear scan from OCV to 5.3 V vs. Li/Li^+ (0.1 mV/s) on a ^{13}C carbon electrode in electrolytes containing only EC (black lines) or VC (red lines) and 1M $LiPF_6$. The experiments were performed using on-line electrochemical mass spectrometry and a sealed 2-compartment cell[21] to avoid crosstalk with the lithium counter electrode.

evolve more gas when held at high potentials compared to the same cells without VC electrolyte. According to the EC oxidation mechanism proposed by Xing et al.[34] and Li et al.,[35] CO_2 is readily abstracted after ring opening of the EC radical cation (Scheme 1, black pathway 1a), while the evolution of CO from EC is energetically less favorable and only occurs with a simultaneous breaking of the CH_2-CH_2 bond after the intial ring opening (see blue pathway 1b in Scheme 1); for further discussion see Ref. 21). Although the decomposition mechanism of EC resulting in CO_2 can easily be applied to VC (see black pathway 2a in Scheme 1), the analogous pathway leading to CO is likely to present a very large barrier in the case of VC, as this would require breaking the much stronger CH=CH bond. Hence, our observation that no CO is produced during VC oxidation (Figure 1b) would be consistent with an analogous ring opening reaction as in the case of EC, which disagrees however with the early modeling predictions made by Zhang et al.[5] As poly(VC) has been found on electrodes cycled to high potentials in VC-containing electrolytes,[17] we assume that the radical cations formed in (2a) can trigger a radical polymerization reaction of VC to poly(VC) (see green pathway 2b in Scheme 1).[9,17]

Extracting the interfacial resistance from the impedance spectra.—As a next step, cells with different VC concentrations are assembled and impedance spectra are collected in order to understand the impact of the anodic decomposition of the additive in a graphite/LNMO full-cell. To extract the interfacial resistance from the anode Nyquist plots, the equivalent circuit shown in Figure 2a is used: i) the high frequency resistance (HFR) R_{HFR} represents the

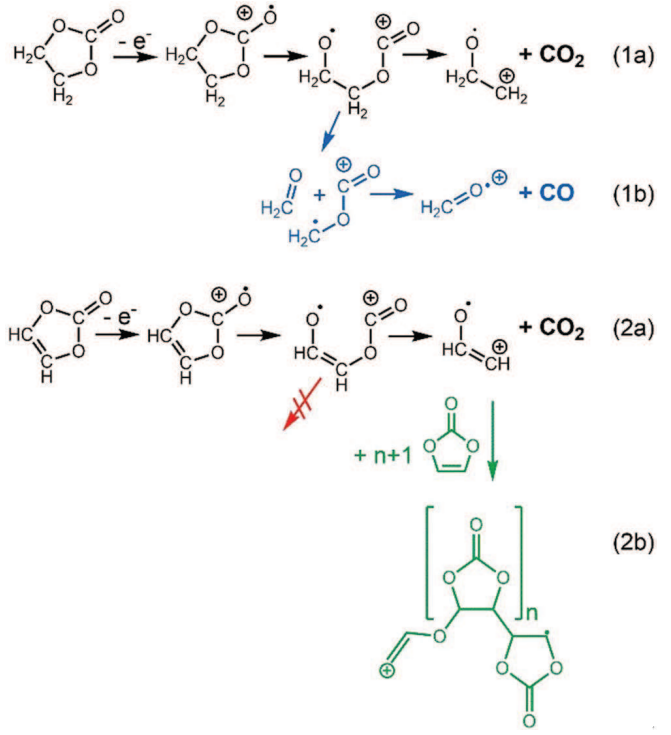

Scheme 1. Oxidation mechanism of EC leading to CO_2 (1a, black) and CO (1b, blue) as proposed by Xing et al.,[34] oxidation mechanism of VC leading to CO_2 (2a, black) and poly(VC) (2b, green).

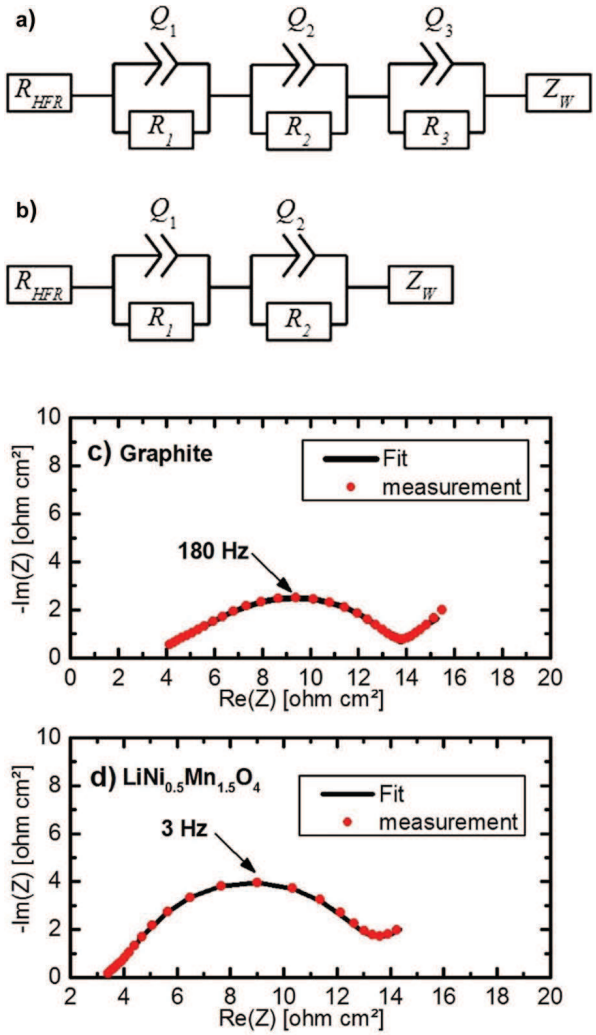

Figure 2. Equivalent circuit models for fitting the anode (a) and the cathode (b) impedance spectra. The Nyquist plots after one formation cycle and recharge to 50% SOC (at 0.1C and 40°C) of graphite/LNMO cells with LP57 electrolyte with 0.09 wt% VC are shown for both the graphite anode (c) and the LNMO cathode (d), whereby the experimental data (red points) are compared to the corresponding fit of the measurement (black line). The impedance is measured from 100 kHz to 100 mHz with an amplitude of 0.6 mA @ 10°C and 50% SOC.

contributions from the ionic conduction in the separator (between the GWRE and the respective electrode) and external electrical contact resistances; ii) up to three RQ-elements (resistor and constant-phase element in parallel) are used to determine the overall resistance of the anode, consisting of contributions from the charge transfer resistance, the solid-electrolyte interphase resistance, and one as yet unknown impedance contribution at low frequencies when high VC concentrations (0.52 and 2 wt%) are used (see Figure 3a); iii) the Warburg element (Z_W) mostly represents the diffusion of lithium in the liquid electrolyte phase as described in Reference 36. For the LNMO cathode, the equivalent circuit shown in Figure 2b is used, representing the analogous processes as in the case of the anode. Since the main focus of this study was to determine the individual impedance growth of anode and cathode during formation and extended charge/discharge cycling, only the overall anode and cathode impedance will be considered in the following ($R_{Anode} = R_1 + R_2 + R_3$, see Figure 2a; $R_{Cathode} = R_1 + R_2$ see Figure 2b). After the 22th cycle, a semi-circle at high frequencies appears in the cathode impedance spectra, which was shown to be due to the formation of a contact resistance at the interface between the cathode electrode and the cathode current collector,[36] and which will be omitted from the fitting process in this study. Unfortunately, a meaningful deconvolution/assignment of the individual impedance contributions to the overall impedance for each electrode would require more elaborate experiments, as we have shown in our recent work for the LNMO cathode impedance.[36] However, as explained above, the main objective of this study was to quantify the individual evolution of anode (R_{Anode}) vs. cathode ($R_{Cathode}$) impedance over extended charge/discharge cycling, for which a deconvolution into the various process is not necessary.

Figures 2c and 2d show exemplary Nyquist plots of a graphite anode and a LNMO cathode after one formation cycle in a graphite/LNMO full-cell with 0.09 wt% VC additive. The red points represent the experimental spectra (100 kHz - 100 mHz, current perturbation of 0.6 mA, 10°C), while the black line represents the fit to the equivalent circuit shown in Figures 2a and 2b. The values for the HFR of anode and cathode are ~4.0 and ~3.5 Ωcm^2, respectively; the cause for the slight difference in these HFR values (which are expected to be identical for a symmetric placement of the GWRE) was described elsewhere.[13] The overall resistances of the anode (R_{Anode}) and the cathode ($R_{Cathode}$) are in both cases ~10 Ωcm^2.

Impedance analysis after the first formation cycle.—The OEMS measurement showed an onset for the anodic decomposition of VC at ~4.3 V vs. Li/Li$^+$, accompanied by the release of CO_2. To understand the effect of the VC decomposition products formed by VC oxidation on the cathode (e.g., poly(VC) and radicals, see Scheme 2a and 2b) and by VC reduction on the anode (discussed in Reference 5) on cathode and anode impedance growth, we conduct impedance measurements with the gold-wire reference electrode (GWRE) after one formation cycle at 25°C and recharge to 50% SOC (state-of-charge) in LP57 with different concentrations of VC (0, 0.09, 0.17, 0.52, and 2 wt%). The additive concentrations were chosen such that some of the VC concentrations in our lab-scale cells yield VC mass to graphite surface area ratios comparable to those tested in the commercial-scale pouch cell experiments by Burns et al.:[10] 0.09, 0.17, and 2 wt% VC in our lab-scale cells approximately corresponds to 1, 2, and 6 wt% VC in their

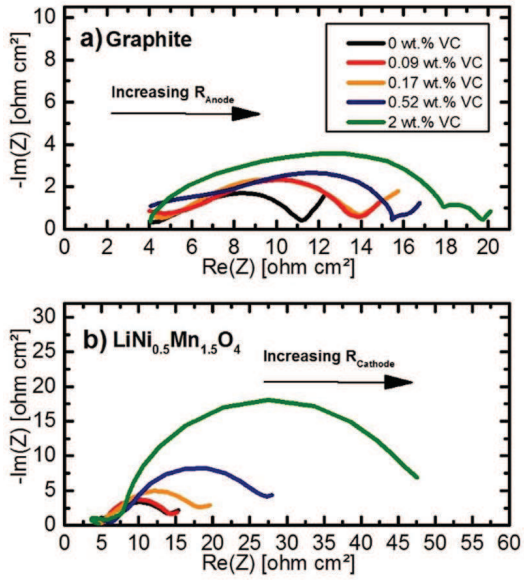

Figure 3. Anode and cathode impedances obtained from graphite/LNMO full-cell with GWRE after one formation cycle and recharge to 50% SOC at 25°C in LP57 with various VC additive concentrations. a) Impedance spectra of the graphite anode of cells containing 0 wt% VC (black lines), 0.09 wt% VC (red lines), 0.17 wt% VC (orange lines), 0.52 wt% VC (blue lines), and 2 wt% VC (green lines); b) analogous impedance spectra of the LNMO cathode. Impedance spectra were measured from 100 kHz to 100 mHz with a current amplitude of 0.6 mA at a temperature of 10°C and at 50% SOC.

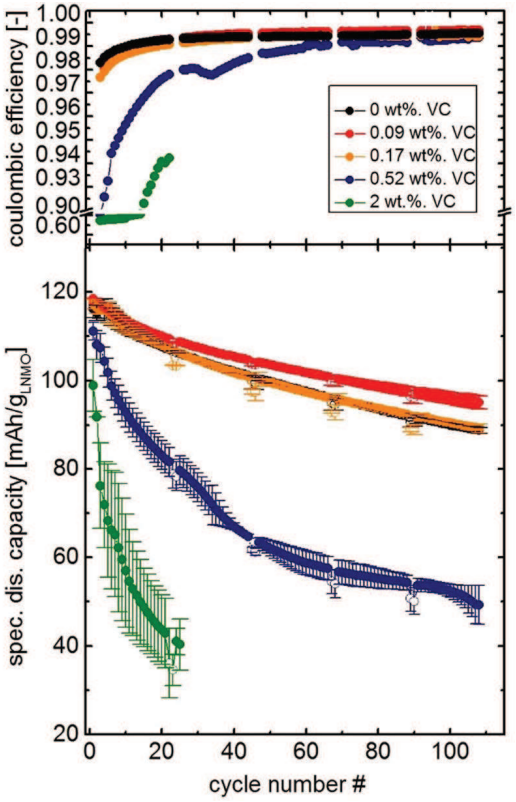

Figure 4. Coulombic efficiency (upper panel) and specific discharge capacity (mAh/g_{LNMO}) (lower panel) of graphite/LNMO cells (without GWRE) over extended charge/discharge cycling at 1C/1C (followed by two 1C/3C cycles after every 20 cycles) and 40°C between 3.5 and 4.8 V in LP57 electrolyte with different VC concentrations: 0 wt% VC (black points), 0.09 wt% VC (red points), 0.17 wt% VC (orange points), 0.52 wt% VC (blue points), and 2.0 wt% VC (green points). The formation of the cells was carried out at 25°C (2 cycles at C/10), while further cycling is done at 40°C. For clarity, the upper panel does not contain data of the two formation cycles and the 1C/3C cycles. The coulombic efficiencies of the two formation cycles (cycle 1 and 2) are given in Table I. Two cells were tested for each electrolyte composition; the figure shows the average of the two cells, with error bars representing the standard deviation. 3C discharge points are filled white for better visibility.

commercial-scale cells. In addition, to allow for a better comparison of the resulting anode and cathode impedance, we also conducted our impedance measurements at 10°C, as done in the latter study. Figures 3a and 3b show the Nyquist plots of the graphite and the LNMO electrodes recorded from a graphite/LNMO full-cell with GWRE.

Without VC additive (black lines), the fitted values for the overall resistance of the anode, R_{Anode}, are ~7 Ωcm² and ~9 Ωcm² for $R_{Cathode}$. When a small amount of VC (0.09 wt%, red lines) is added to the cells, the overall resistance of the anode increases to ~10 Ωcm², whereas the impedance of the cathode stays constant at ~9 Ωcm². When the concentration is increased to 0.17 wt% (orange lines), the impedance of the anode remains at ~10 Ωcm² while now the impedance of the cathode starts to increase to ~13 Ωcm². While the anode impedance only increases very little with a further rise in VC concentration, namely to ~15 Ωcm² for 0.52 wt% VC (blue lines) and to ~16 Ωcm² for 2 wt% VC (green lines), the cathode impedance increases substantially to ~22 Ωcm² for 0.52 wt% VC and to ~41 Ωcm² for 2 wt% VC.

Our interpretation of these observations is as follows: When small amounts of VC (0.09 wt%) are added to the graphite/LNMO cells, it will preferentially be reduced at the graphite anode, leaving no or little VC for oxidation at the LNMO cathode. On the other hand, when higher concentrations of VC are present in the electrolyte (0.17–2 wt%), residual VC remains in the electrolyte after anode SEI formation, allowing for oxidation of VC at the high-voltage LNMO cathode, ultimately leading to cathode impedance growth. As already suggested in previous studies[17] and shown in Scheme 1 (reactions 2a and 2b), the formation of a poly(VC) film on the LNMO cathode is the most likely explanation for the observed impedance increase of the positive electrode shown in Figure 3b. The very high cathode impedance of our lab-scale cell with 2 wt% VC after only one formation cycle indicates that the rapid oxidation of VC at the LNMO cathode potential (shown by OEMS data in Figure 1) leads to the formation of a highly resistive surface film. This would be consistent with the strong capacity fading reported for graphite/LNMO coin cells with 2 wt% VC[14] and will be further examined in the following. These results suggest that the ratio of (anode) additive to graphite surface is crucial for high-voltage lithium-ion cells, and that a successful use of SEI formers like VC will depend on the competition between additive reduction on the anode and its oxidation on the cathode, as will be explained in more detail in the Discussion section.

Cell cycling at elevated temperatures (40°C) with different concentrations of vinylene carbonate (VC).—As a next step, the influence of different VC concentrations on the cycling behavior at elevated temperatures (40°C) will be investigated. The two main questions are: i) can low concentrations of VC have a beneficial effect on the cycling performance of graphite/LNMO cells, despite the current understanding that VC has a detrimental effect; and, ii) how do the VC oxidation products affect the capacity retention of full-cells. To address these questions, graphite/LNMO cells with different VC concentrations are cycled at 40°C at 1C (CCCV charge, CC discharge; for details see Experimental section) after formation at 25°C (two C/10 cycles). After every twentieth 1C/1C charge/discharge cycle, two 1C/3C charge/discharge cycles are employed in order to gain information about the resistance buildup in the cells, which later on will be compared with the anode/cathode impedance data acquired in repeat experiments using T-cells equipped with a gold wire reference electrode. Figure 4 shows both the specific discharge capacity (in mAh/g_{LNMO}) versus the cycle number (bottom panel) and the coulombic efficiency (top panel) of graphite/LNMO cells with different VC concentrations. For clarity, each dataset shown in Figure 4 contains

the average value of two identical cells (error bars represent the standard deviations between the two cells). Starting from cells which contain no VC (0% VC, black dots), the first discharge capacity at C/10 is ~117 (±2) mAh/g_{LNMO}, resulting in a first-cycle coulombic efficiency of ~82%. After 80 cycles, the coulombic efficiency reaches a constant value of ~99.5% while the discharge capacity remains at ~88 (±1) mAh/g_{LNMO} after 108 cycles. When adding VC at a commonly used concentration of 2 wt% VC (Figure 4, green dots), the first-cycle discharge capacity at C/10 is only ~99 (±6) mAh/g_{LNMO}, with a coulombic efficiency of ~54%, i.e, dramatically lower than in cells with VC-free electrolyte. The capacity loss for cells with 2 wt% VC is very high (57 ±3 mAh/g_{LNMO} after 20 cycles), and the difference in capacity between the last 1C/1C (cycle 25) and the previous 3C/1C cycles amounts to ~8 (±5) mAh/g_{LNMO} (in contrast to ~1 (±1) mAh/g_{LNMO} for VC-free electrolyte at the same point), which indicates a dramatic increase in cell impedance. Owing to the already very low capacity after these initial 23 cycles, the test was discontinued here. The poor coulombic efficiency with 2 wt% VC can partly be explained by the early onset of VC oxidation at a cell voltage of ~4.2 V (i.e., at ~4.3 V vs. Li/Li^+), as evidenced by the OEMS data in Figure 1, since a parasitic oxidation reaction would reduce the coulombic efficiency.

When the concentration of VC is lowered to 0.52 wt% (Figure 4, blue points), the first discharge capacity is ~111 (±2) mAh/g_{LNMO} and a first-cycle coulombic efficiency of ~74% is obtained, which is much higher compared to cells with 2 wt% VC (see Table I). After 108 cycles, the discharge capacity is ~49 (±4) mAh/g_{LNMO} and the coulombic efficiency increases up to 97.5% until cycle 30, where it shows an unexplained drop until cycle 40, and then gradually approaches 99% by the end of the test procedure. Also here, the low coulombic efficiency and capacity retention illustrate the negative impact of VC oxidation products on cell performance. When 0.17 wt% VC are added to the full-cell, a first-cycle discharge capacity of ~118 (±2) mAh/g_{LNMO} with a first-cycle coulombic efficiency of 82% are observed, quite similar to the case without VC additive (see Table I). Thus, it is not surprising that after 108 cycles, the discharge capacity of ~88 (±2) mAh/g_{LNMO} is essentially identical to that of the VC-free electrolyte, even though the coulombic efficiency up to cycle 30 is slightly lower (upper panel of Figure 4, orange points). The slightly larger difference between the 1C/1C and the 1C/3C discharge capacity suggests a somewhat higher cell resistance for the 0.17 wt% VC compared to the VC-free electrolyte, which we will correlate with the impedance data in the next section.

So far, the graphite/LNMO cell performance with VC-free electrolyte is clearly superior to VC-containing electrolyte. This observation, however, changes as the VC concentration is lowered to 0.09 wt% (Figure 4, red points), in which case we observe a higher 1st cycle coulombic efficiency (83%), an improved capacity retention (95 (±2) mAh/g_{LNMO} after 108 cycles) compared to cells without VC additive (88 (±1) mAh/g_{LNMO} after 108 cycles), as well as a better coulombic efficiency reaching 99.7% (vs. 99.6%) after 108 cycles.

As shown by Reaction 2a in Scheme 1, the oxidation of VC will release cations into the solution (presumably the cation radicals proposed in Reaction 2a) which will result in one or several of the following processes: i) electroneutrality in the electrolyte requires that lithium ions from the solution must intercalate into the graphite anode (under the reasonable assumption that no intercalation of the radical cations into graphite and/or the PF_6^- anions into LNMO can occur; this is a reasonable assumption, since the amount of C65 is small and as it is not fully graphitized), which would lead to a depletion of lithium ions in the electrolyte; ii) if the released radical cations stabilize by the release of a proton (as evidenced in our previous study[21]), the proton concentration in the electrolyte would increase (simultaneously decreasing the lithium ion concentration), unless proton intercalation into graphite (during charge) and/or LNMO (during discharge) can occur to a significant degree; iii) VC oxidation and the formation of protons could lead to enhanced dissolution of transition metal ions (as this process is known to correlate with the electrolyte oxidation potential),[37] which – together with oxidation products like HF themselves – could damage the SEI and lead to additional irreversible lithium loss at the anode; and, iv) VC oxidation could lead to impedance growth on anode and/or cathode due to reactions involving VC oxidation products. Regarding the latter, we will see in the following that while the observed impedance growth is substantial, it seems too low to explain the dramatic observed capacity fading. Figure 5 shows the full-cell voltage profiles (E_{WE}-E_{CE}) for cells with 0 wt% and 0.52 wt% VC after the 30th and 100th cycle. For cells containing 0 wt% VC one can clearly see that the increase in the overpotential during cycling is minor (black solid line vs. black dotted line) and therefore the loss of active lithium is the most likely reason for the capacity fade. Cells with 0.52 wt% VC show an increased polarization, which increases slightly during cycling (blue line vs. blue dotted line). However, as i) the capacity obtained during the constant voltage (CV) step does not increase significantly between cycle 30 and 100 for cells with 0.52 wt% VC, and ii) the voltage profiles for cells with 0.52 wt% VC at the end of the of the constant-current charge still bend upwards, indicating that the cathode is close to complete delithiation, the capacity loss is most likely connected to a loss of active lithium and cannot be solely explained by an increased polarization.

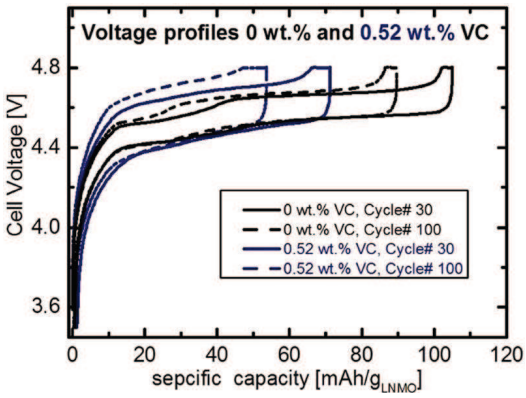

Figure 5. Full cell voltage profiles (E_{WE}-E_{CE}) for cells with 0 wt% and 0.52 wt% VC in graphite/LNMO cells (cycled at 40°C) after cycle 30 and cycle 100.

Thus, we believe that the first two mechanisms are the most likely explanation for the observed rapid capacity fading of cells with high concentrations of VC, even though it is currently unclear which one of these processes might be predominant: according to the first mechanism (i), lithium plating would eventually have to occur at the graphite anode and the lithium ion concentration in the electrolyte would get depleted due to a buildup of cationic oxidation products in the electrolyte; according to the second mechanism (ii), protons formed and accumulated in the electrolyte would be expected to corrode the LNMO cathode, resulting in transition metal dissolution and their

Table I. Coulombic efficiency of graphite/LNMO cells of the first two formation cycles at C/10 (25°C) for cells with 0, 0.09, 0.17, 0.52, and 2 wt% VC in LP57.

Concentration	0 wt% VC	0.09 wt% VC	0.17 wt% VC	0.52 wt% VC	2 wt% VC
1st cycle	82%	83%	80%	74%	54%
2nd cycle	95%	96%	94%	85%	59%

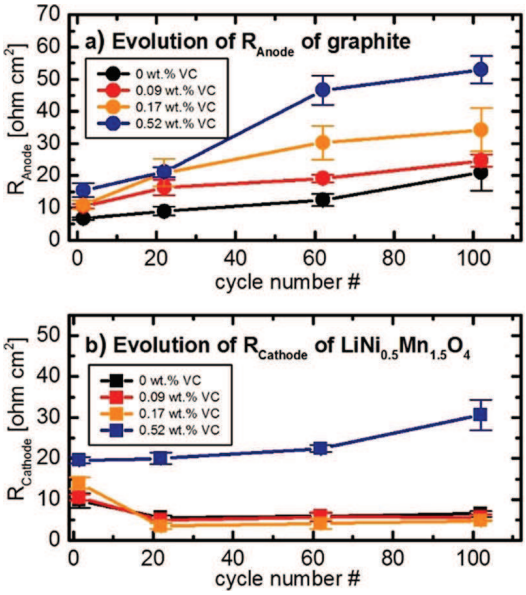

Figure 6. Evolution of the interfacial electrode resistances (R_{Anode} and $R_{Cathode}$) of graphite/LNMO cells (measured with GWRE) over extended charge/discharge cycling at 1C/1C and 40°C between 3.5 and 4.8 V in LP57 electrolyte with different VC concentrations. a) R_{Anode} of the graphite anode over cycling with 0 wt% VC (black line), 0.09 wt% VC (red line), 0.17 wt% VC (orange line), and 0.52 wt% VC (blue line); b) $R_{Cathode}$ of the LNMO cathode for the same electrolytes. Note that the impedance obtained after the first formation cycle at 25°C and C/10 at are included in this figure as cycle 1 (see data shown in Figure 3). Impedance spectra were recorded at 50% SOC and 10°C from 100 kHz to 100 mHz with an amplitude of 0.6 mA. Two cells were tested for each electrolyte composition; the data points show the average of the two cells, with error bars representing the standard deviation.

deposition on the graphite anode. Further studies are currently underway to prove/disprove these hypotheses.

Analysis of the impedance of anode and cathode during cycling.—In this section, we want to investigate the effect of different VC concentrations on the impedance of anode and cathode during cycling. Therefore, the T-cells with GWRE used for the examination of anode and cathode impedance vs. VC concentration after the first formation cycle at 25°C (data shown in Figure 3) were transferred to a 40°C climate chamber where they were was cycled at 1C/1C charge/discharge, The cycling protocol was identical to that used for the cell cycling shown in Figure 4, except that the two 1C/3C charge/discharge cycles after every 20th cycle were omitted. This, however, did not significantly alter the cycle-life: cells equipped with a GWRE and with VC-free electrolyte had a capacity of 87 (±2) mAh/g_{LNMO} after 102 cycles, which is comparable to a capacity of 89 (±1) mAh/g for the cells with the same electrolyte but without reference electrodes (see black symbols in Figure 4). Impedance was measured after the 22nd, 62nd, and 102nd cycle at 50% SOC and 10°C.

Figures 6a and 6b show the overall interfacial resistance of the graphite anode and the LNMO cathode versus cycle number. Note that the data from the first formation cycle are included, where cells were cycled at 25°C.

The anode impedance (Figure 6a) increases roughly linearly with cycle number for cells without VC (black line) and those with 0.09 wt% (red line) and 0.17 wt% VC additive (orange line). For cells with 0 wt% VC, the anode impedance increases from ~7 Ωcm^2 (first cycle) to ~20 Ωcm^2 (102nd cycle). Cells containing 0.09 wt% and 0.17 wt% VC show a similarly gradual impedance increase. For cells with a concentration of 0.17 wt% VC, the impedance increase is slightly higher compared to cells with 0.09 wt% VC, although the initial values for the anode impedance are identical (~10 Ωcm^2). The anode impedance of cells with 0.52 wt% VC increases substantially during cycling, namely up to ~55 Ωcm^2 after the 102nd cycle. An analogous increase of the graphite anode impedance with increasing VC concentrations was also observed by Burns et al.[10] in commercial-scale graphite/LCO cells for >1 wt.%VC. As will be discussed later, the difference in the VC threshold concentration is due to differences in the electrolyte to graphite surface ratio in commercial-scale vs. lab-scale cells.

Figure 6b shows the interfacial resistance versus cycle number for the LNMO cathode. For cells with 0, 0.09, and 0.17 wt% VC, the impedance decreases after the formation cycle, reaching a constant value of ~5 Ωcm^2 after 20 cycles. In contrast, the LNMO cathode interfacial impedance starts out with a significantly higher value after the first formation cycle (~22 Ωcm^2) for the cells with 0.52 wt% VC and increases with cycle number to ~30 Ωcm^2. We believe that the most likely explanation for the LNMO cathode impedance decrease for low VC concentrations is related to the different temperatures during the first formation cycle (25°C) and the subsequent extended charge/discharge cycling (40°C). During cycling at elevated temperatures, the electrolyte/LNMO interface initially formed at 25°C might be restructured at 40°C by the enhanced solubility of some of the interfacial species (e.g., dissolution of organic interfacial species like poly(VC) or of manganese fluoride produced by reaction with HF traces in the original electrolyte), leading to an impedance decrease. For the cells with 0.52% VC, one could imagine that the relatively high VC concentration has led to a thicker cathode surface film, which cannot be dissolved due to a change in temperature. Further, the ongoing cathode impedance growth during cycling could mean that not all VC has been consumed during the initial cycles.

It should be noted that if the content of conductive carbon in the LNMO electrodes is decreased from 5 wt% (used here) to 2 wt%, an increase in LNMO cathode impedance during cycling can be observed even for low VC concentrations. This effect can clearly be attributed to a growing contact resistance at the current collector/electrode interface, as we will show in a future study.[38] However, when 5% carbon black are added to the electrodes (see this study), the increase of the contact resistance is significant.

Discussion

In the following, we will seek to examine why the very low VC concentration of 0.09 wt% in our lab-scale graphite/LNMO cells leads to a clearly improved capacity retention (see Figure 5). This could be understood if these low concentrations of VC are sufficient to form a protective SEI, and if during the first formation cycle, VC reduction at the graphite anode can be completed prior to its oxidation at the LNMO cathode. We will also show that high VC concentrations result in significantly overcharge capacity in the first charging cycle, consistent with the oxidation of the majority of remaining VC at the LNMO cathode. Finally, based on the here observed effect of VC concentration on graphite/LNMO lab-scale cell performance, we will project the VC concentration levels in the electrolyte of commercial-scale cells which would lead to an improved cycling performance of graphite/LNMO cells compared to VC-free electrolyte.

Estimated coverage of VC derived SEI on graphite surface with 0.09 wt% VC additive.—In the following, we want to estimate how many monolayers of poly(VC) can be deposited on the graphite surface by the reduction of all VC contained in the electrolyte with 0.09 wt% VC, i.e., for the concentration which showed the best capacity retention in Figure 4. The purpose of this estimate is to evaluate whether the amount of VC-derived SEI (consisting largely of poly(VC)) at this low VC concentration could yield monolayer thick films, which would be required for surface passivation.

First, we approximate the surface area that can be occupied by one repeat unit of poly(VC), corresponding to the reductive decomposition of one VC molecule.[39] Analogous to Jung et al.,[18] we assume that one adsorbed decomposition product of VC consists of eight atoms (total amount of atoms per poly(VC) repeat unit) and that every atom occupies a square with an average length of a carbon-carbon single

bond of 0.15 nm. Thus, the corresponding area that would be covered by one poly(VC) unit equals to $8 \times (0.15\ nm^2)^2 = 0.18\ nm^2$. Taking into account the Avogadro constant ($N_A = 6.022 \cdot 10^{23}$ atoms/mol) and the total surface area of the graphite anodes used in this study (0.033 $m^2_{Graphite}$, based on a BET surface area of ~5 m^2/g, a loading of ~7 $mg_{Graphite}/cm^2_{electrode}$, and a geometric surface area of 0.95 cm^2), we can now estimate how many moles of VC are required to form one monolayer n_{ML} of poly(VC) on the graphite surface:

$$n_{ML} = \frac{0.033\ m^2}{N_A \times 0.18\ nm^2} = 0.307\ \mu mol/ML \quad [1]$$

To obtain the effective number of monolayers of poly(VC) produced on the graphite anode during the first formation cycles, one would need to estimate the fraction of the added moles of VC which are reduced at the anode compared to the fraction which might be oxidized at the cathode. Based on the impedance data in Figure 3b, the LNMO impedance after formation increases only in the cases where the VC concentration is ≥0.17 wt%, so that it is reasonable to assume that for cells with 0.09 wt% VC, all VC in the electrolyte is only reduced at the anode, since the oxidation of excess VC on the cathode obviously leads to a highly resistive film (presumably also poly(VC)[17]) on the LNMO cathode. Hence, it should be a reasonable estimate that the total amount of VC in the 0.09 wt% VC electrolyte ($n_{VC} = 0.73\ \mu mol_{VC}$ in 60 µL electrolyte) will be reduced at the anode within the first formation cycle to form an SEI layer. In this case, the total number of deposited poly(VC) monolayers N_{ML} in the anode SEI can be estimated as:

$$N_{ML} = \frac{n_{VC}}{n_{ML}} = \frac{0.73\ \mu mol_{VC}}{0.307\ \mu mol/ML} = 2.4\ ML \quad [2]$$

The resulting value on the order of 2–3 monolayer equivalents of poly(VC) could in principle be sufficient to build a passivating VC-derived SEI on the graphite anode. The thickness of this layer, d_{SEI}, can be estimated by assuming that the average monolayer thickness d_{ML} will roughly be the length of a carbon-carbon single bond (0.15 nm):

$$d_{SEI} = N_{ML} \times d_{ML} = 2.4\ ML \times 0.15\ nm/ML = \sim 0.4\ nm \quad [3]$$

In view of the superior cycling performance with 0.09 wt% VC compared to VC-free electrolyte or electrolyte with higher VC concentrations (see Figure 4) and considering the above estimates, we can finally conclude that a VC concentration of 0.09 wt% is on the one hand sufficiently small to be completely reduced within the first cycle, thus avoiding any detrimental side reactions during subsequent oxidation at the LNMO cathode, and on the other hand still large enough to accomplish adequate passivation of the graphite anode with an average SEI thickness of ~0.4 nm. The overall SEI will be thicker than ~0.4 nm as also EC and the PF_6^- anion can be reduced after the initial cycles, however a sufficient fraction of the SEI consists of poly(VC) leading to enhanced stability.

Reduction and oxidation of VC considering the half-cell potentials of graphite and LNMO.—The above analysis tacitly assumed that the quantity of VC in the 0.09 wt% electrolyte can be reduced at the graphite anode prior to the onset of VC oxidation at the LNMO cathode during the first formation cycle. That this is indeed feasible can be shown by examining the graphite and LNMO half-cell potentials during the first charging of graphite/LNMO cells. To follow the half-cell potentials during the first charge, a graphite/LNMO cell with 0 wt% VC and a lithium metal reference electrode was used. Figure 7 shows the potential of the graphite anode vs. Li/Li^+ and of the LNMO cathode vs. Li/Li^+ during the first part of the formation (up to a first charge capacity of 13 mAh/g_{LNMO}, which correspond to ~1 h of charge at C/10). The dark blue line represents the graphite half-cell potential, while the vertical dashed lines indicate the onset for the VC reduction at ~1.8 V vs. Li/Li (blue line) and the reduction of EC at ~0.8 V vs. Li/Li^+ (red line) taken from References 4 and 5. After a charge capacity of only ~0.5 mAh/g_{LNMO} (~2 minutes at C/10), the onset potential for the reduction of VC is reached, whereas after a

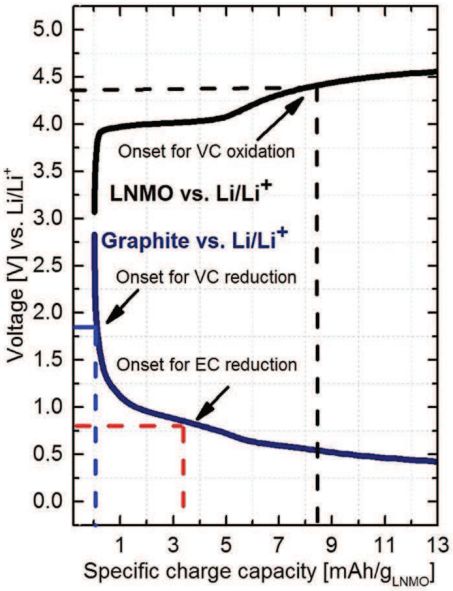

Figure 7. Half-cell potentials of LNMO (black line) and graphite (blue line) vs. Li/Li^+ during the first formation cycle at C/10 and 25°C in an VC-free LP57 electrolyte. The vertical dashed lines mark the onset potentials for VC reduction (blue), EC reduction (red), and VC oxidation (black).

total capacity of ~4.5 mAh/g_{LNMO} (~18 minutes at C/10), the onset potential for EC reduction is reached. At the same time, the half-cell potential of the LNMO cathode (Figure 7, black line) shows a short plateau around ~4.0 V vs. Li/Li^+ for ~6 mAh/g_{LNMO}, corresponding to the Mn^{3+}/Mn^{4+} redox couple. Upon further charging, the LNMO potential gradually increases toward its main voltage plateau at ~4.7 V vs. Li/Li^+, which belongs to the Ni^{2+}/Ni^{3+} redox couple (due to the zoomed-in view of the capacity axis, only the onset for the plateau at 4.7 V vs. Li/Li^+ is visible).[40] An potential of ~4.3 V vs. Li/Li^+, which corresponds to the onset potential for VC oxidation (black vertical line), is reached by the LNMO cathode after ~8.5 mAh/g_{LNMO} (i.e., ~34 minutes) in this first charge of the graphite/LNMO cell. This means that there are ~8 mAh/g_{LNMO} or ~30 minutes during the first charge where the graphite potential is already low enough to reduce VC, but where the LNMO potential is still too low to oxidize VC (illustrated by the difference between the vertical blue and black lines in Figure 6). The capacity of ~8 mAh/g_{LNMO} can now be compared to the theoretical capacities required for the reduction of different amounts of VC in the electrolyte.

Based on a previous study,[5] the first step in the formation of poly(VC) is most likely the one-electron reduction of VC to the radical anions $\bullet CH = CH\text{-}O\text{-}COO^-$ or $\bullet CH = CH\text{-}O^-$ (upon release of CO_2), both of which can react with VC to poly(VC). Thus, the formation of poly(VC) would require ≤0.5 electrons per VC molecule (depending on the number of repeat units in the poly(VC) product). This implies that the reduction of 0.73 µmol VC in the 0.09 wt% VC electrolyte would require a reductive charge of ≤0.010 mAh or, if referenced to the mass of LNMO in the cell (12.9 mg, based on a loading of 13.6 mg_{LNMO}/cm^2 and an electrode area of 0.95 cm^2), a charge of ≤0.76 mAh/g_{LNMO}. Thus, for the 0.09 wt% VC electrolyte, the total amount of VC in the electrolyte can easily be reduced at the graphite anode before the LNMO cathode potential reaches the onset potential for VC oxidation (which occurs at ~8 mAh/g_{LNMO} after the VC reduction onset, as discussed before). The same analysis would suggest that even for our VC concentration of 0.52 wt%, the required reductive charge of ≤4.5 mAh/g_{LNMO} would still be available prior to reaching an LNMO potential of ~4.3 V, which is required to oxidize VC; on the other hand, for 2 wt% VC, the reductive charge which can be passed before the LNMO cathode reaches ~4.3 V would likely not suffice to reduce all of the VC in the electrolyte (which would require

≤17.3 mAh/g_{LNMO}). While these estimates show that even 0.52 wt% VC in our electrolyte could in principle be reduced at the graphite anode before the LNMO cathode potential is high enough to oxidize VC, the LNMO cathode impedance data after the first formation cycle (see Figure 3b) clearly shows a substantial LNMO impedance increase with VC concentrations ≥0.17 wt%, indicating that there is residual VC left in cells with ≥0.17 wt% VC after the initial 8.5 mAh/g_{LNMO} charge. These observations fit well to a study by Petibon et al.,[11] who showed that in commercial-scale NMC/graphite pouch cells with 1% wt.VC (corresponding to 0.09 wt% VC in our cells in terms of VC to graphite surface ratio), more than 80% of the initial VC is already consumed after ∼50% of the first charge, whereas at the same point, about 4.2 wt% VC is left if the cell originally contained 6 wt% VC (i.e., 0.52 wt% VC in our study). Our results suggest that for the formation of a passivating anode SEI, VC concentrations between 0.09 wt% (no LNMO impedance increase compared to 0 wt% VC, see Figure 3b) and 0.17 wt% (LNMO impedance increase, see Figure 3b) are sufficient. Assuming that the reduction of VC is substantially slowed down once this passivation has been reached, any excess VC would be oxidized at the LNMO cathode once it exceeds a potential of ∼4.3 V, as seen in the LNMO impedance for cells with ≥0.17 wt% VC.

Overcharge capacities from the anodic decomposition of VC.— The impedance data in Figure 3b suggest that in the case of higher VC concentrations (≥0.17 wt%), a significant fraction of the VC present in the electrolyte must be oxidized in the first cycle at the LNMO cathode. In this case, the additional oxidative current used for the oxidation of VC should increase the first cycle charge capacity.[16,17] Therefore, we want to analyze the first cycle overcharge capacities in graphite/LNMO cells with different amounts of VC. The formation protocol consists of two C/10 charge (CCCV)/discharge (CC) cycles between 3.5 V – 4.8 V cell voltage with a current limit of C/20 for the CV step. Figure 8a shows the first charge of cells with different VC concentrations. For the cells with a concentration of 0 wt% VC and 0.09 wt% VC, the first charge capacities are ∼140 mAh/g_{LNMO} and ∼141 mAh/g_{LNMO} (black line and red line in Figure 8a). These values correspond to the theoretical capacity of the LNMO electrode, consistent with our above assumption that no VC oxidation occurs in cells with 0.09 wt% VC. When the concentration of VC is increased to 0.17 wt% VC, the capacity increases to ∼144 mAh/g_{LNMO} (yellow line in Figure 8a), indicating that the now occurring electrochemical oxidation of VC causes an additional charge capacity. This is further supported when the concentrations of 0.52 wt% and 2 wt% are taken into account, for which the first charge capacity increases to ∼151 mAh/g_{LNMO} and to ∼183 mAh/g_{LNMO}, respectively (see blue line and green line in Figure 8a).

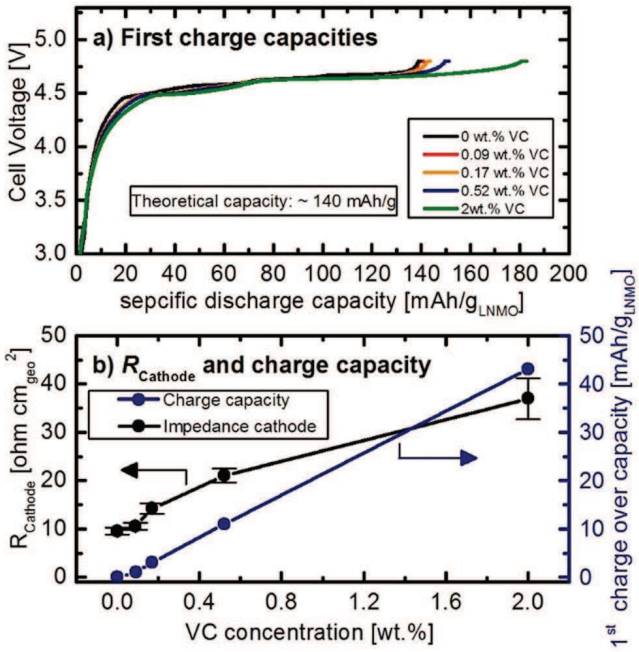

Figure 8. a) First charge of graphite/LNMO cells with 0 wt% VC (black line), 0.09 wt% VC (red line), 0.17 wt% VC (orange line), 0.52 wt% VC (blue line), and 2 wt% VC (green line). The charge is carried out in a constant current constant charge mode (CCCV) with a current limit of C/20 for the CV step. b) First charge capacities of the graphite/LNMO cell and LNMO cathode interfacial impedance, $R_{Cathode}$, after first charge/discharge (data from Figure 3b) vs. VC concentration.

In the following, we want to correlate the overcharge capacities arising from VC oxidation (i.e., the first charge capacity minus 140 mAh/g_{LNMO}, which is the first charge capacity of a cell with VC-free electrolyte) to the impedance of the LNMO electrode. In Figure 8b, the first charge capacities (blue symbols, right y-axis) are plotted vs. VC concentration. It is apparent that for VC concentrations ≥0.17 wt%, the charge capacity increases proportionally with the VC concentration (i.e., doubling the VC concentration leads to a doubling of the overcharge capacity), which is a clear evidence that excess VC is being oxidized quantitatively during the first charge. The lower than predicted overcharge for the cells with 0.09 wt% VC is in agreement with our assumption that in cells with 0.09 wt% VC, nearly all VC is consumed at the anode before its oxidation can occur. This overall trend fits very well with the LNMO impedance data obtained after the first cycle (see Figure 3b), which are re-plotted in Figure 8b (black symbols, left y-axis), demonstrating that the overcharge capacity and the impedance of the LNMO cathode are correlated. As mentioned before, the impedance increase at the positive electrode can be explained by the formation of poly(VC), which can also be formed during oxidation (see reactions 2a and 2b in Scheme 1). In contrast to the first charge capacity, the cathode impedance grows less severely at high VC concentrations. An explanation for this behavior could be the structural or morphological changes in the poly(VC) layer once a certain thickness has been reached, which might affect the cathode impedance.

The slope of the overcharge capacity vs. VC concentration (see blue line in Figure 8a) corresponds to ∼2.4 electrons per VC molecule. However, so far only a ≤1 electron per oxidized VC molecule has been proposed (see reactions 2a and 2b in Scheme 1).[17] We thus propose that the larger number of electrons per VC could arise from a further oxidation of the initially produced radical cation (see reaction 2a in Scheme 2), following its stabilization through the release of a proton (see reaction 2c, Scheme 2). The analogous formation of protons during the oxidation of EC/EMC electrolyte has been proposed by Metzger et al.,[21] based on the observation that H_2 is evolved on the

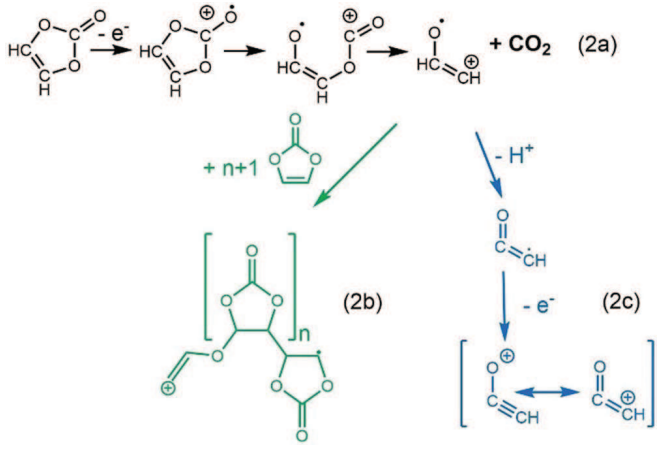

Scheme 2. Extension of the VC oxidation mechanism from Scheme 1 including proton abstraction and a second oxidation step.

anode during electrolyte oxidation, presumably due to the reduction of released protons. After the release of a proton, the intermediate could then be oxidized again, resulting in a mesomerically stabilized cation. Further, this end product of path 2c could again abstract a proton, which would lead to the formation of dicarbon monoxide, a very reactive gas. The so far unexplained 0.4 electrons per molecule VC could be explained by a crosstalk mechanism: oxidation products can diffuse to the anode, where they will be reduced and can then again be oxidized at the cathode, leading to an apparently higher number of electrons per VC. Besides, it is possible that also poly(VC) can be oxidized at high potentials, most likely leading to proton abstraction and additional crosslinking.

Dependence of the graphite anode impedance on the positive electrode (LNMO vs. LFP).—As a next step, we want to understand how the positive electrode affects the impedance of the graphite anode. Therefore, the data of this study is compared with our previous study,[13] where we have investigated the effect of different VC concentrations (0.17 wt% VC and 0.52 wt% VC) on the impedance in graphite/LFP cells. As the upper cutoff potential of the LFP cathode is ~4.1 V vs. Li/Li^+ (compared to ~4.9 V vs. Li/Li^+ for LNMO), the oxidative decomposition of VC does not occur in graphite/LFP cells, which is in accordance with the LFP cathode impedance being independent from VC concentration (see Figure 8 in Reference 13). To compare the anode impedance data of the graphite/LFP cells from our previous study[13] and the graphite/LNMO cells from the present work, we recalculate the VC concentrations used for both cell chemistries in units of $mg_{VC}/m^2_{Graphite}$.

Figure 9 shows graphite anode impedances (R_{Anode}) after the first formation cycle in graphite/LNMO cells (black symbols; data from Figure 3a) and those in graphite/LFP cells (red symbols) vs. the VC concentration in $mg_{VC}/m^2_{Graphite}$. As one would expect, the graphite anode impedances for cells with 0 wt% VC are very similar, with a value of ~7 Ωcm^2 for the graphite/LNMO cells and ~5 Ωcm^2 for the graphite/LFP cells. When VC is added to the graphite/LFP cells, the graphite anode impedances increases linearly with VC concentration (to ~16 and ~47 Ωcm^2 for 0.17 and 0.52 wt% VC, respectively), as described previously.[13] Interestingly, the increase of anode impedance between 0 wt% and 0.09 wt% VC in graphite/LNMO cells matches precisely to the linear slope of the graphite/LFP cells. However, at VC concentrations ≥0.17 wt%, a deviation from the linear trend is observed for graphite/LNMO cells (to ~10 and ~14 Ωcm^2 for 0.17 and 0.52 wt% VC, respectively), i.e., the graphite anode impedance at high VC concentrations is much lower for graphite/LNMO compared to graphite/LFP cells. This effect can be explained by considering the competing reactions at the respective cathode: In graphite/LFP cells, no VC is consumed by the cathode, and the only reaction to occur is the reductive polymerization of VC on the anode, whereas the oxidation of VC on the cathode competes with its reduction in graphite/LNMO cells. Hence, less VC is available for reduction, leading to a lower anode impedance at similar $mg_{VC}/m^2_{Graphite}$ amounts. At this point, we would like to mention that the formation of the graphite/LFP cells was carried out at 40°C, while the graphite/LNMO cells were formed at 25°C, which might also affect the resulting anode impedance (measured at 10°C in both cases); however, as the anode impedance for 0 wt% VC is identical for both cell chemistries, and the graphite/LNMO anode impedance with 0.09 wt% VC fits well to the linear relationship between VC concentration and anode impedance in graphite/LFP cells, we believe that the oxidation of VC at the cathode is the major cause for the observed differences between graphite/LNMO and graphite/LFP cells.

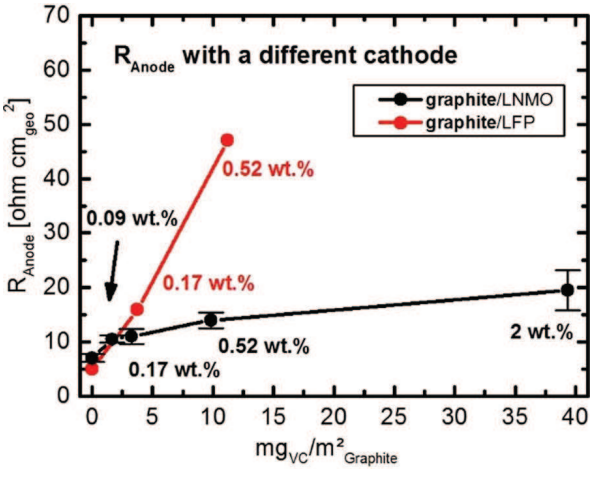

Figure 9. Interfacial resistance of graphite anodes after formation at 25°C in graphite/LNMO cells (this study) compared to graphite anodes in graphite/LFP cells from our earlier study.[13] The VC concentration is recalculated in units of $mg_{VC}/m^2_{Graphite}$ to assess for the slightly different areal loadings (namely ~2.6 mAh/cm^2_{geo} in the graphite/LNMO cells and ~2.2 mAh/cm^2_{geo} in the graphite/LFP cells, based on 340 $mAh/g_{graphite}$). The error bars represent the standard deviation between two measurements. All corresponding impedance spectra were recorded at 10°C from 100 kHz to 100 mHz.

Projected performance of graphite/LNMO commercial-scale cells.—The present study clearly proves that VC can enhance the cycling stability of graphite/LNMO cells, in contrast to previous reports. Yet, it also demonstrates that the concentration of VC in graphite/LNMO cells has to be carefully tuned, as the oxidation of only low amounts of VC can already lead to a deterioration of the capacity retention. The optimal VC concentration, corresponding to the amount of VC that can be reduced before the cathode reaches a potential >4.2 V vs. Li/Li^+, depends on the ratio of electrolyte to graphite surface area as well as the formation procedure (i.e., the time at potentials where VC reduction, but no oxidation can occur). In our case, the best performance in lab-scale cells is achieved with a concentration of 0.09 wt% VC, which corresponds to ~1 wt% VC in commercial-scale cells as used by Dahn's group (for details on this conversion please refer to Ref. 13). While Burns et al.[7] have shown that already 1 wt% VC leads to a significantly better capacity retention in commercial-scale graphite/LCO and graphite/NMC cells, the cycle life of commercial-scale graphite/NMC cells depends strongly on the amount of VC available.[10] Hence, 1 wt% VC by its own might not be sufficient to achieve an outstanding cycling performance with graphite/LNMO cells. Therefore, a combination of 1 wt% VC with other additives, which are either oxidatively stable or whose oxidation products are not detrimental to cell performance, and which can act as "repair additives" for the VC-derived SEI, would be a feasible combination for commercial-scale graphite/LNMO cells. To assure that diffusion of VC in a lab-scale cell is not the limiting factor when these type of cells are compared to commercial-scale cells we estimate the diffusion times for these two cell types: The diffusion time can be estimated as follows:

$$t = \frac{(x \cdot \tau)^2}{D} \quad [4]$$

where t is the characteristic diffusion time, x is the length of the diffusion path, τ is the tortuosity of the separator, and D is the diffusion coefficient. A typical value for the liquid diffusion is in the order of 10^{-6} cm^2/s (J. Landesfeind et al.[40]). In our lab test cells, two glass fiber separators have been used ($x \approx 2 \cdot 200$ µm, $\tau \approx 1$), yielding a diffusion time on the order of:

$$t = \frac{(400\,\mu m)^2}{10^{-6}\,\frac{cm^2}{s}} = 1600\,s \quad [5]$$

In a commercial cell the distance between anode and cathode is ~25 µm with an average tortuosity of $\tau \approx 4$ (see, e.g., J. Landesfeind et al.[41]), yielding an approximate diffusion time constant of:

$$t = \frac{(25\,\mu m \cdot 4)^2}{10^{-6}\,\frac{cm^2}{s}} = 100\,s \quad [6]$$

As the oxidation of VC would only become possible after ≈34 minutes of charge, the rate of VC diffusion to the anode electrode is not limiting. During that initial time period, we believe that VC will be reduced preferentially at the anode, since its reduction potential is substantially higher than that of the EC and EMC solvents in LP57 (≈1.7 V vs. Li/Li^+ for VC compared to ≈0.9 V for LP57).[5]

Conclusions

In this study, we use a combined on-line electrochemical mass spectrometry (OEMS) and impedance analysis with a micro-reference electrode (GWRE), in order to i) understand the oxidative (in-)stability of the additive vinylene carbonate (VC), and, ii) to investigate the impact of the additive in graphite/$LiNi_{0.5}Mn_{1.5}O_4$ cells on the interfacial resistance of both anode and cathode. We have shown that the oxidation of VC occurs at an onset potential of ∼4.3 V vs. Li/Li^+ (by OEMS), which leads to a significant impedance buildup on the LNMO cathode in graphite/LNMO cells. This was shown by monitoring the graphite anode and the LNMO cathode impedance after formation and during extended charge discharge cycling using a micro-reference electrode.

Based on these data, we could conclude that VC oxidation on the cathode is competing with VC reduction on the anode. During the initial charge of graphite/LNMO cells, a charge of ∼8 mAh/g_{LNMO} can be passed before the LNMO cathode potential reaches 4.3 V vs. Li/Li^+ while the anode potential is already low enough to reduce VC to form an anode SEI. As a consequence, if the total amount of VC in the electrolyte is high enough to form a passivating anode SEI during this initial part of the first charge, but low enough so that all VC is being consumed during the initial anode SEI formation, the capacity retention of cells with a VC-containing electrolyte is superior compared to VC-free electrolyte. In our lab-scale cells, this corresponds to the lowest tested VC concentration of 0.09 wt%. Based on our previously discussed metrics for comparing additives in lab-scale vs. commercial-scale cells, this would translate into a ∼1 wt% VC concentration for commercial-scale cells.

Acknowledgment

Financial support by the BASF SE through its Network on Electrochemistry and Batteries is gratefully acknowledged. M. W. acknowledges funding by The German Federal Ministry for Economic Affairs and Energy (funding number 03ET6045D).

References

1. E. Peled, *J. Electrochem. Soc.*, **126**, 2047 (1979).
2. R. Imhof and P. Novák, *J. Electrochem. Soc.*, **145**, 3313 (1998).
3. M. Nie, D. Chalasani, D. P. Abraham, Y. Chen, A. Bose, and B. L. Lucht, *J. Phys. Chem. C*, **117**, 1257 (2013).
4. H. Ota, Y. Sakata, A. Inoue, and S. Yamaguchi, *J. Electrochem. Soc.*, **151**, A1659 (2004).
5. B. Zhang, M. Metzger, S. Solchenbach, M. Payne, S. Meini, H. A. Gasteiger, A. Garsuch, and B. L. Lucht, *J. Phys. Chem. C*, **119**, 11337 (2015).
6. M. Nie, J. Demeaux, B. T. Young, D. R. Heskett, Y. Chen, A. Bose, J. C. Woicik, and B. L. Lucht, *J. Electrochem. Soc.*, **162**, 7008 (2015).
7. J. C. Burns, N. N. Sinha, D. J. Coyle, G. Jain, C. M. VanElzen, W. M. Lamanna, A. Xiao, E. Scott, J. P. Gardner, and J. R. Dahn, *J. Electrochem. Soc.*, **159**, A85 (2012).
8. A. Würsig, H. Buqa, M. Holzapfel, F. Krumeich, and P. NovaŕK, *Electrochem. Solid-State Lett.*, **8**, A34 (2005).
9. L. El Ouatani, R. Dedryvère, C. Siret, P. Biensan, S. Reynaud, P. Iratçabal, and D. Gonbeau, *J. Electrochem. Soc.*, **156**, A103 (2009).
10. J. C. Burns, R. Petibon, K. J. Nelson, N. N. Sinha, A. Kassam, B. M. Way, and J. R. Dahn, *J. Electrochem. Soc.*, **160**, A1668 (2013).
11. R. Petibon, J. Xia, J. C. Burns, and J. R. Dahn, *J. Electrochem. Soc.*, **161**, A1618 (2014).
12. R. Petibon, J. Xia, L. Ma, M. K. G. Bauer, K. J. Nelson, and J. R. Dahn, *J. Electrochem. Soc.*, **163**, A2571 (2016).
13. S. Solchenbach, D. Pritzl, E. J. Y. Kong, J. Landesfeind, and H. A. Gasteiger, *J. Electrochem. Soc.*, **163**, A2265 (2016).
14. J. Hoffmann, M. Payne, and J. Li, *ECS Meet. 224, Abstr*, #1106 (2013).
15. H. Lee, S. Choi, H. Kim, Y. Choi, S. Yoon, and J.-J. Cho, *Electrochem. commun.*, **9**, 801 (2007).
16. Y.-M. Song, J.-G. Han, S. Park, K. Lee, and N.-S. Choi, *J. Mater. Chem. A*, **2**, 9506 (2014).
17. Y. Dong, J. Demeaux, and B. L. Lucht, *J. Electrochem. Soc.*, **163**, A2413 (2016).
18. R. Jung, M. Metzger, D. Haering, S. Solchenbach, C. Marino, N. Tsiouvaras, C. Stinner, and H. A. Gasteiger, *J. Electrochem. Soc.*, **163**, A1705 (2016).
19. E. Markevich, G. Salitra, K. Fridman, R. Sharabi, G. Gershinsky, A. Garsuch, G. Semrau, M. Schmidt, and D. Aurbach, *Langmuir*, **30**, 7414 (2014).
20. N. Tsiouvaras, S. Meini, I. Buchberger, and H. A. Gasteiger, *J. Electrochem. Soc.*, **160**, A471 (2013).
21. M. Metzger, B. Strehle, S. Solchenbach, and H. A. Gasteiger, *J. Electrochem. Soc.*, **163**, A798 (2016).
22. M. Metzger, C. Marino, J. Sicklinger, D. Haering, and H. A. Gasteiger, *J. Electrochem. Soc.*, **162**, A1123 (2015).
23. M. Klett, J. A. Gilbert, S. E. Trask, B. J. Polzin, A. N. Jansen, D. W. Dees, and D. P. Abraham, *J. Electrochem. Soc.*, **163**, A875 (2016).
24. R. Jung, M. Metzger, F. Maglia, C. Stinner, and H. A. Gasteiger, *J. Electrochem. Soc.*, **164**, A1361 (2017).
25. J. A. Seel and J. R. Dahn, *J. Electrochem. Soc.*, **147**, 892 (2000).
26. W. Märkle, N. Tran, D. Goers, M. E. Spahr, and P. Novák, *Carbon.*, **47**, 2727 (2009).
27. M. Metzger, J. Sicklinger, D. Haering, C. Kavakli, C. Stinner, C. Marino, and H. A. Gasteiger, *J. Electrochem. Soc.*, **162**, A1227 (2015).
28. M. Itagaki, N. Kobari, S. Yotsuda, K. Watanabe, S. Kinoshita, and M. Ue, *J. Power Sources*, **148**, 78 (2005).
29. X. Zhang, J. K. Pugh, and P. N. Ross, *J. Electrochem. Soc.*, **148**, E183 (2001).
30. O. Borodin, W. Behl, and T. R. Jow, *J. Phys. Chem. C*, **117**, 8661 (2013).
31. J. Self, C. P. Aiken, R. Petibon, and J. R. Dahn, *J. Electrochem. Soc.*, **162**, A796 (2015).
32. C. P. Aiken, J. Self, R. Petibon, X. Xia, J. M. Paulsen, and J. R. Dahn, *J. Electrochem. Soc.*, **162**, A760 (2015).
33. L. E. Downie, S. Hyatt, and J. R. Dahn, *J. Electrochem. Soc.*, **163**, A35 (2016).
34. L. Xing, W. Li, C. Wang, F. Gu, M. Xu, C. Tan, and J. Yi, *J. Phys. Chem. B*, **113**, 16596 (2009).
35. T. Li, L. Xing, W. Li, Y. Wang, M. Xu, F. Gu, and S. Hu, *J. Power Sources*, **244**, 668 (2013).
36. J. Landesfeind, D. Pritzl, and H. A. Gasteiger, *J. Electrochem. Soc.*, **164**, A1773 (2017).
37. D. H. Jang and S. M. Oh, *J. Electrochem. Soc.*, **144**, 3342 (1997).
38. D. Pritzl, A. Bumberger, M. Wetjen, S. Solchenbach, J. Landesfeind, and H. A. Gasteiger, *Manuscr. prep.*.
39. A. L. Michan, B. S. Parimalam, M. Leskes, R. N. Kerber, T. Yoon, C. P. Grey, and B. L. Lucht, *Chem. Mater.*, **28**, 8149 (2016).
40. B. Li, L. Xing, M. Xu, H. Lin, and W. Li, *Electrochem. commun.*, **34**, 48 (2013).
41. A. Ehrl, J. Landesfeind, W. A. Wall, and H. A. Gasteiger, *J. Electrochem. Soc.*, **164**, A826 (2017).

3.1.3 Development of a novel impedance procedure for lithium-ion batteries – Application for an LNMO cathode

This section presents the article "*An Analysis Protocol for Three-Electrode Li-Ion Battery Impedance Spectra: Part I. Analysis of a High-Voltage Positive Electrode".*[109] The paper was submitted to the peer-reviewed Journal of the Electrochemical Society in March 2017 and published in June 2017. The article is published open access and distributed under the terms of the Creative Commons Attribution Non-Commercial No Derivatives 4.0 License. The authors J.L. and D.P. contributed equally to this work. The permanent web link is available under: http://jes.ecsdl.org/content/164/7/A1773. The article was presented by Daniel Pritzl at the New Orleans, Louisiana, Meeting of the Electrochemical Society (USA) in May 2017 (Paper 534).

With the µ-reference electrode[99] introduced in chapter 3.1.1, anode and cathode impedance can be deconvoluted. When micro-reference electrodes have been used in the literature, only the order or shape of a half-cell impedance spectrum had been described. A quantitative analysis of the cathode impedance is missing in the literature. In this work the LNMO impedance was examined in detail meaning a deconvolution of the cathode impedance Z_{Cathode} into its contribution from the charge transfer (Z_{CT}), the contact between current collector and coating (Z_{Contact}) as reported by Gaberscek et al.[90] and the pore resistance (Z_{Pore}) representing the ionic conduction resistance in the electrolyte phase within the electrode pores. In order to do so, we apply the concept of blocking electrodes which is used to determine the tortuosity of porous electrodes.[89,110,111] Here, the impedance of the pore (Z_{Pore}) can be determined unambiguously as the charge transfer (Z_{CT}) is shifted towards very low frequencies. This technique requires the suppression of the charge transfer, which is achieved either by using an electrolyte without lithium ions[111] or by using a fully lithiated cathode.[89]

If we want to apply this concept in a full-cell (graphite/LNMO) with a gold wire reference electrode (GWRE), blocking conditions for the cathode have to be achieved in-situ. We show that blocking conditions (i.e. a very high or infinitively high charge transfer resistance) can be achieved by delithiating the LNMO cathode

completely (100% cell SOC). Fortunately, an LNMO electrode can be completely delithiated (without gassing and structural collapse) when a full-cell is charged. Hence, an impedance measurement at 4.9 V vs. Li^+/Li gives the required blocking impedance response. We then record an impedance also at 10% SOC, where the typical cathode impedance response is observed. By simultaneously fitting the spectra under blocking conditions (100% SOC) and under non-blocking conditions (10% SOC) with a transmission line equivalent circuit (TLM) we can rather precisely deconvolute the cathode impedance into its contributions from charge transfer (Z_{CT}), pore resistance (Z_{Pore}) and contact resistance ($Z_{Contact}$).

With this novel approach we made two new findings: (i) the charge transfer impedance of an LNMO cathode stays constant over cycling, in contrast to most literature reports which claimed that the charge transfer resistance for the LNMO cathode would increase over cycling, especially at elevated temperatures;[78] and (ii), the high-frequency semi-circle is increasing over cycling and through an analysis of the capacitance we can show that this impedance contribution belongs to the interface current collector/electrode coating rather than to the charge transfer impedance. The origin for the contact resistance increase is shown in detail in chapter 3.1.5.

Author contributions

D.P., J.L. and H.A.G. developed the novel measurement procedure. All electrochemical measurements were performed by D.P. The equivalent circuit and the data was analyzed by J.L. The manuscript was written by J.L., D.P. and H.A.G. All authors discussed the data and commented on the results.

An Analysis Protocol for Three-Electrode Li-Ion Battery Impedance Spectra: Part I. Analysis of a High-Voltage Positive Electrode

Johannes Landesfeind,[=,*] Daniel Pritzl,[=,*,z] and Hubert A. Gasteiger[**]

Chair of Technical Electrochemistry, Department of Chemistry and Catalysis Research Center, Technical University of Munich, Munich, Germany

A key for the interpretation of porous lithium ion battery electrode impedance spectra is a meaningful and physically motivated equivalent-circuit model. In this work we present a novel approach, utilizing a general transmission line equivalent-circuit model to exemplarily analyze the impedance of a porous high-voltage $LiNi_{0.5}Mn_{1.5}O_4$ (LNMO) cathode. It is based on a LNMO/graphite full-cell setup equipped with a gold wire micro-reference electrode (GWRE) to obtain impedance spectra in both, non-blocking conditions at a potential of 4.4 V cell voltage and in blocking configuration achieved at 4.9 V cell voltage. A simultaneous fitting of both spectra enables the deconvolution of physical effects to quantify over the course of 85 cycles at 40°C: a) the true charge transfer resistance (R_{CT}), b) the pore resistance (R_{Pore}), and c) the contact resistance ($R_{Cont.}$). We demonstrate that the charge transfer resistance would be overestimated significantly, if the spectra are fitted with a conventionally used simplified *R/Q* equivalent-circuit compared to our full transmission line analysis.

 [DOI: 10.1149/2.0131709jes]

Manuscript submitted March 27, 2017; revised manuscript received June 6, 2017. Published June 16, 2017. This was Paper 534 presented at the New Orleans, Louisiana, Meeting of the Society, May 28–June 1, 2017.

Advanced analysis techniques for lithium ion batteries are a key requirement to deconvolute the complex interplay between the aging mechanisms occurring at the anode and the cathode. In principle, this can be accomplished by electrochemical impedance spectroscopy (EIS), if the individual contributions of anode and cathode to the overall cell impedance can be determined, and if this EIS response can be fitted unambiguously to physically motivated equivalent-circuit models. In general, the measured cell and/or electrode impedances are usually fitted with a serial connection of an ohmic resistor (*R*), with a parallel circuit of a resistor and a capacitor (*C*), commonly referred to as *R*/*C* element and often also modified to an *R*/*Q* element (*Q* representing a constant-phase element), as well as with a Warburg element (*W*).[1–5] Recently, more elaborate equivalent-circuits using a transmission line model are getting more and more attention.[6–8]

In order to independently obtain the impedance of anode and cathode, there are two possible options: i) the assembly of symmetric cells as shown by Chen et al.[9] or Petibon et al.,[10] where coin cells out of two anodes (impedance of the negative electrode) or two cathodes (impedance of the positive electrode) are assembled in a glove box or dry-room from two (aged) full-cells at a specified state-of-charge (SOC); ii) the use of three-electrode setups consisting of a working electrode (WE), a counter electrode (CE) and a reference electrode (RE), which allows to individually determine the impedance of the anode and the cathode of a lithium ion battery full-cell. The latter is a more convenient approach, as individual impedance spectra can be recorded continuously during battery cycling, so that anode and cathode impedance can be monitored during cycle-life studies on a full-cell instead of obtaining only one set of anode and cathode impedance spectra after disassembly of a full-cell via the symmetric cell approach. A main criterion for a micro-reference electrode suitable for high-quality EIS measurements is a centered position of the reference electrode between working and counter electrode.[11–13] Several approaches are presented in the literature, as for example, a copper wire, where lithium is in-situ plated from anode or cathode,[14] a reference electrode consisting of a lithium-tin alloy,[15] or consisting of a lithium-bismuth alloy.[16] Our group has recently developed a micro-reference electrode consisting of a polyimide-shrouded gold wire with a core diameter of 50 μm and an additional 7 μm polyimide insulation layer which enables the deconvolution of full-cell impedances into anode and cathode contributions after lithiation of the gold wire.[17] The latter was used in this study and will be referred to as gold wire reference electrode (GWRE).

Besides the deconvolution of individual electrode impedances, EIS measurements with the GWRE at different states-of-charge of the electrodes allow to get insight into different physical effects. If conducting EIS analysis at a so-called blocking condition for a specific electrode, where no charge transfer reactions (i.e., no faradaic reactions) can take place, the only impedance contribution from the solid-electrolyte interphase is via capacitive coupling. Blocking conditions of electrodes have been used in the literature before to address individual physical processes like the pore resistance and thus the effective ionic conductivity across the thickness of an electrode.[18,19]

In this work, by using a GWRE and by recording impedance spectra at both blocking and non-blocking conditions, we will demonstrate the ability to deconvolute and quantify the impedance contributions developing during the aging of a high-voltage spinel cathode ($LiNi_{0.5}Mn_{1.5}O_4$ or LNMO) in an LNMO/graphite full-cell cycled at 40°C. For this, we measure half-cell impedance spectra with our GWRE and fit the impedance spectra with a general transmission line model for two distinct points during cycling: i) at 4.4 V cell voltage, corresponding to ~7–12% SOC, where the charge transfer resistance has a typical and reasonably low value; ii) at 4.9 V, where the LNMO is fully delithiated (≡ 100% SOC) and where, as we will demonstrate, the LNMO cathode exhibits nearly perfect blocking behavior. The novelty of our approach lies in the fact that by recording both sets of impedance spectra, individual impedance contributions by the LNMO cathode (contact resistance, charge transfer resistance, and pore resistance) can be deconvoluted mathematically and allow for a rather rigorous quantitative analysis during the course of cycle-life experiments. While this is illustrated for the cycling of an LNMO/graphite cell, the general approach shown here is applicable to many other cell chemistries, and the presented analysis of the cathode impedance contributions is also being extended to the anode in our current work. In the following, we will first review the necessary theoretical impedance background, then provide the experimental data, and finally discuss the analysis of the cathode impedance contributions and their variation during cycling.

[=]These authors contributed equally to this work.
[*]Electrochemical Society Student Member.
[**]Electrochemical Society Fellow.
[z]E-mail: daniel.pritzl@tum.de

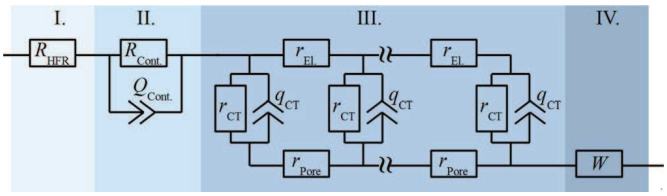

Figure 1. Cathode equivalent circuit model with four parts (from left to right): I. the high frequency resistances from the ionic resistance of the separator and the electronic resistance of the cell setup, II. the contact resistance at the interface between the cathode electrode and its current collector, III. the general transmission line model describing the porous coating, and IV. a Warburg diffusion element.

Theory

The impedance contributions from a porous cathode electrode can be described by a combination of four physical mechanism which are labelled with Roman numerals in the equivalent-circuit depicted in Figure 1 as well as in the simulated Nyquist impedance plot (Figure 2 with parameters given in Table I), using the following assignments: I) the high-frequency resistance (Z_{HFR}), which represents the sum of the ionic resistance of the separator and the electronic resistance of external, electronic cell contacts; II) the contact resistance between the porous electrode and the current collector ($Z_{Cont.}$); III) the impedance contribution from ion and electron conduction across the thickness of the porous cathode electrode (Z_{Pore}), described by the general transmission line model; and, IV) a Warburg diffusion element (Z_W), representing the impedance at very low frequencies. Thus, the overall

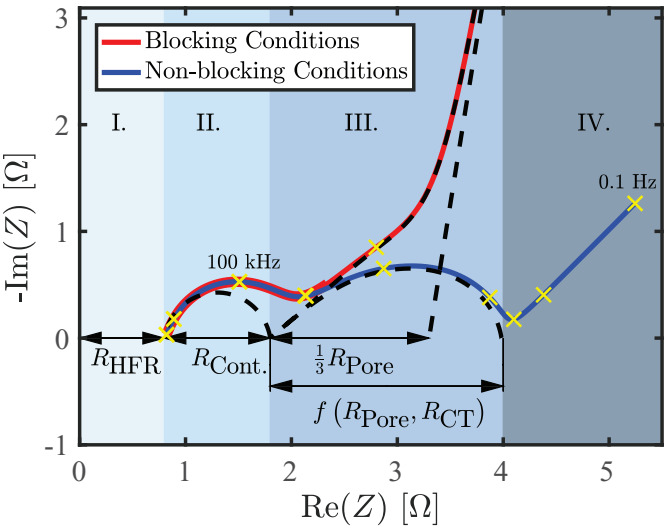

Figure 2. Simulated impedance response of a porous cathode electrode either under blocking conditions (red line) or under non-blocking conditions (blue line), using the parameters listed in Table I for a simulated frequency range from 10 Mhz–0.1 Hz. Each frequency decade is highlighted by a yellow cross. The arrows mark the values of the simulation parameters for the high-frequency resistance (R_{HFR}), the electronic contact resistance ($R_{Cont.}$), and of one third of the pore resistance (R_{Pore}), which are obtained by extrapolating the high- and low-frequency segments of the transmission line response under blocking conditions (dashed black lines). The dashed lines are the modelled impedance responses of only the equivalent-circuit elements in the corresponding region (compare Figure 1), a) the R/Q element due to the contact resistance (region II.), b) the blocking condition transmission line model extending to low frequencies (region III), and, c) the transmission line model in non-blocking condition (region III), and, d) the constant phase behavior of the transmission line model in blocking condition at low frequencies (region III.). The frequency range corresponding to the measurement, from 100 kHz to 0.1 Hz is labelled for the reader's convenience.

cathode impedances is:

$$Z_{cathode} = Z_{HFR} + Z_{Cont.} + Z_{Pore} + Z_W \quad [1]$$

In our following measurements with a GWRE (64 μm total diameter) placed in between two glass fiber separators (each with a compressed thickness of ≈200 μm) located between anode and cathode, the impedance at the highest frequencies is composed of the ionic electrolyte resistance in the separator between the cathode/separator interface and the GWRE ($R_{Sep.}$) as well as of the contact resistances from the cell setup (R_{Setup}), adding up to the overall high-frequency resistance, R_{HFR} (compare region I. in Figures 1 and 2):

$$Z_{HFR} = R_{Sep.} + R_{Setup} = R_{HFR} \quad [2]$$

In terms of an equivalent circuit, the overall cathode impedance can thus be described with the equivalent circuit model depicted in Figure 1. The first element starting from the left is R_{HFR}, which is connected in series to the impedance due to contact resistance between the current collector and the positive electrode, described by the $R_{Cont}/Q_{Cont.}$ element (compare region II. in Figures 1 and 2). The contact resistance circuit element between the cathode current collector and the cathode electrode is a parallel circuit between the interfacial resistance ($R_{Cont.}$) and the generally very small interfacial capacitance (expressed as constant phase element $Q_{Cont.}$), which, based on the definition of the impedance of a constant-phase element ($Z = [Q \cdot (i\omega)^{\alpha}]^{-1}$), equates to:

$$Z_{Cont.} = \frac{R_{Cont.}}{R_{Cont.} \cdot Q_{Cont.} \cdot (i\,\omega)^{\alpha_{Cont.}} + 1} \quad [3]$$

with the angular frequency $\omega = 2\pi f$. In this work constant phase elements rather than capacitors are used to account for the non-ideal capacitive behavior commonly observed for the double layer capacitance of porous electrodes.[20] The contact resistance is followed by a transmission line equivalent circuit, composed of incremental elements of the charge transfer resistance (r_{CT}), the interfacial double layer capacitance of the cathode (q_{CT}), the purely electronic resistance in the electrode ($r_{El.}$), and the purely ionic resistance in the electrode (r_{Ion}) in the mid frequency range (compare region III. in Figures 1 and 2). Thus, the overall charge transfer resistance, the overall electronic and ionic resistances as well as the overall capacitance of the electrode are described by ${R_{CT}}^{-1} = \Sigma({r_{CT}}^{-1})$, $Q_{CT} = \Sigma(q_{CT})$, $R_{El.} = \Sigma(r_{El.})$, and $R_{Pore} = \Sigma(r_{Pore})$. Please note, that the constant phase elements in region II. and region III., namely $Q_{Cont.}$ and $q_{CT.}$, both describe the electrochemical double layer capacitance, $Q_{Cont.}$ at the current collector interface and q_{CT} at the active material and carbon surface respectively.

In this mid-frequency range, the cathode electrode pores dominate the impedance response. In this work, the impedance of the pores is described with a general transmission line model, given by:[21]

$$Z_{Pore} = Z_{||} + Z^* \frac{1 + 2 \cdot p \cdot s\left[\sqrt{1 - \tanh(\nu)^2} - 1\right]}{\tanh(\nu)} \quad [4]$$

with

$$Z_{||} = \frac{Z_P \cdot Z_S}{Z_P + Z_S} \quad [5]$$

$$Z^* = \sqrt{(Z_P + Z_S) \cdot Z_Q} \quad [6]$$

$$p = \frac{Z_P}{Z_P + Z_S} \quad [7]$$

$$s = \frac{Z_S}{Z_P + Z_S} \quad [8]$$

$$\nu = \sqrt{\frac{Z_P + Z_S}{Z_Q}} \quad [9]$$

Here, Z_S, Z_P, and Z_Q represent the impedances of the electron conducting solid phase of the electrode, of the ionically conducting

pore phase of the electrode, and of the solid/electrolyte interface surfaces within the electrode, respectively. In this work, these elements are described by the electrical resistance throughout the electrode ($Z_S \equiv R_{El.}$), by the ionic resistance throughout the electrode ($Z_P \equiv R_{Pore}$), and by an *R/Q* element describing the coupling for the capacitive elements (Q_{CT}) and of the charge transfer resistance (R_{CT}) at the solid/electrolyte interface surface of the active material in the electrode:

$$Z_Q = \frac{R_{CT}}{R_{CT} \cdot Q_{CT} \cdot (i\,\omega)^{\alpha_{CT}} + 1} \quad [10]$$

For the commonly considered special case, where the electronic resistance of the electrode is negligible compared to the ionic resistance in the electrode pores (i.e., $R_{El.} \ll R_{Pore}$), the transmission line model for the pore impedance (Eqs. 4–9) in blocking conditions ($R_{CT} \to \infty$) simplifies to Ref. 19:

$$Z_{Pore} = \sqrt{R_{Pore} \cdot Z_Q} \cdot \coth\left(\sqrt{\frac{R_{Pore}}{Z_Q}}\right)$$

$$= \sqrt{\frac{R_{Pore}}{Q_{CT} \cdot (i\,\omega)^{\alpha_{CT}}}} \cdot \coth\left(\sqrt{R_{Pore} \cdot Q_{CT} \cdot (i\,\omega)^{\alpha_{CT}}}\right) \quad [11]$$

Finally, the last element represents a Warburg impedance, which generally becomes relevant at very low frequencies (compare region IV. in Figures 1 and 2) and which is connected serially to the transmission line model to account for the salt concentration gradients evolving at low frequencies inside the separator. Please note that this placement of a Warburg diffusion element is not in contradiction with the literature, where a diffusion element is generally connected in series to the charge transfer resistances in order to describe a slow solid-state diffusion process inside the active material particles.[20,22] In the literature, the solid-state diffusion is generally assumed to be the slowest step (i.e., the one with the longest characteristic time constant), however, as estimated in the Appendix, liquid diffusion through the separator can have a substantially larger impedance, depending on the experimental setup, e.g., the active area or the diffusion coefficient. Thus, with our placement of a Warburg diffusion element in series to the transmission line model we aim at describing the liquid concentration gradients inside the separator.

Only at the very lowest frequencies, a Warburg (*W*) behavior may be observed, which can be modelled with Ref. 20:

$$Z_W = \frac{W}{\sqrt{\omega}} - i \cdot \frac{W}{\sqrt{\omega}} \quad [12]$$

with the Warburg coefficient *W* as defined in the Appendix. Generally, the boundary conditions for ionic diffusion in the separator domain will yield a finite, transmissive diffusion behavior for very low frequencies (compare, e.g., Ref. 20, page 102 and following). In this work, no signs of a finite length diffusion were observed in the investigated frequency range (100 kHz to 0.1 Hz), i.e., the decline of the negative imaginary impedance toward the real axis at lowest frequencies in a Nyquist plot, which enables modelling of the separator diffusion with a semi-infinite Warburg diffusion element.

An exemplary evaluation of Equations 1–10 is shown in form of a simulated Nyquist plot in Figure 2 (10 MHz to 0.1 Hz), using the specific parameters for an LNMO cathode listed in Table I, whereby two cases are considered: a) blocking conditions (red line), where R_{CT} becomes very large (ideally going to infinity), here using a value of $R_{CT\text{-blocking}}$ of 1 kΩ; and, b) conditions where a typical value for the charge transfer resistance is observed (blue line), which applies throughout most of the SOC region and which here is given as $R_{CT\text{-non-blocking}}$ of 1 Ω. In the first case (red line), the semi-circle for the contact resistance (region II. in Figure 1) can be clearly seen at high frequencies as well as a roughly 45° line produced by the transmission line segment of the circuit shown in Figure 1 (region III.). From this, the value corresponding to one third of the pore resistance (R_{Pore}) can be determined as the difference between the Re(*Z*)-axis intercept of the two black dashed lines, which are the extensions of the high- and low-frequency segments of the transmission line part (region III.) of the equivalent circuit shown in Figure 1. This is derived from the low-frequency limit of Eq. 4, assuming a negligible electronic resistance ($R_{El.} \sim 0$), as explained, e.g., in Ref. 20 (p. 207, Eq. 9.11). The difference between the left dashed line intersecting with the Re(*Z*)-axis and the high-frequency resistance intersect is the value of the contact resistance ($R_{Cont.}$).

Table I. Parameters used in Equations 1–10 for the simulation of the two impedance responses shown in Figure 2, either under blocking conditions where the charge transfer resistance is very large ($R_{CT\text{-blocking}}$) or under normal conditions, where a typical value for the charge transfer resistance is used ($R_{CT\text{-non-blocking}}$; evaluated at 4.4 V_{FC}). Note that the here chosen values are very similar to the ones which will be found in our later cathode impedance analysis during cycling of an LNMO/graphite cell.

Parameter	Value
$R_{HFR.}$	0.8 Ω
$R_{Cont.}$	1.0 Ω
$Q_{Cont.}$	5 μF · $s^{(\alpha_{Cont.}-1)}$
$a_{Cont.}$	0.9
R_{Pore}	4.5 Ω
$R_{El.}$	1 mΩ
$R_{CT-non-blocking}$	1.0 Ω
$R_{CT-blocking}$	1 kΩ
Q_{CT}	1 mF · $s^{(\alpha_{CT}-1)}$
a_{CT}	0.9
W	1 Ω/$\sqrt{s}$

Under non-blocking conditions (blue lines), two semi-circles appear across regions II and III in Figure 2 (plus the onset of the Warburg diffusion branch at low frequencies in region IV), and the low-frequency semi-circle now corresponds to a complex convolution (not simply additive) of the pore ionic conduction and the charge transfer resistance (marked by the arrow labelled $f(R_{Pore}, R_{CT})$). In the most general case, also the magnitude of the electronic resistance influences the shape of the transmission line part (region III. in Figures 1 and 2) but can be neglected when it is much smaller than the ionic resistance inside the pore. The simulated transmission line segment under non-blocking conditions (see region III in Figure 1 with finite R_{CT}) is shown as the dashed semi-circle at low frequencies in Figure 2. Quite clearly, if one were to fit two semi-circles and a Warburg element to the blue EIS response under non-blocking conditions, the diameter of the semi-circle at low-frequencies, which is commonly ascribed to the charge transfer resistance,[23,24] would indeed be much larger than the actual charge transfer resistance (ca. 2.5 Ω as can be seen from Figure 2 in contrast to the 1 Ω (see Table I) which was used in the model). Therefore, as we will illustrate in the Results and discussion section, a quantification of the charge transfer resistance requires impedance spectra at both blocking and non-blocking conditions for an unambiguous assignment. For a better comparison with our experimental data, which were limited to an upper frequency of 100 kHz due to experimental reasons (see Experimental section), each frequency decade of the blocking and the non-blocking equivalent-circuit simulations (from 10 MHz to 0.1 Hz) in the simulations shown in Figure 2 is marked by a yellow cross (the maximum experimental frequency of 100 kHz is labeled in the figure).

Experimental

Electrode preparation.—Cathodes were prepared from $LiNi_{0.5}Mn_{1.5}O_4$ powder (LNMO, BASF SE, Germany), polyvinylene difluoride (PVdF HSV 900, Kynar), and carbon black (SuperC65, Timcal). The powders were mixed in a mass ratio of 92:3:5 (LNMO:PVdF:carbon black) and dissolved in NMP (N-methyl pyrrolidone, anhydrous, Sigma Aldrich, Germany), followed by three sequential mixing steps with a planetary mixer (Thinky Corp.) for a total of 15 minutes. The final ink, which had a solid content

of 60%, was coated on the rough side of an aluminum foil (MTI, thickness ~18μm) at a wet film thickness of ~200 μm with a doctor blade coating device (RK PrintCoat Instruments, UK). The resulting loading of the electrodes was ~13 $mg_{LNMO}/cm^2_{Electrode}$ corresponding to ~1.9 mAh/ $cm^2_{Electrode}$ based on a theoretical capacity of 140 mAh/g_{LNMO}. The electrodes were punched out with a diameter of 11 mm and afterwards compressed to a porosity of ~32% using a KBr press (Mauthe, PE-011).

Anodes were prepared from Graphite powder (commercial, SGL Carbon GmbH) and PVdF with a mass ratio of 95:5. The mixing procedure was identical to the cathodes. The ink (60% solid content) was coated on the rough side of a copper foil (MTI, thickness ~12 μm). The electrodes were punched out with a diameter of 11 mm and compressed to a porosity of ~32%. The final loading was 6.6 $mg_{Graphite}/ cm^2_{Electrode}$, corresponding to ~2.3 $mAh/cm^2_{Electrode}$ based on a theoretical capacity of ~340 $mAh/g_{Graphite}$.

Anode and cathode coatings were dried in a convection oven at 50°C for at least 3 h. The as-prepared electrodes (graphite anodes and LNMO cathodes) were vacuum dried for at least 12 h at 120°C in a vacuum oven (Büchi, Switzerland) and transferred into an Argon-filled glove box without exposure to air.

Cell assembly and testing.—Spring-compressed (at ~1 bar) T-cells (Swageklok, U.S) were assembled in an Argon-filled glove box (<0.1 ppm O_2 and H_2O, MBraun, Germany). The cell components were dried beforehand in a 70°C drying oven for at least 20 h. A gold wire micro-reference (core diameter of 50 μm and an additional 7 μm polyimide shrouding, Goodfellow Ltd., United Kingdom) is used as a reference electrode,[17] placed in between two glass fiber separators (glass microfiber filter, 691, VWR, Germany) with a compressed thickness of ~200 μm each. During cell assembly, 60 μl of LP57 electrolyte (1 M $LiPF_6$ in EC:EMC 3:7 w:w, <20 ppm H_2O, BASF, Germany) was added. The GWRE was lithiated with a constant current of 150 nA for 1h and initially yielded a constant potential of 0.31 V vs. metallic lithium, which drifted toward the potential of an unlithiated gold wire within ca. 10 cycles (caused, we believe, by reaction of alloyed lithium with electrolyte oxidation products from the LNMO cathode at 4.9 V_{FC} cell voltage). However, as shown in our previous work, artefact-free impedance spectra (indicated by the absence of inductive loops at low frequency; see Figure 3 in Reference 17) can be obtained from micro reference electrodes as long as the potential drift of the RE over the course of the impedance measurement is smaller than the chosen voltage amplitude. In the present work the potential drift of the RE over the course of the impedance measurement with a lower limit of 0.1 Hz is ~3–4 mV, which is sufficiently below the perturbation amplitude during the EIS measurement (in this case 15 mV). This is verified by the absence of inductive loops at low frequency and was furthermore verified by comparing the impedance measurement with the micro-reference electrode with a standard EIS measurement using a symmetrical cell configuration (for the LNMO cathode; see Figure 6). It is emphasized that while the potential value of the reference electrode is unstable (i.e., it deviates from 0.31 V vs. metallic lithium after ~10 cycles), the reference electrode potential drift during the time period needed for an impedance measurement (~5 minutes) is still small (<4 mV) compared to the potential perturbation. For details about the cell setup and the preparation of the gold wire, please refer to the original publication.[17]

The full-cells were cycled between 3.0 and 4.9 V cell voltage; for measurements with additional cells, the figure captions give the detailed experimental procedure (e.g., modified amplitudes or frequency ranges of impedance measurements). In the following, all potentials refer to the LNMO/graphite full cell voltage (indicated by the subscript FC) unless stated otherwise. Two formation cycles were carried out at 25°C at a C-Rate of C/10, while cycling was done at 40°C at a C-Rate of C/2. Potential-controlled impedance spectra (15 mV perturbation, from 100 kHz to 0.1 Hz; acquisition time of 10 min./spectrum) were recorded during discharge at 4.4 V_{FC} after a 1 h OCV (open-circuit voltage) phase as well as under blocking condition, which were achieved by fully delithiating the cathode by holding it at 4.9 V_{FC} until a current of <C/40 was obtained and then recording impedance spectra while holding the potential at 4.9 V_{FC}. Analogously, impedance spectra of the anode in blocking condition have been recorded by holding the potential at 3.0 V_{FC} at the end of discharge (completely delithiated graphite) until a current of <C/100 is reached. The cycling protocol was carried out on a potentiostat (VMP 300, BioLogic, France). It should be noted that due to the relatively high impedance of the reference electrode, individual impedance spectra for anode and cathode cannot be obtained at frequencies above 100 kHz.

Results and Discussion

LNMO/graphite cycling data.—First we verified that the charge and discharge potentials are not affected by the OCV holds during discharge at 4.4 V_{FC} and at the end of discharge/charge at 3.0 V_{FC} / 4.9 V_{FC}, which were required for the EIS measurements. Figure 3 exemplarily shows three selected cycles at the beginning, the middle, and the end of the cycling procedure of the LNMO/graphite cell. The peak during discharge (red lines) is caused by the OCV phase and the subsequent impedance measurement, once the cell potential reaches 4.4 V_{FC} (indicated by the black dashed line in Figure 3). From cycle 1 to 75 (at C/2 and 40°C), the capacity drops from ~125 mAh/g to ~90 mAh/g (compare also Figure 4), which is typical for LNMO/graphite cells, due to their high operating potential and instability at elevated temperatures.[25,26] At the same time, the cell polarization increases, which can be seen easily when comparing the potential plateau around 4.65 V_{FC} during charge (dark lines) and at approximately 4.55 V_{FC} during discharge (green lines).

The discharge capacities and the coulombic efficiencies over all 85 charge/discharge cycles are shown in Figure 4 (formation cycles not shown). Discharge capacities slightly above 120 mAh/g_{LNMO} (~16% of the initial capacity are consumed by SEI formation during the first two cycles at C/10) are reached in the initial cycles, but owing to a rather poor coulombic efficiency which never reaches more than ~99.3% (see Figure 4), the initial capacity decreases by ~30% to ~87 mAh/g after only 85 cycles. This compares reasonably well with literature data on LNMO/graphite cells operated at 45°C at a sequence of C-rates (first ten cycles at C/10, followed by 40 cycles at C/4, and another 40 cycles by C/2), which lost ~20% of their initial capacity over the same number of cycles.[27] Our cycling data, capacity loss of 20–30 mAh/g at a cycling rate of C/2 at 40°C, also agrees well with

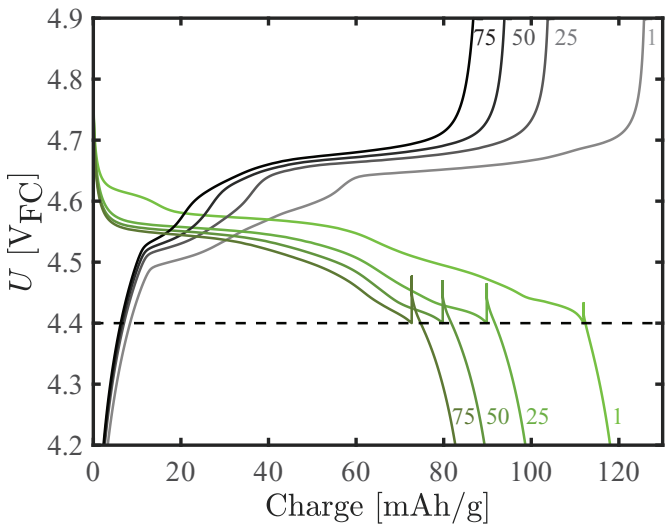

Figure 3. Exemplary charge (dark lines) and discharge (green lines) potential profiles for cycles 1, 25, 50, and 75 (marked in the figure) of the LNMO/graphite cell at 40°C, cycled at C/2 followed by a CV phase after charge until I <C/40 and a CV phase after discharge until I <C/100 between 3.0 and 4.9 V_{FC}. The peaks in the discharge curves are due to a 1 h OCV phase and a subsequent impedance measurement once the discharge potential reaches 4.4 V_{FC}.

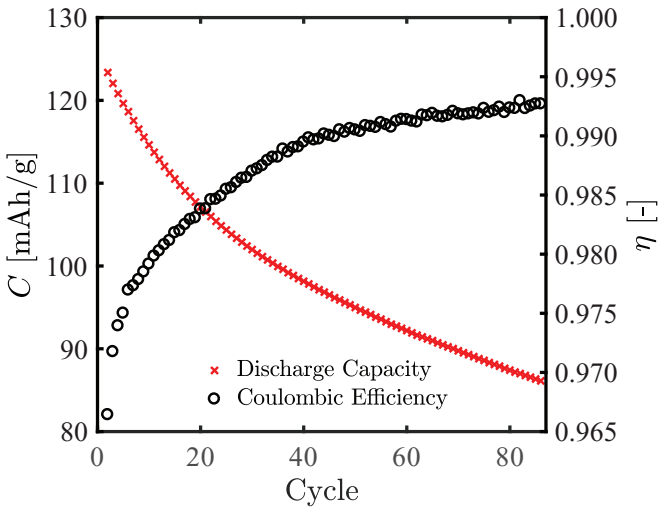

Figure 4. Discharge capacities for the LNMO/graphite cell cycled at 40°C and C/2 rate followed by a CCCV charge until I <C/40 and a CCCV discharge until I <C/100 in a potential window from 3.0 V_{FC} to 4.9 V_{FC} as well as the corresponding coulombic efficiencies.

the capacity loss of 30 mAh/g over 50 cycles at C/5 and 45°C, as reported by the group of Brett Lucht.[28] Thus, we conclude that the cycling data of the LNMO/graphite cells do not seem to be influenced significantly by the GWRE and the OCV periods required by for the EIS measurements. In the following we will focus our analysis to the impedance measurements performed during cycling of the cell.

Blocking conditions for the LNMO cathode in full-cells.—In the following, we will show that blocking conditions can indeed be achieved for the LNMO cathode in an LNMO/graphite full-cell by adding a constant voltage phase at the upper cutoff potential of 4.9 V_{FC} until the current decays below C/40, which leads to a condition where the cathode is fully delithiated so that the charge transfer resistance becomes very large (ideally, for perfect blocking conditions, R_{CT} would become infinitely large). For this purpose, an LNMO/graphite full-cell was built and charged galvanostatically at a C-Rate of C/10. Every 3 minutes during charge, the potential was held at its current value (no OCV phase), and an impedance spectrum with a perturbation of 50 mV was recorded in the frequency range from 100 kHz to 1 Hz (to obtain a short measurement time of ∼2 min per spectrum). After reaching the upper cutoff potential of 4.9 V_{FC}, impedance spectra were recorded continuously (taking ∼2 min each). Figure 5 demonstrates, how the cathode impedance spectra change upon approaching 100% SOC, showing exemplarily the EIS response at various potentials during the galvanostatic charge at potentials of 4.64 V_{FC}, 4.7 V_{FC}, 4.8 V_{FC}, and 4.9 V_{FC} as well as after increasingly long potential holds at the upper cutoff potential of 4.9 V_{FC}, after which EIS spectra are obtained potentiostatically while holding the potential. While the impedance spectra at 4.64 V_{FC} (blue line) resemble those simulated for non-blocking conditions (see blue line in Figure 2 between 100 kHz and 0.1 Hz), the impedance spectra after having held the cell potential at the upper cutoff potential approach those expected for blocking conditions, as is evident by comparing the red lines in Figure 5 with the red line in Figure 2.

To verify our above conclusions that the Nyquist plot of the cathode recorded in blocking conditions of an LNMO/graphite full-cell (i.e., after a 4.9 V_{FC} hold for 5 minutes) indeed follows the transmission line model for a blocking electrode, we prepared two additional cells, viz. one LNMO/graphite full-cell with GWRE and one LNMO/LNMO symmetric cell. The red data points in Figure 6 shows the impedance spectrum of the LNMO cathode of the LNMO/graphite full-cell, filled with the same electrolyte which was used for the cycling experiment (see Experimental), and subsequently charged at C/2 rate to 4.9 V_{FC}

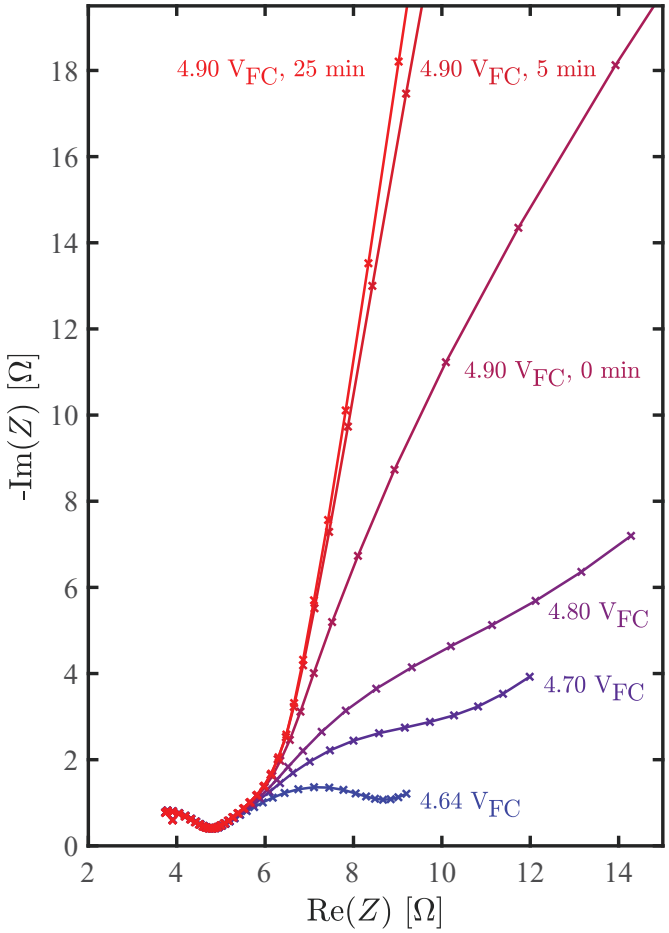

Figure 5. Evolution of the Nyquist plots of an LNMO cathode in an LNMO/graphite full-cell, obtained from EIS measurements (perturbation of 50 mV, 100 kHz–1 Hz) versus a GWRE. The data are recorded at a temperature of 25°C after two formation cycles at 25°C at C/10 followed by 5 C/10 cycles between 4.9 V_{FC} and 3.0 V_{FC}. Impedance spectra were obtained during galvanostatic charging of the cell at a charging rate of C/10 C and are shown from 4.64 V_{FC} up to 4.9 V_{FC}, followed by different holding times at 4.9 V_{FC}.

at 40°C and held at this potential for 5 minutes (after two formation cycles at 25°C and C/10), whereby the x- and y-axis values are multiplied by the conductivity of the electrolyte at the measurement temperature of 40°C ($\kappa = 11$ mS/cm). As can be seen in Figure 6 (red dashed line), the data can be fitted very well with a transmission line model without an $R_{Cont.}/Q_{Cont.}$ circuit element and with an infinitely large R_{CT} which is closely approached by a completely delithiated LNMO cathode. The resulting fit yields a value of 0.043 cm^{-1} for the product of $R_{Pore} \cdot \kappa$. In order to demonstrate that this approach yields reliable and meaningful physical-chemical parameters which describe ionic conductivity in the porous cathode electrode, a symmetric cell with two identical LNMO cathodes (albeit not cycled) and a non-intercalating electrolyte (10 mM $TBAClO_4$ in EC:EMC 3:7 w:w) was built. Its impedance response is shown by the black data in Figure 6 whereby it should be noted that the symmetric cell impedance was divided by two, as it represents the sum of two identical electrodes. The transmission line model for blocking conditions yields a very good fit of the data (see dashed black line) and a value of 0.033 cm^{-1} for $R_{Pore} \cdot \kappa$.

While the impedance spectra from both the LNMO cathode in the LNMO/graphite full-cell (measured with the GWRE) and from the LNMO/LNMO symmetric cell nicely fit the transmission line model for a blocking electrode, it remains to be determined whether the same pore resistance characteristics are observed for both nominally identical cathodes for these two different measurement

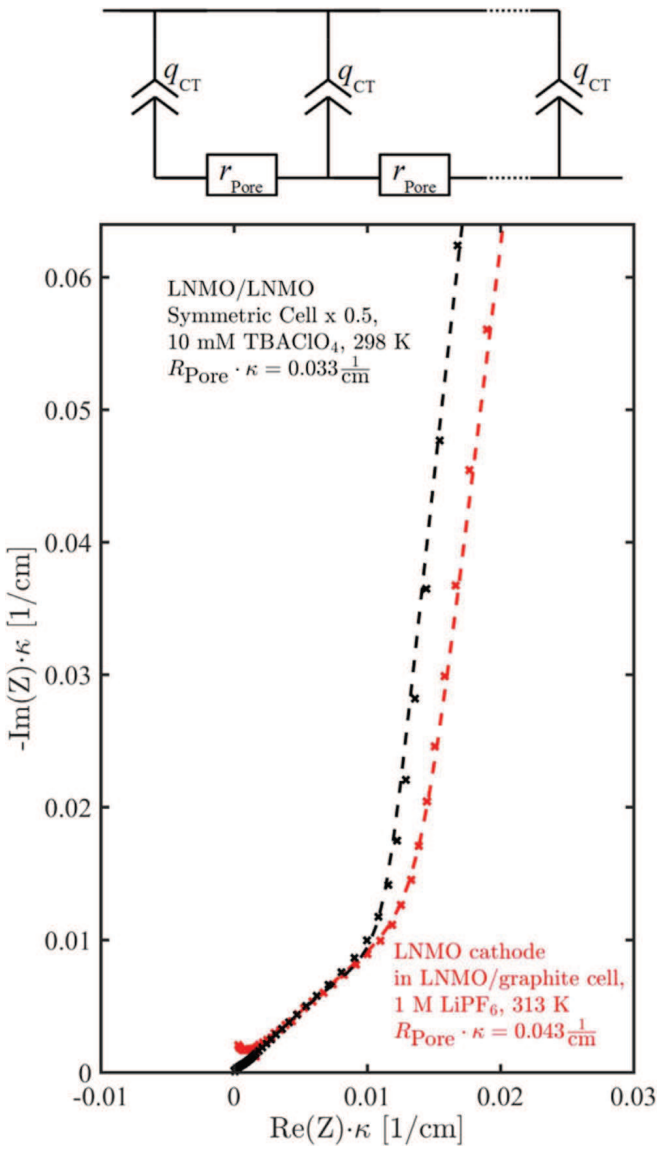

Figure 6. Comparison of the conductivity-scaled Nyquist spectra (i.e., real and imaginary impedances multiplied by the ionic conductivity) of an LNMO cathode in an LNMO/graphite cell (with GWRE) in blocking conditions (red data points) versus an LNMO/LNMO symmetric cell with non-intercalating electrolyte (black data points), whereby the latter impedance spectrum was divided by two in order to obtain the response of one LNMO cathode. The latter was measured after 12 h wetting by a non-intercalating electrolyte (10 mM TBAClO$_4$ in EC:EMC 3:7 w:w) at 25°C and using one CG2500 separator; the conductivity of this electrolyte at 25°C was determined to be $\kappa = 0.332$ mS/cm. The LNMO cathode impedance spectrum was obtained at 40°C after C/2 charging to 4.9 V_{FC} and holding that potential for 5 min (after two formation cycles); the electrolyte was 1 M LiPF$_6$ in EC:EMC (3:7, w:w) and had a conductivity at 40°C of $\kappa = 11$ mS/cm. Impedance spectra were recorded in the frequency range from 100 kHz to 0.1 Hz using an excitation amplitude of 15 mV and 20 mV for the LNMO/graphite cell and the symmetric cell, respectively. Both spectra were shifted to the origin for better comparability. The fit of the data to a simple transmission line model (shown in the figure) is represented by the dashed line and the resulting values of $R_{Pore} \cdot \kappa$ are given in the figure.

approaches. This can be checked by determining the corresponding MacMullin numbers (N_M), which would have to be the same for the nominally identical LNMO cathodes (i.e., having the same porosity (ε) and the same tortuosity (τ)) measured in the two different cell configurations:

$$N_M = \frac{\tau}{\varepsilon} = R_{Pore} \cdot \kappa \cdot \frac{A}{d} \quad [13]$$

where A is the area of the electrodes ($A = 0.95\,cm^2$) and d is their thickness ($d = 58\ \mu m$). The resulting MacMullin numbers obtained from the analysis of the data in Figure 6 are 7.0 ± 0.3 for the LNMO cathode measured in the LNMO/graphite full-cell with the GWRE under blocking conditions and 5.4 ± 0.3 for the nominally identical LNMO cathode measured in the LNMO/LNMO symmetric cell configuration, whereby the error results from the limited accuracy of the coating thickness measurement ($\pm 2\ \mu m$). More important than the measurement error for a given cell is the cell-to-cell variation (due minor differences in cell assembly and/or LNMO electrode coating), which was estimated by analyzing three more LNMO/LNMO symmetric cells and two more LNMO/graphite cells with GWRE (data not shown), yielding overall mean MacMullin numbers of 6.3 ± 0.6 for the LNMO electrodes measured in the LNMO/graphite full-cell setup (based on 3 repeat experiments) and 5.9 ± 0.6 for the LNMO cathode in the LNMO/LNMO symmetric cell setup (based on 4 repeat experiments). Thus, within the experimental error represented by the above standard deviations, both methods yield identical values for the MacMullin number. The fact that these values for the here used LNMO cathode with 5%wt conductive carbon are substantially lower than those we reported previously for an LNMO cathode with 2%wt conductive carbon ($N_M \approx 17$)[19] is simply related to the substantial lowering of the MacMullin number as the conductive carbon content is being increased (e.g., for lithium iron phosphate cathodes with comparable porosity, the MacMullin number decreases from 21 to 12 when the carbon content is increased from 5% to 15% wt.[19]). In summary, the above analysis demonstrates that blocking conditions are reached for an LNMO/graphite full-cell by holding the cell potential at 4.9 V_{FC} (Figure 5), and that reliable values for the ionic conduction characteristics of the LNMO cathode (i.e., its MacMullin number) can be obtained under these conditions via a simple transmission line model (Figure 6). In the following, we will now analyze the evolution of the impedance spectra over extended charge/discharge cycles and will utilize impedance measurements under blocking and non-blocking conditions in order to quantify the contributions derived from R_{Pore}, $R_{Cont.}$, and $R_{CT\text{-}non\text{-}blocking}$.

LNMO cathode impedance evolution in LNMO/graphite cells.— The cycle dependent Nyquist plots for the cathode in non-blocking condition at 4.4 V_{FC} and in blocking condition (i.e,. after a potential hold at 4.9 V_{FC} until I <C/40) are summarized in Figure 7 for every 25th cycle.

At the highest frequencies, a semi-circle can be observed, both, in non-blocking (Figure 7a) and in blocking conditions (Figure 7b), which is identical in magnitude and independent of the SOC and is thus ascribed to the contact resistance ($R_{Cont.}$, region II in Figure 1 and Figure 2). Over the course of charge/discharge cycling, this contact resistance clearly increases, evidenced by a shift of the spectra to larger real resistance values. It must be noted, however, that it is difficult to directly assess the value of the contact resistance, since in the experimentally accessible frequency range (100 kHz to 0.1 Hz; see Experimental section), only part of the contact resistance semi-circle can be obtained (this is illustrated by the modelled impedance response shown in Figure 2, where the 100 kHz data point is marked by the third yellow cross from the left). Therefore, the diameter of the semi-circle corresponding to the contact resistance cannot be determined visually from the acquired spectra without knowing the value of the high frequency resistance (R_{HFR}, region I in Figures 1 and 2). In non-blocking conditions (Figure 7a) the contact resistance semi-circle is followed by another distorted semi-circle, which increases in diameter from initially $\approx 1.5\ \Omega$ to $2\ \Omega$ in cycle 75, while at the lowest frequencies a Warburg type behavior can be observed (W, region IV in Figures 1 and 2). On the other hand, in blocking conditions (Figure 7b), an essentially straight line can be observed at medium frequencies (with an angle of close to 45 degrees in the first cycle), gradually turning into a nearly vertical line at the lowest frequencies, as one would expect for blocking conditions (compare the red line in region III marked in Figure 2). Thus, holding the cell potential at 4.9 V_{FC} does lead to the very large charge transfer resistance (R_{CT}) which is required to closely

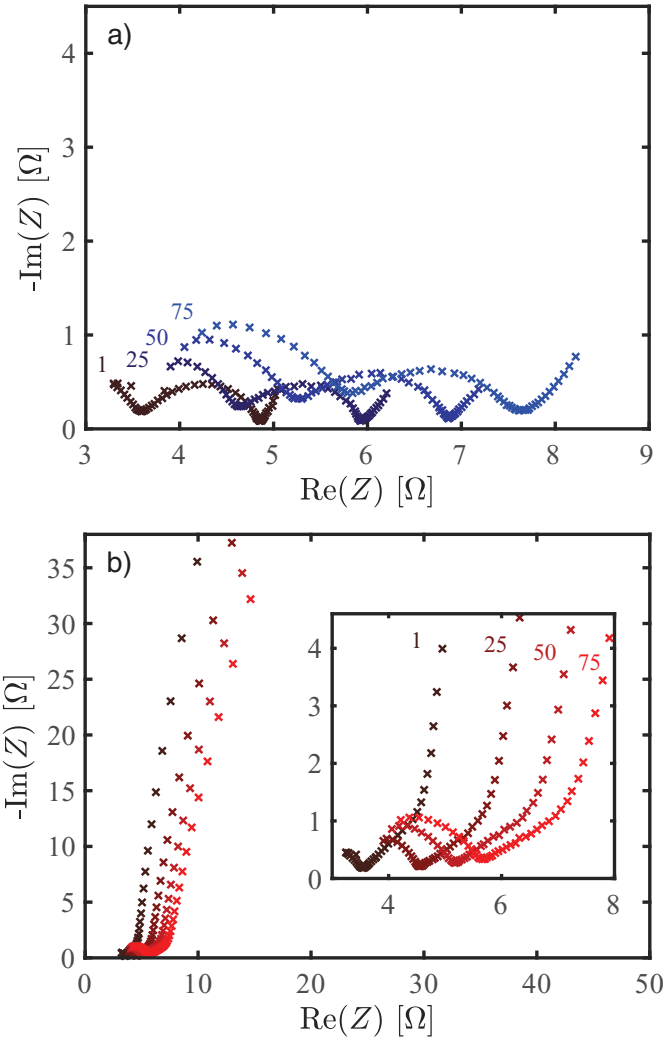

Figure 7. Evolution of the impedance spectra of the LNMO cathode (every 25th cycle; cycle numbers 1, 25, 50 and 75 are marked in the figure) during cycling of an LNMO/graphite cell at a rate of C/2 at 40°C: a) at 4.4 V_{FC} under non-blocking conditions (recorded at OCV after a 1 h OCV period); b) after potential hold at 4.9 V_{FC} under blocking conditions (recorded at a controlled potential of 4.9 V after a potential hold at 4.9 V until the current was below C/40). Potential-controlled EIS spectra were recorded with an amplitude of 15 mV in the frequency range from 100 kHz to 0.1 Hz.

approach blocking conditions. The decrease of the angle in the mid frequency region (initially close to 45 degrees) with cycling could be caused by electrolyte degradation products deposited in the cathode pores (see discussion after Figure 9), which change the pore structure inside the cathode.

In the following, the measured spectra of the half-cell cathode impedances are analyzed using Matlab (v. 2016b). Minimization of the sum of squares using a modulus weighing according to Lasia[20] was performed using Matlab's *fminsearch*[29] algorithm, and 95% confidence intervals are calculated via the Jacobian matrix obtained with the *jacobianest*[30] function. For each charge/discharge cycle, spectra in non-blocking condition at 4.4 V_{FC} and in blocking condition are fitted simultaneously using the equivalent circuit model shown in Figure 1. For the fitting of the spectrum in non-blocking conditions, 10 fitting parameters are required (viz., R_{HFR}, $R_{Cont.}$, $Q_{Cont.}$, $\alpha_{Cont.}$, R_{Pore}, $R_{El.}$, $R_{CT\text{-}non\text{-}blocking}$, Q_{CT}, α_{CT}, and W). In blocking conditions, the numerically identical parameters are used, except that a different value for the charge transfer resistance, referred to as $R_{CT\text{-}blocking}$ (in contrast to $R_{CT\text{-}non\text{-}blocking}$) is fitted and that the Warburg element is omitted. In summary the spectrum in non-blocking condition requires ten and the spectrum in blocking condition nine fitting parameters for an accurate description of the equivalent circuit model in Figure 1. However, since it is reasonable to assume that changes in the properties of the electrode and the active material are negligible within a single charge/discharge cycle, most of the parameters used to fit the blocking and non-blocking spectra within a given cycle are identical (viz., R_{HFR}, $R_{Cont.}$, $Q_{Cont.}$, $\alpha_{Cont.}$, R_{Pore}, $R_{El.}$, Q_{CT}, and α_{CT}), so that only eleven parameters are required to fit both spectra for a given cycle (see Table I).

Seeking to reduce the number of the free parameters in order to increase the accuracy of the fitted parameters, the following simplifications can be made. One is based on the assumption that the electronic resistance within the electrode ($R_{El.}$ in Figure 1) is small compared to the ionic resistance in the electrode and that its value does not change significantly over the course of the cycling experiment (to a good approximation, it would be sufficient that the ratio of $R_{Pore}/R_{El.}$ remains at $\gg 1$).The maximum value of $R_{El.}$ for our pristine LNMO cathodes was obtained by a 2-point probe measurement, placing the LNMO electrode between two copper blocks, each equipped with a current and voltage lead (at a compression of 0.1 MPa using a static material testing machine zwickiLine from ZwickRoell, Ulm, Germany) and using a nanovoltmeter (Keithley 2182) in combination with a DC current source (Keithley 6221). This yielded a value of $R_{El.} \approx 0.1\ \Omega$, (≈30-fold lower than R_{Pore}, as will be shown later), so that $R_{El.} = 0.1\ \Omega$ was used as a fixed and constant resistance in the fitting of all impedance spectra. The other simplification in fitting the impedance spectra is related to the high-frequency resistance (R_{HFR} in Figure 1). While theoretically its value could be obtained from the overall fit of the impedance spectra, it would decrease the quality of the fit, because only a fraction of the contact resistance semi-circle can be observed with the experimentally accessible upper frequency limit of 100 kHz for the GWRE (see Figure 1 and Figure 7). The pure high-frequency resistance for the LNMO/graphite full-cell ($R_{HFR,full\text{-}cell}$), however, could be determined by measuring the *full-cell* impedance between anode and cathode after the cycling test, as in this case an upper frequency limit of 7 MHz could be used, so that despite the LNMO contact resistance the high-frequency real axis intercept can be obtained. This yielded a value of $R_{HFR,full\text{-}cell} = 4.8\ \Omega$, i.e., of 2.4 Ω for each half-cell. In addition, analysis of the graphite impedance data using the GWRE in the same setup (the detailed analysis of the anode data will be submitted soon), where the high frequency resistance even at an upper frequency limit of 100 kHz can be determined unambiguously, yielding a *cycle independent* value of $R_{HFR,anode} = 2.4\ \Omega$. As the GWRE sits in the center of two glass fiber separators, the high frequency resistance of the anode and the cathode half-cells are identical.[17] From this it can be concluded that the high frequency resistance (R_{HFR} in Figure 1), i.e., the resistance caused by the ionic resistance in the separator of the LNMO half-cell, remains essentially constant at a value of 2.4 Ω. Therefore, the value of R_{HFR} in the following impedance fits was kept constant at 2.4 Ω, reducing the number of final fitting parameters to nine (viz., $R_{Cont.}$, $Q_{Cont.}$, $\alpha_{Cont.}$, R_{Pore}, $R_{CT\text{-}non\text{-}blocking}$, $R_{CT\text{-}blocking}$, Q_{CT}, α_{CT}, and W), which are fitted simultaneously to each of the two impedance spectra (blocking and non-blocking conditions) per cycle.

Exemplary fits of the cathode impedance spectra of the LNMO/graphite full-cell after 30 cycles both in blocking condition (potential hold at 4.9 V_{FC}) and in non-blocking condition at 4.4 V_{FC} are shown in Figure 8. The fitted impedance spectra (lines in Figure 8) with the above listed set of 9 fitting parameters provide quite a good fit to the impedance data (black crosses) under both conditions over the entire frequency range (100 kHz to 0.1 Hz).

Figure 9 collects the values of the most relevant equivalent circuit model parameters for the LNMO cathode and depicts their evolution with cycling as well as their 95% confidence intervals. As discussed above, the high frequency resistance (R_{HFR}) and the electronic resistance ($R_{El.}$) are kept constant to allow for an explicit determination of the contact resistance. The contact resistance is found to increase from ≈1 Ω initially to ≈3 Ω after 85 cycles at C/2 at 40°C (yellow symbols in Figure 9a), which confirms the observation made in the discussion

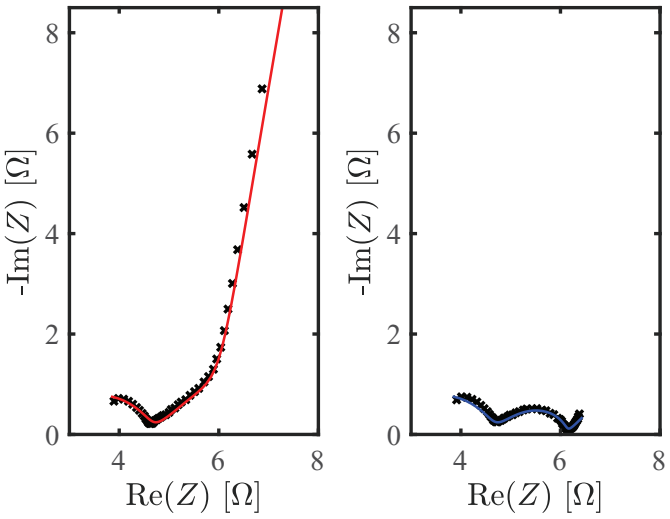

Figure 8. Exemplary fits (shown as solid lines) of the cathode impedance at cycle 30 obtained from the LNMO/graphite full-cell in blocking condition at 4.9 V_{FC} (left) and non-blocking conditions at 4.4 V_{FC} (right). Both spectra are fitted simultaneously, using the equivalent circuit model shown in Figure 1 with the same values for most parameters ($R_{Cont.}$, $Q_{Cont.}$, $\alpha_{Cont.}$, R_{Pore}, Q_{CT}, α_{CT}) and individual values for the charge transfer resistance in blocking condition ($R_{CT\text{-}blocking}$), the charge transfer resistance in non-blocking condition at 4.4 V_{FC} ($R_{CT\text{-}non\text{-}blocking}$), and the Warburg diffusion element (W) which is only used in non-blocking condition. AC impedance data (black crosses) were recorded at 40°C between 100 kHz and 0.1 Hz (15 mV voltage perturbation) after holding the cell potential at 4.9 V_{FC} (blocking condition, left) or at 4.4 V_{FC} after an 1 h OCV period (non-blocking condition, right).

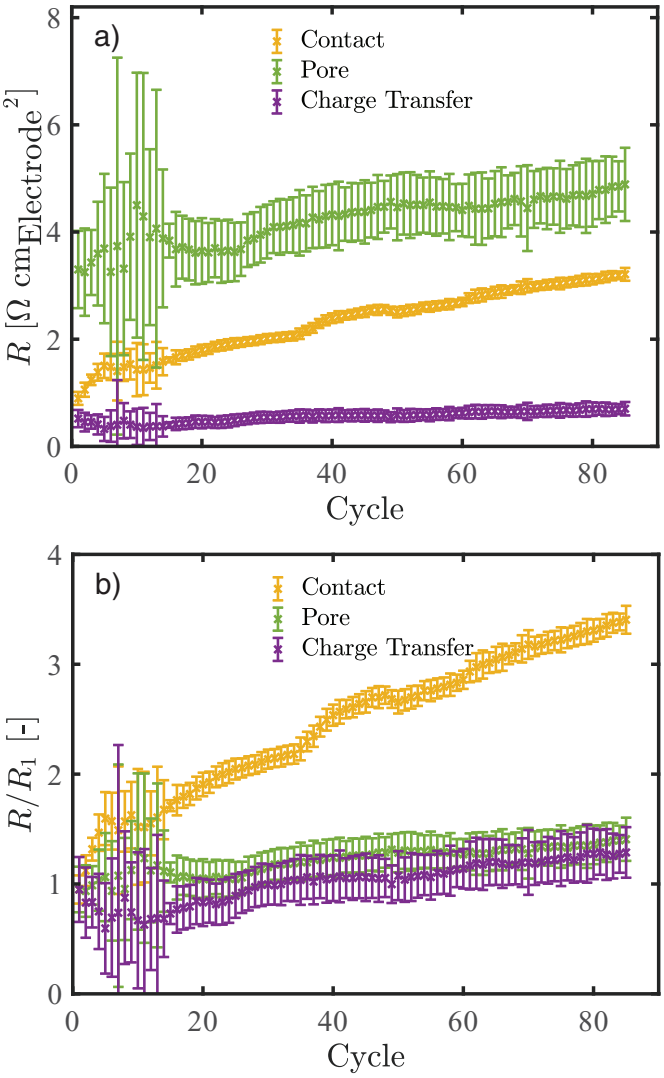

Figure 9. a) Evolution of the contact resistance ($R_{Cont.}$), the charge transfer resistance at 4.4 V_{FC} ($R_{CT\text{-}non\text{-}blocking}$, obtained under non-blocking conditions), and the pore resistance (R_{Pore}, obtained under blocking conditions) of the LNMO cathode, normalized to the electrode area, in the LNMO/graphite full-cell over extended charge/discharge cycling at 40°C at a rate of C/2 between 3.0 and 4.9 V_{FC} (the corresponding capacity vs. time plot and exemplary voltage vs. capacity plots are shown in Figure 4 and Figure 3, respectively; the formation cycles are not included). The shown values were determined by simultaneously fitting two impedance spectra per cycle, one in blocking condition and one in non-blocking condition as shown in Figure 8. The high frequency resistance contribution to the cathode (R_{HFR} in Figure 1) was set to a constant value of 2.4 Ω, and the electronic resistance in the cathode ($R_{El.}$ in Figure 1) was set to 0.1 Ω (see discussion in the text). b) Resistances normalized to their initial value after formation. Error bars indicate the parameters' 95% confidence interval from the fit.

of Figure 7, namely that the shift of the spectra to higher real resistance values is due to an increase of the high-frequency semi-circle representing the contact resistance. This increase of the LNMO cathode's contact resistance fits very well to the observation that a delamination of the LNMO electrode from the current collector occurs during cycling at elevated temperatures (60°C),[31] the underlying mechanism of which will be a subject of a future work.[32] Compared to the contact resistance, the pore resistance (R_{Pore}, green symbols) increases from an initial value of ≈3.5 Ω to ≈5 Ω after 85 cycles, while the charge transfer resistance at 4.4 V_{FC} ($R_{CT\text{-}non\text{-}blocking}$, purple symbols) starts at ≈0.5 Ω and increases to only ≈0.7 Ω after 85 cycles. Thus, the contact resistance shows the strongest increase over the 85 charge/discharge cycles of +300%, while the pore and charge transfer resistance at 4.4 V only increase by ≈45% and ≈30%, respectively (see Figure 9b). The charge transfer resistances in blocking-condition (not shown in Figure 9) is found to be ≈900 Ω, a very large value compared to the other resistances, as would be expected for the observed blocking electrode behavior, i.e., the nearly vertical line at lowest frequencies (see Figure 7b or the left panel of Figure 8). The error bars of all resistances shown in Figure 9 are mostly smaller than 25%, which is quite reasonable considering that two spectra were fitted simultaneously with a restricted parameter set for any given cycle, thus suggesting that the equivalent circuit representation of the LNMO cathode in Figure 1 captures most of the relevant processes. The irregularities observed for the fitted contact and pore resistance around cycles five to fifteen can be explained with the drift of the GWRE potential from its lithiated state to its unlithiated potential (see Experimental).

Over the course of the 85 charge/discharge cycles at 40°C, the overall resistance of the LNMO cathode ($R_{Cont.} + f(R_{Pore}, R_{CT\text{-}non\text{-}blocking})$) increases from an initial value of ≈5 Ω to ≈9 Ω (see Figure 9a). At the given charge/discharge current of ≈1 mA (based on a capacity of ≈2 mAh and a rate of C/2), this would predict an increase in cathode polarization of only ≈4 mV and would thus be rather negligible. As can be seen from the cell voltage vs. capacity data in Figure 3, the increase in the polarization of the LNMO/graphite cell seems to be much larger than 4 mV, which is due to the fact that the largest contribution to the cell polarization with cycling is caused by a substantial gain in the impedance of the anode (this analysis will be subject of a future publication).

Using the charge transfer resistances at 4.4 V of ≈0.5–0.7 Ω (see purple lines in Figure 9a), the linearized Butler-Volmer equation allows to estimate the exchange current density:

$$i_0 = \frac{RT}{F} \cdot \frac{1}{A_{LNMO} \cdot R_{CT-non-blocking}} \quad [14]$$

with R, T, and F being the gas constant (8.831 kJ/mol K), temperature (303 K), and the Faraday constant (96485 As/mol),

respectively. In addition, A_{LNMO} represents the active surface area of the LNMO, which can be estimated using the mass of LNMO (13.7 mg) in the cell and its BET surface area (0.9 m^2/g), equating to $A_{LNMO} = 123\ cm^2_{LNMO}$. Based on this, we find an exchange current density of 0.43–0.30 mA/cm^2_{LNMO} at 4.4 V_{FC} (i.e., at ≈7–12% SOC, s. Figure 3), which is within the range of exchange current densities for intercalation materials reported in the literature (0.02–0.3 mA/cm^2_{LNMO} for LNMO,[33] 0.17 mA/cm^2_{LFP} for $LiFePO_4$,[34] and 2.5 $mA/cm^2_{Graphite}$ for graphite[35]).

The observed increase in the pore resistance with cycling (see green lines in Figure 9) can be explained by a decrease of the effective electrolyte conductivity in the pores, likely caused by a partial blockage of the cathodes' pore volume by electrolyte oxidation fragments, thereby decreasing the cathode's void volume, which would probably also be accompanied by an increase in the cathode's tortuosity. In the literature, it is reported that the electrode/electrolyte interface at the LNMO cathode (often referred to as CEI) is not stable, compared to the solid electrolyte interface (SEI) on the graphite anode, so that electrolyte oxidation would happen at the surface of the LNMO particles.[2,25,26] This is consistent with the observation that both, charge transfer resistance at 4.4 V and the pore resistance, increase over the 85 charge/discharge cycle by 30% and 45% respectively.

The feasibility of the obtained fitting parameters for the impedance spectra can also be checked by examining the values the fit yielded for the capacitive constant phase elements related to both the LNMO cathode material (Q_{CT}, see Figure 1) and the contact resistance ($Q_{Cont.}$, see Figure 1). A rough order of magnitude estimate of the capacitances can be done by neglecting the constant phase factor, yielding values of $Q_{Cont.}$ ≈10 μF and Q_{CT} ≈1 mF. If normalized to the exposed areas of the current collector/electrode interface (≈1 cm^2) and the LNMO area ($A_{LNMO} = 123\ cm^2_{LNMO}$), the resulting area specific capacitance amounts to ≈10 $\mu F/cm^2_{surface}$ in either case, which is a reasonable value for the double layer capacitance.

The results obtained from this study suggest that the charge transfer resistance of the LNMO cathode is not increasing substantially during extended charge/discharge cycling, which is in disagreement with reports in the literature. For example, Aurbach et al. analyzed the impedance of LNMO/graphite cells by measuring the impedance of the LNMO electrode versus a lithium wire reference electrode, showing that the impedance in the high-to-medium frequency range increases during cycling, which they ascribed to an increase of a combination of a surface film (inferred from an increase in the LiF surface coverage measured by XPS) and a charge transfer resistance at the LNMO/electrolyte interface.[26] However, examining the semi-circle at high-to-medium frequencies in their measurements (apex-frequency = 1.58 kHz, $R_{semi\text{-}circle} = 126\ \Omega$), one obtains a capacitance value of ≈1 μF, which is more consistent with a contact resistance between the LNMO cathode and the current collector rather than with the capacitance of the high surface area of the porous LNMO cathode. This suggests that their reported increase in LNMO surface/charge transfer resistance is likely incorrect and that the impedance increase in their study is propably due to an increase in $R_{Cont.}$, analogous to what is shown in Figure 9. Similarly, Lu et al. analyzed the impedance of LNMO/graphite cells (full-cell impedance) and claimed that the observed increase of the high frequency semi-circle is related to an increase in the thickness of a resistive film on the LNMO surface.[25] In summary, these studies claim the formation of a resistive film and/or an increase in the charge transfer resistance during extended cycling of an LNMO cathode, contrary to our analysis shown in Figure 9, which we believe is due to an incorrect assignment of the impedance data, caused primarily by the interference from contact and/or pore resistances with the charge transfer resistance. Here it may be noted that similarly incorrect assignments were discussed previously for LFP/graphite electrodes by Gaberscek et al.[36]

By exemplary analysis of LNMO half-cell data we have demonstrated that it is possible to analyze the impedance of an LNMO cathode in an LNMO/graphite full-cell with a GWRE in both blocking and in non-blocking conditions over the course of cycling, which

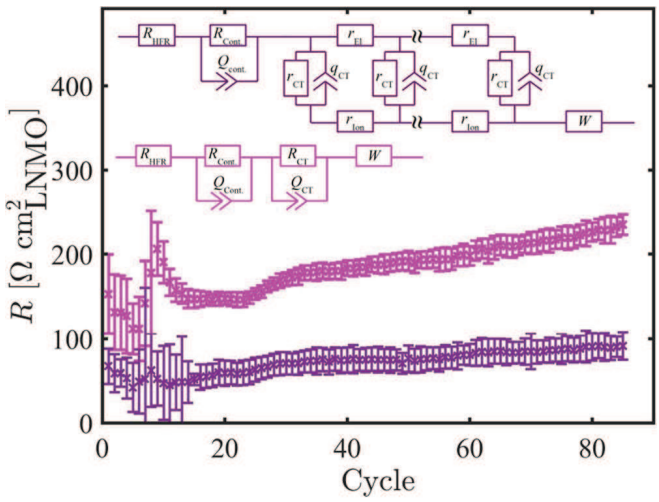

Figure 10. Comparison of the areal charge transfer resistances, normalized to the LNMO BET surface area (123 cm^2), obtained from the transmission line model including pore resistance (lilac) with the *apparent* charge transfer resistance extracted from the conventionally used simplified equivalent circuit (magenta) with one *R/Q* element to describe the mid frequency region (region III in Figure 1 and Figure 2), while one *R/Q* element is used to describe the high-frequency region semi-circle (region II in Figure 1 and Figure 2).

in turn allows for an unambiguous determination of all parameters in the general transmission line model with small errors. The obtained resistances are found to be of reasonable magnitude and in good agreement with the literature and can be monitored in-situ over the course of extended cell cycling. This minimizes the required number of cells compared to the rather cumbersome conventional approach, in which pairs of cells are cycled to a certain number of cycles and the impedances of the half-cells are obtained after cell disassembly and reassembly of anodes and cathodes into symmetric cells–clearly advantageous from an experimental point of view. Furthermore, in most impedance studies in the literature, the observed distorted semi-circle of the impedance spectra in non-blocking condition (compare Figure 7a) are fitted and interpreted in terms of a single *R/Q* equivalent circuit element in the mid frequency region, yielding an apparent charge transfer resistance,[10,26,37] even though this frequency region also contains the pore resistance (region III in Figure 1 and Figure 2). To highlight the difference in the charge transfer resistance values obtained by these two approaches, we compare the charge transfer resistance obtained from our simultaneous fit in blocking and non-blocking conditions (see data in Figure 9, fitted to the equivalent circuit shown in Figure 1) with the apparent charge transfer resistance obtained when the distorted semi-circle (see Figure 7a, second semi-circle from the left) is simply fitted with an *R/Q* element (i.e., using the conventionally applied simplified equivalent circuit depicted in Figure 10 (magenta)). The two different equivalent circuit models are depicted together with the resulting charge transfer resistances (including 95% confidence intervals) in Figure 10.

Figure 10 (magenta symbols) illustrates the stark overestimation of the apparent charge transfer resistance using the simplified equivalent circuit model, which neglects the ionic resistance within the porous electrode: the obtained apparent charge transfer resistance larger by a factor of two to three (magenta symbols) compared to the charge transfer resistance obtained from our transmission line model evaluated simultaneously in blocking and non-blocking conditions (lilac symbols), which is due to the fact that in the former approach the pore resistance (R_{Pore}) is added erroneously to the charge transfer resistance. Thus, in our opinion, the simplified equivalent circuit model is a coarse oversimplification for a porous electrode, and the true charge transfer resistance constitutes only a fraction of the observed mid-frequency semi-circle width.

Conclusions

We utilize a gold wire micro-reference electrode to separate anode and cathode spectra in an LNMO/graphite full-cell over the course of extended charge/discharge cycling. The LNMO cathode impedance spectra could be deconvoluted into individual resistance contributions by measuring in non-blocking conditions at 4.4 V_{FC} and in blocking conditions by holding the LNMO/graphite full-cell potential at 4.9 V_{FC}. This novel impedance analysis approach, i.e., the simultaneous fitting of impedance spectra measured in blocking and non-blocking condition, enables the in-situ quantification of the cycle dependent charge transfer, contact, and pore resistances, over the course of extended charge/discharge cycling, which is a powerful analysis tool for aging studies. We applied our approach exemplarily to an LNMO cathode, but generally the technique could also be applied to other active materials which can be brought into a blocking condition in a full-cell configuration, such as, e.g., lithium iron phosphate, graphite, or LTO.

Acknowledgment

J. L. gratefully acknowledges the funding by the Bavarian Ministry of Economic Affairs and Media, Energy, and Technology for its financial support under the auspices of the EEBatt project. D. P. acknowledges funding from BASF SE within the framework of the Network on Electrochemistry and Batteries. The authors thank Werner Strunz from Zahner for his helpful remarks regarding the general transmission line model and Andrzej Lasia for his comments on proper weighing of impedance spectra and his critical feedback on the equivalent circuit model.

Appendix

Diffusion impedances of solid diffusion and liquid diffusion.—As outlined in the Theory section, the imaginary part of the impedance of a diffusion process depends on the diffusion coefficient of the diffusing species as well as the cross sectional area, bulk concentration of the species in the medium, and the temperature. The diffusion coefficient of lithium in the liquid electrolyte is on the order of 10^{-10} m^2/s for typical lithium ion battery electrolytes at room temperature.[38] For the solid state diffusion coefficient, the range of reported diffusion coefficients in various cathode materials range from 10^{-12} m^2/s to 10^{-19} m^2/s.[39] Mohamedi et al. report an apparent solid state diffusion coefficient for LNMO of 10^{-14} m^2/s to 10^{-16} m^2/s.[33] In the following, we will present our own conservative estimate of the lower limit for the solid state diffusion coefficient of lithium in LNMO (for even larger solid state diffusion coefficients, the impact of the solid state diffusion on the impedance spectrum would be reduced further).

LNMO electrodes with a very small loading of 10 $\mu g/cm^2$ were cycled at 25°C versus metallic lithium in a three electrode configuration with a lithium reference electrode in the potential range from 3 V to 4.9 V vs. lithium using a standard electrolyte ($LiPF_6$ in EC:EMC 3:7, w:w) and two glass fiber separators. The LNMO was always deintercalated (charged) at a constant current of C/3 until the cutoff of 4.9 V vs. the lithium RE was reached. Constant current intercalation (discharge) was done at C-Rates from 1C to 500C until the lower cutoff potential of 3.0 V vs. lithium was reached. By minimizing the loading, the total current in the cell is small (at 500C, $I = 5\ mA$) and all overpotentials from separator resistances, contact resistances, and the concentration gradients in the liquid electrolyte play an insignificant role. The intercalation direction was chosen on purpose to allow large overpotentials. In these measurements, ~20% of the full (1C) capacity could be extracted from the low loaded LNMO cathodes at a C-Rate of 100C. Assuming, conservatively, that all limitations in this experiment are a result of the solid state diffusion inside the active material particles (s. above), i.e., neglecting all other resistances and/or a concentration buildup in the liquid phase, we can now estimate the lower limit of the solid state diffusion coefficient. 20% of the capacity of the LNMO particles (15 μm diameter, based on SEM images) can be extracted from the particle shell region between $r = 7.0\ \mu m$ to $r = 7.5\ \mu m$ (corresponding to 20% of the particle volume). During 20% of the time of a 100C intercalation ($t = 0.2 \cdot 36s = 7.2$ s), the lithium in the LNMO has to travel at least $\Delta r = 0.5\ \mu m$, equating to an estimated diffusion coefficient of $D = \Delta r^2/t = 3.5 \cdot 10^{-14}\ \frac{m^2}{s}$.

With the above estimates for the solid and the liquid diffusion coefficient,[38] the diffusion impedance can be estimated (strictly valid only for semi-infinite diffusion inside a film) with Equation 12 and the definition of the Warburg coefficient (compare Reference 40, Eq. 5–40 for the same kinetic rate constants for forward and backward reaction $k_f = k_b$)
;

$$W = \frac{4 \cdot RT}{z^2F^2\ A\ C\ \sqrt{2 \cdot D}} \qquad [A1]$$

The Warburg coefficient of the liquid electrolyte phase at a frequency of 0.1 Hz thus yields a value of

$$W_{Liquid} = \frac{4 \cdot RT}{z^2\ F^2 \cdot 0.95\ cm^2 \cdot 1000\frac{mol}{m^3}\sqrt{2 \cdot 10^{-10}\frac{m^2}{s}}} = 792\frac{m\Omega}{\sqrt{s}} \qquad [A2]$$

while for solid state diffusion the Warburg coefficient at a frequency of 0.1 Hz can be estimated as

$$W_{Solid-state} = \frac{4 \cdot RT}{z^2\ F^2 \cdot 123\ cm^2 \cdot 10700\frac{mol}{m^3}\sqrt{2 \cdot 3.5 \cdot 10^{-14}\frac{m^2}{s}}} = 31\frac{m\Omega}{\sqrt{s}} \qquad [A3]$$

Here, the lithium concentration in the solid (10700 mole/m^3) is calculated for an LNMO particle at 50% SOC ($\equiv$ 70 mAh/g_{LNMO} = 252 As/g_{LNMO}), using a bulk density of 4.4 g/cm^3 (252 As/g ·4.4 g/cm^3/96485 As/mol ·10^6 cm^3/m^3 = 10700 mol/m^3). With the above Warburg coefficients, Warburg impedances of $Z_W^{Liquid}(0.1\ Hz) = 1\ \Omega$ and $Z_W^{Solid-state}(0.1\ Hz) = 39\ m\Omega$ are obtained. This means that the contribution of the solid state diffusion impedance at the lowest frequency measured in this work (0.1 Hz) is 1.5 orders of magnitude smaller than the diffusion impedance caused by the liquid electrolyte. Based on this result, the solid state diffusion inside the active material is negligible, i.e., we can omit the Warburg element in series to the charge transfer resistance in the equivalent circuit model in Figure 1, but must place a Warburg element in series to the separator resistance to capture the effect of liquid diffusion.

References

1. K. Xu, *J. Electrochem. Soc.*, **154**, S9 (2007).
2. S. R. Li, C. H. Chen, X. Xia, and J. R. Dahn, *J. Electrochem. Soc.*, **160**, A1524 (2013).
3. T. R. Jow, M. B. Marx, and J. L. Allen, *J. Electrochem. Soc.*, **159**, A604 (2012).
4. J. P. Schmidt, T. Chrobak, M. Ender, J. Illig, D. Klotz, and E. Ivers-Tiffée, *J. Power Sources*, **196**, 5342 (2011).
5. J. Illig, M. Ender, T. Chrobak, J. P. Schmidt, D. Klotz, and E. Ivers-Tiffee, *J. Electrochem. Soc.*, **159**, A952 (2012).
6. D. W. Abarbanel, K. J. Nelson, and J. R. Dahn, *J. Electrochem. Soc.*, **163**, A522 (2016).
7. N. Ogihara, Y. Itou, T. Sasaki, and Y. Takeuchi, *J. Phys. Chem. C*, 150209102507001 (2015).
8. J. N. Illig, *Dr. Diss., Karlsruhe* (2014).
9. C. H. Chen, J. Liu, and K. Amine, *J. Power Sources*, **96**, 321 (2001).
10. R. Petibon, C. P. Aiken, N. N. Sinha, J. C. Burns, H. Ye, C. M. VanElzen, G. Jain, S. Trussler, and J. R. Dahn, *J. Electrochem. Soc.*, **160**, A117 (2012).
11. S. Klink, E. Madej, E. Ventosa, A. Lindner, W. Schuhmann, and F. La Mantia, *Electrochem. commun.*, **22**, 120 (2012).
12. M. Ender, A. Weber, and E. Ivers-TiffeÉe, *J. Electrochem. Soc.*, **159**, A128 (2012).
13. C. Bünzli, H. Kaiser, P. Novák, C. Bunzli, H. Kaiser, and P. Novak, *J. Electrochem. Soc.*, **162**, A218 (2014).
14. J. Zhou and P. H. L. Notten, *J. Electrochem. Soc.*, **151**, A2173 (2004).
15. D. P. Abraham, S. D. Poppen, A. N. Jansen, J. Liu, and D. W. Dees, *Electrochim. Acta*, **49**, 4763 (2004).
16. J. L. Gómez-Cámer and P. Novák, *Electrochem. commun.*, **34**, 208 (2013).
17. S. Solchenbach, D. Pritzl, E. J. Y. Kong, J. Landesfeind, and H. A. Gasteiger, *J. Electrochem. Soc.*, **163**, A2265 (2016).
18. N. Ogihara, S. Kawauchi, C. Okuda, Y. Itou, Y. Takeuchi, and Y. Ukyo, *J. Electrochem. Soc.*, **159**, A1034 (2012).
19. J. Landesfeind, J. Hattendorff, A. Ehrl, W. A. Wall, and H. A. Gasteiger, *J. Electrochem. Soc.*, **163**, A1373 (2016).
20. Andrzej Lasia, *Electrochemical Impedance Spectroscopy and its Applications*, Springer (2014).
21. H. Göhr, in *Electrochemical Applications*, p. 2, ZAHNER-elektrik GmbH & Co. KG (1997).
22. M. E. Orazem and B. Tribollet, *Electrochemical Impedance Spectroscopy*, WILEY A (2008).
23. J. A. Gilbert, J. Bareño, T. Spila, S. E. Trask, D. J. Miller, B. J. Polzin, A. N. Jansen, and D. P. Abraham, *J. Electrochem. Soc.*, **164**, A6054 (2017).
24. R. Petibon, J. Xia, L. Ma, M. K. G. Bauer, K. J. Nelson, and J. R. Dahn, *J. Electrochem. Soc.*, **163**, A2571 (2016).
25. D. Lu, M. Xu, L. Zhou, A. Garsuch, and B. L. Lucht, *J. Electrochem. Soc.*, **160**, A3138 (2013).
26. D. Aurbach, B. Markovsky, Y. Talyossef, G. Salitra, H. J. Kim, and S. Choi, *J. Power Sources*, **162**, 780 (2006).
27. B. Michalak, B. B. Berkes, H. Sommer, T. Bergfeldt, T. Brezesinski, and J. Janek, *Anal. Chem.*, **88**, 2877 (2016).
28. Y. Dong, J. Demeaux, and B. L. Lucht, *J. Electrochem. Soc.*, **163**, A2413 (2016).
29. *Matlab Ref.*, 2016b https://de.mathworks.com/help/matlab/ref/fminsearch.html.
30. *Matlab File Exch.*, 2016b http://de.mathworks.com/matlabcentral/fileexchange/13490-adaptive-robust-numerical-differentiation/content/DERIVESTsuite/jacobianest.m.
31. T. Yoon, S. Park, J. Mun, J. Heon, W. Choi, Y. Kang, J. Park, and S. M. Oh, *J. Power Sources*, **215**, 312 (2012).
32. D. Pritzl, M. Wetjen, J. Landesfeind, S. Solchenbach, and H. A. Gasteiger, in preparation.
33. M. Mohamedi, M. Makino, K. Dokko, T. Itoh, and I. Uchida, *Electrochim. Acta*, **48**, 79 (2002).

34. C. Heubner, M. Schneider, and A. Michaelis, *J. Power Sources*, **288**, 115 (2015).
35. Y.-C. Chang, J.-H. Jong, and G. T.-K. Fey, *J. Electrochem. Soc.*, **147**, 2033 (2000).
36. M. Gaberscek, J. Moskon, B. Erjavec, R. Dominko, and J. Jamnik, *Electrochem. Solid-State Lett.*, **11**, A170 (2008).
37. J. Xia, L. Ma, K. J. Nelson, M. Nie, Z. Lu, and J. R. Dahn, *J. Electrochem. Soc.*, **163**, 2399 (2016).
38. A. Ehrl, J. Landesfeind, W. A. Wall, H. A. Gasteiger, and W. A. Wall, *J. Electrochem. Soc.*, **164**, A826 (2017).
39. M. Park, X. Zhang, M. Chung, G. B. Less, and A. M. Sastry, *J. Power Sources*, **195**, 7904 (2010).
40. V. F. Lvovich, *Impedance Spectroscopy Applications to Electrochemical and Dielectric Phenomena*, p. 78, John Wiley & Sons, Ltd, New Jersey (2012).

3.1.4 Application of the novel impedance procedure for a graphite anode

This section presents the article "*An Analysis Protocol for Three-Electrode Li-Ion Battery Impedance Spectra: Part II. Analysis of a Graphite Anode Cycled vs. LNMO".*[112] The paper was submitted to the peer-reviewed Journal of the Electrochemical Society in April 2018 and published in July 2018. The article is published open access and distributed under the terms of the Creative Commons Attribution Non-Commercial No Derivatives 4.0 License. The authors D.P. and J.L contributed equally to this work. The permanent web link is available under: http://jes.ecsdl.org/content/165/10/A2145. The article was presented by Daniel Pritzl at the Seattle, Washington Meeting of the Electrochemical Society (USA) in May 2018 (Paper 402).

With the new reference electrode (GWRE)[99] and the novel impedance procedure[109] at hand, we seek to apply the same concept for the anode that was applied for the LNMO cathode in chapter 3.1.3. This will give new insights, as in the literature it is generally reported that the graphite anode is responsible for the cell failure of the graphite/LNMO cells at elevated temperatures. The effect is attributed to an instable solid electrolyte interphase (SEI)[21] on the graphite anode, due to manganese and nickel dissolution from the LNMO cathode.[20,77] Therefore, a detailed impedance analysis of the graphite anode could be very helpful in order to determine its failure mechanism.

In the LNMO case (chapter 3.1.3), the cathode showed a blocking impedance response upon complete delithiation. By transferring this concept to a graphite anode we show that at 1.9 V vs. Li^+/Li also a blocking behavior of the anode in a graphite/LFP cell chemistry can also be achieved. When switching from an LFP cathode to an LNMO cathode, the impedance response is no longer purely blocking but shows a semi-circle at the highest frequencies which increases drastically over cycling. It is known that LFP is not affected by transition metal dissolution, whereas LNMO shows severe transition metal dissolution.[77] By adding a manganese salt to graphite/LFP cells we can also detect a high-frequency semi-circle in the blocking

impedance spectrum. With this, we can for the first time correlate the impedance response of a graphite anode with transition metal dissolution from the cathode. Thus, this method should be a powerful and efficient tool to study additives and different electrolytes to minimize or prevent transition metal dissolution.

By temperature-dependent impedance measurements and frequency analysis of the spectra we could show that the high-frequency semi-circle stems from a novel interface forming between the graphite anode and the separator. Lastly, we combine the analysis from the cathode impedance[109] with the analysis of the anode impedance[112] and show that there are two dominating impedance features increasing over cycling. One is the increase of the contact resistance between the current collector and the cathode coating, and the other is the formation of an interface graphite adjacent to the separator, caused by an accelerated SEI growth due to the preferential deposition of dissolved manganese ions in the interfacial region (graphite/separator).

Author contributions

All electrochemical measurements were conducted by D.P. D.P., S.S. and J.L. developed the equivalent circuit model. Data analysis was done by J.L. and D.P. The manuscript was written by D.P., J.L. and H.A.G. All authors discussed the data and commented on the results.

An Analysis Protocol for Three-Electrode Li-Ion Battery Impedance Spectra: Part II. Analysis of a Graphite Anode Cycled vs. LNMO

Daniel Pritzl,[=,*] Johannes Landesfeind,[=,*,z] Sophie Solchenbach, and Hubert A. Gasteiger[**]

Chair of Technical Electrochemistry, Department of Chemistry and Catalysis Research Center, Technical University of Munich, Munich, Germany

Lithium-Ion batteries consisting of LNMO ($LiNi_{0.5}Mn_{1.5}O_4$) cathodes and graphite anodes show severe capacity fading at elevated temperatures due to a damage of the solid electrolyte interface (SEI) on the anode. Hence, a detailed investigation of the anode with electrochemical impedance spectroscopy (EIS) can provide valuable insight into the phenomenon of anode degradation. In this study, we use a modified version of our novel impedance procedure (Part I of this study), where the anode impedance is measured at non-blocking conditions (10% SOC) and blocking conditions (0% SOC) in a graphite/LNMO full-cell with a gold wire micro-reference electrode (GWRE). We show that during cycling an ionic contact resistance ($R_{Cont.Ion}$) at the separator/anode interface evolves, which is most likely caused by manganese dissolution from the high-voltage cathode (LNMO). By simultaneously fitting EIS spectra in blocking and non-blocking conditions, we can deconvolute the anode impedance evolving over 86 cycles at 40°C into contributions of: a) the separator resistance ($R_{Sep.}$), b) the true charge transfer resistance (R_{CT}), and, c) the ionic contact resistance ($R_{Cont.Ion}$) evolving at the separator/anode electrode interface. We also show that the main contributor to a rising anode impedance is the ionic contact resistance ($R_{Cont.Ion}$).

 [DOI: 10.1149/2.0461810jes]

Manuscript submitted April 25, 2018; revised manuscript received June 25, 2018. Published July 11, 2018. This was Paper 402 presented at the Seattle, Washington Meeting of the Society, May 13–17, 2018.

In view of the growing concerns with regards to cobalt supply constraints for Lithium-Ion batteries,[1] $LiNi_{0.5}Mn_{1.5}O_4$ (LNMO) as cathode active material with a theoretical energy density of ≈690 Wh/kg_{LNMO}[2] is an interesting alternative for Co-free Lithium-Ion batteries. However, graphite/LNMO cells do suffer from a drastic capacity decay when cycled at elevated temperatures (> 40°C),[3–5] which is related to electrochemical electrolyte oxidation[6] followed by transition metal dissolution (both manganese and nickel) from the spinel cathode,[5,7] ultimately leading to a loss of active lithium on the graphite anode due to ongoing SEI formation.[3,5] As the degradation of the graphite anode is a key failure mechanism of graphite/LNMO cells, a detailed impedance analysis of the anode in graphite/LNMO full-cells is necessary to better understand this degradation process, particularly at elevated temperatures.

In the literature, there are several approaches in order to investigate the anode impedance. One type of studies focuses on the solid electrolyte interface (SEI) formation on graphite anodes and model setups in order to investigate the formation of the SEI.[8–11] The impedance is recorded at different potentials during lithiation of a graphite anode and the impedance response is generally fitted with two R/C (resistor/capacitor) or R/Q (resistor/constant phase element) elements connected in series, representing the charge transfer resistance and the SEI resistance. In these studies the graphite impedance is measured versus the lithium metal counter electrode in a two-electrode configuration, despite the fact that the lithium metal anode dominates the EIS response due to its small surface area[12] and thus obviously prevents a rigorous analysis of the graphite electrode impedance. Another type of studies uses a symmetric cell approach in order to deconvolute the anode impedance from the full-cell impedance.[13,14] However, as the symmetric cell approach is a destructive method, the determination of the anode (or cathode) impedance as a function of the number of charge/discharge cycles or of the state-of-charge (SOC) requires the testing/cycling of a large number of cells. A third group of papers uses micro-reference electrodes, where a deconvolution of the anode impedance from the full-cell impedance is possible during cycling without disassembly of the cells (contrary to the symmetric cell approach).[12,15,16] Here the reference electrode has to fulfill certain criteria, as for example being centered between two separators[17] and being thin relative to the separator thickness.[18] Yet, also the deconvolution into separate impedances for anode and cathode do not suffice to fully understand the origin of the anode impedance buildup as the characteristic frequencies overlap. In summary, in order to quantify the evolution of the impedance of an individual electrode with cycle number and/or SOC in the absence/presence of additives, either a micro-reference electrode must be incorporated or the more cumbersome symmetric cell approach must be used.

In a previous study of our group[19] we analyzed the impedance of an LNMO cathode in graphite/LNMO full-cells, where we introduced a new method based on determining the LNMO impedance in non-blocking conditions (i.e., at ≈4.4 V cell voltage (≈10% SOC) under open-circuit conditions) and in blocking conditions (i.e., holding the cell voltage at 4.9 V cell at 100% SOC) utilizing a micro-reference electrode (GWRE[12]). We were able to deconvolute the total LNMO cathode impedance ($R_{Cathode}$) evolving over 86 charge/discharge cycles into contributions of: (i) a contact resistance between the current collector and the LNMO electrode ($R_{Cont.}$), (ii) the true LNMO charge transfer resistance (R_{CT}), and, (iii) the ionic resistance of the electrolyte within the LNMO cathode pores (R_{Pore}). This deconvolution was possible, as from the spectrum in blocking conditions (i.e., in the absence of faradaic reactions, as the cathode does not contain lithium) the pore resistance could be obtained unambiguously from the 45° transmission line feature, clearly separated in frequency space from the charge transfer resistance feature, which under this condition is shifted to very low frequencies in the impedance spectrum. By simultaneously fitting both the blocking and non-blocking spectra with a general transmission line model (TLM), a deconvolution of the various above described resistance contributions with very low uncertainties was possible.

Here we will apply our impedance analysis concept to study the impedance evolution of a graphite anode in a full-cell over extended charge/discharge cycling. Our approach will be to measure the impedance of the graphite anode either in a graphite/LFP cell or in a graphite/LNMO cell at low full-cell voltages (≈1.7 −1.9 V vs.

[=]These authors contributed equally to this work.
[*]Electrochemical Society Student Member.
[**]Electrochemical Society Fellow.
[z]E-mail: j.landesfeind@tum.de

Li/Li^+) where the graphite anode in the cell is in its fully delithiated state, demonstrating that blocking electrode behavior can be achieved for the graphite anode. Over the course of 86 charge/discharge cycles of a graphite/LNMO full-cell at 40°C, we observe the appearance of a high-frequency semi-circle in the graphite blocking impedance spectra, which we will ascribe to the formation of a resistive region at the anode/separator interface, likely induced by manganese dissolution from the cathode. Further insights into the evolving anode impedance in a graphite/LNMO full-cell will be gained by simultaneously fitting the impedance spectra for a given cycle to a general transmission line model under both blocking conditions (at a full-cell voltage of 3.0 V_{FC}, i.e., when graphite is fully delithiated) and non-blocking conditions (at 4.4 V_{FC}, i.e., when graphite is partially lithiated), which enables us to clearly deconvolute the overall anode impedance. Last, we will show the overall impedance of a graphite/LNMO full-cell and provide a detailed analysis of the various impedance contributions from anode and cathode over the course of extended charge/discharge cycling at 40°C.

Experimental

Electrode preparation.—$LiNi_{0.5}Mn_{1.5}O_4$ (LNMO) electrodes were prepared by mixing LNMO (BASF SE, Germany), carbon black (Super C65, Timcal), and polyvinylene difluoride (PVdF, Kynar) at a mass ratio of 92/5/3 with NMP (N-methyl pyrrolidone, anhydrous, Sigma-Aldrich, Germany) in a planetary mixer (Thinky Corp.) for 15 min. The ink was coated onto aluminum foil (MTI, 18 μm) with a doctor blade coater and dried afterwards at 50°C in a convection oven for at least 3 h. The final LNMO coating had a loading of ≈13.6 mg_{LNMO}/cm^2, corresponding to ≈1.9 mAh/cm^2. Electrodes with a diameter of 11 mm (≡0.95 cm^2) were punched out and compressed to ≈32% porosity with a KBr press (Mauthe, PE-011). $LiFePO_4$ (LFP) electrodes with a mass ratio of 93/4/3 (LFP/PVdF/carbon black) were prepared using the same mixing- and coating procedure as for the LNMO cathodes. The final loading was ≈16.5 mg_{LFP}/cm^2, corresponding ≈2.0 mAh/cm^2, and the cathodes (11 mm diameter) were compressed to a porosity of 30%.

Graphite electrodes were prepared by mixing graphite (T311, SGL Carbon, Germany) and PVdF at a mass ratio of 95/5 with NMP by applying the same procedure as for the positive electrodes. The graphite ink was coated onto copper foil (MTI, ∼12 μm) and dried in a convection oven at 50°C for 3 h. The loading of the graphite coating was ≈6.6 $mg_{graphite}/cm^2$ corresponding to ≈2.3 mAh/cm^2. The electrodes were punched out with a diameter of 11 mm and compressed to a porosity of ≈32%. All electrodes were dried under dynamic vacuum at 120°C for at least 12 h in a vacuum oven (Büchi, Switzerland) and then transferred into an Argon-filled glove box (MBraun, Germany) without exposure to air.

Cell assembly and battery testing.—T-cells (Swagelok, U.S) were assembled in an Argon-filled glove box (< 0.1 ppm O_2 and H_2O, MBraun, Germany) and dried beforehand in a 70°C convection oven. The graphite anode and the LNMO or LFP cathodes were assembled into a cell with two glass fiber separators (glass microfiber filter, 691, VWR Germany). As electrolyte, 60 μL of LP57 (1 M $LiPF_6$ in EC/EMC 3:7 w:w < 20 ppm H_2O, BASF SE, Germany) were used. Between the separators a gold wire micro-reference electrode (GWRE) was placed (the detailed assembly procedure can be found in Reference 12). The GWRE was lithiated in the fully assembled cell with a constant current of 150 nA for 1 h at 40°C (note that the amount of lithium provided by the cathode for charging of the GWRE (0.15 μAh) is negligible compared to the total lithium inventory (≈1.9 mAh)). While the pure noble metal gold wire is not a suitable reference electrode for the lithium ion containing organic electrolytes, the in-situ lithiation forms a lithium-gold alloy with a very stable potential of ≈0.31 V versus metallic lithium.[12] In the present study, the transition metal dissolution from the cathode leads to a gradual delithiation of the lithiated GWRE. Although the GWRE can be lithiated again[20] to obtain a good reference electrode, in the present study the GWRE is only used as a pseudo reference (i.e., only for EIS measurements not for referencing potentials). Due to the electrochemical electrolyte oxidation on LNMO cathodes, protic species and other electrolyte oxidation fragments are produced[21] which apparently cause a gradual delithiation of the lithiated GWRE, leading to a loss of its stable reference potential after several cycles.[20] However, as shown in Part I of this publication,[19] the potential drift of the GWRE is smaller than < 0.4 mV over the course of a full impedance measurement, and hence this drift does not affect the EIS measurements with an AC perturbation of 15 mV. This means that over cycling the lithiated GWRE acts as a pseudo-reference electrode with an undefined potential. In order to convert the full-cell potential (graphite/LNMO) into a half-cell potential (graphite/Li) identical T-cells were assembled with a lithium metal reference electrode.

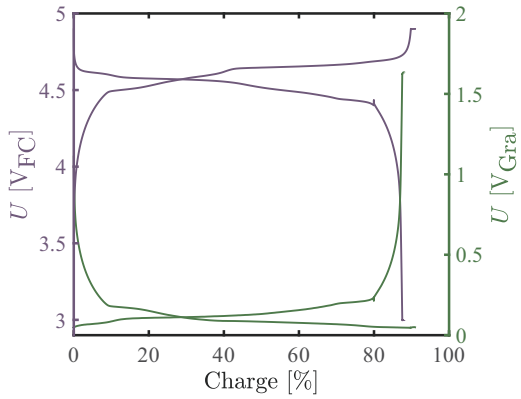

Figure 1. Charge/discharge potential profiles of the first cycle at C/2 (after formation) of a LNMO/graphite cell at 40°C equipped with a lithium reference electrode. The graphite anode potential is shown in green color with the corresponding right y-axis, while the potentials of the cathode is depicted by the left hand y-axis. Impedance spectra were recorded at the end of charge/discharge in blocking condition as well as after the full-cell potential of the LNMO/graphite cell reached 4.4 V after one hour of OCV phase.

The cycling procedure is identical to the cells cycled in Reference 19. The full-cells (graphite/LNMO) were cycled between 3.0 and 4.9 V_{FC} (full cell voltage). Two formation cycles were carried out at 25°C with a C-rate of C/10 (1/h) by applying a CCCV charge (constant current followed by a constant voltage) with a current limit of C/20 for the CV phase as well as a CC discharge. The subsequent extended charge/discharge cycling was carried out with C/2 at 40°C with a CCCV charge to 4.9 V_{FC} (current limit for CV = C/40) and a CCCV discharge to 3.0 V_{FC} (current limit for CV = C/100); the CV step at the end of discharge is required to bring the graphite anode into blocking conditions. The impedance was recorded at OCV (open circuit voltage) in non-blocking conditions at 4.4 V_{FC} after a 1 h OCV period as well as in blocking conditions at 3.0 V_{FC} ($E_{Gra} \approx$ 1.7 V_{Li}) during a constant voltage hold and after the current had dropped below C/100. The impedance was recorded from 100 kHz to 100 mHz with a perturbation of 15 mV (acquisition time of 10 min/spectrum). Figure 1 shows the graphite/LNMO full cell potential (in purple) and the graphite versus metallic lithium potential (in green) during charge and discharge (C/2 at 40°C).

Graphite/LNMO cells for reaching blocking conditions were conditioned the following (data shown in Figure 2): Formation (2 cycles at C/10 and 25°C) was carried out and afterwards the cell was charged to the upper cutoff potential of 4.9 V_{FC} (at C/2 and 40°C) and during the subsequent discharge (3 min at C/20 and 40°C) the impedance was recorded under open-circuit potential. Once the lower cell cutoff potential of 3.0 V_{FC} ($E_{Gra} \approx$ 1.7 V_{Li}) was reached the impedance was measured around this potential.

Graphite/LFP cells were also equipped with a GWRE and two formation cycles were carried out at C/10 at 25°C with a CCCV charge to 4.0 V_{FC} (current limit of C/20) and a CC discharge to 2.0 V_{FC}. After formation, five cycles at C/2 and 40°C from 1.5 V_{FC}

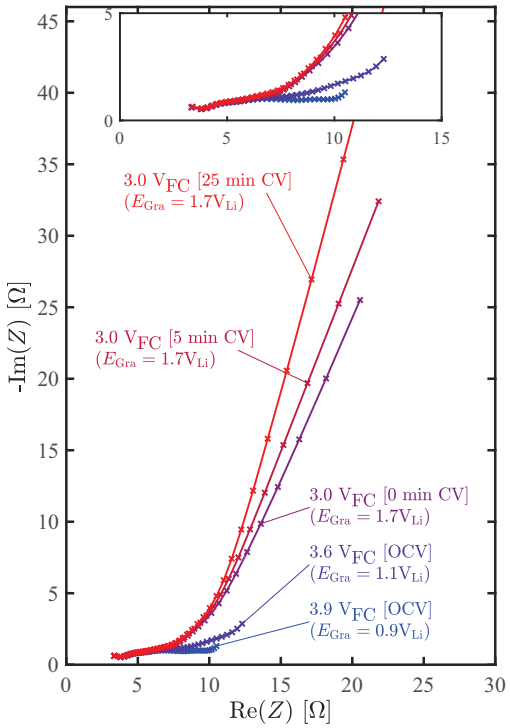

Figure 2. Graphite anode impedance spectra measured with a micro-reference electrode (GWRE) in a graphite/LNMO cell. The impedance spectra shown at 3.9, 3.6, and 3.0 V_{FC} are recorded under open circuit conditions (labeled as [OCV]) and those at 3.0 V_{FC} while holding a constant voltage (CV-hold) for either 5 or 25 minutes (labeled as [# min CV]). The graphite potentials vs. Li/Li^+ (E_{Gra}) are also shown by the graph labels; the values were obtained from measurements conducted in an identical T-cell equipped with a lithium metal reference electrode flag. The impedance is recorded at 40°C from 100 kHz to 100 mHz with a perturbation of 15 mV.

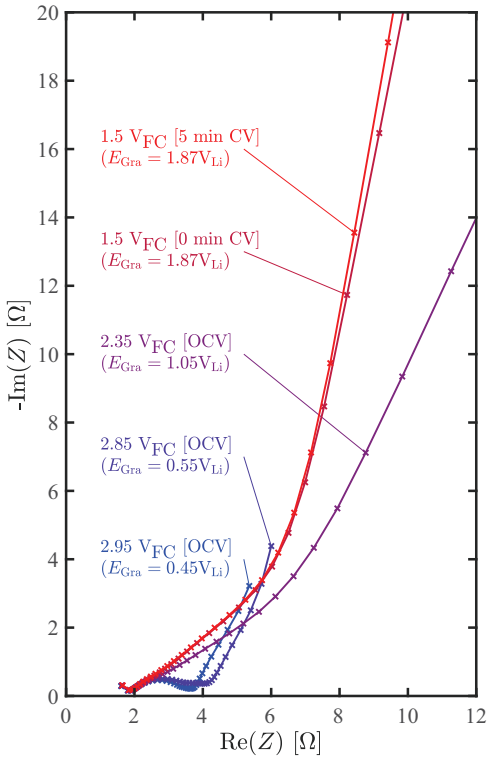

Figure 3. Graphite anode impedance spectra measured with a micro-reference electrode (GWRE) in a graphite/LFP cell. The impedance spectra shown at 2.95, 2.85, and 2.35 V_{FC} are recorded under open circuit conditions (labeled as [OCV]), and those at 1.5 V_{FC} are recorded while holding a constant potential (CV-hold) for either 0 or 5 minutes (labeled as [# min CV]). The graphite potentials vs. Li/Li^+ (E_{Gra}) is also shown by the graph labels; its values were obtained from the GWRE (see text). The impedance is recorded at 40°C from 100 kHz to 100 mHz with a perturbation of 15 mV.

and 4.0 V_{FC} were conducted and the impedance was recorded at 1.5 V_{FC} ($E_{Gra} \approx 1.87$ V_{Li}) under constant voltage conditions, after the current dropped below C/100.

For the cells reaching blocking conditions for a graphite anode cycled versus LFP (data shown in Figure 3) the following procedure was used: After two formation cycles at C/10 and 25°C and one charge to 4.0 V cell voltage (C/2 and 40°C), the graphite/LFP cell was discharged (C/20, delithiation of the graphite anode) and impedance spectra were recorded every 2 min in open circuit condition and after 0 and 5 minutes of CV phase when the potential reached 1.5 V_{FC} ($E_{Gra} \approx 1.87$ V_{Li}).

As electrolyte, 60 µL of either LP57 (1M $LiPF_6$ in EC/EMC 3:7 w:w < 20 ppm H_2O, BASF SE, Germany) or LP57 with 50 or 100 mM $Mn(TFSI)_2$ (Solvionic, France) were used.

Results and Discussion

Blocking conditions for a graphite anode cycled vs. LFP or LNMO at 40°C.—In Part I of this study,[19] we successfully deconvoluted the impedance contributions from contact resistance ($R_{Cont.}$), porous electrode resistance (R_{Pore}), and charge transfer resistance (R_{CT}) of an LNMO cathode by simultaneous analysis of recorded impedance spectra in blocking and non-blocking configuration for the LNMO cathode. To apply this technique to a graphite anode (or any electrode for this matter), it is necessary to check if blocking conditions can be obtained. Blocking conditions imply that the charge transfer reaction resistance is getting very large (ideally infinite), so that the corresponding impedance feature will be moved to very low frequencies, which allows for an unambiguous interpretation of the remaining impedance contributions.

To check at which potentials blocking conditions of the graphite anode can be reached in a full-cell, a graphite/LNMO cell with a gold wire micro-reference electrode (GWRE) was assembled and two formation cycles were done at C/10 at 25°C. Afterwards the cell was charged to the upper cutoff potential of 4.9 V_{FC} cell voltage (at C/2 and 40°C) and during the subsequent discharge steps (each 3 min at C/20 and 40°C) the impedance was recorded under open-circuit potential. Once the lower cell cutoff potential of 3.0 V_{FC} was reached the impedance was measured around this potential. The spectra are shown in Figure 2. At 3.9 V_{FC}, which corresponds to a graphite potential of ≈0.9 V vs. Li/Li^+, the impedance spectrum conducted at OCV consists of a suppressed semi-circle and a 45° Warburg branch (blue line). During subsequent discharge of the full-cell (nearly complete delithiation of the anode) to 3.6 V_{FC} (graphite at ≈1.1 V vs. Li/Li^+) and 3.0 V_{FC} (graphite at ≈1.7 V vs. Li/Li^+), the impedance spectra taken at OCV show a significant increase of the imaginary part of the impedance at low frequencies, which indicates a significantly increased charge transfer resistance. When the cell potential is held at 3.0 V_{FC} (graphite at ≈1.7 V vs. Li/Li^+) for 5 min. (dark red line) or 25 min., lithium reintercalation into the graphite anode is completely suppressed, as can be seen from the now nearly vertical straight line at low frequencies, i.e., blocking conditions are achieved. At the same time, at medium frequencies a 45° transmission line can be observed in Figure 2, from which the ionic resistance within the porous graphite (R_{Pore}) anode can be determined.[22] The points at the lowest measured frequencies (100 mHz) shift toward higher values on the (negative) imaginary axis with increasing length of the constant voltage phase, which is analogous to what was observed when putting an LNMO cathode under blocking conditions.[19] At high frequencies (left in the Nyquist plot), a strongly depressed semi-circle is present in the anode blocking spectra (see inset of Figure 2). This suppressed semi-circle is

already apparent directly after formation of the LNMO/graphite cells and will be analyzed in detail below.

To investigate whether the anode impedance depends on the cathode active material via a cross-talk mechanism,[23] the above experiments were repeated with a graphite/LFP full-cell. After two formation cycles at C/10 and 25°C and one charge to 4.0 V cell voltage (C/2 and 40°C), the graphite/LFP cell was discharged (C/20, delithiation of the graphite anode) and impedance spectra were recorded every 2 min in open circuit condition and after 0 and 5 minutes of CV phase when the potential reached 1.5 V_{FC}. Figure 3 shows the anode impedance spectra of a graphite/LFP cell measured at different voltages. The potential versus metallic lithium (V_{Li}) was obtained from the known potential of the lithiated GWRE (≈ 0.31 V vs. Li/Li$^+$), which for an LFP cathode remained stable over hundreds of cycles.[12] At a graphite potential of 0.45 V_{Li} (≈70% SOC) and 0.55 V_{Li} (≈80% SOC), the impedance spectrum consists of one suppressed semi-circle, which includes contributions from both the charge transfer resistance and the SEI resistance (R_{CT} and R_{SEI}) as well as of a 45° Warburg diffusion branch representing lithium ion concentration gradients within the separator. By further delithiating the graphite anode (see spectrum at 1.05 V_{Li}) the semi-circle turns into a ≈40° line and the points at lower frequencies show the typical onset of the transition into blocking conditions, as at 1.05 V_{Li} lithium reintercalation into graphite becomes thermodynamically unfavorable. By going to a graphite potential of 1.87 V_{Li}, i.e., to a similar high anode potential at which blocking conditions were observed for the graphite/LNMO cell (see spectra at 1.7 V vs. Li/Li$^+$ in Figure 2), the graphite anode impedance spectra after 0 and 5 minutes CV phase also show a blocking electrode behavior, as one would expect. However, for the graphite anode in a graphite/LFP cell (see Figure 3) the 45° transmission line region is clearly pronounced and unperturbed up to the highest measured frequency (100 kHz), while for the same procedure the graphite impedance in the graphite/LNMO cells shows a depressed semicircle at high frequencies (see inset in Figure 2). The origin of this difference will be examined further below. Please note that a cutoff in the graphite/LNMO cell of 3.0 V_{FC} gives an anode potential of ≈1.7 V vs. Li/Li$^+$ and a cutoff in the graphite/LFP cell of 1.5 V_{FC} an anode potential of ≈1.87 V vs. Li/Li$^+$. As the graphite potential is very steep starting from 1.0 V vs. Li/Li$^+$ (see Figure 1) we are sure that both anode potentials (from the LNMO and LFP cells) are well comparable.

Graphite impedance evolution over charge/discharge cycling of graphite/LNMO cells at 40°C.—In the following section, we want to analyze both blocking and non-blocking impedance spectra of a graphite anode in a graphite/LNMO full-cell over the course of 86 charge/discharge cycles and investigate the evolution of the suppressed semi-circle at higher frequencies with cycling (a feature which above was shown to be absent when cycling a graphite anode with an LFP cathode). The cycle dependent Nyquist plots for the anode under non-blocking (at 4.4 V_{FC} corresponding to ≈10% SOC, Figure 4a) and blocking conditions (the current dropped below C/100 during the CV phase at 3.0 V_{FC}, Figure 4b) are shown for the 1st, 25th, 50th and 75th cycle at C/2 (≡0.95 mA/cm^2) and 40°C. The capacity retention of this cell is shown in Figure 4 of Part I of this study.[19] For the spectra in non-blocking conditions (Figure 4a)), the impedance spectrum consists of the separator resistance (high-frequency resistance, HFR) and a semi-circle, which is a convolution of the charge transfer resistance, the SEI resistance, and the pore resistance. At lowest frequencies, a 45° line for the Warburg diffusion is observable. The diameter of the semi-cirlce increases from ≈2 Ωcm^2 (cycle 1 after formation) to ≈15 Ωcm^2 (cycle 75 afterformation). The capacitance obtained from a constant-phase element (Q) fit after 25 cycles is 8.9 mF $\cdot$ s$^{(\alpha_{CT}-1)}$/cm$^2_{geo.}$ (normalized to the geometric area of the electrode), with the constant-phase element exponent value of α_{CT}≈ 0.75. To a first order approximation, this can be approximated with a real capacitance of 8.9 mF/cm$^2_{geo.}$; if referenced to the roughness factor of the graphite anode (30 cm$^2_{BET}$/mg$_{graph.}$ × 6.6 mg$_{graph.}$/cm$^2_{geo.}$ ≈ 200 cm$^2_{BET}$/cm$^2_{geo.}$), this yields a BET surface normalized capacitance of ≈ 4.5 μF/cm$^2_{BET}$, which is reasonably consistent with the electrochemical double-layer capacitance of graphite. In consequence the semi-circle observed in non-blocking conditions results from a resistance occurring everywhere in the graphite anode.

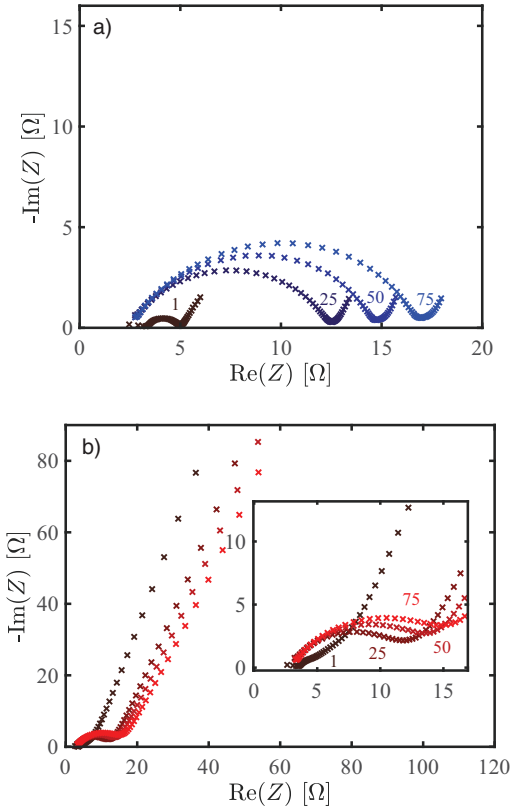

Figure 4. Evolution of the impedance spectra of the graphite anode (cycle numbers 1, 25, 50 and 75 as marked in the figure) during cycling of an LNMO/graphite cell at a rate of C/2 at 40°C: a) at 4.4 V_{FC} in non-blocking conditions at 10% SOC (EIS recorded at OCV after 1 h OCV period); b) after a potential hold at 3.0 V_{FC} under blocking conditions at 100% SOC (recorded at a controlled potential of 3.0 V_{FC} after a potential hold at 3.0 V_{FC} until the current dropped below C/100). Potential controlled EIS spectra were recorded with an amplitude of 15 mV in the frequency range from 100 kHz to 100 mHz.

The blocking spectra (Figure 4b) show a slightly distorted transmission line after the first cycle (convolution of a semi-circle at high frequencies and a 45° line at medium frequencies), followed by the onset of a very large charge transfer resistance which indicates blocking behavior. After 25 cycles, the blocking spectra show a distinct semi-circle with a diameter of ≈10 Ωcm^2, which increases to ≈15 Ωcm^2 after 75 cycles. A semi-circle under blocking conditions (no faradaic process during the impedance measurement) has so far only been observed if there is a contact resistance ($R_{Cont.}$) between an aluminum current collector and a cathode coating.[19,24,25] However, for a graphite anode coated on a copper collector – both materials being excellent electronic conductors – we do not expect a contact resistance between the current collector and the anode coating. Also, in graphite/LFP cells cycled at 40°C (data not shown in here), no semi-circle evolves in the graphite anode blocking spectra. Further insights might be gained by examining the capacitance associated with this semi-circle. Its constant-phase capacitance after the 25th cycle is ≈ 73 μF $\cdot$ s$^{(\alpha_{blocking}-1)}$/cm$^2_{geo.}$ (with $\alpha_{blocking}$ ≈ 0.74), which is two orders of magnitude lower compared to the semi-circle capacitance in the respective non-blocking spectrum discussed above. If this value was used to estimate the double-layer capacitance of the graphite surface as done above, this would yield a double-layer capacitance of 0.4 μF/cm$^2_{BET}$, which clearly is too low and suggests that this resistance dervives from only a fraction of ≈10% of that of the entire graphite area, e.g., only from a layer of the anode which corresponds

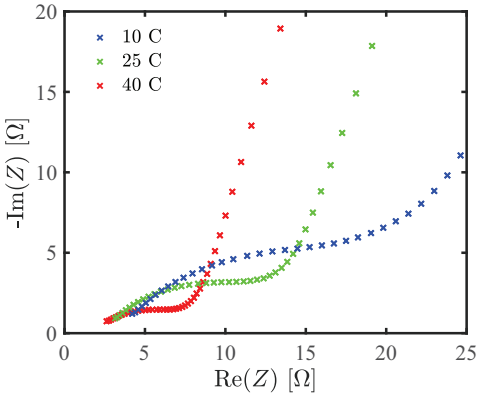

Figure 5. Impedance spectra of a graphite anode measured versus the GWRE in a graphite/LNMO cell after formation (two cycles at C/10 and 25°C) and 5 cycles at C/2 (40°C). The impedance is recorded at 10°C, 25°C and 40°C in blocking conditions (3.0 V_{FC} potential hold after a CV phase at 3.0 V_{FC} with a current limit of C/100). The impedance is measured from 100 kHz to 100 mHz with a perturbation of 15 mV. Before starting the measurement, an open-circuit period (1 h) at the specific temperature is carried out to ensure thermal equilibration.

to ≈10% of its thickness. It is emphasized that a similar double layer capacitance as in non-blocking conditions (≈ 4.5 $\mu F/cm^2_{BET}$) would be expected in blocking conditions if the origin of the resistance would occur everywhere in the graphite anode. A possible explanation for the localized effect might be type of high-resistance region at the top-layer of the anode adjacent to the separator which was suggested by Burns et al.[26] In the next section, we will further examine the origin for this semi-circle in the graphite anode blocking impedance spectra.

Origin of the high frequency semi-circle in the graphite impedance spectra under blocking conditions in graphite/LNMO cells.—In order to elucidate the physical origin of the high frequency semi-circle in blocking conditions (Figure 4b), temperature-dependent EIS measurements of a graphite/LNMO cell with a GWRE were recorded in blocking conditions (3.0 V_{FC}) after formation (two C/10 cycles at 25°C) and five subsequent C/2 charge/discharge cycles at 40°C. The impedance was measured at 10°C (blue points), at 25°C (green points), and at 40°C (red points) in order to discriminate its origin to be of electronic or ionic nature (see Figure 5). The diameter of the suppressed semi-circle increases from ≈9 Ωcm^2 at 40°C to ≈14 Ωcm^2 at 25°C and ≈22 Ωcm^2 at 10°C. From this data, the apparent activation energy is calculated using the Arrehnius equation. A similar analysis examining several types of resistances occuring in porous electrodes was done by Ogihara et al.[27] We find an apparent activation energy of ≈9 kJ/mol, which is close to the value for ionic resistances according to Ogihara et al.[27] (≈16 kJ/mol) and differs largely from the expected activation energy of electronic processes (≈0.8 kJ/mol from Ogihara et al.[27]). In principle, there are three options where this interface can be allocated: a) the current collector/coating interface, b) the surface of the active material, or c) the coating/separator interface. The three interfaces can be distinguished distinctly by their activation energies and capacitances. For case a), the resistance would be an electron conduction resistance and one would expect a small activation energy (< 1 kJ/mol)[28] and an active surface area of ≈1 cm^2 corresponding to the current collector surface area. Thus, a typical double layer capacitance of non-aqueous electrolytes of ≈5 $\mu F/cm^2$, a capacitance of ≈5 $\mu F/cm^2_{geo.}$ would be expected, which should be consistent with the value obtained from the analysis of the semicircle peak frequency. However, the capacitance of this newly formed interface is 73 $\mu F/cm^2_{geo}$, so that case a) cannot be true. For case b), the activation energy should correspond to a charge transfer reaction (on the order to ≈50–60 kJ/mol)[28] and the capacitance of the observed semicircle should be on the order of 10 $mF/cm^2_{geo.}$ based on a typical double layer capacitance of 5 $\mu F/cm^2_{geo.}$ and a roughness factor of ≈ 200 cm^2_{BET}/cm^2_{geo} (based on a loading of ≈6.6 $mg_{graphite}/cm^2$ and a graphite BET surface area of 3 m^2/g, as shown in the previous section). Thus, case b) is neither consistent with the obtained capacitance nor with the observed activation energy (9 kJ/mol). In case c) the activation energy should correspond to a value typical for ionic conduction in the electrolyte (≈ 10–20 kJ/mol)[28] which is consistent with the data; in this case, the observed capacitance would suggest a thickness of this coating/separator interface layer of ≈10% of the anode electrode thickness. The formation of such a layer has also been hypothesized previously in order to explain the observed roll-over fading.[26]

Burns et al.[26] explained the rapid capacity drop after extended cycling (>700 cycles) of 18650-sized graphite/NMC111 cells with a crosstalk phenomenon: electrolyte oxidation products from the cathode, which diffuse to the anode and are reduced on top of the graphite anode in the vicinity of the separator (i.e., at the anode/separator interface region). They suggested that after significant reaction of crosstalk species at this region, a sufficiently thick and dense layer would form in the anode electrode in this region, slowing down ion transport in the electrolyte phase and thus lowering the maximum C-rate at which the cell can be cycled. These conclusions were drawn from SEM top-view images of the anode/separator interface before and after cycling. For LNMO cathodes it is well known that transition metal dissolution[7] (e.g., manganese dissolution) and subsequent deposition on the anode is a key failure mechanism of these cells, especially when cycled at elevated temperatures. Hence, a deposition of manganese at the anode/separator interface region accompanied by excessive SEI growth[29–31] could lead to a region of low porosity in the graphite electrode layer adjacent to the separator and thus to a locally increased ionic resistance in the electrolyte phase. If so, this would be the most likely origin of the semi-circle in the anode blocking impedance spectra.

In order to prove this hypothesis, graphite/LFP cells (where no transition metal dissolution occurs under typical cycling conditions) were prepared without and with a defined amount (50 or 100 mM) of deliberately added $Mn(TFSI)_2$ salt to mimic the transition metal dissolution in LNMO/graphite cells. Formation of the graphite/LFP cells was done by two cycles at C/10 and 25°C from 2.0 V_{FC} to 4.0 V_{FC}. After formation, five cycles at C/2 and 40°C from 1.5 V_{FC} and 4.0 V_{FC} were recorded and the impedance was measured at 1.5 V_{FC} ($E_{Gra.}$ ≈ 1.87 V_{Li}) under constant voltage conditions, after the current dropped below C/100. Three types of cells were investigated: (i) graphite/LFP cells cycled in pure LP57 electrolyte; (ii) graphite/LFP cells which first underwent formation in metal-free LP57 electrolyte, then were opened in an Ar-filled glove box, and finally reassembled with fresh separators and LP57 to which 50 mM $Mn(TFSI)_2$ has been added; and, (iii) graphite/LFP cells prepared as in (ii) but with LP57 with 100 mM $Mn(TFSI)_2$ as the final electrolyte. Figure 6 shows the spectra in blocking configuration ($E_{Gra.}$ ≈ 1.87 V_{Li}) after the 5th cycle. The anode impedance spectrum of the cell with pure LP57 (in light blue) shows almost perfect blocking behavior – i.e., a transmission line followed by a capacitive branch (identical to the data in Figure 3). When 50 mM $Mn(TFSI)_2$ were added to a graphite/LFP cell (in purple) the 45° transmission line turns into a distinct semi-circle, expanding to a large semi-circle when the $Mn(TFSI)_2$ concentration is increased to 100 mM (in pink). From these results we conclude that manganese deposition and a concomitant enhanced SEI formation are also the cause for the semi-circle in the blocking anode impedance spectra of the graphite/LNMO cells (see Figure 4b). This in turn implies that transition metals are deposited preferentially in a thin layer within the graphite anode adjacent to the separator, in which an enhanced SEI formation occurs, blocking the electrolyte pores in this region of the graphite electrode (evident from the activation energy typical for ionic conduction). Studies on the analysis of the SEI distribution across the thickness of graphite anodes are currently under way to validate this hypothesis.

Anode impedance spectra fitting of graphite/LNMO cells under blocking and non-blocking conditions.—In the following, graphite

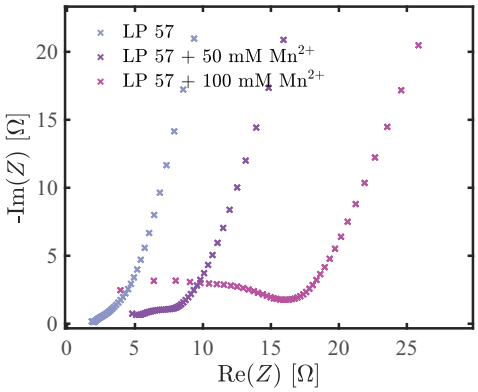

Figure 6. Impedance spectra of a graphite anode measured versus the GWRE in graphite/LFP cells with and without added $Mn(TFSI)_2$ to the electrolyte after formation in metal-free LP57 (2 cycles at C/10 with a CCCV charge and a CC discharge at 25°C). Light blue: 5 cycles at C/2 at 40°C between 1.5–4.0 V_{FC}; purple line: after formation, the cell was reassembled with new separators and refilled with LP57 + 50 mM $Mn(TFSI)_2$ and then cycled 5 times C/2 at 40°C between 1.5–4.0 V_{FC}; pink line: same as for the purple line, except that 100 mM $Mn(TFSI)_2$ were used. The impedance is recorded at 1.5 V_{FC} ($E_{Gra.} \approx 1.87$ V_{Li}) under blocking conditions after the current dropped below C/100 at 40°C.

anode impedance spectra of a graphite/LNMO cell cycled at C/2 and 40°C (see Figure 4) are fitted simultaneously for a given cycle in both blocking and non-blocking conditions, using the equivalent circuit shown in Figure 7. The used equivalent circuit consists of: (i) a separator resistance ($R_{Sep.}$) representing the ionic resistance within the separator (section I of the equivalent circuit given in Figure 7); (ii) an R/Q element for the futheron called "ionic contact resistance" ($R_{Cont.Ion}$), which represents the increased ionic transport resistance of a thin layer in the graphite electrode adjacent to the separator and accounts for the semi-circle evolving in the anode blocking impedance spectra (section II in Figure 7); (iii) the general transmission line model composed of differential elements for the charge transfer resistance (r_{CT}) connected in parallel with the double layer capacitance (q_{CT}), the pure ionic (r_{Pore}) and electrical resistance ($r_{El.}$; here assumed to be negligible compared to r_{Pore}[32] due to the high electronic conductivity of graphite) in the porous anode (R_{Pore}), which is section III in Figure 7; and, (iv) a Warburg diffusion element (W, section IV in Figure 7), accounting for concentration gradients within the separator (discussed in Part I[19] of this study). The interested reader is referred to Ref. 19 for details on the simultaneous fitting procedure. As the 45° transmission line is only observable in the very first cycles (afterwards, the ionic contact resistance ($R_{Cont.Ion}$) dominates in the impedance spectra), the pore resistance is fitted from the spectrum of the first cycle (Figure 4b) using a transmission line model (see Figure 7) without the R/Q element for the ionic contact resistance, and fixed for all the

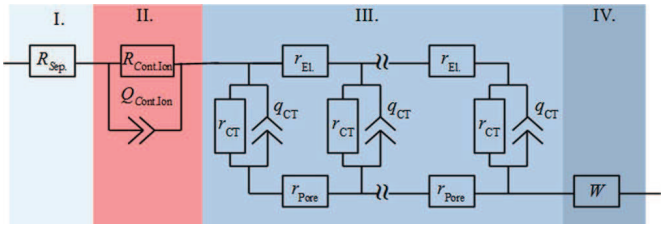

Figure 7. Anode equivalent circuit model with four sections (from left to right): I. separator resistance (R_{Sep}) from the ionic resistance of the separator and the electronic/contact resistances of the cell setup; II. the "ionic contact resistance", representing the increased ionic transport resistance of a thin layer in the graphite electrode adjacent to the separator; III. the general transmission line model (TLM) describing the porous anode electrode; and, IV. a Warburg diffusion element describing concentration gradients within the separator.

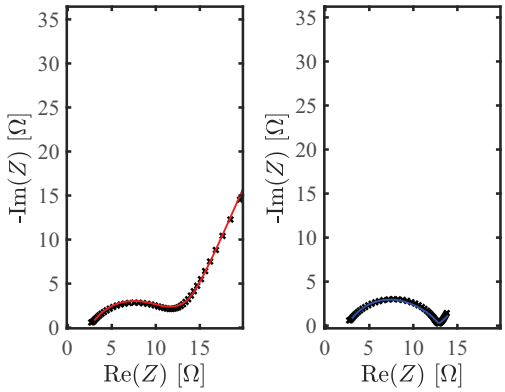

Figure 8. Exemplary fits (shown as solid lines) of the graphite anode impedance in a graphite/LNMO cell after the 30th cycle (at C/2 at 40°C between 3.0–4.9 V_{FC}) in blocking condition (left) at 3.0 V_{FC} and non-blocking conditions at 4.4 V_{FC} corresponding to ≈10% SOC (right). Both spectra are fitted simultaneously using the equivalent circuit shown in Figure 7. AC impedance spectra (black crosses) were recorded at 40°C between 100 kHz and 100 mHz with a perturbation of 15 mV.

subsequent cycles to its 1st cycle value. The obtained 1st cycle pore resistance is ≈10.6 Ωcm^2, with an uncertainy of ±17% (confidence interval based on a 95% standard deviation).

Figure 8 shows one of the exemplary simultaneous fit results of the graphite anode impedance for the 30th cycle. The black crosses in Figure 8a show the EIS data under blocking conditions (3.0 V_{FC} recorded under CV conditions and after the current dropped below C/100, black crosses) and the fit is given by the red line. Figure 8b shows the spectrum under non-blocking conditions (at 4.4 V_{FC} corresponding to ≈10% SOC; recorded at OCV) with experimental data (black crosses) and the corresponding fit (blue line). The following parameters are fitted from the blocking and non-blocking spectrum: $R_{Sep.}$, $R_{Cont.Ion}$, $Q_{Cont.Ion}$, $\alpha_{Cont.Ion}$, $R_{CT\text{-}non\text{-}blocking}$, $R_{CT\text{-}blocking}$, Q_{CT}, α_{CT} and the Warburg element W. The pore resistance (R_{Pore}) and the electronic resistance ($R_{El.}$, assumed as 1 mΩ for the graphite anode) are fixed for all cycles. Table I summarizes the fitting results obtained from simultaneous fitting of the two spectra from cycle 30.

Figure 9 presents the fitting results from simultaneously fitting the blocking and non-blocking spectra for each cycle over 86 cycles. Figure 9a shows the absolute values of the fitted resistances normalized to the geometrical area of the graphite electrode, whereas Figure 9b shows the fitted resistances normalized to their value in the first cycle (R/R_1). The fitted ionic contact resistance ($R_{Cont.Ion}$), which we ascribe to the increased ionic transport resistance of a thin

Table I. Fit parameters of the equivalent circuit in Figure 7 for a simultaneous fit of impedance spectra under blocking conditions ($R_{CT\text{-}blocking}$) and non-blocking conditions ($R_{CT\text{-}non\text{-}blocking}$) taken in cycle 30 (see Figure 8). The geometrical area of the electrode is 0.95 cm^2. The error describes the confidence interval based on a 95% standard deviation (obtained using the confint function in Matlab).

Parameter	Value
$R_{Sep.}$	2.4 Ω ± 16%
$R_{Cont.\ Ion}$	7.3 Ω ± 6.1%
$Q_{Cont.\ Ion}$	90 μF · s$^{(\alpha_{Cont.}-1)}$ ± 21%
$a_{Cont.\ Ion}$	0.74 ± 4.3%
R_{Pore}	10.6 Ω ± 17% (fixed to 1st cycle value)
$R_{El.}$	1 mΩ (fixed)
$R_{CT-non-blocking}$	0.8 Ω ± 19%
$R_{CT-blocking}$	9 · 10^8 Ω
Q_{CT}	6.7 mF · s$^{(\alpha_{CT}-1)}$ ± 3.4%
a_{CT}	0.74 ± 0.50%
W	0.9 Ω/$\sqrt{s}$ ± 31%

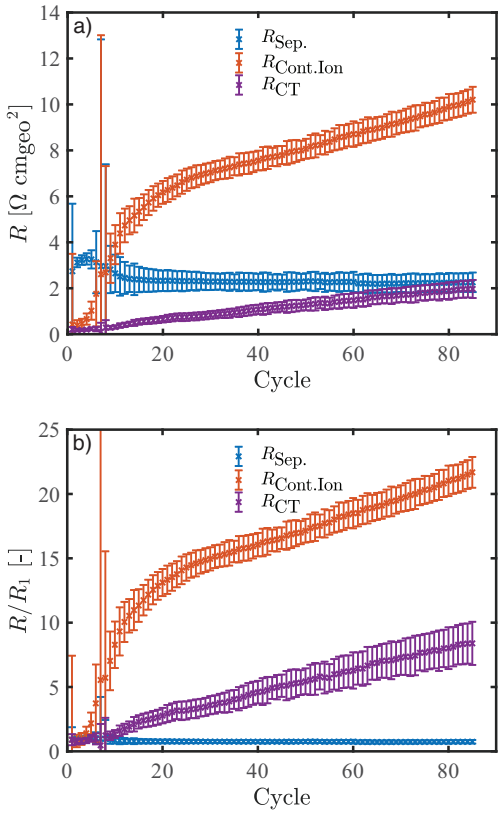

Figure 9. a) Evolution of the high frequency resistance ($R_{Sep.}$), the charge transfer resistance (R_{CT}) and the ionic contact resistance ($R_{Cont.Ion}$) of the graphite anode (normalized to the electrode area) in the LNMO/graphite full-cell over extended charge/discharge cycling between 3.0 and 4.9 V_{FC} at 40°C and C/2. The values are obtained by simultaneously fitting impedance spectra in blocking (4.4 V_{FC}, corresponding to ≈10% SOC) and non-blocking (3.0 V_{FC}) conditions for each cycle. b) Resistances normalized to their initial value after formation. The error bars represent the 95% confidence intervals of the fitted resistances.

layer in the graphite electrode adjacent to the separator is small in the beginning and then increases rapidly to ≈5 Ωcm^2 until cycle 18. Afterwards, it increases only gradually, reaching $R_{Cont.Ion}$ ≈10 Ωcm^2 after 86 charge/discharge cycles at 40°C. The separator resistance ($R_{Sep.}$) has a value of ≈2.4 Ωcm^2 after formation and stays constant during cycling. The charge transfer resistsance (R_{CT}) increases from ≈0.2 Ωcm^2 after formation to ≈2 Ωcm^2 after 86 cycles, which is likely due to a continuous growth of the graphite SEI. The normalized values in Figure 9b show that while $R_{Sep.}$ stays constant during cycling, $R_{Cont.Ion}$ increases by a factor of 20 and the SEI/charge transfer resistance (R_{CT}) increases linearly by a factor of 5. As already stated above, the ionic contact resistance ($R_{Cont.Ion}$) increases very rapidly in the beginning and then flattens out, which could be explained by the following scenario: In the beginning, the deposited manganese ions lead to a strong SEI formation. After several charge/discharge cycles, the insulating SEI layer on the graphite particle surface may be sufficiently thick to slow down preferential manganese deposition near the separator interface, leading to a more homogeneous SEI growth across the anode. Due to the dominating $R_{Cont.Ion}$ a deconvolution of the SEI resistance (covered over the whole graphite electrode) from the charge transfer resistance is not possible. However we are currently trying this deconvolution in graphite/LFP cells with the same blocking/non-blocking approach.[25]

Overview–LNMO/graphite full-cell impedance.—Based on our previous analysis of the LNMO cathode of LNMO/graphite cells[19] and the above investigation of the graphite anode impedance contributions,

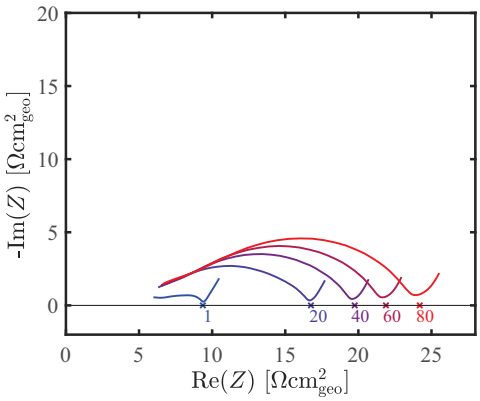

Figure 10. Full-cell impedance spectra of LNMO/graphite cells at 40°C from cycle 1 (blue) to cycle 80 (red; cycle numbers are given in the figure), measured at 4.4 V_{FC} (≈10% SOC), in the frequency range from 100 kHz to 0.1 Hz using an excitation amplitude of 15 mV. Crosses on the x-axis indicate the low frequency extrapolation (LFE, last 3 frequency points) which are shown as $R_{Full-Cell}$ (LFE) in Figure 12.

we are now able to combine all impedance results and compare them to the full-cell spectra.

Figure 10 shows the increase of the LNMO/graphite full cell impedance in non-blocking conditions, i.e., at a full cell potential of 4.4 V_{FC} (≈10% SOC), over the course of cycling. The idea of showing Figure 10 is to exemplify the ambiguity in the impedance analysis of full-cell spectra, which include anode and cathode impedance contributions. The full-cell impedance mainly shows a single smeared out semi-circle in the Nyquist plot, with a low frequency resistance (inflection point) of ≈10 Ωcm^2 in cycle 1 up to ≈25 Ωcm^2 in cycle 80. From the analysis of full-cells measured to higher frequencies (see text in Part I of this study[19]), we could show that the full-cell high frequency resistance equals ≈4.8 Ωcm^2. Based on this known value of the high frequency resistance we were able to show that the full-cell EIS response includes a second R/Q feature at very high frequencies, which could be ascribed to a contact resistance at the interface between the cathode electrode and the aluminum current collector ($R_{Cont.Cath.}$).[19]

Thus, while only two features could be discerned in the full-cell graphite/LNMO impedance spectra, the combined use of a micro-reference electrode (GWRE) and of simultaneously fitting blocking and non-blocking impedance spectra in every cycle, we could successfully disentangle not only the origin of the observed ≈4 fold increase of the full-cell low frequency resistance (note that the separator resistance is invariant at ≈4.8 Ωcm^2) but also quantify the individual resistances.

In order to visualize the disentangled resistance contribution a schematic overview of a graphite/LNMO cell is depicted in Figure 11. The individual resistances are: the ionic resistance in the electrolyte

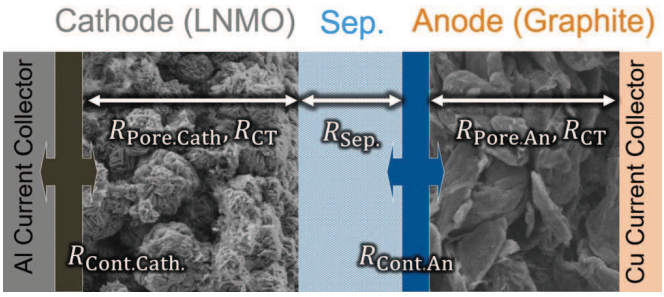

Figure 11. Schematic drawing of a graphite/LNMO cell with (from left to right) the cathode current collector, the porous LNMO electrode, the separator, the porous graphite electrode and the anode current collector. The disentangled resistances are marked in the schematic drawing.

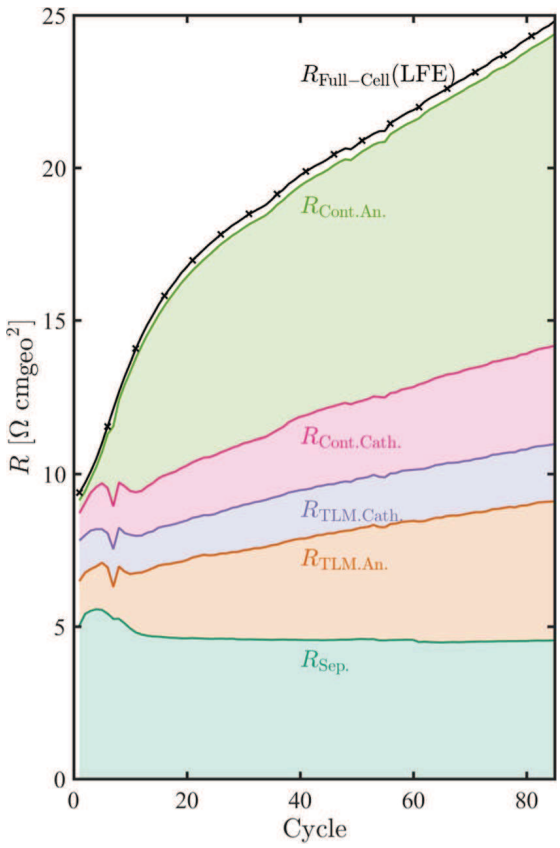

Figure 12. Evolution of the various impedance contributions in a graphite/LNMO full-cell upon extended cycling at C/2 and 40°C. Individual contributions were determined using half-cell impedance spectra obtained by means of a micro-reference electrode (GWRE) in combination with simultaneously fitting two impedance spectra for each cycle, namely one under blocking and one under non-blocking conditions (from bottom to top): (i) the total HFR resistance due to the separator resistance ($R_{\text{Sep.}}$); (ii) the anode resistance described by the transmission line model (TLM), a convolution of R_{Pore} and R_{CT} of the anode ($R_{\text{TLM.An.}}$); (iii) the cathode TLM resistance, a convolution of R_{Pore} and R_{CT} of the cathode ($R_{\text{TLM.Cath.}}$); (iv) the contact resistance at the cathode / current collector interface ($R_{\text{Cont.Cath.}}$); and, (v) the pore resistance in a thin layer of the anode electrode adjacent to the separator ($R_{\text{Cont.Ion}}$ (at the anode)). The extrapolated low frequency resistance of the full-cell impedance is also plotted as a reference ($R_{\text{Full-Cell}}$ (LFE)) and illustrates the good agreement between the half-cell analyses and the full-cell impedance (every fifth cycle indicated by cross, see Figure 10).

phase within anode and cathode pores ($R_{\text{Pore.An.}}$ and $R_{\text{Pore.Cath.}}$), the anode and cathode charge transfer resistance ($R_{\text{CT-non-blocking}}$, evaluated at ≈10% SOC), the contact resistance at the current collector/cathode interface ($R_{\text{Cont.Cath.}}$) and the ionic contact resistance ($R_{\text{Cont.Ion.}}$) in the anode/separator region. The evolution of these resistances over extended charge/discharge cycling of a graphite/LNMO full-cell is summarized in Figure 12.

Figure 12 shows the total separator resistance ($R_{\text{Sep.}}$), mainly remaining constant over the course of 86 cycles, the cathode contact resistance at the cathode/current collector interface[19] ($R_{\text{Cont.Cath.}}$), the pore resistance in a thin layer of the anode electrode adjacent to the separator ($R_{\text{Cont.Ion}}$ (at the anode), described in the previous sections), as well as the resistances obtained from the simplified transmission line model for both anode and cathode ($R_{\text{TLM.An.}}$ and $R_{\text{TLM.Cath.}}$) which include the respective charge transfer and the pore resistances. It is emphasized that the resistance contributions from the ionic resistance with the anode/cathode pores (R_{Pore}) and the respective anode/cathode charge transfer resistance (including the anode SEI resistance) cannot be added individually in this figure (as was done in Figure 9), since these two resistance elements are not serially connected in the transmission line model and, consequently, not additive with regards to the total effective resistance. Therefore, rather than showing R_{Pore} and R_{CT} individually, Figure 12 shows the low frequency resistance of the simplified transmission line model ($R_{\text{TLM}}(f \to 0)$, neglecting electronic resistances) instead of individual values for R_{Pore} and R_{CT}. In the low frequency limit, the simplified transmission line model yields a low frequency resistance of

$$R_{\text{TLM}}(f \to 0) = \frac{\sqrt{R_{\text{Pore}} \cdot R_{\text{CT}}}}{\tanh\left(\sqrt{\frac{R_{\text{Pore}}}{R_{\text{CT}}}}\right)} \quad [1]$$

which is independent of the surface capacitance (Q_{CT}). The reader is referred to the previous section as well as part I of this work[19] regarding the absolute values for pore resistance and charge transfer of the LNMO cathode. Figure 12 shows the full-cell low frequency extrapolation (LFE), here we used the intercept of the linear extrapolation of the last three frequency points (compare Figure 10) with the x-axis. The cumulative sum of all the individual resistance contributions shown in Figure 12 is in very good agreement with $R_{\text{Full-Cell}}$ (LFE) obtained from the full-cell spectra.

In summary, the impedance spectra of full-cells over the course of extended charge/discharge cycling can be analyzed for their individual resistance contributions by means of a micro-reference electrode and the simultaneous fitting of spectra under both non-blocking and blocking conditions (the requirements for the latter are different for different active materials). This approach was shown exemplarily for LNMO/graphite cells in Part I of this work[19] as well as in the current study. It allows to get a profound understanding of the individual aging mechanisms in full-cells based on in-situ impedance measurements, going quite beyond of what would be possible by the symmetric cell diagnostics, where blocking conditions for a given electrode could not be attained. The mechanistic insights which can be obtained by our new approach are illustrated in Figure 9 and Figure 12, revealing the strong impedance buildup at the graphite anode/separator interface which could not have been discerned in the full-cell impedance data (Figure 10) nor in the anode impedance data under the conventionally used non-blocking conditions (Figure 4a). Similarly, the major impedance contribution during the aging of the LNMO cathode in a graphite/LNMO full-cell, viz., the growing contact resistance at the cathode/current collector interface,[19] could not have been detected by the conventional impedance analysis approach. Therefore, we are certain that the application of the presented impedance analysis methodology will help to get a better understanding of the dominant aging mechanisms when cycling full-cells based on a variety of cell chemistries.

Conclusions

Using a gold wire micro-reference electrode (GWRE), the evolution of the graphite anode impedance of a graphite/LNMO is analyzed over the course of 86 charge/discharge cycles at 40°C. First, we show that a graphite anode in a graphite/LFP full cell can be brought into blocking conditions, yielding the expected transmission line mode response which enables a more detailed analysis of the overall graphite impedance. However, when the cathode in the graphite/LFP full-cell is replaced by LNMO, the graphite impedance spectrum under blocking conditions shows an unexpected additional semi-circle at rather high frequencies. This feature evolves over 86 cycles in a graphite/LNMO cell and becomes the dominating contribution to the overall anode as well as to the overall full-cell impedance. By analyzing both temperature-dependent impedance measurements and the effect of the addition of manganese ions to the electrolyte in graphite/LFP cells, we are able to show that the observed semi-circle in the anode impedance spectra can be ascribed to an increased ionic transport resistance within a thin layer in the graphite electrode adjacent to the separator. By fitting simultaneously the impedance spectra for each given charge/discharge cycle under both blocking and non-blocking spectra with a general transmission line model (TLM), the anode impedance can ultimately be deconvoluted into its contributions

from the ionic transport resistance in the separator ($R_{Sep.}$), from the interfacial charge transfer/SEI resistance, and from this newly measured ionic resistance at the anode/separator interface.

Acknowledgment

Financial support by the BASF SE through its Research Network on Electrochemistry and Batteries is gratefully acknowledged. J. L. gratefully acknowledges the funding by the BMBF (Federal ministry of Education and research, Germany) for its financial support under the auspices of the ExZellTUM II project, grant number 03XP0081.

ORCID

Daniel Pritzl https://orcid.org/0000-0002-9029-107X
Johannes Landesfeind https://orcid.org/0000-0003-0333-2185
Sophie Solchenbach https://orcid.org/0000-0001-6517-8094

References

1. Frank Holmes, *https://www.forbes.com/sites/greatspeculations/2018/02/27/the-worlds-cobalt-supply-is-in-jeopardy/* (2018).
2. D. Andre, S.-J. Kim, P. Lamp, S. F. Lux, F. Maglia, O. Paschos, and B. Stiaszny, *J. Mater. Chem. A*, **3**, 6709 (2015).
3. D. Lu, M. Xu, L. Zhou, A. Garsuch, and B. L. Lucht, *J. Electrochem. Soc.*, **160**, A3138 (2013).
4. L. Yang, B. Ravdel, and B. L. Lucht, *Electrochem. Solid-State Lett.*, **13**, A95 (2010).
5. J.-H. Kim, N. P. W. Pieczonka, and L. Yang, *ChemPhysChem*, **15**, 1940 (2014).
6. S. R. Li, C. H. Chen, X. Xia, and J. R. Dahn, *J. Electrochem. Soc.*, **160**, A1524 (2013).
7. N. P. W. Pieczonka, Z. Liu, P. Lu, K. L. Olson, J. Moote, B. R. Powell, and J.-H. Kim, *J. Phys. Chem. C*, **117**, 15947 (2013).
8. P. Lu, C. Li, E. W. Schneider, and S. J. Harris, *J. Phys. Chem. C*, **118**, 896 (2014).
9. S. S. Zhang, K. Xu, and T. R. Jow, *Electrochim. Acta*, **51**, 1636 (2006).
10. S. Zhang, M. S. Ding, K. Xu, J. Allen, and T. R. Jow, *Electrochem. Solid-State Lett.*, **4**, A206 (2001).
11. S. S. Zhang, *J. Power Sources*, **163**, 713 (2007).
12. S. Solchenbach, D. Pritzl, E. J. Y. Kong, J. Landesfeind, and H. A. Gasteiger, *J. Electrochem. Soc.*, **163**, A2265 (2016).
13. C. H. Chen, J. Liu, and K. Amine, *J. Power Sources*, **96**, 321 (2001).
14. R. Petibon, C. P. Aiken, N. N. Sinha, J. C. Burns, H. Ye, C. M. VanElzen, G. Jain, S. Trussler, and J. R. Dahn, *J. Electrochem. Soc.*, **160**, A117 (2013).
15. M. Klett, J. A. Gilbert, S. E. Trask, B. J. Polzin, A. N. Jansen, D. W. Dees, and D. P. Abraham, *J. Electrochem. Soc.*, **163**, A875 (2016).
16. J. Zhou and P. H. L. Notten, *J. Electrochem. Soc.*, **151**, A2173 (2004).
17. M. Ender, A. Weber, and E. Ivers-Tiffée, *J. Electrochem. Soc.*, **159**, A128 (2012).
18. A. N. Jansen, D. W. Dees, D. P. Abraham, K. Amine, and G. L. Henriksen, *J. Power Sources*, **174**, 373 (2007).
19. J. Landesfeind, D. Pritzl, and H. A. Gasteiger, *J. Electrochem. Soc.*, **164**, A1773 (2017).
20. D. Pritzl, S. Solchenbach, M. Wetjen, and H. A. Gasteiger, *J. Electrochem. Soc.*, **164**, A2625 (2017).
21. M. Metzger, B. Strehle, S. Solchenbach, and H. A. Gasteiger, *J. Electrochem. Soc.*, **163**, A798 (2016).
22. J. Landesfeind, J. Hattendorff, A. Ehrl, W. A. Wall, and H. A. Gasteiger, *J. Electrochem. Soc.*, **163**, A1373 (2016).
23. D. J. Xiong, R. Petibon, M. Nie, L. Ma, J. Xia, and J. R. Dahn, *J. Electrochem. Soc.*, **163**, 546 (2016).
24. M. Gaberscek, J. Moskon, B. Erjavec, R. Dominko, and J. Jamnik, *Electrochem. Solid-State Lett.*, **11**, A170 (2008).
25. D. Pritzl, A. Bumberger, M. Wetjen, J. Landesfeind, S. Solchenbach, and H. A. Gasteiger, *Manuscr. prep.*.
26. J. C. Burns, A. Kassam, N. N. Sinha, L. E. Downie, L. Solnickova, B. M. Way, and J. R. Dahn, *J. Electrochem. Soc.*, **160**, A1451 (2013).
27. N. Ogihara, S. Kawauchi, C. Okuda, Y. Itou, Y. Takeuchi, and Y. Ukyo, *J. Electrochem. Soc.*, **159**, A1034 (2012).
28. N. Ogihara, S. Kawauchi, C. Okuda, Y. Itou, Y. Takeuchi, and Y. Ukyo, *J. Electrochem. Soc.*, **159**, A1034 (2012).
29. M. Ochida, Y. Domi, T. Doi, S. Tsubouchi, H. Nakagawa, T. Yamanaka, T. Abe, and Z. Ogumi, *J. Electrochem. Soc.*, **159**, A961 (2012).
30. C. Zhan, J. Lu, A. Jeremy Kropf, T. Wu, A. N. Jansen, Y. K. Sun, X. Qiu, and K. Amine, *Nat. Commun.*, **4**, 1 (2013).
31. T. Joshi, K. Eom, G. Yushin, and T. F. Fuller, *J. Electrochem. Soc.*, **161**, 1915 (2014).
32. J. Landesfeind, M. Ebner, A. Eldiven, V. Wood, and H. A. Gasteiger, *J. Electrochem. Soc.*, **165**, 469 (2018).

3.1.5 Investigation of the increasing contact resistance in LNMO cathodes

This section presents the article "*Identifying Contact Resistances in High-Voltage Cathodes by Impedance Spectroscopy*". [113] The paper was submitted to the peer-reviewed Journal of the Electrochemical Society in December 2018 and published in February 2019. The article is published open access and distributed under the terms of the Creative Commons Attribution Non-Commercial No Derivatives 4.0 License. The permanent web link is available under: http://jes.ecsdl.org/content/166/4/A582. The article was presented by Daniel Pritzl at the National Harbor, Maryland Meeting of the Electrochemical Society (USA) in October 2017 (Paper 111).

This article is an extension of the cathode impedance study from chapter 3.1.3., where we showed that an increasing contact resistance ($R_{Contact}$) between the LNMO coating and the aluminum current collector was the major contribution to the impedance increase upon cycling of an LNM cathode in a graphite/LNMO cell. In the literature, different reports contradict each other. On the one hand Gaberscek et al.[90] showed that the high frequency semi-circle in cathode impedance spectra indeed stem from a contact resistance. On the other hand, Aurbach et al.[78] and Duncan et al.[91] attributed the high-frequency semi-circle is attributed to a surface film resistance on the LNMO cathode.

In order to fully understand the cathode impedance, a detailed investigation of it is carried out in this study. First, by a simple estimation of the capacitance of the high frequency semi-circle it can be shown that the interface (corresponding to this semi-circle) has a surface areas of roughly 1 cm^2, which fits well to the area of the current collector in the T-cell. Furthermore, by temperature-dependent impedance measurement the activation energy of this resistance is found to be in the order of 1 kJ/mol which fits very nicely to an electronic activation energy according to Ogihara et al.[89] In order to fully prove that the resistance is indeed a contact resistance, an LNMO electrode coated on an aluminum foil is compared to one coated on a glassy carbon electrode. The electrode coated on aluminum foil shows the increase of the contact resistance over cycling, whereas the LNMO cathode

coated on the glassy carbon disc shows almost no increase of the resistance at all. This clearly shows that the origin of the high frequency semi-circle can be ascribed to the cathode coating/current collector interphase.

This finding can be explained by the electrochemical electrolyte oxidation[68] which is known to release protic species[79] (e.g. HF), which then can corrode the native Al_2O_3 layer on the aluminum current collector to form thick layers of ALF_3 leading to an increased contact resistance. This hypothesis is then confirmed by further experiments with a graphite/LFP cell, where the potential is too low for electrolyte oxidation to occur and hence also no increase of the contact resistance can be seen. By adding defined amounts of HF to the graphite/LFP cell, we can directly observe an increasing high-frequency semi-circle, which fits well to our hypothesis from above.

Author contributions

All electrochemical measurements were conducted by D.P. and A.B. M.W. and D.P. developed the glassy carbon setup. Data analysis was done by D.P. and A.B. The manuscript was written by D.P., A.B. and H.A.G. All authors discussed the data and commented on the results.

Identifying Contact Resistances in High-Voltage Cathodes by Impedance Spectroscopy

Daniel Pritzl,*,z Andreas E. Bumberger, Morten Wetjen, Johannes Landesfeind, Sophie Solchenbach,* and Hubert A. Gasteiger**

Chair of Technical Electrochemistry, Department of Chemistry and Catalysis Research Center, Technical University of Munich, Munich, Germany

$LiNi_{0.5}Mn_{1.5}O_4$ (LNMO) cathodes cycled versus a graphite anode at elevated temperatures usually show severe capacity fading upon extended charge/discharge cycling. In the literature, the impedance increase at the cathode is often related to the formation of a so-called cathode/electrolyte interphase (CEI) and is presented as one of the possible failure mechanisms. In this study, we show that the main reason for the increasing cathode impedance is a contact resistance ($R_{Cont.}$) between the aluminum current collector and the cathode electrode rather than a surface film resistance (R_{CEI}). First evidence is presented by temperature-dependent impedance measurements and external compression of the electrode stack in the cell, which suggest an electronic nature of the commonly observed high-frequency semi-circle in a Nyquist plot. Further, by coating the LNMO cathode onto a glassy carbon disk, we demonstrate that the impedance increase arises from the interface between the cathode electrode and the aluminum current collector. Finally, we examine whether $R_{Cont.}$ correlates with the release of protic species (e.g., HF) formed upon electrolyte oxidation. This is done by cycling graphite/LFP cells in the absence/presence of deliberately added HF, showing that a contact resistance upon cycling only develops upon HF addition.

 [DOI: 10.1149/2.0451904jes]

Manuscript submitted December 6, 2018; revised manuscript received February 4, 2019. Published February 21, 2019. This was Paper 111 presented at the National Harbor, Maryland Meeting of the Society, October 1–5, 2017.

Commercial Li-Ion batteries based on a graphite/$LiCoO_2$ chemistry have reached their limits regarding energy density.[1] In order to increase the energy density of Li-Ion batteries, either the capacity or the voltage of the cathode active materials (CAMs) has to be increased. Furthermore, cobalt is considered a supply-limited critical raw material[2] and a significant fraction of cobalt is produced by hazardous artisanal mining in the Democratic Republic of Congo,[3] so that a reduction/elimination of the cobalt content in CAMs is required. A promising cobalt-free cathode material which also fulfills the criterion of a high energy density[4] is the so-called high-voltage spinel $LiNi_{0.5}Mn_{1.5}O_4$ (LNMO). However, while graphite/LNMO cells have a reasonable cycle life at room temperature, they usually show severe capacity fading at elevated temperatures (> 40°C).[5,6] The reasons for the poor capacity retention are frequently related to: i) manganese dissolution from the LNMO cathode and its subsequent reduction on the surface of the graphite anode (often described as cross-talk phenomenon), which damages the solid-electrolyte-interphase (SEI) on the graphite anode and catalyzes further electrolyte decomposition,[3,6–9] thereby resulting in a loss of active lithium; (ii) electrochemical electrolyte oxidation at the high LNMO cathode potential,[10,11] which leads to the release of protic species (e.g., HF),[12] often seen as a key driver for transition metal dissolution and concomitant SEI damage;[6,13] and, (iii) an increase of the full-cell impedance over cycling.[6] Based on detailed impedance studies, the latter is often ascribed to an increase of the LNMO cathode impedance.[14,15] For example, Aurbach et al.[14] measured the impedance of the LNMO cathode versus a lithium wire reference electrode after cycling at elevated temperatures (60°C), and observed both a high-frequency semi-circle (apex frequency ≈1 kHz) and a low frequency semi-circle (apex frequency ≈100 mHz). They attributed the former to a surface film resistance (often referred to as cathode electrolyte interphase (CEI) resistance) and the latter to a charge-transfer resistance. Similarly, Duncan et al.[15] used a lithium ring as reference electrode in order to monitor the impedance evolution of the LNMO cathode upon cycling. They observed the same impedance features as Aurbach et al.,[14] i.e., two semi-circles at high and low frequency, respectively, which they attributed to the surface chemistry of the LNMO cathode. As the semi-circle at high frequency could already be observed prior to applying current to the cell, the authors attributed it to the spontaneous formation of a surface layer on the LNMO particles once they get in contact with the electrolyte, analogous to the prior assignment of the high-frequency semi-circle to the CEI by Aurbach et al.[14] Upon cycling, this feature gradually increased, which Duncan et al. tentatively ascribed to the growth of the CEI.[15]

In contrast to the above interpretation reached for graphite/LNMO cells, Gaberscek et al.[16] assigned the high-frequency semi-circle in cathode impedance spectra observed for graphite/$LiFePO_4$ (LFP) cells to a contact resistance between the aluminum current collector and the LFP cathode electrode interface. This was based on impedance measurements in symmetric cells, where an LFP cathode was coated either onto pristine aluminum foil or onto an aluminum foil coated with a silver paste. When using the pristine aluminum foil, a high-frequency semi-circle was observed, while this feature was absent when using the silver paste coated aluminum foil. Further, they reported that the high-frequency semi-circle is independent of LFP particle size and LFP mass loading, and that it always has the same characteristic capacitance of $\approx 10^1$ μF/cm^2. Since the typical double-layer capacitance is also on the order of 10^1 μF/cm^2,[17] this indicates that the interface which is responsible for this feature must have a very small surface area (on the order of a few cm^2), from which the authors concluded that the high-frequency semi-circle in cathode impedance spectra originates from the interfacial resistance between the current collector and the cathode electrode rather than from the cathode active material interface with the electrolyte. Recently, similar results have been reported by our group for graphite/LNMO cells,[18] where the impedance of an LNMO cathode was analyzed in-situ, utilizing a gold wire reference electrode (GWRE)[19] and a novel impedance procedure. Thereby, it was possible to deconvolute the contact resistance between the current collector and the cathode electrode ($R_{Cont.}$) from the charge transfer resistance (R_{CT}) of the LNMO active material and from the pore resistance (R_{Pore}) which is due to the ionic conduction resistance in the electrolyte phase within the porous electrode. We found that the main resistance increase over the course of extended charge/discharge cycling of graphite/LNMO cells at 40°C indeed comes from an increase of $R_{Contact}$ rather than from an increase in the LNMO charge-transfer or surface film (CEI) resistance that was suggested previously.[14,15]

*Electrochemical Society Member.
**Electrochemical Society Fellow.
zE-mail: daniel.pritzl@tum.de

Table I. Specifications of the different cathodes (LNMO and LFP) used in this study, i.e., composition, used current collector, and compression.

electrode type	cathode active material (CAM)	Composition (CAM/carbon black/PVdF)	current collector	Compression (MPa)
Type I	LNMO	92/5/3	Al	200
Type II	LNMO	95/1.5/3.5	Al	200
Type III	LNMO	95/1.5/3.5	Al	0
Type IV	LNMO	95/1.5/3.5	glassy carbon	0
Type V	LFP	94/3/4	Al	200

While in this previous aging study on graphite/LNMO cells we identified the origin of the high-frequency semi-circle based on a simple estimate of the interfacial capacitance and the associated surface area, we here want to expand on our previous results and elucidate more clearly (i) the origin of the high-frequency semi-circle, (ii) its increase upon cycling, and, (iii) the parasitic reactions occurring in high-voltage Li-Ion cells which cause this resistance increase. In the first part, we investigate the influence of the carbon black content, the temperature, and the external cell compression on the cathode impedance spectra by using the GWRE to deconvolute the full-cell impedance spectra. From these experiments, we can show that the high-frequency semi-circle resistance is indeed an electronic contact resistance between the cathode electrode and the current collector ($R_{Cont.}$), and that is not caused by an LNMO cathode surface film (CEI). In the second part, we will examine $R_{Cont.}$ with regard to the current collector material, comparing a standard aluminum current collector with a glassy carbon disk as model current collector. As conventional impedance analysis does not allow a precise quantification of $R_{Cont.}$, we will use the blocking electrode methodology[18,20] to quantify the $R_{Cont.}$ evolution over extended cycling. Finally, we will investigate whether the $R_{Cont.}$ increase at the cathode is related to the formation of protic species (e.g., HF) upon electrolyte oxidation. This is done by comparing the impedance obtained with an LP57 electrolyte with our without intentionally added HF in graphite/LFP cells, where no electrochemical electrolyte oxidation and thus no formation of protic species should occur.

Experimental

Electrode preparation.—$LiNi_{0.5}Mn_{1.5}O_4$ (LNMO) inks were prepared by mixing LNMO powder (BASF SE, Germany, with a BET area of ≈0.9 m^2/g), carbon black (Super C65, Timcal, Switzerland, with a BET area of ≈65 m^2/g), and polyvinylene difluoride (PVdF, Kynar) at mass ratios of 92/5/3 and 95/1.5/3.5 with NMP (N-methyl pyrrolidone, anhydrous, Sigma-Aldrich, Germany) at a solid content of 60% in a planetary mixer (Thinky Corp.) for 15 min. These inks were then used to prepare the four different types of LNMO electrodes detailed in Table I. As a current collector, aluminum foil (MTI, 18 μm) was used for Type I, II, and III electrodes, while a glassy carbon disk (HTW, Germany, 500 μm, 11 mm diameter) was used for type IV electrodes. For all electrodes, the ink was coated onto the current collector with a doctor blade coater and dried at 50°C in a convection oven for at least 3 h. To coat the glassy carbon disk with the electrode ink, the disk was fitted into a copper-plate with a height of 500 μm and a hole with a diameter of 11 mm. All LNMO coatings had a loading of ≈14 mg_{LNMO}/cm^2, corresponding to a theoretical areal capacity of ≈2.0 mAh/cm^2. From the coatings on aluminum foil, electrodes with a diameter of 11 mm (≡0.95 cm^2) were punched out. A cross-sectional SEM image of an LNMO coating (dried at 50°C for 3h) on a glassy carbon disk is shown in Figure 1. The Type I and II electrodes were compressed with a KBr press at ≈200 MPa (2 $tons/cm^2$) for 60 s to ≈30% porosity (determined by areal weight and thickness measurements, using the bulk density values for the electrode components), while Types III and IV electrodes were left uncompressed. Additionally, $LiFePO_4$ (LFP) cathodes with a composition of 93/3/4 (LFP/carbon black/PVdF, by mass) and a theoretical areal capacity of ≈2.0 mAh/cm^2 (corresponding to ≈11.5 mg_{LFP}/cm^2) were prepared the same way as the LNMO Type I cathodes. Detailed information about the cathode coatings is summarized in Table I.

Graphite electrodes were prepared by mixing graphite (T311, SGL Carbon, Germany) and PVdF at a mass ratio of 95/5 with NMP by applying the same coating process as for the cathodes, but coated onto a copper foil (MTI, ≈12 μm) and dried in a convection oven at 50°C for 3 h. The loading of the graphite coatings was ≈6.3 $mg_{graphite}/cm^2$, corresponding to a theoretical areal capacity of ≈2.3 mAh/cm^2. The electrodes were punched out with a diameter of 11 mm and compressed at ≈50 MPa (0.5 $tons/cm^2$) for 60 s to a porosity of ≈30%. Finally, all electrodes were dried under dynamic vacuum at 120°C for at least 12 h in a vacuum oven (Büchi, Switzerland) and then transferred into an argon-filled glove box (MBraun, Germany) without exposure to ambient atmosphere.

Battery testing.—Swagelok T-cells with a gold wire reference electrode (GWRE)[19] were assembled in a glove box filled with argon (O_2 and H_2O <0.1 ppm) by sandwiching anode (graphite) and cathode (LNMO or LFP) between two glass fiber separators (11 mm diameter, 200 μm thickness, glass microfiber #691, VWR, Germany) and adding 60 μL of standard LP57 electrolyte (1M $LiPF_6$ in EC/EMC (3:7 wt/wt), water content < 10 ppm, BASF SE, Germany). Battery cycling was carried out in a climate chamber (25°C or 40°C, Binder, Germany) using a multi-channel battery cycler (Series 400, Maccor, USA). The cycling protocol consisted of two formation cycles with C/10 (0.2 mA/cm^2) at 25°C, followed by 98 cycles with 1C (2.0 mA/cm^2) at 40°C. All cycles were conducted between 3.5 and 4.8 V cell voltage by applying a constant current constant voltage (CCCV) charge with a current limit of C/20 for the CV phase at 4.8 V and a constant current (CC) discharge procedure. The C-rate is defined by the theoretical capacity of LNMO (≈140 mAh/g) or LFP (≈170 mAh/g), i.e., 1C corresponds to 140 mA/g (≈2.0 mA/cm^2) for LNMO or 170 mA/g (≈2.0 mA/cm^2) for LFP. After each 25th cycle (up to 100 cycles), the cells were stopped in their discharged state, transferred to a 25°C climate chamber, and connected to a Biologic (VMP300) potentiostat for impedance measurements.

For graphite/LFP cells, formation was carried out 25°C with C/10 (0.2 mA/cm^2). Afterwards, 50 cycles were conducted at 40°C with a 1C rate (2 mA/cm^2) between 2.0 and 4.0 V cell voltage, using a

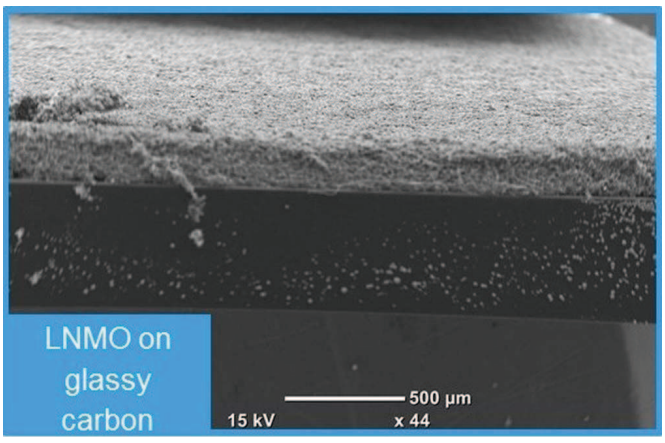

Figure 1. Cross sectional SEM image of an LNMO electrode coating with ≈14 mg_{LNMO}/cm^2 (gray top layer) on a glassy carbon disk model current collector (lower black layer), prepared via a slot-coating process.

CC discharge and a CCCV charge protocol with a current limit of C/20. Impedance was measured at 50% SOC after formation and after 50 cycles at 25°C. As electrolyte, a standard LP57 electrolyte (described above) and an LP57 electrolyte containing ≈2000 ppm HF were used. The HF-containing LP57 was prepared by adding 1000 ppm (by weight) of deionized water to the electrolyte and stirring for 5 days. As expected based on the literature,[21] a quantitative conversion of water into HF was confirmed: Karl-Fischer analysis showed that after stirring only 27 ppm of water remained and ^{19}F-NMR Spectroscopy showed that ≈2000 ppm of HF were formed.

Electrochemical impedance spectroscopy.—The GWRE was lithiated with a constant current of 150 nA for 1 h after cell assembly, using the cathode electrode as lithium source (note that the lithiation capacity of 0.15 μAh is negligible compared to the cathode capacity of ≈2 mAh). The detailed procedure for the assembly of T-cells with the GWRE can be found in Reference 19. Potential-controlled impedance spectra were recorded from 100 kHz to 100 mHz with a perturbation of 15 mV at 25°C (acquisition time of 10 min./spectrum). Spectra were recorded at two distinct state-of-charge (SOC) values: i) at 4.4 V cell voltage (corresponding to ≈10% SOC) during discharge at open-circuit (after a prior 1 h open-circuit hold), and, ii) while holding at 4.9 V cell voltage (≡100% SOC, i.e., for a fully lithiated cathode), after the voltage had been held at that potential until the current dropped below C/40. The latter procedure brings the cathode electrode into blocking conditions that are characterized by a very high charge-transfer resistance, so that its impedance response shifts to very low frequencies, enabling a more straightforward impedance analysis in the high- and mid-frequency range. The detailed procedure can be found in Reference 18. In a former study of our group, we showed that the potential stability of the lithiated GWRE is only on the order of several hours in graphite/LNMO cells operating at 40°C, due to a chemical delithiation of the reference electrode by electrolyte oxidation products.[22] Therefore, in order to avoid a potential drift of the reference electrode during the impedance measurements, a relithiation of the GWRE with 150 nA for 1 h was carried out before each electrochemical impedance spectroscopy (EIS) measurement.

Results and Discussion

Physical origin of the high-frequency semi-circle in LNMO cathodes.—So far, the literature offers two different interpretations about the origin of the high-frequency semi-circle in cathode impedance spectra. On the one hand, this feature has been ascribed to a surface film resistance associated with the formation/growth of a CEI on LNMO cathodes;[14,15] on the other hand, it has been ascribed to an electronic contact resistance at the cathode electrode/aluminum current collector interface for LFP and LNMO cathodes.[18,23] Therefore, to clarify this discrepancy in interpretation, we first investigate the effect of the carbon black content of the LNMO cathodes on the high-frequency impedance response, using LNMO cathodes with a carbon black content of either 5% or 1.5% at a constant porosity of ≈30% (Type I and Type 2 cathodes, see Table I), which were cycled in a three-electrode cell with graphite as anode and equipped with a gold wire reference electrode (GWRE) to monitor the impedance of the LNMO cathode.

Figure 2a shows the LNMO cathode impedance spectra taken at 4.4 V_{Cell} (≡10% SOC) for the LNMO cathode with a carbon black content of 5% after two formation cycles at 25°C (in black) and after 50 cycles at 40°C (in red). The overall cathode impedance $R_{Cathode}$ (sum of high and low frequency resistance, highlighted in Figure 2 by blue points) after formation is ≈5 Ωcm^2 and increases to ≈7 Ωcm^2 during cycling at 40°C. The low-frequency semi-circle (apex frequency of 450 Hz after 50 cycles), which represents a convolution of the charge transfer- and pore resistance,[18] stays almost constant in size over 50 charge/discharge cycles, but is shifted to higher values on the real axis, owing to the increase of the high-frequency semi-circle (apex frequency 31000 Hz after 50 cycles). When the carbon black content within the electrode is decreased to 1.5% (see Figure 2b), $R_{Cathode}$ after formation (in black) is higher (≈10 Ωcm^2), as inidicated by the more pronounced high-frequency semi-circle already after formation. After 50 cycles, $R_{Cathode}$ increases to ≈30 Ωcm^2 for the electrodes with 1.5% carbon black (in contrast to ≈7 Ωcm^2 for the electrodes with 5% carbon black), shown by the substantial increase of the high-frequency semi-circle (apex frequency of 6300 Hz). Quite clearly, the magnitude of the high-frequency semi-circle increases by ≈4-fold after 50 cycles when the carbon black content is decreased from 5% to 1.5%. If this impedance feature were related to the CEI resistance of the LNMO, its characteristic capacitance would have to be related to the overall exposed LNMO and carbon black surface area. The latter can be estimated from the BET area (0.9 m^2_{LNMO}/g_{LNMO}) and loading (14 $mg_{LNMO}/cm^2_{electrode}$) of the active material LNMO, equating to ≈126 $cm^2_{LNMO}/cm^2_{electrode}$. The surface area of the carbon equates to 447 cm^2 for the LNMO cathode with 5% carbon black (Type I) calculated with a loading of 0.76 $mg_{carbonblack}/cm^2$ and a BET area of 62 m^2/g. The cathode with 1.5% carbon black (Type II) has a carbon surface area of 129 cm^2 calculated with a loading of 0.22 $mg_{carbonblack}/cm^2$ and a BET area of 62 m^2/g. By performing an order of magnitude estimate of the characteristic capacitances of the high-frequency semi-circle (fitted with a simple R/Q element, and neglecting the constant phase exponent), the capacitance values after the 50th cycle for the LNMO cathodes with 5% and 1.5% carbon black are ≈2.5 $\mu F/cm^2_{electrode}$ and ≈1.3 $\mu F/cm^2_{electrode}$. If this were due to the LNMO surface, i.e., due to a CEI resistance, the surface area normalized capacitances would equate to ≈0.004 $\mu F/cm^2_{LNMO+carbon\ black}$ for the cathode with 5% carbon black and to ≈0.005 $\mu F/cm^2_{LNMO+carbon\ black}$ for the cathode with 1.5% carbon black, which unquestionably is far too low for a typical electrochemical double-layer capacitance that, if referenced to the actual surface area, should be on the order of ≈10^1 μF/cm^2.[17] On the other hand, if normalized to the aluminum current collector surface (≈1 cm^2), a reasonable double-layer capacitance of ≈1.3 – 2.5 $\mu F/cm^2_{Al}$ is obtained, which strongly suggests that the electrochemically active surface which is represented by the high-frequency semi-circle is the interface between the cathode electrode and the aluminum current collector.

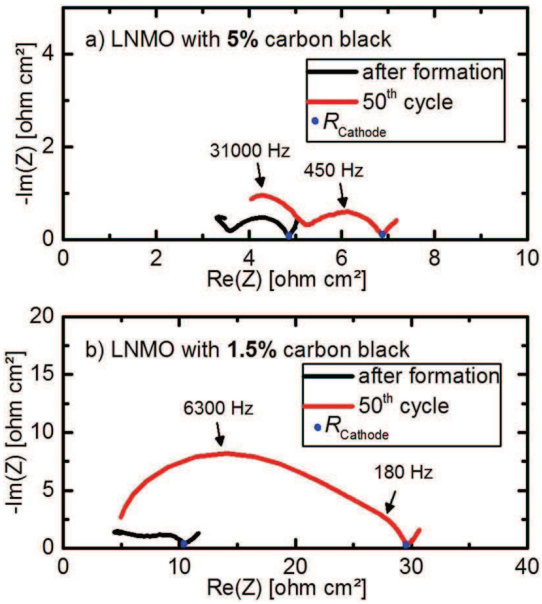

Figure 2. LNMO cathode impedance spectra obtained in graphite/LNMO full-cells after formation at C/10 and 25°C (black line) and after 50 cycles at (2x C/10 + 48 × 1C cycles) and 40°C (red line): a) for an LNMO cathode with 5% carbon black (Type I, see Table I); b) for an LNMO cathode with 1.5% carbon black (Type II, see Table I). The impedance was measured from 100 kHz to 100 mHz with a perturbation of 15 mV at 25°C; it was conducted at 4.4 V_{Cell} (≡10% SOC) under open circuit conditions.

In order to confirm that the high-frequency semicircle indeed is due to an electronic resistance at the LNMO cathode/aluminum current

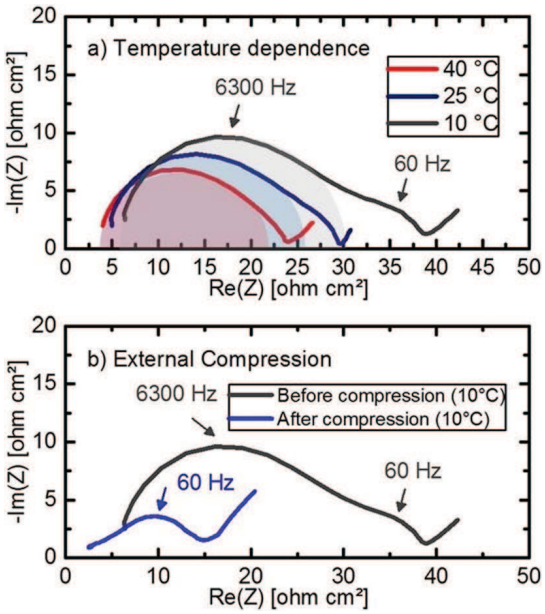

Figure 3. LNMO cathode impedance spectra obtained after 50 cycles at 1C and 40°C in graphite/LNMO cells based on LNMO cathodes with 1.5% carbon black (Type II cathode, see Table I). a) Cathode impedance measured at 10°C, 25°C, and 40°C; before recording the impedance, two hours of an OCV period was carried out to assure thermal equilibration. b) Impedance spectrum (recorded at 10°C) of a cycled LNMO cathode before and after external compression of the T-cell. The impedance was measured from 100 kHz to 100 mHz with a perturbation of 15 mV at 25°C; it was conducted at 4.4 V_{Cell} (≡10% SOC) under open circuit conditions.

collector interface, the impedance of an LNMO cathode with 1.5% carbon black after 50 cycles is measured at different temperatures. Temperature-dependent impedance measurements give information about the activation energy of processes happening at interfaces in porous electrodes.[24] Figure 3a shows the cathode impedance spectra measured at three different temperatures, namely 40°C (red), 25°C (blue), and 10°C (gray). As expected, the cathode impedance over the whole frequency range increases when reducing the temperature; however, the extent of the change differs considerably for the different impedance features. The high-frequency semi-circle (simply fitted with an R/Q element, shown by the shaded areas in Figure 3a) increases from ≈17 Ωcm^2 (at 40°C) to ≈19 Ωcm^2 (at 25°C) to ≈23 Ωcm^2 (at 10°C). The associated activation energy, determined by fitting a linear regression line to a plot of the logarithm of $1/R_{high\text{-}frequency}$ versus $1/T$ (in Kelvin) and by multiplying the slope by the universal gas constant R (8.314 J/molK), results in an apparent activation energy of ≈3 kJ/mol. This is in reasonably good agreement with the activation energy of an electronic resistance of ≈1 kJ/mol as reported by Ogihara et al.,[24] and is much lower than what one would expect for the CEI resistance and what was reported for the charge-transfer resistance (≈60 kJ/mol[24]). This, however, leaves the question as to where the LNMO charge-transfer resistance would appear in the impedance spectra of Figure 3a. For LNMO cathodes with 5% carbon black (identical to Type I), we determined its value at 40°C to be ≈0.5 Ωcm^2, which explains why it can only be discerned vaguely in the impedance spectrum at 40°C in Figure 3a.[18] However, as the temperature is being decreased, a well pronounced low-frequency semi-circle appears, which we associate with the LNMO charge-transfer and pore resistance. At 10°C, the resistance of this low-frequency semi-circle is ≈10 Ωcm^2 (this will be seen more clearly in Figure 3b) and it has an apex frequency of 60 Hz, which corresponds to a capacitance of ≈265 μF/cm$^2_{electrode}$. By including the pore resistance in the calculation of the double layer capacitance, an error is introduced. However, in order to get information about the order of magnitude we think that taking both charge transfer and pore resistance is sufficient. If normalized to the LNMO and carbon black surface area (≈126 cm$^2_{LNMO}$/cm$^2_{electrode}$ and ≈129 cm$^2_{carbon\ black}$/cm$^2_{electrode}$), a very reasonable interfacial capacity of ≈$0.1 \cdot 10^1$ μF/cm$^2_{LNMO}$ is again obtained, clearly indicating that the low-frequency feature is related to the LNMO charge-transfer resistance. This is further supported by the strong temperature dependence of the low-frequency semi-circle resistance, increasing by approximately one order of magnitude when lowering the temperature from 40°C to 10°C (unfortunately, the error in determining the low-frequency semi-circle resistance at 40°C from Figure 3a is too large for a precise quantification, which would require an experimental methodology as described in Reference 18).

After performing temperature-dependent impedance measurements, the T-cell was compressed by applying an external force. It is expected, that a compression of the cathode will improve the quality of the contact between the current collector and the LNMO coating, while the charge transfer resistance across a possible surface film (CEI) should stay relatively constant. Figure 3b shows the impedance spectrum of the LNMO cathode measured at 10°C before compression (gray line, already shown in Figure 3a and discussed above). After external compression of the T-cell, several changes can be observed in the impedance spectrum (Figure 3b, in blue): (i) the high-frequency semi-circle with an apex frequency of 6300 Hz is no longer present, (ii) the low-frequency semi-circle retains the same apex frequency of 60 Hz but shifts to lower values along the x-axis, and, (iii) the high-frequency resistance intercept also shifts toward lower values, as the thickness of the glass fiber separators decreases substantially upon compression. The external compression clearly leads to an improved electrical contact at the interface between the cathode electrode and the aluminum current collector, analogous to what has been observed before with LFP electrodes.[23,25] Thus, the analysis of its characteristic capacitance, of its temperature-dependence, and of its dependence upon cell compression clearly demonstrates that the semi-circle at high-frequencies is due to an electronic contact resistance at the interface between the cathode electrode and the aluminum current collector. It therefore rules out definitively the interpretation in the literature that it be due to a surface-film (CEI) resistance.

Aluminum vs. glassy carbon current collector.—In order to find out if the increase in the contact resistance ($R_{Contact}$) is due to the corrosion of the conductive carbon at the interface or from the formation of a resistive surface film on the aluminum current collector, the aluminum cathode current collector is replaced by a glassy carbon disk. The rationale of this approach is that the glassy carbon surface cannot form a resistive passivation layer at high voltages, contrary to the possible formation of, for example, a resistive AlF_3 layer on the aluminum current collector. As the glassy carbon disks break upon compression, the following cathodes – LNMO on aluminum and LNMO on glassy carbon – are both tested without compression (see Type 3 and Type 4 in Table I), even though LNMO electrodes usually are compressed or calendered. As before, formation of these cells is done at C/10 at 25°C for two cycles, followed by 98 cycles at 1C and 40°C. After each 25th cycle, the cells are transferred to a 25°C chamber, where the EIS experiments are performed. Figure 4a shows the specific discharge capacity for graphite/LNMO cells with the cathode coated either on glassy carbon (red dots) or on aluminum foil (green dots), and Figure 4b shows the voltage profiles of the graphite/LNMO cells after the 2nd and the 25th cycle at 1C.

For both cathode types, the first discharge capacity at 0.1C is ≈121 ± 1 mAh/g_{LNMO}, which is in good agreement with previous measurements with LNMO cathodes (compressed, with 5% carbon black) tested under identical conditions.[20] After formation, the full-cell voltage profiles of the 2nd cycle at 1C are essentially identical for the cell with an LNMO cathode coated on an aluminum current collector (Figure 4b, dashed green line) and for that with an LNMO cathode coated on a glassy carbon disk (Figure 4b, dashed red line), indicating a similar impedance after formation. After 98 cycles at 1C (i.e., the 100th cycle in Figure 4a), the remaining discharge capacity is ≈91 ±1 mAh/g_{LNMO} for cells with LNMO coated on glassy carbon and ≈86 ±7 mAh/g_{LNMO} for cells with an aluminum current collector.

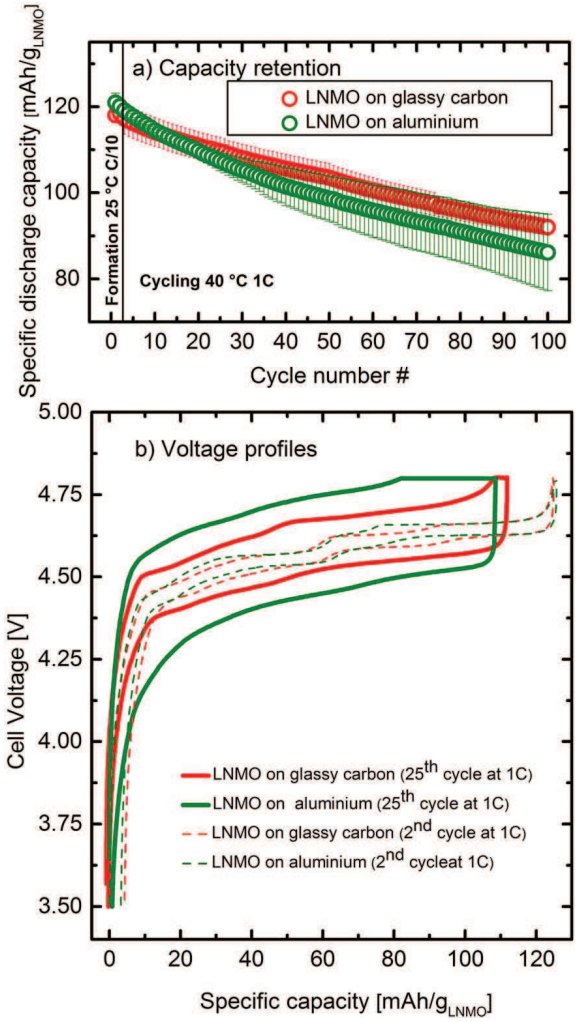

Figure 4. a) Specific discharge capacity (in mAh/g_{LNMO}) versus cycle number of graphite/LNMO cells with uncompressed LNMO cathodes either coated on aluminum (green circles; Type III electrodes, see Table I) or on glassy carbon (red circles; Type IV electrodes, see Table I) over extended charge/discharge cycling at 1C (CCCV charge, CC discharge) between 3.5–4.8 V cell voltage at 40°C with an LP57 electrolyte. Formation (2 cycles) was carried out at C/10 and 25°C. The error bars represent the standard deviation of two cells. b) Corresponding cell voltage profiles of the 2nd cycle at 1C (dotted lines) and for the 25th cycle at 1C (solid lines).

The cycling performance of these full-cells lies well within the capacity retention obtained in our previous study (≈90 ±1 mAh/g_{LNMO} after the 98th cycle at 1C and 40°C).[22] Here it may be noted that while the capacity fading of both cells is initially very similar, it starts to differ after ≈25 cycles, where the capacity of the LNMO cathodes coated on aluminum fade slightly faster and where a significant capacity variation between the two nominally identical cells starts to develop (green symbols in Figure 4a). This is accompanied by the development of a substantial cell impedance, particularly in the case of the LNMO cathodes coated on aluminum, as can be seen from the voltage profiles after the 25th cycle at 1C (solid lines in Figure 4b). The much more increased polarization of the cells with the LNMO coated on aluminum compared to the LNMO coated on glassy carbon results in a rapid increase of the capacity contribution from the CV step for the former. The nevertheless similar capacity retention of both cathode types can thus only be reached because the CV step with a current limit of C/20 compensates for the much higher overpotential apparent in the cell using the LNMO cathode coated on aluminum (note that its energy retention would be inferior due its much lower average discharge voltage).

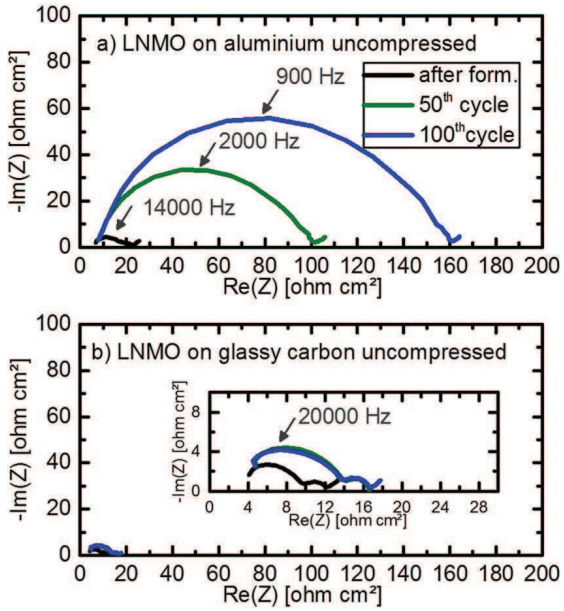

Figure 5. Impedance spectra of uncompressed LNMO cathodes with 1.5% carbon black after two formation cycles at 0.1C at 25°C, and after the 50th and 100th cycle (i.e, after 48 and 98 cycles at 1C and 40°C) in a graphite/LNMO cell. a) Impedance response of an uncompressed LNMO cathode coated on an aluminum current collector (Type III electrodes, see Table I); b) Impedance response of an LNMO cathode coated on a glassy carbon disk; the inset is a magnified view. The impedance was measured from 100 kHz to 100 mHz with a perturbation of 15 mV at 25°C; it was conducted at 4.4 V_{Cell} (≡10% SOC) under open circuit conditions.

In order to investigate the origin of the increased overpotential of graphite/LNMO cells with an aluminum current collector, the cathode impedance responses at 4.4 V cell voltage (i.e., at ≈10% SOC) are shown for graphite/LNMO cells with an aluminum current collector (Figure 5a) and graphite/LNMO cells with a glassy carbon current collector (Figure 5b). Figure 5a shows the large increase of the overall impedance over cycling, which is consistent with the above observed increased cell polarization (Figure 4b). The observed impedance response in each case is dominated by a high-frequency semi-circle, whereby the approximate capacitances derived from a simple R/Q fit are ≈0.8 μF/cm^2 for the 50th cycle (in green) and ≈1.1μF/cm^2 after the 100th cycle (in blue), consistent with an electronic contact resistance. The overall cathode resistance $R_{Cathode}$ increases from ≈22 Ωcm^2 after formation to ≈100 Ωcm^2 after 50 cycles and to ≈160 Ωcm^2 after 100 cycles, an increase which is clearly governed by the large increase of the high-frequency semi-circle. Compared to compressed cathodes from the experiments before (see Figure 2 and Figure 3), the high-frequency semi-circle impedance is substantially larger, thus indicating that uncompressed electrodes have an inferior electrical contact at the interface of the cathode electrode and the current collector. A more rigorous deconvolution of the high-frequency semi-circle from the low-frequency semi-circle will be shown in the next section.

Interestingly, the cathode impedance of graphite/LNMO cells with a glassy carbon current collector (see Figure 5b) is much lower compared to cells with an aluminum current collector (compare 5a). The cathode resistance $R_{Cathode}$ after formation is ≈12 Ωcm^2 and increases only slightly to ≈16 Ωcm^2 after 50 cycles due to an increase in the high-frequency semi-circle and then stays constant up to 100 cycles. The slight increase of the high-frequency semi-circle might arise from the corrosion of the glassy carbon substrate or the carbon black in the coating when the temperature is increased from 25°C (during formation) to 40°C (during cycling). Quite clearly, after 100 cycles, the overall cathode resistance $R_{Cathode}$ of cells with an aluminum current collector is an order of magnitude higher (≈160 Ωcm^2) compared to

the cells with LNMO coated on glassy carbon (≈16 Ωcm^2). In summary, we can now clearly attribute the high-frequency semi-circle to a contact resistance ($R_{Cont.}$) between the aluminum current collector and the LNMO coating, whereby the major increase of $R_{Cont.}$ over extended cycling seems to be caused by the formation of a resistive surface film on the aluminum current collector. In addition, the strong dependence of the evolution of $R_{Cont.}$ on the type of current collector also rules out an inter-particle contact resistance within the LNMO electrode, as this effect would be independent of the current collector material.

Quantification of $R_{Cont.}$ by the blocking condition methodology.—In a recent study[18] of our group, we introduced a novel impedance procedure which enabled a quantitative deconvolution of the LNMO cathode impedance ($R_{Cathode}$) into contributions from the charge transfer resistance (R_{CT}), the pore resistance (R_{Pore}), and the contact resistance between current collector and cathode electrode ($R_{Cont.}$). At that time, we quantified the various resistances by recording impedance spectra at two distinct state-of-charge (SOC) values of an LNMO cathode in a graphite/LNMO cell: (i) at 4.4 V cell voltage (corresponding to ≈10% SOC) during discharge, acquired at open-circuit voltage (after a 1 h open-circuit hold), and, (ii) while holding at 4.9 V cell voltage, after the potential had been held at this voltage until the current had dropped to C/40, so that the LNMO is completely delithated, corresponding to a full-cell SOC of 100%. At the latter condition, the LNMO charge-transfer resistance becomes very large due to the suppression of lithium intercalation (representing blocking conditions), so that its impedance response shifts to very low frequencies. Therefore, by recording the impedance at 4.9 V cell voltage, the impedance spectrum shows features distinctly separated in frequency space: a high-frequency semi-circle for the contact resistance ($R_{Contact}$), a mid-frequency 45° transmission-line feature representing 1/3 of the pore resistance (R_{Pore}), and at very low frequencies a very large charge transfer resistance (R_{CT}). Meaningful quantitative values for these resistances can be obtained by simultaneously fitting the spectra at 4.4 V cell voltage (non-blocking conditions) and at 4.9 V cell voltage (blocking conditions) to a transmission-line model equivalent circuit that is connected in series with an R/Q element for the contact resistance ($R_{Cont.}$), and with a Warburg element accounting for concentration gradients within the separator (for further details, see Reference 18). The same principle is applied in this study, and an exemplary impedance spectrum in blocking- and non-blocking conditions for an LNMO cathode (1.5% carbon black, compressed) after the 48th cycle at 1C and 40°C is shown in Figure 6.

Figure 6 shows the non-blocking impedance spectrum (blue symbols) and the blocking impedance spectrum (red circles) after 48 cycles at 1C and 40°C. The high-frequency semi-circle is present in both spectra, which supports its assignment to a contact resistance ($R_{Cont.}$), as this resistance should not change with SOC. At lower frequencies, a Warburg 45°-line is observed for the spectrum in non-blocking conditions, whereas in the blocking spectrum a large impedance feature is observed for the large charge transfer resistance (R_{CT}). In our previous study,[18] using an LNMO cathode with a carbon black content of 5%, a pronounced 45° transmission-line feature at mid-frequencies was observed in the blocking spectrum. However, for the low carbon black content (1.5%) in the LNMO cathodes used in this study, the larger values for the contact resistance ($R_{Cont.}$) result in a larger high-frequency semi-circle that masks the 45° transmission-line feature in the mid-frequency range. As shown in our previous study, the value for the pore resistance after formation is $R_{Pore} \approx 3.2$ Ωcm^2, which only increases slightly upon cycling at 40°C (≈1.5-fold over 85 cycles).[18] Hence, we here use this R_{Pore} value for fitting the spectra in non-blocking and blocking condition with a transmission-line equivalent circuit, neglecting the slight increase of R_{Pore} over extended cycling. While it is clear that this simplification will not allow a deconvolution of all resistances with a high accuracy, the error for quantifying $R_{Cont.}$ is rather small, as it represent the by far largest contribution to the overall cathode impedance.

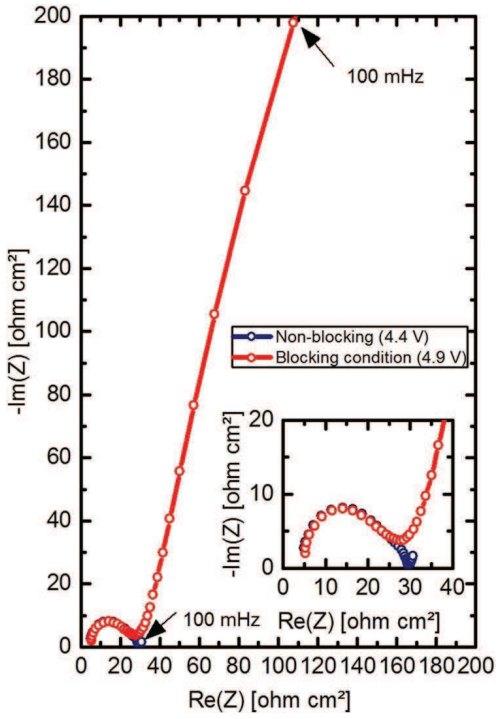

Figure 6. Impedance spectra of a compressed LNMO cathode with 1.5% carbon black (Type II in Table I) after the 48th cycle in a graphite/LNMO cell at 1C and 40°C measured in non-blocking conditions (at 4.4 V cell voltage or ≈10% SOC, in blue) or in blocking conditions (at 4.9 V cell voltage or 100% SOC, in red). The impedance was recorded from 100 kHz to 100 mHz with a perturbation of 15 mV at 25°C. For blocking conditions, the cell voltage was held at 4.9 V until the current decreased to C/40 and the impedance was recorded while holding at 4.9 V; for non-blocking conditions, the impedance was recorded at open-circuit. The inset is a magnified view of the high- to mid-frequency region.

Figure 7 shows the thus fitted $R_{Cont.}$ values for three different LNMO cathodes with 1.5% carbon black, cycled in graphite/LNMO cells at 1C and 40°C (including two formation cycles at 0.1 C and 25°C), namely for: (i) LNMO coated on glassy carbon (Type IV in Table I; red circles), (ii) LNMO coated on aluminum and uncompressed (Type III in Table I green circles), and, (iii) LNMO coated on aluminum which is compressed at 200 MPa to 30% porosity (Type II in Table I; black circles). Cells with an uncompressed cathode on aluminum (green circles in Figure 7) show a large linear increase of $R_{Cont.}$ over 100 cycles to ≈160 ± 12 Ωcm^2. When the same electrodes were compressed to a porosity of 30% prior to cycling, $R_{Cont.}$ increases less dramatically to ≈38 ± 8 Ωcm^2 after 100 cycles. In contrast, LNMO electrodes coated on a glassy carbon disk show essentially no increase in contact resistance over cycling, exhibiting a contact resistance of ≈14 ±6 Ωcm^2 after 100 cycles.

It is well known that the aluminum current collector in lithium-ion batteries is covered by a thin layer of native oxide Al_2O_3 which protects the otherwise reactive metal from corrosion up to potentials of about 4 V vs. Li^+/Li.[26–28] It has also been shown that the aluminum surface is further passivated by a layer of AlF_3 when fluorinated species such as $LiPF_6$ or $LiBF_4$ are used as conductive salt in non-aqueous electrolytes,[28–31] or when HF is added to electrolytes containing more stable salts like $LiCF_3SO_2$ or $Li(CF_3SO_2)_2N$.[27] Since graphite/LNMO full cells are typically cycled up to a cathode potential of 4.9 V vs. Li^+/Li, it is reasonable to assume that the (electro)chemical oxidation of the electrolyte might result in reaction products which can either oxidize or other passivate the aluminum surface, thereby increasing the contact resistance at the Al/LNMO interface. We recently provided evidence that the (electro)chemical oxidation of alkyl carbonates in commonly used electrolytes leads to the formation of protic species,[12] later on, Ma et al.[30] argued that these protic species would react with

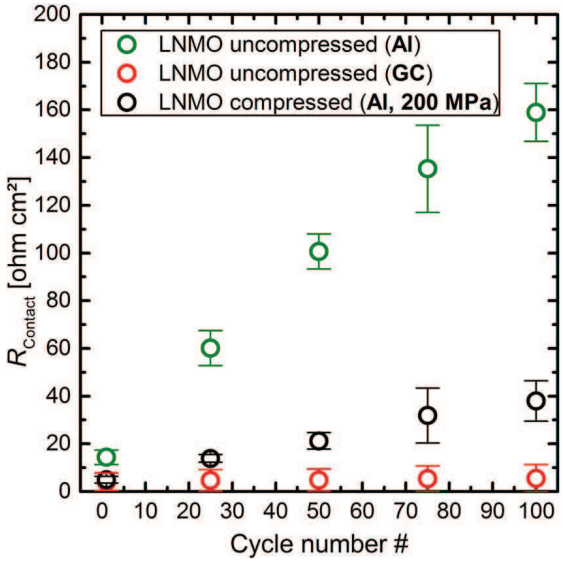

Figure 7. Contact resistances for LNMO cathodes (with 1.5% carbon black) cycled in graphite/LNMO cells (at 1C and 40°C, after 2 formation cycles at 0.1C and 25°C), as determined from a simultaneous fit of impedance spectra measured in blocking- and non-blocking conditions (see Figure 6) with a transmission-line equivalent circuit as described in Reference 18. Green circles: uncompressed LNMO cathodes on aluminum (Type III, see Table I); black circles: compressed LNMO cathodes on aluminum (Type II, see Table I); red circles: LNMO cathodes on glassy carbon (Type IV, see Table I). The error bar represents the standard deviation of two cells and the first data points represent $R_{Cont.}$ after two formation cycles at C/10.

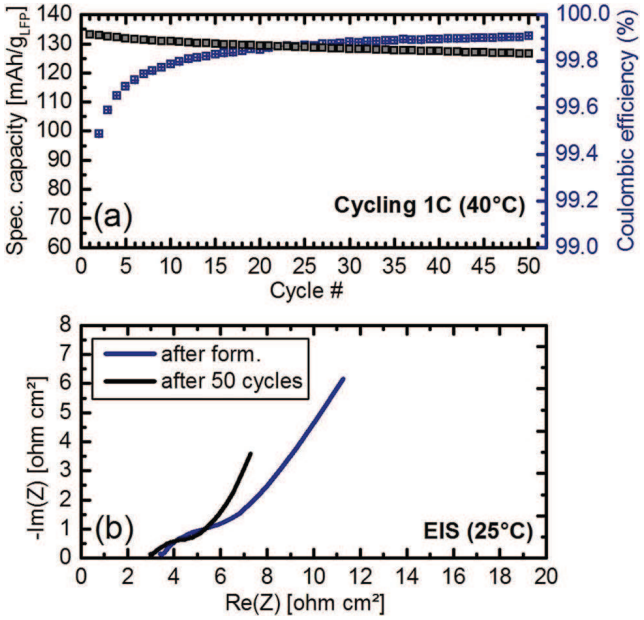

Figure 8. a) Specific discharge capacity (black symbols) and coulombic efficiency (blue symbols) of graphite/LFP cells cycled with pristine LP57 electrolyte between 2.0–4.0 V at 1C and 40°C (CCCV charge until C/20, and CC discharge). Two Formation was done at C/10 and 25°C (2 cycles, not shown). b) Impedance spectra of an LFP cathode measured at 50% SOC after formation (blue line) and after 50 cycles (black line). The impedance is recorded from 100 kHz to 100 mHz with a perturbation of 15 mV at 25°C under open circuit conditions.

$LiPF_6$ to HF, which in turn would convert the (oxidized) aluminum surface to the AlF_3 surface layer they had observed by XPS. This is consistent with the facts that (i) protic species rapidly react with $LiPF_6$ to HF,[32] and that (ii) the addition of HF into electrolytes with more stable salts also leads to AlF_3 formation, as determined by XPS.[27] We therefore believe that the protic species produced by the electrochemical electrolyte oxidation reaction at the LNMO cathode in graphite/LNMO full cells gradually converts the native aluminum oxide surface film into a growing layer of AlF_3, thereby degrading the quality of the electronic contact at the Al/LNMO interface. Furthermore, the reported pitting corrosion on aluminum current collectors cycled in an $LiPF_6$ containing electrolyte could also contribute to the observed increasing contact resistance over cycling.[28] In either case, this explains why a growing contact resistance is only observed for LNMO cathode coated on aluminum and not on glassy carbon, which would not form an insulating layer with HF (see Figure 7). Comparing compressed and uncompressed LNMO electrodes coated on aluminum (green and black symbols in Figure 7), the linear increase of $R_{Cont.}$ over cycling is lower for compressed electrodes, underlining that the Al/LNMO interface conductivity upon compression is improved, even though an insulating surface layer continues to grow over cycling. This result also demonstrates that compression of high-voltage cathodes is very important, as the increasing resistance lowers the energy density of the cells. In the following section, we investigate the evolution of $R_{Cont.}$ in the absence of electrolyte oxidation, which can be done by examining $R_{Cont.}$ vs. cycle number in graphite/LFP cells.

Investigation of the cathode/aluminum contact resistance in graphite/LFP cells.—In order to prove that the presence/formation of HF really causes the growth of the above discussed interfacial contact resistance, we introduced a controlled amount of HF into the electrolyte of a graphite/LFP cell. Since these cells are typically cycled to an upper cutoff cell voltage of 4.0 V, corresponding to a maximum cathode potential of only ≈4.1 V vs. Li^+/Li, the electrolyte should be stable against oxidation, so that the impact of HF on the cathode impedance response can be observed independent of other effects which might be caused by electrolyte oxidation. For this purpose, a sample of the standard LP57 electrolyte was mixed with 1000 ppm of deionized water and stirred for 5 days. As previously reported in the literature, water reacts with $LiPF_6$ according to the following mechanism:[33,34]

$$LiPF_6 \rightleftharpoons LiF \downarrow + PF_5 \quad [1]$$

$$PF_5 + H_2O \rightarrow POF_3 + 2\,HF \quad [2]$$

Consistent with the literature,[21] the completion of these reactions after 5 days was confirmed by Karl-Fischer-Titration and by ^{19}F NMR (experimental section), yielding ≈2000 ppm HF. To investigate the effect of HF on the cathode impedance, T-cells with the LP57 electrolyte without and with ≈2000 ppm HF were assembled as described in the experimental section. For each cell, impedance spectra of the cathode were acquired at open circuit-conditions at 50% SOC and 25°C (non-blocking conditions), both after two formation cycles (C/10 at 25°C) and after 50 charge/discharge cycles (1C at 40°C). The cycling data and the cathode impedance spectra of the cell containing the pure LP57 electrolyte (without added HF) are shown in Figure 8. The specific discharge capacity at 1C decreases from ≈133 mAh/g_{LFP} to ≈127 mAh/g_{LFP} over the course of 50 cycles (capacity retention of ≈95%), with coulombic efficiencies increasing from 99.4% to 99.9%. The impedance spectra at 50% SOC both before and after cycling do not show a visible high frequency semi-circle, which indicates that the contact resistance is negligible. We believe that the minor but noticeable onset for a contact resistance at highest frequencies stems from the contact between LFP and the aluminum foil, which likely has a thin oxide or fluoride surface layer that may impose a small electronic resistance.

The cycling data and impedance spectra of the cells containing the LP57 electrolyte with ≈2000 ppm HF are shown in Figure 9. Here, the specific discharge capacity at 1C decreases from ≈111 mAh/g_{LFP} to ≈94 mAh/g_{LFP} (capacity retention of ≈85%), with coulombic efficiencies increasing from 99.2% to 99.8%. Thus, the graphite/LFP cell

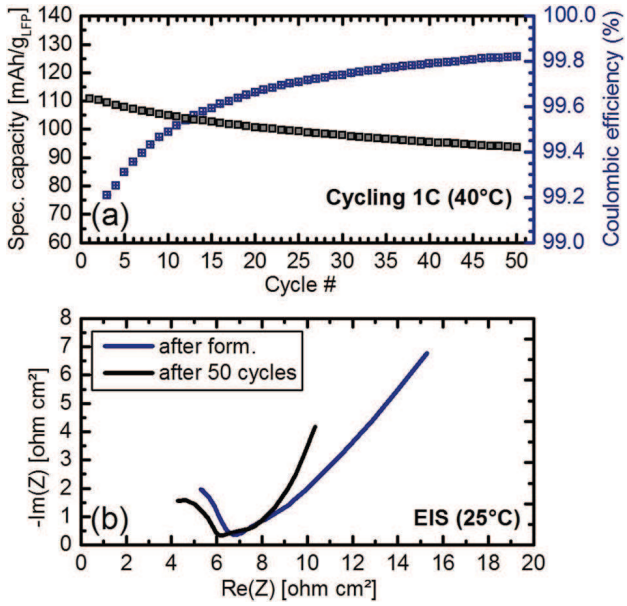

Figure 9. a) Specific discharge capacity (black symbols) and coulombic efficiency (blue symbols) of graphite/LFP cells cycled with LP57 electrolyte + ≈2000 ppm HF between 2.0–4.0 V at 1C and 40°C (CCCV charge until C/20, and CC discharge). Two Formation was done at C/10 and 25°C (2 cycles, not shown). b) Impedance spectra of an LFP cathode measured at 50% SOC after formation (blue line) and after 50 cycles (black line). The impedance is recorded from 100 kHz to 100 mHz with a perturbation of 15 mV at 25°C under open circuit conditions.

containing HF-contaminated electrolyte shows a significantly lower initial discharge capacity as well as poorer coulombic efficiencies and inferior capacity retention than the graphite/LFP cell cycling with LP57 electrolyte without intentionally added HF. This could be caused by (i) reaction of parts of the HF with the lithiated graphite anode to H_2 and LiF,[21] and/or (ii) by HF-facilitated dissolution of iron from the LFP lattice, which has previously been reported by Amine et al.[35] Most notably, however, the impedance spectra of the cathode in Figure 9b show a clearly pronounced semi-circle in the high-frequency region, which is present before and after cycling and remains almost constant in magnitude. The capacitance of this semi-circle is in the order of ≈0.5 μF/cm^2, what clearly indicates the interface coating/current collector. In light of the above experiments on graphite/LNMO cells, this means that the addition of HF to a graphite/LFP cell leads to the formation of a contact resistance at the Al/LFP interface. The fact that this contact resistance does not change significantly over cycling implies either that the HF added to the electrolyte is likely being consumed directly after cell assembly or within the first few cycles (e.g., by reaction with the cell materials or by its reduction to LiF and H_2 at the anode);[21] it could also be due to the rather large carbon content of the compressed LFP cathode, which slows down the growth of $R_{Cont.}$ (see Figure 2). While this question cannot be resolved here, it is clear that HF present in the electrolyte does lead to a contact resistance at the Al/cathode interface due to the formation of an insulating surface film on the aluminum current collector. Since HF is most likely formed upon electrolyte oxidation in PF_6^- based electrolytes (see above discussion), Figure 9b provides further evidence that the increase of $R_{Cont.}$ upon cycling graphite/LNMO cells at elevated temperature is a consequence of continuous electrolyte oxidation and HF formation.

These results show that the impedance increase of high-voltage cathodes is caused by electrochemical electrolyte oxidation and concomitant formation of an insulating surface film on the aluminum current collector. In graphite/LNMO cells, electrolyte oxidation and the subsequent deposition of transition metals on the anode are the main ageing phenomena at elevated temperatures.[8] However, as the voltage profile is very flat, the increased overpotential (from $R_{Cont.}$) is not very strongly reflected in the capacity retention of graphite/LNMO cells (see Figure 4), particularly when charging is conducted in CCCV mode. However, a growing $R_{Cont.}$ will more strongly affect the energy retention and the round-trip efficiency of graphite/LNMO cells, as it increases/lowers the average charge/discharge voltage. When other high voltage cathodes are considered, as for example overlithiated manganese-rich NCMs (also referred to as HE-NCM) which operate at up to 4.7 V,[36] an increase in the cathode impedance caused by contact resistances with the Al/cathode interface is expected to lead to a more significant capacity fading (and energy fading) to the steeper voltage profile.

Conclusions

The impedance of a high-voltage LNMO cathode is dominated by a high-frequency semi-circle which increases upon cycling at elevated temperatures (≥40°C). It was shown that this impedance feature is characterized by a low interfacial capacitance, a very weak temperature-dependence, and a strong cell stack compression dependence, based on which it can be ascribed unambiguously to an electronic contact resistance at the LNMO cathode/aluminum current collector interface ($R_{Cont.}$). By comparing LNMO cathodes coated either on aluminum or glassy carbon current collectors, it could be shown that this interfacial contact resistance is mainly caused by the formation of an insulating surface film on the aluminum current collector rather than by the corrosion of the conductive carbon in the cathode electrode. The evolution of $R_{Cont.}$ upon cycling of graphite/LNMO cells with a micro-reference electrode was quantified by an impedance methodology where cathode impedance spectra are acquired under both non-blocking (10% SOC) and blocking conditions (100% SOC), the simultaneous fitting of which enables a straightforward deconvolution of the various resistances contributing to the overall cathode impedance.

As the literature suggests that protic species can be formed upon electrolyte oxidation at high potential, which in turn react with $LiPF_6$ to HF, we examined the effect of HF on the formation of a contact resistance in graphite/LFP cells. Indeed, adding an HF-contaminated electrolyte to a graphite/LFP cell, which operates at potentials where no electrolyte oxidation occurs, we could demonstrate that this results in the appearance of a high-frequency semi-circle corresponding to a contact resistance at the Al/LFP interface. This phenomenon will be also critical for other high-voltage cathode active materials like overlithiated manganese-rich NCM.

Acknowledgment

Financial support by the BASF SE through its Research Network on Electrochemistry and Batteries is gratefully acknowledged. M. W. acknowledges funding by the German Federal Ministry for Economic Affairs and Energy (project LiMo, grant number 03ET6045D) and J. L. acknowledges support by the German Federal Ministry of Education and Research (project ExZellTUM II, grant number 03XP0081).

ORCID

Daniel Pritzl https://orcid.org/0000-0002-9029-107X
Andreas E. Bumberger https://orcid.org/0000-0001-9346-4864
Morten Wetjen https://orcid.org/0000-0002-2357-1151
Johannes Landesfeind https://orcid.org/0000-0003-0333-2185
Sophie Solchenbach https://orcid.org/0000-0001-6517-8094

References

1. V. Etacheri, R. Marom, R. Elazari, G. Salitra, and D. Aurbach, *Energy Environ. Sci.*, **4**, 3243 (2011).
2. A. H. Tkaczyk, A. Bartl, A. Amato, V. Lapkovskis, and M. Petranikova, *J. Phys. D. Appl. Phys.*, 51 (2018).
3. C. Banza Lubaba Nkulu, L. Casas, V. Haufroid, T. De Putter, N. D. Saenen, T. Kayembe-Kitenge, P. Musa Obadia, D. Kyanika Wa Mukoma, J. M. Lunda Ilunga, T. S. Nawrot et al., *Nat. Sustain.*, **1**, 495 (2018).
4. J.-H. Kim, N. P. W. Pieczonka, and L. Yang, *ChemPhysChem*, **15**, 1940 (2014).

5. H. Duncan, D. Duguay, Y. Abu-Lebdeh, and I. J. Davidson, *J. Electrochem. Soc.*, **158**, A537 (2011).
6. D. Lu, M. Xu, L. Zhou, A. Garsuch, and B. L. Lucht, *J. Electrochem. Soc.*, **160**, A3138 (2013).
7. A. Bhandari and J. Bhattacharya, *J. Electrochem. Soc.*, **164**, A106 (2017).
8. N. P. W. Pieczonka, Z. Liu, P. Lu, K. L. Olson, J. Moote, B. R. Powell, and J.-H. Kim, *J. Phys. Chem. C*, **117**, 15947 (2013).
9. K. Leitner, H. Wolf, A. Garsuch, F. F. Chesneau, and M. Schulz-Dobrick, *J. Power Sources*, **244**, 548 (2013).
10. R. Jung, M. Metzger, F. Maglia, C. Stinner, and H. Gasteiger, *J. Phys. Chem. Lett.*, **8**, 4820 (2017).
11. R. Jung, M. Metzger, F. Maglia, C. Stinner, and H. A. Gasteiger, *J. Electrochem. Soc.*, **164**, A1361 (2017).
12. M. Metzger, B. Strehle, S. Solchenbach, and H. A. Gasteiger, *J. Electrochem. Soc.*, **163**, A798 (2016).
13. J. Cha, J. G. Han, J. Hwang, J. Cho, and N. S. Choi, *J. Power Sources*, **357**, 97 (2017).
14. D. Aurbach, B. Markovsky, Y. Talyossef, G. Salitra, H.-J. Kim, and S. Choi, *J. Power Sources*, **162**, 780 (2006).
15. H. Duncan, Y. Abu-Lebdeh, and I. J. Davidson, *J. Electrochem. Soc.*, **157**, A528 (2010).
16. M. Gaberscek, J. Moskon, B. Erjavec, R. Dominko, and J. Jamnik, *Electrochem. Solid-State Lett.*, **11**, A170 (2008).
17. S. Srinivasan, *Fuel Cells: From Fundamentals to Applications*.
18. J. Landesfeind, D. Pritzl, and H. A. Gasteiger, *J. Electrochem. Soc.*, **164**, A1773 (2017).
19. S. Solchenbach, D. Pritzl, E. J. Y. Kong, J. Landesfeind, and H. A. Gasteiger, *J. Electrochem. Soc.*, **163**, A2265 (2016).
20. D. Pritzl, J. Landesfeind, S. Solchenbach, and H. A. Gasteiger, *J. Electrochem. Soc.*, **165**, A2145 (2018).
21. D. Strmcnik, I. E. Castelli, J. G. Connell, D. Haering, M. Zorko, P. Martins, P. P. Lopes, B. Genorio, T. Østergaard, H. A. Gasteiger, F. Maglia, B. K. Antonopoulos, V. R. Stamenkovic, J. Rossmeisl, and N. M. Markovic., *Nat. Catal.*, **1**, 255 (2018).
22. D. Pritzl, S. Solchenbach, M. Wetjen, and H. A. Gasteiger, *J. Electrochem. Soc.*, **164**, A2625 (2017).
23. M. Gaberscek, J. Moskon, B. Erjavec, R. Dominko, and J. Jamnik, *Electrochem. Solid-State Lett.*, **11**, A170 (2008).
24. N. Ogihara, S. Kawauchi, C. Okuda, Y. Itou, Y. Takeuchi, and Y. Ukyo, *J. Electrochem. Soc.*, **159**, A1034 (2012).
25. J. Landesfeind, J. Hattendorff, A. Ehrl, W. A. Wall, and H. A. Gasteiger, *J. Electrochem. Soc.*, **163**, A1373 (2016).
26. J. W. Braithwaite, A. Gonzales, G. Nagasubramanian, S. J. Lucero, D. E. Peebles, J. A. Ohlhausen, and W. R. Cieslak, *J. Electrochem. Soc.*, **146**, 448 (1999).
27. K. Kanamura, T. Umegaki, S. Shiraishi, M. Ohashi, and Z. Takehara, *J. Electrochem. Soc.*, **149**, A185 (2002).
28. X. Zhang and T. M. Devine, *J. Electrochem. Soc.*, **153**, B375 (2006).
29. X. Zhang, B. Winget, M. Doeff, J. W. Evans, and T. M. Devine, *J. Electrochem. Soc.*, **152**, B448 (2005).
30. T. Ma, G. L. Xu, Y. Li, L. Wang, X. He, J. Zheng, J. Liu, M. H. Engelhard, P. Zapol, L. A. Curtiss, J. Jorne, K. Amine, and Z. Chen, *J. Phys. Chem. Lett.*, **8**, 1072 (2017).
31. S. S. Zhang, K. Xu, and T. R. Jow, *J. Electrochem. Soc.*, **149**, A586 (2002).
32. S. Solchenbach, M. Metzger, M. Egawa, H. Beyer, and H. A. Gasteiger, *J. Electrochem. Soc.*, **165**, A3022 (2018).
33. D. Aurbach, A. Zaban, Y. Ein-Eli, I. Weissman, O. Chusid, B. Markovsky, M. Levi, E. Levi, A. Schechter, and E. Granot, *J. Power Sources*, **68**, 91 (1997).
34. T. Kawamura, A. Kimura, M. Egashira, S. Okada, and J. I. Yamaki, *J. Power Sources*, **104**, 260 (2002).
35. K. Amine, J. Liu, and I. Belharouak, *Electrochem. commun.*, **7**, 669 (2005).
36. M. M. Thackeray, S.-H. Kang, C. S. Johnson, J. T. Vaughey, R. Benedek, and S. A. Hackney, *J. Mater. Chem.*, **17**, 3112 (2007).

3.2 Washing of Ni-rich cathode materials

This section presents the article *Washing of nickel-rich cathode materials for lithium ion batteries – Towards a mechanistic understanding* which is on the way to be submitted to a peer-reviewed Journal. The article was presented by Daniel Pritzl at the Cancun, Mexico Meeting of the Electrochemical Society in October 2018.

Compared to an LNMO cathode, Ni-rich cathode materials show a very high reactivity towards moisture and CO_2 from the air. This leads to the rapid formation of LiOH and Li_2CO_3 on the surface of the materials.[81] The surface impurities deteriorate the cycling performance and lead to severe gassing and impedance increase.[83] In order to remove these surface impurities, a very simple method can be used called *washing*. Here the cathode material is stirred in water for a certain amount of time and then dried. Xiong et al.[114] shows that washing removes LiOH and Li_2CO_3 from the surface and that a more stable cycling could be achieved with a washed material versus a non-washed material. The only drawback is that upon washing, active lithium is lost and therefore the initial discharge capacity is lower. Kim et al.[84] showed similar results for an NCA cathode.

The purpose of this study is a detailed understanding of the washing process,which so far is lacking in the literature. The materials were washed in an argon-filled glovebox twice (20 minutes with a water/CAM ratio of 5/:1) and the wash solutions were analyzed by titration. We expected to find LiOH in the first wash solution and the absence of it in the second solution (after washing the once washed material again). Surprisingly, we can find LiOH also in the second wash solution what correlates well with pH measurements. OEMS measurement show that a washed material shows a drastically reduced gassing of O_2 and CO_2 in the first cycle. Interestingly, the gas amounts are getting lower with increasing drying temperature after washing. Impedance measurements show that the washing process leads to an increased cathode resistance, which scales with drying temperature. By TGA-MS measurements we could show that the oxygen release from the cathode is not happening during the washing (via MS) but during the drying process (TGA-MS). Combining all the results, we propose a mechanism on how the washing process of NCM cathode materials proceeds: First, the surface is

transformed into a NiOOH structure through a proton exchange with lithium ions. Afterwards, the NiOOH phase is thermally decomposed above 80 °C, leading to an O_2-defiecient layer on the surface, which is consistent with the OEMS and impedance measurements.

The very important finding of this study, which has not been shown in any previous publication (to the best of our knowledge) is that a surface transformation (layer to spinel/rock salt) is achieved after washing leading to a decreased O_2 release from the surface of the NCM's. Jung et al.[67] showed that this surface oxygen leads to the oxidation of the electrolyte and then to a decrease in cycling performance. Whenever this oxygen release is absent, no chemical electrolyte oxidation can happen and explain the improved cycling after washing reported by Xiong et al.[114] and Kim et al.[84]

Author contributions

The washing experiments were performed by D.P. and T.T. The OEMS measurement was performed by T.T, A.T.S.F. and D.P. The mechanism was developed by J.S., D.P. and H.A.G. Data analysis was done by D.P. and T.T. and A.T.S.F. The manuscript was written by D.P., and T.T. All authors discussed the data and commented on the results.

Washing of nickel-rich cathode materials for lithium-ion batteries – Towards a mechanistic understanding

Daniel Pritzl[1#,=], Tobias Teufl[1,2,=], Anna T.S. Freiberg[1], Benjamin Strehle[1], Johannes Sicklinger[1], Heino Sommer[2], Pascal Hartmann[2] and Hubert A. Gasteiger[1]

[1] Chair of Technical Electrochemistry, Department of Chemistry and Catalysis Research Center,

Technical University of Munich, Munich, Germany

[2] BASF SE, New Battery Materials and Systems, Ludwigshafen, Germany

[#]corresponding author

[=]equal contribution

Abstract

Washing is a commonly used method to remove surface impurities of cathode materials for lithium-ion batteries. However, a clear mechanistic understanding of the washing process is missing in the literature. In this study, we will investigate the effect of washing of nickel-rich NCM cathodes (85% nickel) with respect to gassing and impedance of the washed cathodes. By on-line electrochemical mass spectrometry (OEMS), we will show a drastic reduction of the O_2 release above 80% SOC for a sample washed in water, suggesting a reduction of the NCM cathode's surface. The modification of the surface can be confirmed by a strong impedance increase of the washed cathode measured via a reference electrode in a full-cell. Last, we will show a conclusive mechanism about the washing process of nickel-rich NCM materials and identify the drying temperature after washing as the dominant factor influencing the surface properties.

Introduction

Lithium-ion batteries are considered as a viable option for energy storage in electric vehicles (EV's). In order to reach the goal of a widespread application in electrical vehicles, many obstacles have to be overcome with respect to cost, driving range and charging times.[1, 2] The most critical factor for an increase in energy density (and hence an increase in driving range) for future Li-ion batteries is the capacity of the cathode active material (CAM).[2] One of the most promising class of cathode materials therefor are the so called NCM and NCA materials, both having a layered structure with the sum formula $LiMeO_2$ (Me = Ni, Co, Mn for NCM and Me = Ni, Co, Al for NCA). In state of the art vehicles mid nickel NCM-523 (Ni:Co:Mn = 5:2:3) cathodes are already used,[3] showing good structural stability during lithium extraction/insertion and reasonable capacities of ≈160mAh/g.[3] However, to increase the specific capacity with acceptable upper cutoff voltages, recent trends tend to increasing nickel contents, leading to nickel rich NCMs (Ni:Co:Mn ≥ 8:1:1).[4] These nickel-rich materials can lead to reversible capacities of up to ≈180 mAh/g at reasonable cutoff potentials (4.2 V vs. graphite). For these high nickel materials not only manganese can be used to stabilize the structure,[5] but it can also be replaced by aluminum leading to nickel-rich NCA, which Tesla had been using for many years.[3]

However, the increasing capacity of nickel-rich materials comes at the cost of faster capacity fading and higher sensitivity towards storage and cycling conditions.[6, 7] It turned out that Ni-rich materials are very sensitive toward storage under humidity and CO_2 containing atmospheres,[6-9] leading to the formation of large amounts of hydroxides and carbonates on the surface of the particles.[10-16] These surface impurities do not only lead to a deterioration of the capacity retention,[6, 8, 9] but also cause high gas evolution in commercial cells[8, 17-20] and lead to a high pH causing gelation of the slurry during electrode preparation.[21, 22] As a very simple and practical solution to remove surface contaminants most cell and material manufacturer included a washing step in which the active material is washed in an aqueous solution.[22, 23] This washing step can significantly lower the pH value of the slurry[22, 24] and can thus prevent gelation during the electrode coating process. Kim et al.[25] have also shown that washing of nickel-rich cathodes can efficiently prevent gas evolution during high temperature storage experiments. It has been initially suggested that washing of NCA simply removes carbonate and hydroxide impurities from the cathode material surface and therefore improves the material properties[24] whereas other reports suggest also a reaction with the active material itself.[22, 26] While washing of NCA powder significantly improves the cycling stability at room temperature and C-rates as low as

C/5,[24] there is clear evidence that washing of NCA has a negative effect on the 45 °C cycle performance at 1C discharge,[22] pointing towards a thermal instable surface which in consequence leads to the formation of a resistive surface layer.[26] On the other hand, heat treatment of the washed samples could show that a recalcination at 700 °C can regain the initial surface structure and thus recover the electrochemical performance after removal of the surface impurities.[26] While it seems obvious that a NCM surface without any hydroxides or carbonates should perform best, it turned out that synthesis of an entirely virgin surface shows poor electrochemistry and a certain exposure to ambient conditions is required for a sufficient surface termination.[11] In this respect, it has been shown that nickel-rich NCMs strongly tend to the formation of a spinel type structure at SOCs > 80%, induced by oxygen release,[27, 28] leading to chemical electrolyte oxidation[29] and a high impedance build-up,[27] following a similar mechanism thatw as described for Li- and Mn-rich NCMs.[30] At the moment many different surface stabilizations strategies are under investigation to stabilize the surface of nickel-rich layered cathode materials, such as surface sulfatation,[31] recalcination after storage,[8, 9, 32] as well as surface coatings with spinel structures[33] or core-shell particles.[34] Considering the results by Paulsen et al.[11], we suggest that washing of nickel-rich materials does not only remove the surface impurities but also induces a significant reaction with the active material surface, e.g. by lithium proton exchange that has been suggested from literature.[9, 35, 36] While washing of nickel-rich cathode materials is a well-known industrial process and is already implemented by most of the battery manufacturers there is still a significant lack of scientific literature providing a profound understanding about the exact mechanism and the effect of these washing procedures. Therefore, we think that a detailed understanding of the washing process can open a new path towards surface modification strategies of nickel-rich cathode materials.

In this study we will examine the reactions that occur during the washing of nickel-rich cathode materials in deionized water and its effect onto the electrochemistry and the gas evolution. These studies will be conducted with a Ni-rich material, having the sum formula $LiNi_{0.85}Co_{0.10}Mn_{0.05}O_2$, also referred to as NCM 851005. For this study, we measured the pH during washing, as well as the LiOH and Li_2CO_3 contents of the wash solution. By on-line electrochemical mass spectrometry (OEMS) we could prove that washing has a significant influence on the oxygen release and the gas evolution of the material which can be rationalized by the formation of an oxygen deficient surface layer during the drying step. While washing can prevent oxygen release and can remove hydroxide and carbonate impurities from the surface, we can clearly show by impedance and OEMS that the drying temperature influences the properties of the newly formed interface. Thus, we prove that washing of nickel-rich

materials not only removes the surface impurities but also strongly reacts with the materials surface and therefore needs to be analyzed in detail in order to stabilize nickel-rich cathode materials.

Experimental

Washing process of NCM851005 powder — For the washing process, deionized water (18 MΩcm, Merck KGaA, Germany) was used. 20 g of NCM851005 were given into 100 mL of purified water and stirred for 20 minutes. The solution was then filtered, and the washed material dried in a vacuum oven for at least 4h (either at 25 °C or 65 °C, see Table 1). The once washed material was then washed again (20 g material in 100 g of purified water) and the suspension was filtered again. In both wash solutions (from the first and second washing), the concentration of LiOH and Li_2CO_3 were determined by titration with HCl. The pH-measurements and the titration experiments were carried out in an argon atmosphere. All other experiments conducted in ambient air. The material after the second washing was dried for 12h with four different drying conditions: 80 °C, 180 °C and 300 °C in a vacuum oven and one sample was freeze dried and used for further analysis. The freeze drying was carried out in a vessel with washed material, which was put into liquid nitrogen and dynamic vacuum was applied for 12h. The detailed drying conditions of all used materials with water to CAM ratio, atmosphere, drying temperature between first and second washing and final drying temperature are listed in Table 1.

Table 1: Summarized information about the washing procedure with information about the experiment, water to CAM ratio, atmosphere and drying temperatures (under dynamic vacuum).

NCM powder	H_2O/CAM ratio	Atmosphere (washing)	Drying temperature between 1. and 2. Washing in vacuum	Final drying temperature
Pristine	---	air	---	120 °C (12h)
25 °C sample	5/1	air	25 °C for 4h	Freeze dry, 25 °C (12h)
80 °C sample	5/1	air	65 °C for 4h	80 °C (12h)
180 °C sample	5/1	air	65 °C for 4h	180 °C (12h)
300 °C sample	5/1	air	65 °C for 4h	300 °C (12h)

Electrode preparation — Electrodes for OEMS measurements were prepared by dispersing 96 wt.% $LiNi_{0.85}Co_{0.10}Mn_{0.5}O_2$ (NCM851005) (BASF SE, Germany), 2 wt.% conductive carbon (Super-C65, Timcal, Switzerland), and 2 wt.% polyvinylene difluoride PVDF binder (Kynar HSV 900, Arkema, France) in N-methyl-2-pyrrolidone NMP (anhydrous, Sigma-Aldrich, USA). A high solid content of 70% for the slurry was chosen to enable coating onto a porous stainless-steel mesh (SS316, aperture 26 µm, wire diameter 25 µm, The Mesh Company Ltd., UK). The slurry was mixed in a planetry mixer (Thinky Corp.) for 10 min. and coated onto the stainless-steel mesh, yielding a NCM loading of ≈12 mg/cm^2, corresponding to ≈3.3 mAh/cm^2 (based on a theoretical capacity of 275 mAh/g for 100% delithiation). Electrodes for OEMS experiments were punched out with a diameter of 15 mm.

For impedance measurements, NCM851005 electrodes were prepared by mixing $LiNi_{0.85}Co_{0.10}Mn_{0.5}O_2$ (NCM851005) (commercial, BASF SE, Germany), carbon black (Super C65, Timcal), and polyvinylene difluoride (PVDF, Kynar) at a mass ratio of 96/2/2 with NMP (N-methyl pyrrolidone, anhydrous, Sigma-Aldrich, Germany) in a planetary mixer (Thinky Corp.) for 15 min. The ink was coated onto aluminum foil (MTI, 18 µm) with a doctor blade coater and dried afterwards at 50 °C in a convection oven for at least 3h. The final NCM851005 coating had a loading of ≈9 mg_{NCM}/cm², corresponding to ≈2 mAh/cm² (based on a first charge capacity of 215 mAh/g at 4.2 V cell cut-off). In this specific case, the theoretical capacity was defined by the first charge capacity in order to guarantee sufficient full-cell balancing. Electrodes with a diameter of 11 mm (≡0.95 cm^2) were punched out and compressed to ≈30% porosity with a KBr press.

Graphite electrodes were prepared by mixing graphite (commercial, T311, SGL Carbon, Germany) and PVdF at a mass ratio of 95/5 with NMP by applying the same procedure as for the positive electrodes. The graphite ink was coated onto copper foil (MTI, 12 µm) and dried in a convection oven at 50 °C for 3 h. The loading of the graphite coating was ≈6 $mg_{graphite}$/cm² corresponding to ≈2.05 mAh/cm² (based on a specific capacity of 340 mAh/g). The electrodes were punched out with a diameter of 11 mm and compressed to a porosity of ≈30%. All anodes were dried under dynamic vacuum at 120 °C. The cathodes were dried at 25 °C (for the freeze dried material), at 80 °C (for the CAM which was dried at 80 °C prior to coating, see Table 1) and all other cathodes at 120 °C for at least 12 h in a vacuum oven (Büchi, Switzerland) and then transferred into an Argon-filled glovebox (MBraun, Germany) without exposure to air.

***On-line electrochemical mass spectrometry (OEMS)* —** For OEMS experiments, electrodes coated onto a stainless-steel mesh (see above) were used to have a porous medium as current collector in order to allow fast diffusion of evolved gases from the electrode to the capillary.[37] For OEMS measurements a custom-made one-compartment cell is used; the cell design as well as the OEMS setup were reported previously.[38] OEMS cells were assembled with a lithium metal counter electrode, one glassfiber separator (200 µm thickness, VWR, Germany), a NCM working electrode and 120 µl of electrolyte composed of EC-only with 1.5M $LiPF_6$ (BASF SE, Germany). The cells were connected to the mass spectrometer, held for 4 h at OCV (open circuit voltage), and then charged to 5.0 V vs. Li^+/Li at a C/10 rate (C-rates here are calculated based on a nominal capacity of 275 mAh/g). For quantification of the mass spectrometer currents, a calibration gas containing O_2 and CO_2, (each 2000 ppm) in Argon (Linde AG, Germany) was used. All currents were normalized to the current at m/z = 36 (Ar isotope) in order to correct for effects of minor pressure and temperature deviations. The currents m/z = 32 (O_2) and m/z = 44 (CO_2) were converted into gas concentration.

***Modified OEMS setup for water addition to NCM powder* —** The above described setup was modified in order to add a defined amount of water to an NCM851005 powder. Consequently, the OEMS cell was replaced by a Swagelok T-fitting, which was connected to the MS system. The other two openings of the Swagelok fitting were equipped with a septum in order to introduce water with a syringe and with a standard closed nut where 0.5 g NCM851005 powder was added. After a 40 minutes rest phase, a syringe with argon from the glovebox was added to the system in order to check for the tightness of the septum. After 60 minutes of recording the mass traces of O_2, H_2O and N_2, 2.5 mL of purified water were dozed to the NCM powder and the mass traces were further recorded.

***Electrochemical Impedance Spectroscopy (EIS)* and charge/discharge cycling —** The impedance of the cathode was measured with a gold wire reference electrode (GWRE) as reported in an earlier publication.[39] Before measuring the impedance, two formation cycles of the graphite/NCM851005 cells were carried out at 25 °C in the voltage range of 4.2 V – 3.0 V Cell Voltage. The charging protocol consisted of a constant current constant voltage (CCCV) charge with a cut-off for the CV phase of C/20. The discharge was carried out in CC mode. After formation, the cells were charged to 50% SOC by a 5h charge with C/10 based on the second discharge capacity. After 1h of a rest phase, the impedance was recorded in

potentiostatic mode from 100 kHz to 100 mHz with a perturbation of 10 mV. Afterwards charge discharge cycling was carried out with a CCCV charge to 4.2 V with C/2 and a CC discharge to 3.0 V with 1C at 25 °C for 198 cycles.

X-ray photoelectron spectroscopy (XPS) — Surface analysis of the pristine and 2x washed sample (dried at 180 °C) was carried out by X-ray photoelectron spectroscopy (Axis, Supra, Kratos, UK). The powders were pressed to pellets inside an argon-filled glovebox and mounted on an electrically insulated sample holder, which can be transferred from the glovebox into the XPS system without any air exposure. The sample was kept in the pre-antechamber until a pressure of $\approx 10^{-8}$ Torr and was then transferred to the sample analysis chamber (SAC) where the pressure was always kept below $\approx 10^{-9}$ Torr during the whole measurement period. Sample irradiation was carried out with a monochromated Al Kα radiation (1486.6 eV) with an emission current of 15 mA. Survey spectra were recorded for all samples with a stepsize of 0.5 eV and at a pass energy (PE) 160 eV. Elemental spectra were recorded with a stepsize of 0.2 eV and an emission current of 15 mA. For all measurements, a charge neutralizer was used, and the spectra were calibrated to the adventitious carbon peak with a binding energy (BE) of 284.8 eV.

Thermogravimetric Analysis with coupled Mass Spectrometry (TGA-MS)

For TGA-MS analysis a TGA system (Mettler Toledo, Switzerland) coupled to a mass spectrometer (Pfeiffer Vacuum, Germany) was used. All samples analyzed by TGA-MS were dried in a vacuum oven (Büchi, Switzerland) for at least 3 h at 120 °C under dynamic vacuum. The as dried samples, washed twice in water and the pristine NCM851005 were analyzed with the following protocol: First a conditioning at 25 °C for 10 minutes with an argon flow rate of 200 mL/min. Afterwards the flow rate was changed to 20 mL/min and again a rest phase of 10 minutes at 25 °C was carried out. Then the temperature was increased from 25 °C to 120 °C at 10 K/min. Here, the temperature was held for 40 minutes. The last step includes a heat ramp (10 K/min) to 450 °C with a hold phase of 50 minutes. All mass traces from the MS were normalized to the nitrogen signal (m/z = 28).

Results

Li_2CO_3 & LiOH concentration and pH-value of NCM851005 in water — For the washing process, the cathode material NCM851005 was selected as it is known that the formation of surface contaminants, such as LiOH and Li_2CO_3, is most crucial for nickel-rich materials.[9, 21] For the determination of LiOH and Li_2CO_3, the washing process is carried out in an argon-filled glovebox in order to exclude any effects of CO_2 from the air. 20 g of NCM851005 are dissolved in a solution of 100 mL degassed water and stirred for 20 minutes (referred to as "First Washing"). Afterwards the wash solution is filtered, and the powder is then stored in a drying oven at 65 °C for at least 4h. After that, the powder is washed again in 100 mL of water for 20 minutes (referred to as " Second Washing").

The lithium carbonate content is determined by titration and shown in Figure 1. After the first washing, the amount of lithium carbonate is found to be ≈6.4 ± 0.2 mg Li_2CO_3 per gram NCM (red bar). This would correspond to 6450 ppm of Li_2CO_3 on the surface of the active material which compares well with the high carbonate impurities reported by Noh et al.[21] who found roughly 15000 ppm on their 85% nickel containing NCM material. The differences in ppm might be found in the specific storage conditions and surface areas of the materials, which are different for each research group. After the first washing, the material is dried in a vacuum oven in the glovebox and then washed again in the glovebox. Interestingly, no more lithium carbonate can be detected in the wash solution after the second washing. The absence of lithium carbonate in the second wash solution can easily be rationalized by the low values of CO_2 in the glovebox, the high solubility of Li_2CO_3 in the washing water, the long washing time and the high water/CAM ratio.

The LiOH content is also determined by titration and the amount after washing the material once is shown in Figure 1. After the first washing ≈4.6 ± 0.35 mg LiOH (0.19 $mmol_{LiOH}$) per gram NCM (1 g_{NCM} = 10.26 $mmol_{NCM}$) (red bar) are found in the wash solution. This corresponds to an amount of LiOH on the cathode active material of ≈4600 ppm. Noh et al.[21] also determined the amounts of LiOH on an 85% nickel containing NCM and found ≈11000 ppm on their material showing that our levels are reasonably high. Generally, one expects that after washing the material once, no more or only little amounts of LiOH from surface impurities should be found in the wash solution as also all Li_2CO_3 has been washed away under these conditions. However, when we analyze the second wash solution we still find ≈2.8 ± 0.15 mg LiOH (0.12 $mmol_{LiOH}$) per gram NCM wash solution (black bar). This would correspond to a LiOH amount on the cathode material of ≈2800 ppm. We think that this amount

cannot stem form impurities, which are still left on the surface of the cathode material and the origin of the large amounts of LiOH in the wash solution must be caused by a different mechanism. In order to translate the LiOH concentration from Figure 1 into a molar lithium loss, the molar ratios of lithium loss and lithium in the NCM material have to be taken into account. After washing the sample twice ≈ 0.31 mmol Li^+ were found in the wash solutions as LiOH, which stems from 10.26 mmol NCM (data in Figure 1 are normalized to 1g). Therefore, the mol.% of Li^+ loss from the structure can be calculated:

$$\frac{n_{Li+}}{n_{NCM}} = \frac{0.31\ \text{mmol}}{10.26\ \text{mmol}} = 3\ \text{mol.\%} \tag{1}$$

This means that during the two washing steps in total 3 mol.% of lithium are dissolved from the NCM material; this value will be used for further calculations during the discussions section.

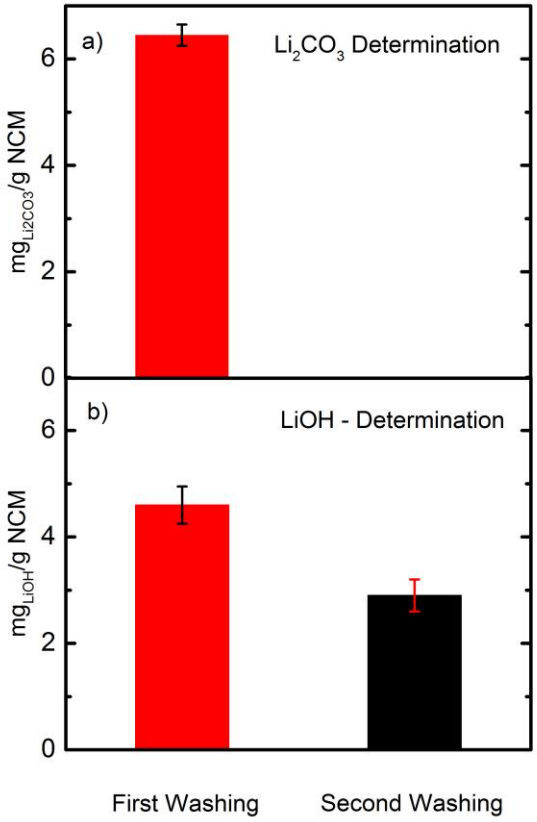

Figure 1: a) Li_2CO_3 & b) LiOH amounts of 20 g NCM851005 powder washed in 100 mL degassed water for 20 minutes under argon atmosphere. The carbonate and hydroxide amounts are determined by titration with HCL. The material was washed once and then the titration was carried out of the wash solution and is referred to as "First Washing". After that, the powder was dried in a vacuum oven in the glovebox at 65 °C for at least 4h. The as-dried powder was then washed again and the wash solution is used for titration and the amounts are referred to as "Second Washing". The error bars show the deviation of three repeat measurements.

In order to understand the behavior of LiOH found in both wash solutions we recorded the pH-value during the first and second washing under argon over the course of 20 minutes, which is identical to the washing experiment (20 g NCM in 100 g water). The results are shown in Figure **2**. By adding NCM851005 to the wash solution for the first time (open round symbols) the pH-value immediately jumps to a value of ≈11.3. After ten minutes, the pH is ≈12.1 and after 20 minutes, the pH saturates with a value of ≈12.2. When the once washed and afterwards dried material is washed again (square symbols), the pH again immediately jumps to a very high value of 11.1. After ten minutes, the pH is 11.5 and after 20 minutes, the pH-value saturates at a value of 11.6. Interestingly, when the materials are put into water a sudden pH jump occurs both for the first- and for the second washing. This implies a fast-chemical reaction must happen which is then controlled via diffusion. Please note that the plateaus observed are caused by the sensitivity of the pH meter of 0.1 pH.

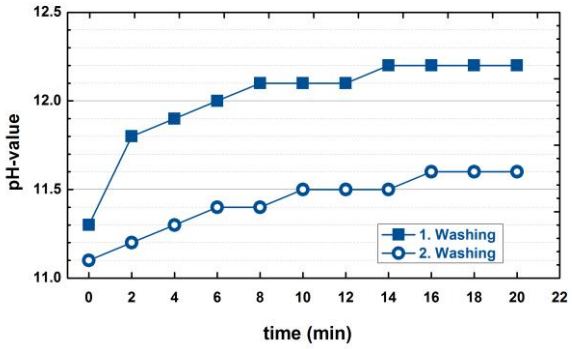

Figure 2: pH-value over time of 20 g NCM851005 in 100 g water while stirring the solution in an argon-filled glovebox. The rectangular symbols show the pH-value when the NCM851005 powder is first washed. The open round symbols show the pH-value of the NCM851005 powder that was washed beforehand and dried afterwards in a vacuum oven at 65 °C for at least 4h.

Next, we have to rationalize these results from a mechanistic perspective. Regarding the mechanism of the washing process, we think that the first step is a proton (H^+) exchange with a lithium ion (Li^+) leading to the formation of LiOH (explaining the strong pH increase) and to a HMO_2 surface. For a nickel-rich material the HMO_2 structure is isostructural with a NiOOH like surface. The reaction path is shown in equation 2. Shkrob et al.[7] have already shown by XRD that a lithium/proton exchange occurs, when the material is exposed to ambient air and stored under improper conditions. Jeong et al.[40] recently published a study, which is related to the washing process of an LCO cathode and they have shown that the first step during washing is a lithium/proton exchange on the surface of the LCO cathode.

$$LiMO_2 + H_2O \rightarrow LiOH + HMO_2 \quad (2)$$

We think that the lithium/proton exchange occurs on the surface of the NCM and penetrates into the structure, which is limiting at the end and leads to the lower Li^+-leaching after the first washing. As a next step, the material washed twice was heated to 180 °C (to remove residual water) and analyzed in terms of residual reactive lithium on the surface via XPS, gassing via on-line electrochemical mass spectrometry (OEMS) and charge transfer resistance changes by impedance spectroscopy with a gold wire reference electrode (GWRE).

Surface- and electrochemical analysis of the 2x washed NCM851005 material (dried at 180 °C) — In order to prove that no more residual lithium (LiOH & Li_2CO_3) is on the surface as claimed by the literature[24], we performed XPS measurements of the pristine NCM851005 material and the NCM851005 material, which was washed 2x and dried at 180 °C. The samples were transferred to the vacuum system of the XPS without any exposure to air. The Li 1s region was recorded from 58 eV to 52 eV BE. In the top panel of Figure 3, the spectrum is shown for the pristine NCM851005 that was received by the material manufacturer. One can nicely observe two peaks in the spectrum. One is located around 54.0 eV (in green) and attributed to the intercalated lithium ($Li_{intercalated}$) and one peak is located at 55.3 eV (in blue), which is attributed to the surface lithium ($Li_{surface}$, = LiOH and Li_2CO_3). The assignment of the peaks is further validated by storing the as received material in humid air, leading to a severe increase of the surface lithium peak (data not shown). Interestingly, when the material is washed twice in argon, no more surface lithium can be detected by XPS whereas the intercalated lithium peak (in green) is still present. This result fits well with the literature where Kim et al.[24] could show by FT-IR measurements that the amounts of LiOH and Li_2CO_3 drastically decrease after washing. With that, we can show that washing leads to a decrease in residual LiOH and Li_2CO_3 on the surface of the cathode material. Next, we want to check if the washing process has an influence on the gassing and the impedance of the NCM851005 material.

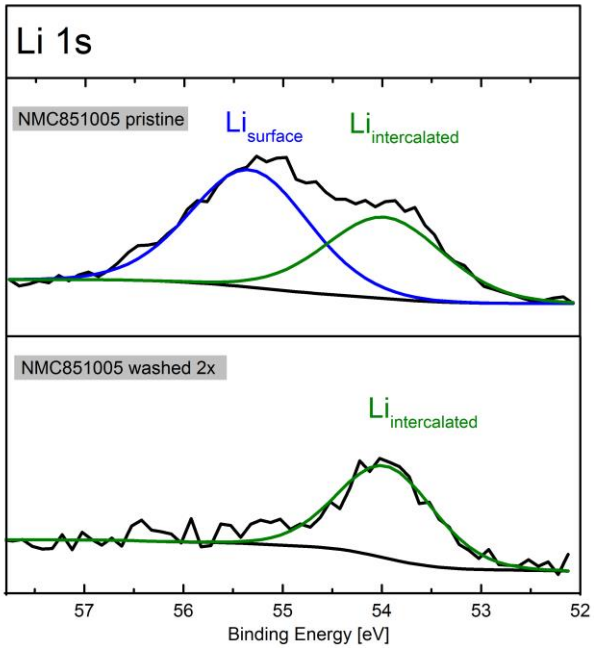

Figure 3: Li 1s region of NCM851005 pristine and washed under argon twice by XPS (data shown in black). The pristine sample (NCM851005 as received) was dried at 120 °C and the washed sample (NCM851005 washed 2x) was dried at 180 °C prior to the measurement. The samples are transferred to the vacuum chamber without any air exposure. For peak fitting, a Shirley background (in black) was subtracted and two peaks with a center energy of 54.0 eV ($Li_{intercalated}$) and 55.3 eV ($Li_{surface}$) and a FWHM of 1.4 were used.

Recently, it has been shown that oxygen release from nickel-rich layered materials significantly alters the electrolyte and mainly causes gas evolution during the first cycles, leading to a strong capacity degradation.[19, 27, 29] Furthermore, it has been shown that hydroxide species on the material surface can react with the electrolyte leading to the formation of CO_2.[8, 19] In order to investigate the effect of a washing step onto the gas evolution of a nickel-rich NCM material, we performed on-line electrochemical mass spectrometry on the pristine and the washed sample. Therefore, we used an electrolyte based on pure EC mixed with 1.5 M $LiPF_6$. This model electrolyte is on the one hand sufficient due to its low vapor pressure, leading to a high sensitivity of the measurement by an increased signal to noise ratio.[41] On the other hand, the only gases that evolve during EC reduction on the lithium counter electrode are CO and ethylene[42-44] which can be clearly differentiated from the O_2 and CO_2 evolved from the cathode material.[29] Results of the OEMS measurements on both samples are shown in Figure 4. The upper panel shows the galvanostatic charge profiles from OCV (≈3 V) up to 5.0 V against a Li counter electrode, and the middle/lower panels depict the concentration of the concomitantly evolved O_2 (m/z = 32, middle panel) and CO_2 (m/z = 44, lower panel); concentrations are given in terms of μmol/g_{AM} (left axis). The gas evolution for the pristine material is shown by the grey lines in Figure 4, showing a capacity of ≈267 mAh/g during the first charge to 5.0 V vs. Li^+/Li. The O_2 evolution can be observed at 84% SOC (≈4.32 V vs. Li^+/Li) which is in one line with the results reported by Jung et al.[19, 27] and Teufl et al.[30], where the oxygen release is followed by a sharp increase in the CO_2 evolution. In contrast to that, the electrode made from the washed material (red lines, middle and bottom panel in Figure 4) show nearly no gassing up to 5.0 V vs Li^+/Li for both, the O_2 and the CO_2 evolution.

The oxygen release for the pristine NCM in Figure 4 (middle panel) is in accordance with literature and can be rationalized by thermodynamic instabilities of layered oxides at SOC's > 80%.[19, 27, 28, 30] However, concerning the CO_2 evolution during the first charge of layered oxides there is an ongoing debate about its origin; it has been assumed by Luo et al.[45] that the CO_2 evolution completely evolves due to electrolyte oxidation with lattice oxygen, Renfrew et al.[18] proposed the opposite, suggesting that CO_2 evolution is exclusively triggered by the oxidative decomposition of Li_2CO_3 from surface regions. However, Jung et al.[19, 27] showed detailed analysis of the CO_2 evolution, suggesting that the CO_2 evolved at ≈4.2 V vs. Li^+/Li is produced due to surface impurities, while the oxygen released at higher potentials is suggested to react with the carbonate electrolyte causing a rapid increase in the CO_2 evolution.[29] Recently Jung et al.[19] could prove their concept by temperature dependent measurements with an ^{13}C labeled electrolyte showing a reaction of surface hydroxides with the electrolyte at low

potentials and a strong reaction of lattice oxygen with the electrolyte > 4.3 V vs. Li^+/Li; for that reason we will adopt the mechanistic view proposed by Jung et al.[27] and Strehle et al.[37] As mentioned above a striking observation is the variation in the gases evolved from the washed material, compared to the pristine material. By the end of the first charge to 5.0 V vs. Li^+/Li, a total amount of ≈3.1 µmol/g O_2 and ≈171 µmol/g CO_2 can be detected for the pristine sample, in contrast only about ≈0.025 µmol/g O_2 and ≈12 µmol/g CO_2 are evolved from the washed material (capacity ≈244 mAh/g), meaning that the total gas evolution is ≈25-fold lower after the washing procedure. While the titration experiments in Figure 1 were carried out without exposure to air, the electrodes prepared for the OEMS experiments were exposed to air after washing. Therefore, we cannot exclude a minor contribution of surface carbonates to the CO_2 signal after the washing step; However, the 25-fold difference in the gas evolution after washing is very significant and quite striking. As already shown in previous studies, oxygen release caused by a chemical layer-to-spinel/rocksalt formation leading to a resistive surface layer and concomitant oxygen release from near-surface regions can explain the phenomena of oxygen release for stochiometric[27, 28] as well as for overlithiated layered oxides.[30, 37] According to this mechanism we expect that a reaction between the surface of the nickel-rich cathode and the water in the washing solution takes place, leading to strong changes of the surface phases and probably leading to an resistance increase after washing. This resistance increase can already be seen in the voltage profiles in Figure 4 (upper panel), showing an increased overpotential in the initial charge profile after washing and a steep increase of the potential towards the end of the first charge (> 4.5 V vs. Li^+/Li);[6] therefore, a detailed impedance analysis will be shown next.

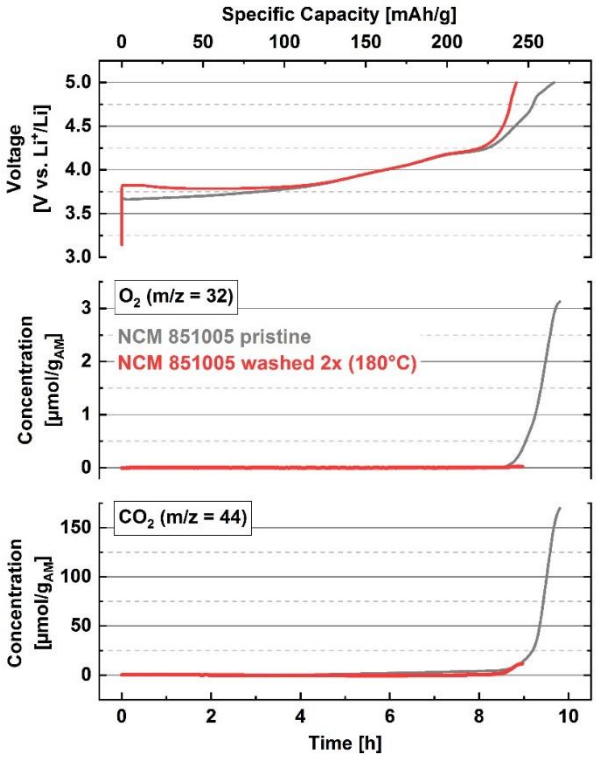

Figure 4: OEMS measurements for the first charge cycles in a half-cell for the pristine and the 2x washed NCM (dried at 180 °C) Upper panel: charge voltage vs. time and capacity; middle/lower panel: evolution of the concentrations of concomitantly evolved O_2/CO_2 given in units of either µmol/g_{AM}. Cells were charged at C/10 rate to 5.0 V. Cells were composed of metallic Li counter electrode and a glassfiber separator and experiments were conducted at 25 °C in EC-only with 1.5M $LiPF_6$. The vertical dashed red line indicates the potential of 4.32 V where the onset of O_2 evolution occurs (≈ 84% SOC; onset determined with zoom).

The OEMS results suggest that surface oxygen is depleted when the material is washed in water; Jung et al.[27] observed such a loss of surface oxygen for NCM materials when they are charged above ≈80% SOC. This oxygen then leads to the chemical oxidation of the electrolyte and a detoriation of the cell performance.[27, 29] During cycling a increase in the overpotential of NCM cathodes was shown when oxygen is released and found a severe increase of the cathode overpotential, which they attribute to the formation of a spinel or rock salt layer.[27] If oxygen is depleted after the washing process, an increase in the charge transfer resistance (R_{CT}) of the cathode material must be observed. For this reason, graphite/NCM851005 cells are assembled with a gold wire reference electrode (GWRE[39]). This reference electrode allows for the recording of artefact-free half-cell impedance spectra. In this study, cells with a pristine NCM851005 and with a twice-washed cathode are assembled and two formation cycles at C/10 and 25 °C are carried out. Afterwards the cells are charged to 50% SOC (based on the second discharge capacity, roughly 3.7 V - 3.8 V cell voltage) and the impedance is recorded. The impedance spectra of the different NCM851005 cathodes are shown in Figure 5. The high frequency semi-circle observed in both spectra is attributed to a contact resistance ($R_{Contact}$) between the cathode coating and the aluminum current collector. More details on this can be found in the work by Landesfeind et al.[46] The pristine NCM851005 shows a small impedance response with a value for the cathode resistance $R_{Cathode}$ (determined by an R/Q fit) of ≈5 Ωcm². When the same material is washed twice in water $R_{Cathode}$ increases to ≈20 Ωcm² what is an increase of a factor 4. The increase of the $R_{Cathode}$ fits well to the data of Jung et al.[27] for an electrochemically initiated oxygen depletion.

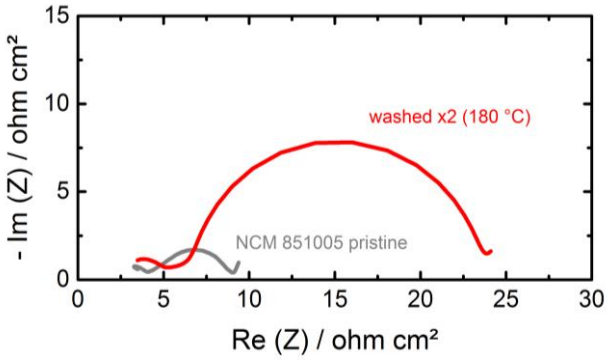

Figure 5: Impedance response of NCM851005 samples (pristine and washed twice and dried at 180 °C) measured versus a gold-wire reference electrode (GWRE) after two formation cycles with C/10 and after a charge to 50% SOC. The grey impedance spectrum represents the NCM851005 material without washing. The red impedance spectrum shows the NCM851005 material washed twice and dried at 180 °C.

Mechanistic understanding of the washing process — Up to now, we have observed a rather continuous formation of LiOH when NCM851005 is added into a solution of water. Further, we have evidence for an oxygen-depleted layer after washing and drying as suggested by OEMS and impedance measurements. Mechanisms that are already suggested in literature can partially explain these results and will be shortly discussed. Mosthev et al.[47] suggested that the extraction of Li^+ from an $LiNiO_2$ powder in an aqueous solution is charge compensated by the evolution of oxygen from the layered lattice. Furthermore, Liu et al.[48] investigated the deterioration of LNO powder under ambient air und suggested that Ni^{3+} from the lattice is reduced to Ni^{2+} and the corresponding oxidation reaction again happens by the oxidation of the lattice oxygen to gaseous O_2. If either of the suggestions in literature were true, the addition of water to a NCM851005 powder should show the evolution of O_2. In order to study this, we used a modified version of our current OEMS setup. A Swagelok T-fitting was connected to the capillary leading to the MS system. To one of the other connections, a septum was installed in order to add water with a syringe and the remaining inlet was equipped with a nut where NCM851005 powder was added.

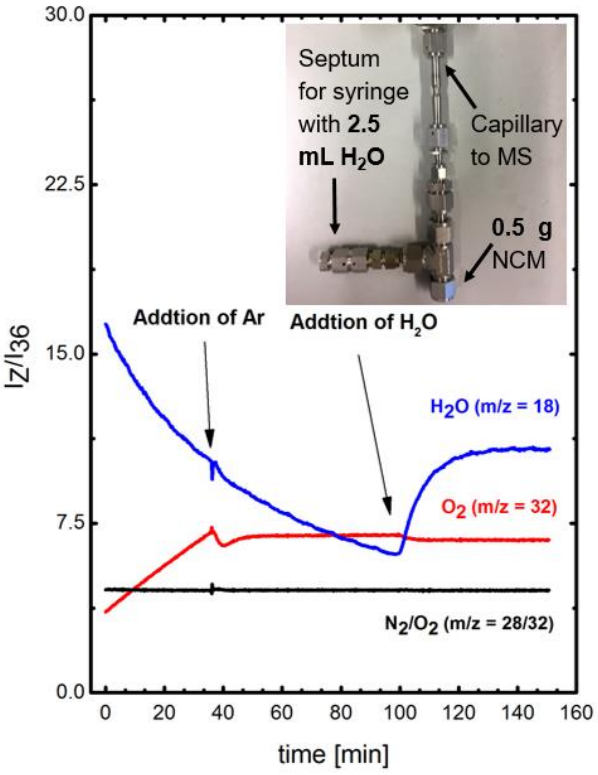

Figure 6: Mass traces of O_2 (m/z = 32, in red), H_2O (m/z = 18, in blue) and of the N_2/O_2 ratio (m/z = 28/32, in black) recorded with a modified version of the OEMS setup. The first 40 minutes consisted of a rest phase followed by the addition of a syringe with pure argon in order to check the stability of the septum. After further 60 minutes, a syringe with 2.5 mL was added to 0.5 g NCM and the mass traces were recorded for further 60 minutes.

After assembly of the cell in an argon-filled glovebox, the mas traces of O_2 (m/z = 32) and of H_2O (m/z = 18) were recorded. The first 40 minutes consisted of a rest period where the residual water amount decreases and the O_2 signal increases. The increase of the oxygen signal can easily be rationalized by a small leakage of the system, as by dividing the mass signal of N_2 (m/z = 28) by the oxygen signal, a straight line is obtained which clearly indicated the intrusion of air. After the rest period of 40 minutes, a syringe with argon from the glovebox atmosphere is added in order to check the tightness of the septum. One can nicely see that during the addition of a syringe, no increase in the oxygen or water masses are observed. After 100 minutes, 2.5 mL of water are added to 0.5 g of powder (same water/CAM ratio as in the previous experiments) and we do not observe any oxygen evolution (red line after 100 minutes) when water is added to the powder. Therefore, we think that the evolution of lattice oxygen from a nickel-rich material during the contact with water is very unlikely.

Based on our suggested lithium/proton exchange from equation 1, a NiOOH like structure is created on the surface of the NCM material. It is known in the literature, that NiOOH is thermally very instable and starts to decompose already at temperatures as low as 80 °C.[49] The total thermal decomposition after heating the material to 550 °C is then a rocksalt structure (NiO) followed by O_2 and H_2O release. The drying temperature of the washed sample shown in the previous results section was 180 °C; heating a delithiated Ni-rich NCM material in this temperature window we assume the formation of an O_2-deficient layer, which has a M'_3O_4 ($M^{'}$ = Li+Me) spinel-type structure, as suggested by Bak et al.[50] The thermal reduction of the NiOOH phase is shown in equation 5 (Nickel (III)-oxide reduction during drying of the washed powders):

$$2\ NiOOH \rightarrow 2\ \text{"NiO"} + 0.5\ O_2 + H_2O \quad (3)$$

Jeong et al.[40] showed for an LCO cathode material that the washing leads to a CoOOH like structure, which is then thermally decomposed to a CoO or CO_3O_4 structure during the drying process and leads to an impedance increase of the washed material. Based on this concept, we have designed further experiments, which should underline this reaction path. First, we have carried out thermogravimetric analysis (TGA) coupled to a mass spectrometer (MS) of a washed material (compared to a pristine material which was not washed) in order to mimic the drying process. All samples were dried beforehand at 120 °C under dynamic vacuum for at least 3h. The TGA protocol consisted of five parts with argon as carrier gas, including a rest phase (10 minutes) an argon flow rate of 200 mL/min, which is changed to 20 mL/min (and used for all further steps) and held again 10 minutes, both at 25 °C. This is followed by a heat ramp to

120 °C with 10 K/min followed by a hold phase there of 40 minutes. As a next step, the material was heated to 450 °C (10 K/min) and the temperature was held there for 20 minutes. The results of this experiment are shown in Figure 7. When the flow rate of argon is changed after 10 minutes also the mass signals decrease due to the lower rate now. By ramping the temperature from 25 °C to 120 °C, no severe change in the mass loss (top panel) and no change in the mass traces (middle and bottom panel) is observed. However, when ramping the temperature from 120 °C to 450 °C, first a H_2O evolution takes place (bottom panel) until 250 °C followed by a strong O_2 evolution (middle panel). This oxygen evolution goes hand in hand with a mass loss of 0.4 wt%. In contrast to that, the pristine sample shows only a very little mass loss and no oxygen or water evolution in this temperature range. The thermal reduction of NiOOH first releases water starting from temperatures of 120 °C and probably lower as a mass loss during the 120 °C hold phase can be observed parallel to an increase in the water signal. This is consistent with the results from Pan et al.[49], who showed that NiOOH loses water from the interlayers already at 100 °C. Around 250 °C a strong oxygen release is observed which converts the partially reduced NiOOH structure into a rocksalt phase of NiO (see equation 3). Pan et al.[49] showed that this process happens for a pure NiOOH at 262 °C. We think that first a spinel like structure is formed from the NiOOH phase (loss of water) and followed by the total reduction to a rock salt phase starting from 250 °C (loss of oxygen), which is in one line with the results shown by Bak et al.[50]

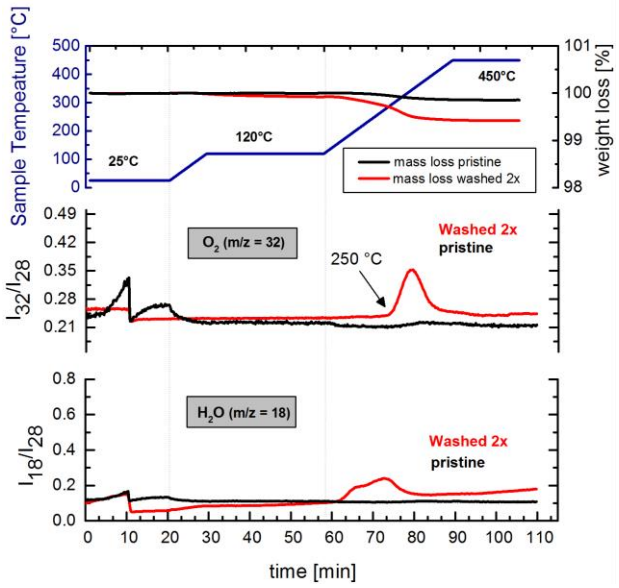

Figure 7: TGA-MS analysis of a 2x washed NCM851005 powder and as reference a NCM851005 material which was stored in an argon-filled glovebox. All materials were dried beforehand in a Büchi oven at 120 °C under dynamic vacuum for at least 3 h. The top panel shows the temperature program with heating ramps and hold phases (left y-axis) and the corresponding mass loss (right y-axis) of the pristine sample (in black) and the sample washed twice (in red). The panel in the middle shows the O_2 signal (m/z = 32) normalized by nitrogen (m/z = 28) of both pristine and washed sample. The bottom panel shows the mass traces of water H_2O (m/z = 18) normalized by the nitrogen signal (m/z = 28).

If this concept is valid, a higher drying temperature must cause a lower gas evolution (O_2 and CO_2) and a higher impedance as the NiOOH phase is more gradually decomposed at higher temperatures. In order to prove this, we have carried out further OEMS and impedance measurements where the cathodes were dried at different temperatures. We have chosen the following conditions for the washed cathodes: One sample was freeze-dried and has seen a maximum temperature of 25 °C. Next, washed CAMs were dried at 80 °C, 180 °C (already shown above), and 300 °C; the OEMS results are shown in Figure 8. As already depicted in Figure 4 the gas evolution of the sample, which was washed and dried at 180 °C, showed nearly no O_2 and CO_2 evolution during the first charge cycle, whereas the pristine sample showed a high gas evolution of ≈3.1 µmol/g O_2 and ≈171 µmol/g CO_2. The systematic variation of the drying temperature is therefore shown in Figure 8 where the data from Figure 4 (pristine sample and dried at 180 °C) are also included. All samples were washed 2 x 20 minutes as described in the experimental section. As gentle drying procedure, we freeze dried the washed powder and afterwards vacuum dried the electrode at 25 °C. The freeze dried sample still shows a significant O_2 and CO_2 evolution corresponding to ≈0.35 µmol/g O_2 and ≈90 µmol/g CO_2 detected during the first charge. By increasing the drying temperature to 80 °C a tremendous decrease of the O_2 (≈0.1 µmol/g) and the CO_2 (≈26 µmol/g) can be observed, pointing towards thermal NiOOH decomposition starting already at temperatures around 80 °C. This thermal decomposition at these low temperatures cannot clearly be observed in the TGA experiment. However, we think when the sample is dried in vacuum for 12 h, a thermal reduction can occur (indicated by the OEMS measurement). In the TGA experiment, a fast heat ramp is used and therefore the thermal reduction might not be observed. A further increase of the drying temperature to 180 °C leads to a further decrease of the gas evolution, with decreased amounts of O_2 (0.025 µmol/g) and CO_2 (12 µmol/g) evolution for the sample. Next, we investigated the sample dried at 300 °C in the OEMS, which is also shown in Figure 8. Literally, we cannot detect any O_2 evolution and only very small amounts of CO_2 (6 µmol/g) for the sample dried at 300 °C. From these results we expect that a drying starting from 80 °C might form an oxygen deficient meta-stable surface structure that largely preserves its structure during delithiation and does only release very small amounts of oxygen (e.g. spinel-type phase) but can be thermally decomposed to a thermodynamic more stable phase as shown in Figure 7 e.g. rocksalt structure (when dried at 300 °C), which shows no oxygen evolution at all. Such a thermal instability for delithiated Ni-rich layered oxides was characterized in detail by Bak et al.[50], showing a spinel to rocksalt transformation >200 °C accompanied by oxygen release. Thus, we are confident that the oxygen evolution at drying temperatures >250 °C (Figure 7) stems from surface rocksalt

formation of the washed NCM particles. However, Figure 8 does not only give information about the gas evolution during different drying procedures but also about the electrochemistry, showing an identical charge capacity for the freeze dried sample as observed for the pristine material (both ≈267 mAh/g, Figure 4 and Figure 8). This can be rationalized by the fact that the surface has still a layered structure remaining its electrochemical activity during the first charge without trapping Li^+ in an inactive surface layer. The specific charge capacity of the samples dried at 80 °C, 180 °C and 300 °C is lower with a similar charge capacity of ≈244 mAh/g. From the LiOH determination in Figure 2, we expect a total lithium loss of ≈3% that cannot explain the observed capacity loss (≈23 mAh/g) during the first charge. Therefore, we expect that the lower capacity stems from a phase transformation into a lithium containing spinel and/or rock salt phase leading to a material loss, this finding will in the end be underlined by quantification of the results and the capacity loss. Similar findings have been seen from Teufl et al.[30] who could show a large capacity contribution from a spinel phase to the capacity of a Li- and Mn-rich NCM by a dQ/dV analysis; while for the Li-rich case a Mn spinel can be reversible charged/discharged at potentials around 3 V vs. Li^+/Li,[51, 52] there is no evidence of such a electrochemical active spinel-type phase for Ni-rich NCM materials. Rather we expect that lithium can get trapped within such a surface phase leading to a loss of active lithium by the formation of an electrochemical inactive $(Li+M)_3O_4$ spinel-type phase or a (Li+M)O rocksalt-type phase.[50] To further investigate these findings, impedance measurements for the different samples are shown in Figure 9.

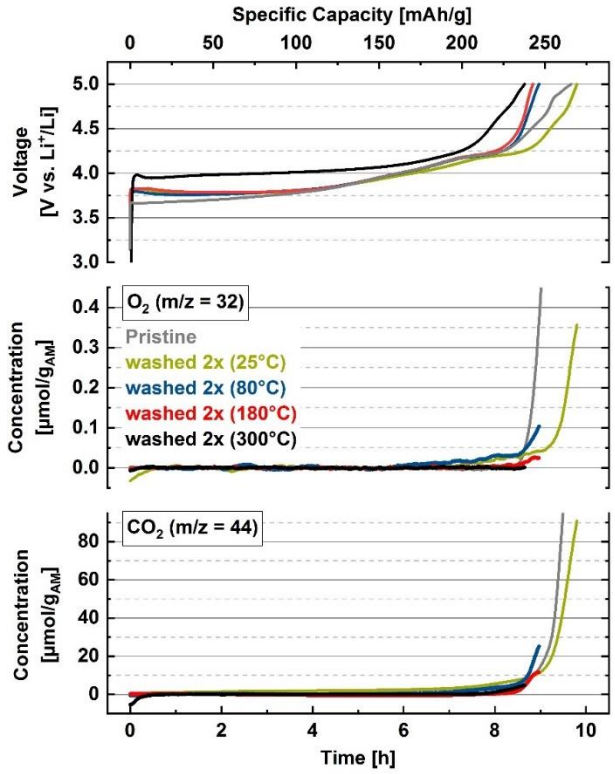

Figure 8: OEMS measurements for the first charge cycles in a half-cell for the 2x washed NCM with different drying temperatures after the washing procedures. Upper panel: charge voltage vs. time and capacity; middle/lower panel: evolution of the concentrations of concomitantly evolved O_2/CO_2 given in units of µmol/g_{AM}. Cells were charged at C/10 rate to 5.0 V. Cells were composed of metallic Li counter electrode and a glassfiber separator and experiments were conducted at 25 °C in EC-only with 1.5M $LiPF_6$.

The impedance of NCM851005 cathodes dried at different temperatures is analyzed with a GWRE in order to analyze the interfacial resistance of the cathode and the data is shown in Figure 9. The resistance ($R_{Cathode}$) of a pristine cathode is in the order of ≈5 Ωcm². When the cathode material is now washed twice in water and then freeze dried and afterwards dried in dynamic vacuum at 25 °C the cathode impedance is in the same order with a value of ≈6 Ωcm². This agrees well with the first part of our mechanism, where only a lithium/proton exchange occurs on the surface. The freeze drying takes away the water from the cathode powder but does avoid the thermal decomposition of the NiOOH phase. The intercalated protons are then charged during the formation cycle and most likely reduced on the graphite anode to H_2 gas. As we can see from the cathode impedance, drying at maximum 25 °C does not alter the cathode interface. When the drying temperature is switched to 80 °C, we can indeed observe an increase of the cathode resistance with a value of ≈10 Ωcm². This fits also well to the second part of our mechanism and to the TGA measurement from Figure 7, where the thermal reduction of a NiOOH already occurs at 80 °C. When the material is dried at 180 °C, the cathode resistance increases to ≈20 Ωcm², which can be explained by a stronger reduction of the NiOOH phase to

an O_2-deficient layer. Interestingly, when the cathode powder is dried at 300 °C the cathode impedance shoots to a very high value of ≈130 Ωcm². At this temperature, we saw a strong oxygen evolution from the cathode material in the TGA-MS measurement (Figure 7) explaining the high cathode impedance. These results are perfectly in line with the phase transformations of delithiated NCM materials suggested by Bak et al.[50]; they clearly showed that a meta-stable spinel phase can form at temperatures between 100 °C and 200 °C, while heating >200 °C clearly ends up with the formation of a rocksalt type phase. This is essentially what can be seen in the impedance spectra (Figure 9b), showing a slight increase in impedance up to 180 °C due to surface-spinel formation, while heating to 300 °C ends up with a very high impedance due to the formation of a resistive rocksalt structure on the surface. In summary, the EIS measurements underline the strong influence of the drying temperature being the main driver for the decreased gassing and increased impedance.

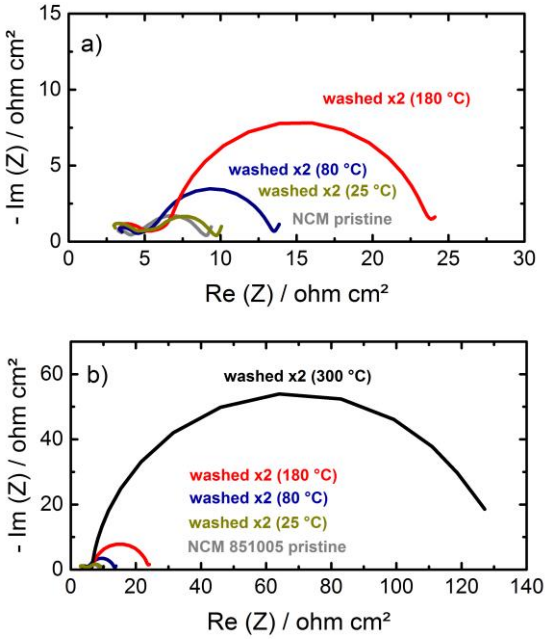

Figure 9: Cathode impedance spectra measured with a gold-wire reference electrode in a graphite//NCM851005 cell configuration. The analyzed cathodes were washed twice in water and then dried with the following conditions as can be seen in panel a): pristine cathode (not washed, dried at 120 °C, in grey), freeze dried cathode (dried at 25 °C, in yellow), dried at 80 °C (in blue) and dried at 180 °C (in red). Panel b) is a zoom out of panel a) in order to show the impedance, or a cathode dried at 300 °C. The impedance was recorded from 100 kHz to 100 mHz with a perturbation of 15 mV at 25 °C.

Influence of harsh washing conditions on the full-cell cycling performance at 25 °C — In order to investigate the effect of different drying conditions for the NCM powders on the cycling performance we have assembled graphite/NCM851005 full cells with a gold wire reference electrode (GWRE). After formation (2 cycles at C/10) and a subsequent charge to 50% SOC the impedance is recorded and shown in Figure 9. After the impedance measurement, the cells are further analyzed by a charge/discharge cycling protocol consisting of a C/2 charge (CCCV) and a 1C (CC) discharge for 198 cycles. The results of this test are shown in Figure 10.

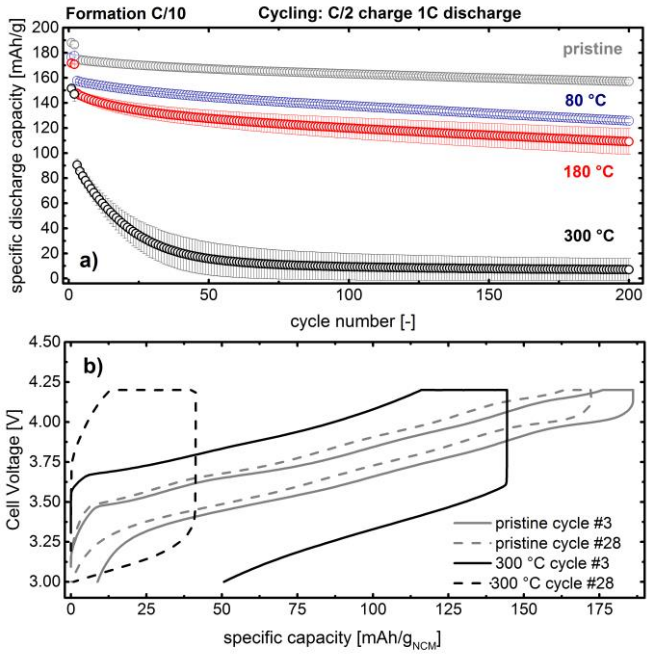

Figure 10: Charge/discharge cycling test of graphite/NCM851005 cells containing a gold-wire reference electrode (GWRE) and an LP57 electrolyte. The cycling is carried out with a CCCV charge to 4.2 V with a cut-off for the CV phase of C/20. The discharge is carried out in CC mode until 3.0 V. a) contains the discharge capacity of the C/10 cycles (2x formation) and the subsequent cycles with a C/2 charge and 1C discharge of the pristine cathode (not washed, dried at 120 °C, in grey), of a NCM cathode dried at 80 °C (in blue), dried at 180 °C (in red) and dried at 300 °C (in black). b) contains the full-cell voltage profiles of the first and 25th cycle during the C/2 charge and 1C discharge protocol of the pristine cathode (in grey) and of NCM dried at 300 °C.

The pristine cathode (in grey) shows a first discharge capacity of 188 ± 1 mAh/g_{NCM} at C/10 which drops to 178 ± 2 mAh/g_{NCM} when the discharge C-rate is increased to 1C. After 200 cycles (formation plus faster cycling), the specific discharge capacity is 157 ± 1 mAh/g_{NCM}. When the cathode material is washed and dried at 80 °C (in blue) the first discharge capacity is 178 ± 2 mAh/g_{NCM} (10 mAh/g less compared to the pristine sample). When the discharge C-rate is increased from C/10 to 1C, the specific discharge capacity is 158 ± 1 mAh/g_{NCM}, which can be explained by the impedance increase after washing and drying at 80 °C. After 200 cycles

the specific discharge capacity drops to 126 ± 2 mAh/g_{NCM} By drying the cathode material at 180 °C the first discharge capacity is similar to the sample washed and dried at 80 °C with 175 ± 2 mAh/g_{NCM} and when switching the C-rate to 1C a discharge capacity of 147 ± 3 mAh/g_{NCM} is obtained. This is 11mAh/g lower compared to the cells were the cathode is dried at 80 °C and fits well to a further increased impedance of the cathode (see Figure 9). After 200 cycles the specific discharge capacity is 109 ± 10 mAh/g_{NCM} for electrodes where the powder was dried at 180 °C. For cells cycled at 300 °C very low discharge capacities at C/10 of 151 ± 3 mAh/g_{NCM} are obtained which fit well to the severely increased cathode impedance to a value of ≈130 Ωcm² compared to ≈6 Ωcm² for the pristine material. The first discharge capacity at 1C is 90 ± 5 mAh/g_{NCM} what further underlines the drastic increase in cathode impedance. Interestingly, the cells with the cathode active material dried at 300 °C show also a drastic fading with a final specific discharge capacity of 7 ± 6 mAh/g_{NCM}. In order to understand that, we have to take a closer look into Figure 10 b). Here the voltage profiles of the third cycle (first cycle with 1C discharge) and the 37th cycle are shown. The voltage profiles of the pristine sample (in grey) show very little overpotential and short CV phases as expected for a non-washed material. The voltage profile of the third cycle of the cells with cathodes dried at 300 °C a strong overpotential is observed (compared to the pristine sample). Further, the CV phase is increased during the charge and during discharge, the high impedance causes a capacity drop of approximately 50 mAh/g_{NCM}. After 28 cycles, the impedance must have increased further drastically as the cut-off of 4.2 V is reached immediately. Unfortunately, the impedance after cycling was not recorded, however the voltage profiles clearly indicate a non-stable cathode surface which has a drastic impedance buil-up leading to very low discharge capacities. From this we conclude that washing with high water to CAM ratios (5:1) and drying at 300 °C leads to a very instable structure, which further decomposes when cycled in a real cell configuration. In order to optimize this process with regards to low impedance and stable surfaces after washing, further studies are carried out.

Discussion

Estimated surface layer thickness calculated from LiOH titration — It has been shown in literature that oxygen release at the surface of nickel rich NCM materials can lead to electrochemically formed surface layers on NCM cathode materials.[27, 28] These surface layers lead to an immediate capacity loss during cycling due to significant impedance build-up.[27] In order to get an estimate on the spinel/rocksalt layer thickness after the washing and drying procedure the layer thickness will be estimated from LiOH amounts gained from the titration experiments; details for the calculations of the layer thicknesses are shown by Jung et al.[6, 27] and Strehle et al.[37] As a first step we derive the particle size of a spherical particle from the measured BET surface area, with r being the radius, A_{BET} the BET surface area of the washed material and ρ being the crystallographic density of the NCM material. For the calculation we used the BET surface area that we got after washing, which was as high as 2.4 m^2/g:

$$r = \frac{1}{2} \cdot \frac{6}{A_{\mathrm{BET}} \cdot \rho} = \frac{1}{2} \cdot \frac{6}{2.4\ \mathrm{m^2\ g^{-1}} \cdot 4.8\ \mathrm{g\ cm^{-3}}} \approx 260\ \mathrm{nm} \quad (4)$$

A particle radius of 260 nm is therewith calculated. Knowing the particle size, one can calculate the radius of the bulk particle without the surface layer. Detailed derivation of this calculations can again be found by Strehle et al.[37] and Jung et al.[6, 27] whereas it shall be noted that complete cation disorder is allowed. Hereby the mol-fraction of surface phase is required, this fraction is estimated by the exchange of 3 mol.% lithium by 3 mol.% of protons, as derived from the LiOH titration before and shown in Figure 1. From this estimation we expect a surface phase fraction of $x_{\mathrm{surface\ phase}}$ = 3 mol.%; with these values the radius of the still layered bulk r´ can be calculated:

$$\frac{V_{\mathrm{shell}}}{V} = \frac{r^3 - r'^3}{r^3} = 1 - \left(\frac{r'}{r}\right)^3 = x_{\mathrm{surface\ phase}} \leftrightarrow r' = r \cdot \left(1 - x_{\mathrm{surface\ phase}}\right)^{\frac{1}{3}} \quad (5)$$

Plugging in the actual numbers this leads to a radius of 257.4 nm of still layered bulk.

$$r' = r \cdot \left(1 - x_{\mathrm{surface\ phase}}\right)^{\frac{1}{3}} = 260\ \mathrm{nm} \cdot (1 - 0.03)^{\frac{1}{3}} = 257.4\ \mathrm{nm} \quad (6)$$

Out of this value the thickness of the surface phase $t_{surface\ phase}$ can be easily calculated, ending up with roughly 2.6 nm of disordered surface phase.

$$t_{\text{surface phase}} = 2.6\ \text{nm} \tag{7}$$

Estimated surface layer thickness calculated from O_2-loss in TGA-MS — In order to verify this layer thickness, the amount of spinel/rocksalt formed on the surface cannot only be estimated from the LiOH loss, but can also be derived from the mass loss at 250 °C in the TGA-MS experiment shown in Figure 7. At 250 °C the only gas that can be detected is oxygen, which allows the assumption that the 0.4 % mass loss are caused by an oxygen loss during heating (only a minor fraction from the water). These 0.4% weight loss (4 mg_{loss}/g_{CAM}) can therefore be transformed into a O_2 loss of 125 µmol/g_{NCM} ($4_{mg}/32_{g/mol}$) which can be used to calculate the thickness of the rocksalt surface layer. According to Bak et al.[50] the delithiated Ni-rich cathodes undergo a transformation from a M'_3O_4 spinel type structure to a MO rocksalt phase (M = Ni, Co, Mn) at temperatures >200 °C which is accompanied by an oxygen loss and can be ascribed to the following equations:

$$0.33\ M_3O_4 \rightarrow MO + 0.16\ O_2 \tag{8}$$

This equation gives the theoretical loss of oxygen per mole NCM for a 100% spinel to rocksalt transformation (O_2^{theo}), from which the moles of oxygen released for a 100% conversion of the entire particle into the rocksalt ($n(O_2^{theo})$) can be easily calculated according to formula 9, using the molar mass of the NCM851005; detailed information for these calculations can be found by Jung et al.[27], Strehle et al.[37] and Teufl et al.[30]

$$n\ (O_2^{theo}) = \frac{O_2^{theo}}{M} \tag{9}$$

The ratio of oxygen release expected for a 100% phase transformation ($n(O_2^{theo})$) into a rocksalt structure (1638 µmol/g) and the actual oxygen evolution derived from the mass loss in the TGA-MS (Figure 7, 125 µmol/g) can be used to calculate the molar fraction of spinel converted into a rocksalt layer.

$$x_{\text{rocksalt layer}} = \frac{n\,(O_2^{meas})}{n\,(O_2^{theo})} \tag{10}$$

These calculations lead to a fraction of 7.6 mol.% that is transformed into a rocksalt surface layer, this value is now derived from the mass loss in the TGA-MS experiment (Figure 7) and can also be translated into a surface layer thickness with equations 5-7. Discussing this surface transformation to a capacity loss caused by a loss of cathode active material due to the formation of a chemical inactive surface layer, 7.6 mol.% would result in a capacity loss of 21 mAh/g for total delithiation (based on a theoretical capacity of 274 mAh/g). The capacity loss after washing that can be observed for total delithiation in the OEMS experiment (Figure 4) results in 23 mAh/g, which is in one line with the 21 mAh/g calculated from the mass loss in the TGA. Therefore, we suggest that the capacity loss fur full delithiation at slow C-rates can be explained by lithium captures within the inactive spinel/rocksalt surface layer. The calculation of the surface layer thickness derived from the weight loss in the TGA-MS results in a layer thickness of 6.8 nm, which is substantially thicker than the thickness derived from the pH values of the pure Li/H^+ exchange (2.6 nm as calculated above), this can be explained due to Li^+-mobility during phase transformation. Hereby, one has to note that the first estimation from the pH and the fraction of Li/H^+-exchange accounts for a surface spinel/rocksalt that does not contain any lithium, which is unlikely. The formation of a lithium containing spinel/rocksalt layer would therefore cause a thicker layer assuming the same proton intercalation.

This concept is schematically shown in Scheme 1. Hereby the blue gradient with the thickness d_1 depicts the theoretical layer that is estimated from a pure diffusion process without any Li^+-mobility during the wash and drying process; this hypothetical layer was calculated from the pH values and equals to 2.6 nm. However, in reality the lithium gradient after the washing and drying might look different, which was proven by the layer estimation form the actual oxygen loss during the TGA experiment. This model is shown by the green Li-gradient (Scheme 1) and is expected the more practical one. In addition to the oxygen loss from the TGA-MS the layer with the thickness d_2 can also explain the capacity that is observed during the OEMS experiments which can be rationalized by the quantifications shown above.

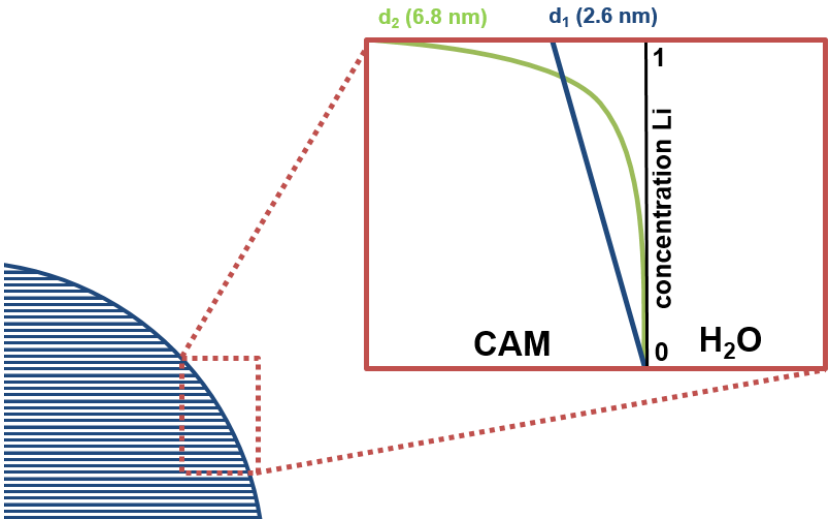

Scheme 1: Schematic presentation of the surface process during the wash and dry procedure of the Ni-rich CAM. The inset shows the particle surface and the different surface layers that we calculated from the pH and from the TGA-MS. The value derived from the pH only takes pure Li^+/H^+ exchange into account, resulting in a thinner, entirely delithiated surface layer. The model for the layer d_2 takes lithium mobility and a lithium gradient into account and the layer thickness was derived from the practical oxygen loss in the TGA-MS experiments.

Conclusions

In this study, we have analyzed the washing process of nickel-rich cathode materials (NCM 851005). We showed that the removal of Li_2CO_3 follows a simple dissolution mechanism, whereas the formation of LiOH proceeds continuously during washing. The washed samples were analyzed in terms of gassing (OEMS) and showed decreased O_2 & CO_2 release above 80% SOC by one order of magnitude going hand in hand with an increased cathode impedance. With a detailed TGA-MS analysis we could show the evolution of oxygen and water during the drying process, which lead us to the conclusion that the first step of the washing must be a lithium/proton exchange on the surface (NiOOH like structure), which is then thermally decomposed in an oxygen-deficient layer. This theory is confirmed by OEMS & Impedance measurements with samples dried at different temperatures, where we could show that the cathode impedance increases with increasing drying temperature and the gassing decreases with increasing drying temperature.

Acknowledgment

Financial support by the BASF SE through its Research Network on Electrochemistry and Batteries is gratefully acknowledged.

References

1. D. Larcher and J. M. Tarascon, *Nat. Chem.,* **7** (1), 19-29 (2015).
2. D. Andre, S.-J. Kim, P. Lamp, S. F. Lux, F. Maglia, O. Paschos, and B. Stiaszny, *J. Mater. Chem. A,* **3** (13), 6709-6732 (2015).
3. G. E. Blomgren, *J. Electrochem. Soc.,* **164** (1), A5019-A5025 (2016).
4. M.-H. Kim, H.-S. Shin, D. Shin, and Y.-K. Sun, *J. Power Sources,* **159** (2), 1328-1333 (2006).
5. P. Rozier and J. M. Tarascon, *J. Electrochem. Soc.,* **162** (14), A2490-A2499 (2015).
6. R. Jung, R. Morasch, P. Karayaylali, K. Phillips, F. Maglia, C. Stinner, Y. Shao-Horn, and H. A. Gasteiger, *Meeting Abstracts,* **MA2017-02** (4), 216 (2017).
7. I. A. Shkrob, J. A. Gilbert, P. J. Phillips, R. Klie, R. T. Haasch, J. Bareño, and D. P. Abraham, *J. Electrochem. Soc.,* **164** (7), A1489-A1498 (2017).
8. J. Sicklinger, M. Metzger, H. Beyer, D. Pritzl, and H. A. Gasteiger, *manuscript in preparation*.
9. N. V. Faenza, L. Bruce, Z. W. Lebens-Higgins, I. Plitz, N. Pereira, L. F. J. Piper, and G. G. Amatucci, *J. Electrochem. Soc.,* **164** (14), A3727-A3741 (2017).
10. J. Paulsen, H.-K. Park, and Y.-H. Kwon, *US 2009/0224201 A1 (2009)*.
11. J. Paulsen and J. H. Kim, *WO 2012/107313 A1 (2012).*
12. D.-H. Kim and J. Paulsen, *United States Pat. Appl. 2016036557, WO 2015/128722 A1 (2015)*.
13. J. Paulsen, H. P. Hong, and H. S. Ahn, *WO 2015/036882 A2 (2015)*.
14. J. Paulsen, H. P. Hong, and J. D. Oh, *WO 2016/055911 A1 (2016)*.
15. J. R. Dahn, R. Fong, and U. v. Sacken, *US 2, 264, 201 (1993)*.
16. G. V. Zhuang, G. Chen, J. Shim, X. Song, P. N. Ross, and T. J. Richardson, *J. Power Sources,* **134** (2), 293-297 (2004).
17. Y. Kim, *J. Mater. Sc.* **48** (24), 8547-8551 (2013).
18. S. E. Renfrew and B. D. McCloskey, *J. Am. Chem. Soc.,* **139** (49), 17853-17860 (2017).
19. R. Jung, P. Strobl, F. Maglia, C. Stinner, and H. A. Gasteiger, *J. Electrochem. Soc.,* **165** (11), A2869-A2879 (2018).
20. M. Metzger, B. Strehle, S. Solchenbach, and H. A. Gasteiger, *J. Electrochem. Soc.,* **163** (7), A1219-A1225 (2016).
21. H.-J. Noh, S. Youn, C. S. Yoon, and Y.-K. Sun, *J. Power Sources,* **233** 121-130 (2013).
22. J. Kim, H. Lee, H. Cha, M. Yoon, M. Park, and J. Cho, *Adv. Ener. Mater.,* **8** (6), (2018).
23. S. Arimoto, K. Tsuruta, R. Leblanc, and R. Melsert, *US 2017/02946521 A1 (2017)*.
24. J. Kim, Y. Hong, K. S. Ryu, M. G. Kim, and J. Cho, *Electrochem. Solid State Lett.,* **9** A19-A23 (2006).
25. Y. Kim, *J. Solid State Electrochem.,* **17** (7), 1961-1965 (2013).
26. X. Xiong, Z. Wang, P. Yue, H. Guo, F. Wu, J. Wang, and X. Li, *J. Power Sources,* **222** 318-325 (2013).

27. R. Jung, M. Metzger, F. Maglia, C. Stinner, and H. A. Gasteiger, *J. Electrochem. Soc.,* **164** (7), A1361-A1377 (2017).
28. D. Streich, C. Erk, A. Guéguen, P. Müller, F.-F. Chesneau, and E. J. Berg, *J. Phys. Chem. C,* **121** (25), 13481-13486 (2017).
29. R. Jung, M. Metzger, F. Maglia, C. Stinner, and H. A. Gasteiger, *J. Phys. Chem. Lett.,* **8** (19), 4820-4825 (2017).
30. T. Teufl, B. Strehle, P. Müller, H. A. Gasteiger, and M. A. Mendez, *J. Electrochem. Soc.,* **165** (11), A2718-A2731 (2018).
31. J. Sicklinger, H. Beyer, L. Hartmann, F. Riewald, and H. A. Gasteiger, *mansucript in preparation*.
32. Z. Chen, J. Wang, J. Huang, T. Fu, G. Sun, S. Lai, R. Zhou, K. Li, and J. Zhao, *J. Power Sources,* **363** 168-176 (2017).
33. Y. Cho, S. Lee, Y. Lee, T. Hong, and J. Cho, *Adv. Ener. Mater.,* **1** (5), 821-828 (2011).
34. Y.-K. Sun, S.-T. Myung, B.-C. Park, J. Prakash, I. Belharouak, and K. Amine, *Nat. Mater.,* **8** 320 (2009).
35. D. Larcher, M. R. Palacin, G. G. Amatucci, and J.-M. Tarascon, *J. Electrochem. Soc.,* **144** 408-417 (1997).
36. G. G. Amatucci, J. M. Tarascon, D. Larcher, and L. C. Klein, *Solid State Ionics,* **84** (3), 169-180 (1996).
37. B. Strehle, K. Kleiner, R. Jung, F. Chesneau, M. Mendez, H. A. Gasteiger, and M. Piana, *J. Electrochem. Soc.,* **164** (2), A400-A406 (2017).
38. N. Tsiouvaras, S. Meini, I. Buchberger, and H. A. Gasteiger, *J. Electrochem. Soc.,* **160** (3), A471-A477 (2013).
39. S. Solchenbach, D. Pritzl, E. J. Y. Kong, J. Landesfeind, and H. A. Gasteiger, *J. Electrochem. Soc.,* **163** (10), A2265-A2272 (2016).
40. S. Jeong, J. Kim, and J. Mun, *J. Electrochem. Soc.,* **166** (3), A5038-A5044 (2019).
41. M. Metzger, C. Marino, J. Sicklinger, D. Haering, and H. A. Gasteiger, *J. Electrochem. Soc.,* **162** (7), A1123-A1134 (2015).
42. M. Metzger, B. Strehle, S. Solchenbach, and H. A. Gasteiger, *J. Electrochem. Soc.,* **163** (5), A798-A809 (2016).
43. B. Zhang, M. Metzger, S. Solchenbach, M. Payne, S. Meini, H. A. Gasteiger, A. Garsuch, and B. L. Lucht, *J. Phys. Chem. C,* **119** (21), 11337-11348 (2015).
44. S. Solchenbach, G. Hong, A. Freiberg, R. Jung, and H. A. Gasteiger, *J. Electrochem. Soc.,* **165** (14), A3304-A3312 (2018)
45. K. Luo, M. R. Roberts, R. Hao, N. Guerrini, D. M. Pickup, Y.-S. Liu, K. Edström, J. Guo, A. V. Chadwick, L. C. Duda, and P. G. Bruce, *Nat. Chem.,* **8** 684 (2016).
46. J. Landesfeind, D. Pritzl, and H. A. Gasteiger, *J. Electrochem. Soc.,* **164** (7), A1773-A1783 (2017).
47. R. Moshtev, *J. Power Sources,* **81-82** 434-441 (1999).
48. H. S. Liu, *Electrochem. Solid State Lett.,* **7** (7), A190-A193 (2004).
49. J. Pan, Y. Sun, P. Wan, Z. Wang, and X. Liu, *Electrochem. Commun.,* **7** (8), 857-862 (2005).
50. S. M. Bak, E. Hu, Y. Zhou, X. Yu, S. D. Senanayake, S. J. Cho, K. B. Kim, K. Y. Chung, X. Q. Yang, and K. W. Nam, *ACS Appl. Mater. Interfaces,* **6** (24), 22594-22601 (2014).
51. P. G. Bruce, A. R. Armstrong, and L. Gitzendanner, *J. Mater. Chem.,* **9** 193-198 (1998).
52. M. M. Thackeray, *Prog. Solid State Chem.,* **25** 1-71 (1997).

4 Conclusions

The goal of this PhD thesis was on the one hand to understand the degradation mechanism of graphite/LNMO cells at elevated temperatures (40 °C) by means of detailed electrochemical impedance spectroscopy (EIS). Therefore, an appropriate micro-reference electrode was developed, referred to as gold-wire reference electrode (GWRE). The GWRE was then used in order to understand the degradation mechanism of this cell system by introducing a novel analysis procedure for impedance spectra. On the other hand, the effect of cathode material washing was investigated with a variety of analytical techniques. Here, the findings are very novel and could lead to new strategies in order to stabilize nickel-rich NMC cathode materials. The key findings from this thesis are summarized in Figure 4.1.

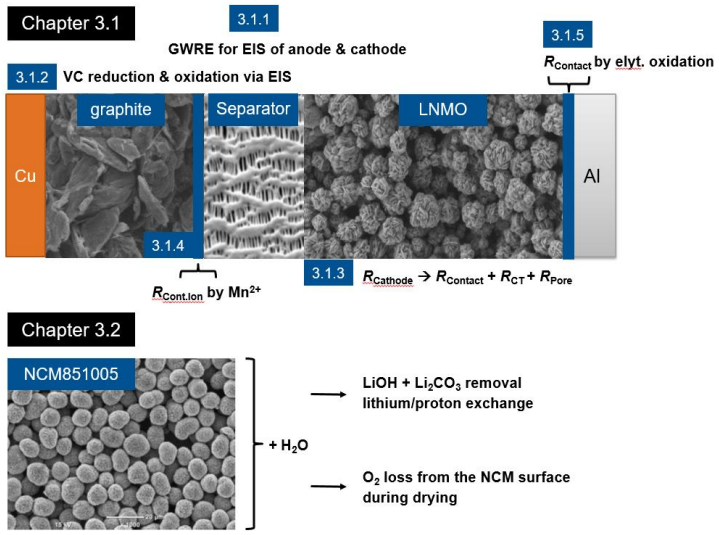

Figure 4.1: Graphical Summary of the key research findings made in this thesis, namely findings based on a novel EIS analysis on the ageing of graphite/LNMO cells (chapter 3.1) and of the processes occurring during the washing of NCM cathode active materials.

In the first study (chapter 3.1.1), a micro-reference electrode was developed in order to be able to record in-situ half-cell impedance spectra of anode & cathode versus the reference electrode. The so-called gold wire reference electrode (GWRE)[99] consists of a gold wire (50 µm) with a polyimide insulation (7 µm). Following the constraints from the literature for artefact-free half-cell impedance spectra, we showed that true half-cell impedance spectra could be obtained, as the GWRE satisfied the following requirements: (i) a small diameter of the wire (57 µm) versus the separators (2 glass fiber separators with a total thickness of ~ 400 µm), (ii) an insulation that only the tip is active for sensing, (iii) central placement of the GWRE between the separators (far away from the edges) and (iv) in-situ alloying of the gold wire with lithium to obtain a stable potential. To validate the GWRE based on EIS analysis, we reproduced the impedance response of a graphite anode with different concentrations of the additive VC from the literature[105] and showed that our data match with the data of the study.

With the newly developed micro-reference electrode at hand, we switched from a graphite/LFP cell chemistry (used for the development of the GWRE) to a graphite/LNMO cell chemistry, which is promising due to its high energy density. Here (chapter 3.1.2), we investigated the use of VC[106], which was shown in the literature to always decrease the cell performance. We examined different concentrations of VC and showed that starting from VC concentrations as low as 0.17% (in a lab-scale test cells with high electrolyte/active material ratio), a deterioration of the cell performance occurs. This is accompanied by an increase of the cathode impedance, which can be related to VC oxidation on the cathode (confirmed by on-line electrochemical mass spectrometry (OEMS) measurements). For a lower VC concentration of 0.09 % we showed that VC is only consumed on the anode (i.e., no VC oxidation occurs on the cathode as the impedance is identical to the case with 0 % VC), improving the capacity retention of graphite/LNMO cells at elevated temperatures (40 °C). The main conclusion from this study is that the concentration of anode additives in a high-voltage cell chemistry hast to be assessed very carefully and that impedance analysis with a micro-reference electrode is a powerful tool to optimize additives and the concentrations at which they can be used.

By making use of the micro-reference electrode in the study of the high-voltage cells, we have developed a novel impedance testing approach in order to learn more about the failure mechanism of graphite/LNMO cells. First, we analyze the cathode impedance (LNMO) in detail with this novel method (chapter 3.1.3).[109] We use the concept of blocking electrode conditions, which allows for the unambiguous assessment of the pore resistance (R_{Pore}) due to an absence of a charge transfer reaction. This method is usually carried out ex-situ. By delithiating the LNMO electrode completely, we can achieve blocking conditions during operation of the battery. By fitting spectra in blocking condition (no lithium in the LNMO electrode) and non-blocking condition (10% of the cell lithium inventory in the LNMO electrode) to a transmission-line equivalent circuit we can deconvolute the cathode impedance response. The LNMO impedance is deconvoluted in the contributions from the charge transfer (R_{CT}), the pore resistance (R_{Pore}) and the contact resistance (R_{Contact}) with very low uncertainties. We further show that it is not the charge transfer resistance which is increasing over cycling – as stated often in the literature – but the contact resistance between current collector and cathode coating (R_{Contact}).

Having now developed the novel impedance procedure, we also adopt it to analyze the anode impedance (chapter 3.1.4) in the same graphite/LNMO cells.[112] First we show that blocking conditions can also be achieved for a graphite anode by a complete delithiation, i.e. by completely discharging the graphite/LNMO cell. However, the perfect transmission-line response is only achieved in a graphite/LFP cell chemistry. When going to the graphite/LNMO cell chemistry, the blocking spectra show a semi-circle at the highest measured frequencies. This feature is analyzed by a frequency analysis and by temperature-dependent impedance measurements and we can show that the newly developed interface must be of ionic origin with a surface area of roughly 10 % of the total graphite surface area. By investigating the effect of manganese dissolution on the graphite anode impedance response we show that the high-frequency semi-circle stems from a narrow region of the graphite anode adjacent to the separator, which is formed during long-term cycling due to accelerated SEI formation caused by manganese ions. By fitting both spectra in blocking and non-blocking conditions we deconvolute the anode impedance into its contributions of: the high frequency resistance (R_{HFR}), the charge

transfer resistance (R_{CT}) and the newly developed interphase region in the graphite anode ($R_{Cont.Ion}$).

In the study that deconvoluted the LNMO cathode impedance response[109] (chapter 3.1.3), we could show that the resistance, which is increasing most is the contact resistance between current collector and cathode coating ($R_{Contact}$). Here (chapter 3.1.5), we further investigated this contribution to the cathode impedance, as there is still a debate in the literature if this impedance feature can truly be attributed to the current collector or rather to the so-called cathode electrolyte interphase (CEI). By a frequency analysis and by temperature-dependent impedance measurements, we showed that the resistance corresponds to a small interfacial area (matching to the current collector) and has a low activation energy (~1 kJ/mol) typical for electronic resistances. This was further underlined by coating the LNMO on a glassy carbon disc. In this case, the contact resistance is almost non-existent and also does not increase with cycling what brings us also to the origin of this resistance. It is known that in high-voltage cells protic species, which are formed upon electrolyte oxidation (e.g. HF) can then corrode the aluminum current collector leading to the increasing contact resistance. This finding is important as for the first time, electrolyte oxidation could be correlated to the cathode impedance response.

In chapter 3.2, the washing process of nickel-rich cathode materials is investigated. Here we analyzed the wash solutions after the first and second washing, revealing that LiOH is also found in the second wash solution. This is surprising, as it is generally assumed that LiOH in the wash solution stems from surface contaminants, which should be removed after the first washing step. By further investigating the washed powders, we can see that O_2 and CO_2 evolution above 80% SOC from the NCM materials are lowered by an order of magnitude when the samples are washed, compared to a pristine NCM. On-line mass spectrometry during washing and TGA-MS analysis during drying of washed NCM's showed that O_2 is released during the drying step. In addition, the extent of O_2 release during drying increases with drying temperature, what is in line with an increase in the NCM cathode impedance.

References

1. Tarascon, J. M. ; The Li-Ion Battery: 25 Years of Exciting and Enriching Experiences. *Electrochem. Soc*. *Interface.* **25,** 79–83 (2016).

2. Mizushima, K., Jones, P. C. & Goodenough, J. B. ; $LiCoO_2$: A New Cathode Material For Batteries Of High Energy Density. *Solid State Ionics* **4,** 171–174 (1981).

3. Whittingham, M. S. ; The Role of Ternary Phases in Cathode Reactions. *J. Electrochem. Soc.* **123,** 315 (1976).

4. Nitta, N., Wu, F., Lee, J. T. & Yushin, G. ; Li-ion battery materials: Present and future. *Mater. Today* **18,** 252–264 (2015).

5. Che, G., Jirage, B. K., Fisher, E. R. & Martin, C. R. ; Chemical-Vapor Deposition-Based Template Synthesis of Microtubular TiS_2 Battery Electrodes. *J. Electrochem. Soc.* **144,** 4296 (1997).

6. Infomine. Cobalt Price. (2018). Available at: http://www.infomine.com/investment/metal-prices/cobalt/5-year/. (Accessed: 5th June 2018)

7. Infomine. Nickel Price. (2018). Available at: http://www.infomine.com/investment/metal-prices/nickel/5-year/. (Accessed: 5th June 2018)

8. Frankel, T. C. The Washington Post. (2016). Available at: https://www.washingtonpost.com/graphics/business/batteries/congo-cobalt-mining-for-lithium-ion-battery/?noredirect=on. (Accessed: 5th June 2018)

9. Yabuuchi, N. & Ohzuku, T. ; Novel lithium insertion material of $LiCo_{1/3}Ni_{1/3}Mn_{1/3}O_2$ for advanced lithium-ion batteries. *J. Power Sources* **121,** 171–174 (2003).

10. Blomgren, G. E. ; The Development and Future of Lithium Ion Batteries. *J. Electrochem. Soc.* **164,** A5019–A5025 (2017).

11. Martha, S. K., Haik, O., Zinigrad, E., Drezen, T., Miners, J. H. & Aurbach, D. ; On the Thermal Stability of Olivine Cathode Materials for Lithium-Ion Batteries. *J. Electrochem. Soc.* **158,** A1115 (2011).

12. Andre, D., Kim, S-J., Lamp, P., Lux, S. F., Maglia, F., Paschos, O. & Stiaszny, B. ; Future generations of cathode materials: an automotive industry perspective. *J. Mater. Chem. A* **3,** 6709–6732 (2015).

13. Li, J., Downie, L. E., Ma, L., Qiu, W. & Dahn, J. R. ; Study of the Failure Mechanisms of $LiNi_{0.8}Mn_{0.1}Co_{0.1}O_2$ Cathode Material for Lithium Ion Batteries. *J. Electrochem. Soc.* **162,** A1401–A1408 (2015).

14. Schipper, F., Erickson, E. M., Erk, C., Shin, J-Y., Chesneau, F. F. & Aurbach, D. ; Review—Recent Advances and Remaining Challenges for Lithium Ion Battery Cathodes. *J. Electrochem. Soc.* **164,** A6220–A6228 (2017).

15. Jung, R., Morasch, R., Karayayali, P., Phillips, K., Maglia, F., Stinner, C., Shao-Horn, Y. & Gasteiger, H. A. ; Effect of Ambient Storage on the Degradation of Ni-Rich Positive Electrode Materials (NMC811) for Li-Ion Batteries. *J. Electrochem. Soc.* **165,** A132–A141 (2018).

16. Dahn, J. R., Sacken von, U., Juzkow, M. W. & Al-Janaby, H. ; Rechargeable $LiNiO_2$/ Carbon Cells. *J. Electrochem. Soc.* **138,** 6–10 (1991).

17. Thackeray, M. M., David, W. I. F., Bruce, P. G. & Goodenough, J. B. ; Lithium Insertion into Manganese Spinels. *Mat. Res. Bul.* **18,** 461–472 (1983).

18. Amine, K., Tukamoto, H., Yasuda, H. & Fujita, Y. A ; New Three-Volt Spinel $Li_{1+x}Mn_{1.5}Ni_{0.5}O_4$ for Secondary Lithium Batteries. *J. Electrochem. Soc.* **143,** 1607–1613 (1996).

19. Zhong, Q., Bonakclarpour, A., Zhang, M. & Dahn, J. R. ; Synthesis and Electrochemistry of $LiNi_xMn_{2-x}O_4$. *J. Electrochem. Soc.* **144,** (1997).

20. Kim, J.-H., Pieczonka, N. P. W. & Yang, L. ; Challenges and Approaches for High-Voltage Spinel Lithium-Ion Batteries. *ChemPhysChem* **15,** 1940–1954 (2014).

21. Lu, D., Xu, M., Zhou, L., Garsuch, A. & Lucht, B. L. ; Failure Mechanism of Graphite/$LiNi_{0.5}Mn_{1.5}O_4$ Cells at High Voltage and Elevated Temperature. *J. Electrochem. Soc.* **160,** A3138–A3143 (2013).

22. Fong, R., von Sacken, U. & Dahn, J. R. ; Studies of Lithium Intercalation usinginto Carbons Using Nonaqueous Electrochemical Cells. *J. Electrochem. Soc.* **137,** 2009–2013 (1990).

23. Armand, M. & Tarascon, J.-M. ; Issues and challenges facing rechargeable lithium batteries. *Science.* **414,** 359–367 (2001).

24. Zhang, S. S., Xu, K. & Jow, T. R. ; Evaluation on a water-based binder for the graphite anode of Li-ion batteries. *J. Power Sources* **138,** 226–231 (2004).

25. Li, J., Lewis, R. B. & Dahn, J. R. ; Sodium Carboxymethyl Cellulose. *Electrochem. Solid-State Lett.* **10,** A17 (2007).

26. Wakihara, M. ; Recent developments in lithium ion batteries. *Mater. Sci. Eng. Reports* **33,** 109–134 (2001).

27. Marks, T., Trussler, S., Smith, A. J., Xiong, D. & Dahn, J. R. ; A Guide to Li-Ion Coin-Cell Electrode Making for Academic Researchers. *J. Electrochem. Soc.* **158,** A51 (2011).

28. Park, M., Zhang, X., Chung, M., Less, G. B. & Sastry, A. M. ; A review of conduction phenomena in Li-ion batteries. *J. Power Sources* **195,** 7904–7929 (2010).

29. Zhang, X., Winget, B., Doeff, M., Evans, J. W. & Devine, T. M. ; Corrosion of Aluminum Current Collectors in Lithium-Ion Batteries with Electrolytes Containing $LiPF_6$. *J. Electrochem. Soc.* **152,** B448–B454 (2005).

30. Zhang, W. J. ; A review of the electrochemical performance of alloy anodes for lithium-ion batteries. *J. Power Sources* **196,** 13–24 (2011).

31. Lin, D., Liu, Y. & Cui, Y. ; Reviving the lithium metal anode for high-energy batteries. *Nat. Nanotechnol.* **12,** 194–206 (2017).

32. Brandt, K. ; Historical development of secondary lithium batteries. *Solid State Ionics* **69,** 173–183 (1994).

33. Brissot, C., Rosso, M., Chazalviel, J. N. & Lascaud, S. ; Dendritic growth mechanisms in lithium/polymer cells. *J. Power Sources* **81,** 925–929 (1999).

34. Peled, E. ; The Electrochemical-Behavior of Alkali and Alkaline-Earth Metals in Non-Aqueous Battery Systems - the Solid Electrolyte Interphase Model. *J. Electrochem. Soc.* **126,** 2047–2051 (1979).

35. Peled, E. ; Advanced Model for Solid Electrolyte Interphase Electrodes in Liquid and Polymer Electrolytes. *J. Electrochem. Soc.* **144,** L208 (1997).

36. Aurbach, D. ; Identification of Surface Films Formed on Lithium in Propylene Carbonate Solutions. *J. Electrochem. Soc.* **134,** 1611 (1987).

37. Xu, W., Wang, J., Ding, F., Chen, X., Nasybulin, E., Zhang, Y. & Zhang, J-G. ; Lithium metal anodes for rechargeable batteries. *Energy Environ. Sci.* **7,** 513–537 (2014).

38. Winter, M. & Besenhard, J. O. Lithiated Carbons. *Handb. Batter. Mater. Second Ed.* 433–478 (2011).

39. Joshi, T., Eom, K., Yushin, G. & Fuller, T. F. ; Effects of Dissolved Transition Metals on the Electrochemical Performance and SEI Growth in Lithium-Ion Batteries. *J. Electrochem. Soc.* **161,** A1915–A1921 (2014).

40. Vetter, J., Novák, P., Wagner, M. R., Veit, C., Möller, K-C., Besenhard, J O., Winter, M., Wohlfahrt-Mehrens, M., Vogler, C. & Hammouche, ; A. Ageing mechanisms in lithium-ion batteries. *J. Power Sources* **147,** 269–281 (2005).

41. Ferg, E., Gummow, R. J., Kock, A. De & Thackeray, M. M. ; Spinel Anodes for Lithium-Ion Batteries. *J. Electrochem. Soc.* **141,** 9–12 (1994).

42. He, Y.-B., Li, B., Liu, M., Zhang, C., Lv, W., Yang, C., Li, J., Du, H., Yang, Q-H., Kim, J-Y. & Kang, F. ; Gassing in $Li_4Ti_5O_{12}$-based batteries and its remedy. *Sci. Rep.* **2,** 913–921 (2012).

43. Chevrier, V. L. Liu, L., Ba Le, D., Lund, J., Molla, B., Reimer, K., Krause, L. J., Jensen, L. D., Figgemeier, E. & Ebermann, K. W. ; Evaluating Si-Based Materials for Li-Ion Batteries in Commercially Relevant Negative Electrodes. *J. Electrochem. Soc.* **161,** A783–A791 (2014).

44. Besenhard, J. O., Yang, J. & Winter, M. ; Will advanced lithium-alloy anodes have a chance in lithium-ion batteries? *J. Power Sources* **68,** 87–90 (1997).

45. Yoon, T., Nguyen, C. C., Seo, D. M. & Lucht, B. L. ; Capacity Fading Mechanisms of Silicon Nanoparticle Negative Electrodes for Lithium Ion Batteries. *J. Electrochem. Soc.* **162,** A2325–A2330 (2015).

46. McDowell, M. T., Lee, S. W., Nix, W. D. & Cui, Y. ; 25th anniversary article: Understanding the lithiation of silicon and other alloying anodes for lithium-ion batteries. *Adv. Mater.* **25,** 4966–4985 (2013).

47. Aurbach, D., Talyosef, Y., Markovsky, B., Markevich, E., Zinigrad, E., Asraf, L., Gnanaraj, J. S. & Kim, H-J. & Design of electrolyte solutions for Li and Li-ion batteries: A review. *Electrochim. Acta* **50,** 247–254 (2004).

48. Zhang, S. S. ; A review on electrolyte additives for lithium-ion batteries. *J. Power Sources* **162,** 1379–1394 (2006).

49. Imhof, R. & Novák, P. ; In Situ Investigation of the Electrochemical Reduction of Carbonate Electrolyte Solutions at Graphite Electrodes. *J. Electrochem. Soc.* **145,** 3313–3319 (1998).

50. Zhang, B., Metzger, M., Solchenbach, S., Payne, M., Mein, S., Gasteiger, H. A., Garsuch, A. & Lucht, B. L. ; Role of 1,3-Propane Sultone and Vinylene Carbonate in Solid Electrolyte Interface Formation and Gas Generation. *J. Phys. Chem. C* **119,** 11337–11348 (2015).

51. Xu, K. ; Nonaqueous liquid electrolytes for lithium-based rechargeable batteries. *Chem. Rev.* **104,** 4303–4417 (2004).

52. Zhang, X. & Devine, T. M. ; Factors That Influence Formation of AlF3 Passive Film on Aluminum in Li-Ion Battery Electrolytes with LiPF6. *J. Electrochem. Soc.* **153,** B375 (2006).

53. Aurbach, D., Gamolsky, K., Markovsky, B., Gofer, Y., Schmidt, M. & Heider, U. On the use of vinylene carbonate (VC) as an additive to electrolyte solutions for Li-ion batteries. *Electrochim. Acta* **47,** 1423–1439 (2002).

54. Nie, M., Demeaux, B., Young, B., Heskett, D. R., Chen, Y., Bose, A., Woicik, J. C. & Lucht, B. L. ; Effect of Vinylene Carbonate and Fluoroethylene Carbonate on SEI Formation on Graphitic Anodes in Li-Ion Batteries. *J. Electrochem. Soc.* **162,** 7008–7014 (2015).

55. Xiong, D., Burns, J. C., Smith, A. J., Sinha, N. & Dahn, J. R. ; A High Precision Study of the Effect of Vinylene Carbonate (VC) Additive in Li/Graphite Cells. *J. Electrochem. Soc.* **158,** A1431 (2011).

56. Burns, J. C., Sinha, N. N., Coyle, D. J., Jain, G., VanElzen, C. M., Lamanna, W. M., Xiao, A., Scott, E., Gardner, J. P. & Dahn, J. R. & The Impact of Varying the Concentration of Vinylene Carbonate Electrolyte Additive in Wound Li-Ion Cells. *J. Electrochem. Soc.* **159,** A85 (2012).

57. Dong, Y., Demeaux, J. & Lucht, B. L. ; Investigation of the Effect of Added Methylene Ethylene Carbonate (MEC) and Vinylene Carbonate (VC) on LiNi0.5Mn1.5O4 /Graphite Cell Performance. *J. Electrochem. Soc.* **163,** A2413–A2417 (2016).

58. Ohzuku, T., Kitagawa, M. & Hirai, T. ; Electrochemistry of Manganese Dioxide in Lithium Nonaqueous Cell. *J. Electrochem. Soc.* **137,** 769 (1990).

59. Thackeray, M. M. ; Manganese oxides for lithium batteries. *Prog. Solid State Chem.* **25,** 1–71 (1997).

60. Padhi, A. K., Nanjundaswamy, K. & Goodenough, J. B. ; Phospho-olivines as Positive-Electrode Materials for Rechargeable Lithium Batteries. *J. Electrochem. Soc* **144,** 195–205 (1997).

61. Zhang, W.-J. ; Comparison of the Rate Capacities of $LiFePO_4$ Cathode Materials. *J. Electrochem. Soc.* **157,** A1040 (2010).

62. Sides, C. R., Croce, F., Young, V. Y., Martin, C. R. & Scrosati, B. ; A High-Rate, Nanocomposite $LiFePO_4$/Carbon Cathode. *Electrochem. Solid-State Lett.* **8,** A484 (2005).

63. Joachin, H., Kaun, T. D., Zaghib, K. & Prakash, J. ; Electrochemical and Thermal Studies of Carbon-Coated LiFePO4 Cathode. *J. Electrochem. Soc.* **156,** A401 (2009).

64. Noh, H. J., Youn, S., Yoon, C. S. & Sun, Y. K. Comparison of the structural and electrochemical properties of layered $Li[Ni_xCo_yMn_z]O_2$(x = 1/3, 0.5, 0.6, 0.7, 0.8 and 0.85) cathode material for lithium-ion batteries. *J. Power Sources* **233,** 121–130 (2013).

65. Buchberger, I., Seidlmayer, S., Pokharel, A., Piana, M., Hattendorff, J., Kudejova, P., Gilles, R. & Gasteiger, H. A. ; Aging Analysis of Graphite/$LiNi_{1/3}Mn_{1/3}Co_{1/3}O_2$ Cells Using XRD, PGAA, and AC Impedance. *J. Electrochem. Soc.* **162,** A2737–A2746 (2015).

66. Streich, D., Erk. C., Guéguen, A., Müller, P., Chesneau, F-F. & Berg, E. J. *;* Operando Monitoring of Early Ni-mediated Surface Reconstruction in Layered Lithiated Ni-Co-Mn Oxides. *J. Phys. Chem. C* **121,** 13481–13486 (2017).

67. Jung, R., Metzger, M., Maglia, F., Stinner, C. & Gasteiger, H. A. ; Oxygen Release and Its Effect on the Cycling Stability of $LiNi_xMn_yCo_zO_2$ (NMC) Cathode Materials for Li-Ion Batteries. *J. Electrochem. Soc.* **164,** A1361–A1377 (2017).

68. Jung, R., Metzger, M., Maglia, F., Stinner, C. & Gasteiger, H. ; Chemical vs. Electrochemical Electrolyte Oxidation on NMC111, NMC622, NMC811, LNMO, and Conductive Carbon. *J. Phys. Chem. Lett.* **8,** 4820–4825 (2017).

69. Wandt, J., Freiberg, A. T. S., Ogrodnik, A. & Gasteiger, H. A. ; Singlet oxygen evolution from layered transition metal oxide cathode materials and its implications for lithium-ion batteries. *Mater. Today* **21,** 825-833(2018).

70. De Biasi, L., Kondrakov, A. O., Geßwein, H., Brezesinski, T., Hartmann, P. & Janek, J. ; Between Scylla and Charybdis: Balancing among Structural Stability and Energy Density of Layered NCM Cathode Materials for Advanced Lithium-Ion Batteries. *J. Phys. Chem. C* **121,** 26163–26171 (2017).

71. Lu, Z. & Dahn, J. R. ; Understanding the Anomalous Capacity of $Li/Li[Ni_xLi_{(1/3-2x/3)}Mn_{(2/3-x/3)}]O_2$ Cells Using In Situ X-Ray Diffraction and Electrochemical Studies. *J. Electrochem. Soc.* **149,** A815 (2002).

72. Thackeray, M. M., Kang, S-H., Johnson, C. S., Vaughey, J. T., Benedek, R. & Hackney, S.A. ; Li_2MnO_3-stabilized $LiMO_2$ (M = Mn, Ni, Co) electrodes for lithium-ion batteries. *J. Mater. Chem.* **17,** 3112 (2007).

73. Rozier, P. & Tarascon, J. M. ; Review—Li-Rich Layered Oxide Cathodes for Next-Generation Li-Ion Batteries: Chances and Challenges. *J. Electrochem. Soc.* **162,** A2490–A2499 (2015).

74. Strehle, B., Kleiner, K., Jung, R., Chesneau, F., Mendez, M., Gasteiger, H. A. & Piana, M. ;The Role of Oxygen Release from Li- and Mn-Rich Layered Oxides during the First Cycles Investigated by On-Line Electrochemical Mass Spectrometry. *J. Electrochem. Soc.* **164,** A400–A406 (2017).

75. Hong, J., Gwon, H., Jung, S.-K., Ku, K. & Kang, K. ; Review—Lithium-Excess Layered Cathodes for Lithium Rechargeable Batteries. *J. Electrochem. Soc.* **162,** A2447–A2467 (2015).

76. Ochida, M., Domi, Y., Doi, T., Tsubouchi, S., Nakagawa, H., Yamanaka, T., Abe, T. & Ogumi, Z. Influence of Manganese Dissolution on the Degradation of Surface Films on Edge Plane Graphite Negative-Electrodes in Lithium-Ion Batteries. *J. Electrochem. Soc.* **159,** A961–A966 (2012).

77. Pieczonka, N. P. W., Liu, Z., Lu, P., Olson, K. L., Moote, J., Powell, B. R. & Kim, J-H. ; Understanding Transition-Metal Dissolution Behavior in $LiNi_{0.5}Mn_{1.5}O_4$ High-Voltage Spinel for Lithium Ion Batteries. *J. Phys. Chem. C* **117,** 15947–15957 (2013).

78. Aurbach, D., Markovsky, B., Talyossef, Y., Salitra, G., Kim, H-J. & Choi, S. ; Studies of cycling behavior, ageing, and interfacial reactions of $LiNi_{0.5}Mn_{1.5}O_4$ and carbon electrodes for lithium-ion 5-V cells. *J. Power Sources* **162,** 780–789 (2006).

79. Metzger, M., Strehle, B., Solchenbach, S. & Gasteiger, H. A. ; Origin of H_2 evolution in LIBs: H_2O reduction vs electrolyte oxidation. *J. Electrochem. Soc.* **163,** A798–A809 (2016).

80. Leitner, K. W., Wolf, H., Garsuch, A., Chesneau, F. & Schulz-Dobrick, M. Electroactive separator for high voltage graphite/$LiNi_{0.5}Mn_{1.5}O_4$ lithium ion batteries. *J. Power Sources* **244,** 548–551 (2013).

81. Zhao, Y., Wang, S., Ren, W. & Wu, R. ; Storage Characteristics and Surface Basicity Properties of Li-Rich Cathode Materials Used in Lithium Ion Batteries. *J. Electrochem. Soc.* **160,** A82–A86 (2012).

82. Liu, H. S., Zhang, Z. R., Gong, Z. L. & Yang, Y. ; Origin of Deterioration for $LiNiO_2$ Cathode Material during Storage in Air. *Electrochem. Solid-State Lett.* **7,** 190–193 (2004).

83. Liu, H., Yang, Y. & Zhang, J. ; Investigation and improvement on the storage property of $LiNi_{0.8}Co_{0.2}O_2$ as a cathode material for lithium-ion batteries. J. Power Sources. **162,** 644–650 (2006).

84. Kim, J., Hong, Y., Ryu, S., Kim, M. G. & Cho, J. ; Washing Effect of a $LiNi_{0.83}Co_{0.15}Al_{0.02}O_2$ Cathode in Water. *Electrochem. Solid-State Lett.* **9,** 19–23 (2006).

85. Lvovich, V. F. Impedance Spectroscopy. 1–87 (2012).

86. Andrzej Lasia. Electrochemical Impedance Spectroscopy and its Applications. 1–117 (2004).

87. Gasteiger, H. A. Lecture: Electrochemistry for Energy Materials. (2017).

88. Hirschorn, B., Orazem, M., Tribollet, B., Vivier, V., Frateur, F. & Musiani, M. ; Determination of effective capacitance and film thickness from constant-phase-element parameters. *Electrochim. Acta* **55,** 6218–6227 (2010).

89. Ogihara, N., Kawauchi, S., Okuda, C., Itou, Y., Takeuchi, Y. & Ukyo, Y. ; Theoretical and Experimental Analysis of Porous Electrodes for Lithium-Ion Batteries by Electrochemical Impedance Spectroscopy Using a Symmetric Cell. *J. Electrochem. Soc.* **159,** A1034–A1039 (2012).

90. Gaberscek, M., Moskon, J., Erjavec, B., Dominko, R. & Jamnik, J. The Importance of Interphase Contacts in Li Ion Electrodes: The Meaning of the High-Frequency Impedance Arc. *Electrochem. Solid-State Lett.* **11,** A170–A174 (2008).

91. Duncan, H., Abu-Lebdeh, Y. & Davidson, I. J. ; Study of the Cathode–Electrolyte Interface of $LiMn_{1.5}Ni_{0.5}O_4$ Synthesized by a Sol–Gel Method for Li-Ion Batteries. *J. Electrochem. Soc.* **157,** A528 (2010).

92. Chen, C. H., Liu, J. & Amine, K. ; Symmetric cell approach and impedance spectroscopy of high power lithium-ion batteries. *J. Power Sources* **96,** 321–328 (2001).

93. Petibon, R., Aiken, C. P., Sinha, N. N., Burns, J. C., Ye, H., VanELzen, C. M., Jain, G., Trussler, S. & Dahn, J. R. ; Study of Electrolyte Additives Using Electrochemical Impedance Spectroscopy on Symmetric Cells. *J. Electrochem. Soc.* **160,** A117–A124 (2012).

94. Ender, M., Weber, A. & Ivers-Tiffée, E. ; Analysis of Three-Electrode Setups for AC-Impedance Measurements on Lithium-Ion Cells by FEM simulations. *J. Electrochem. Soc.* **159,** A128 (2012).

95. Dees, D. W., Jansen, A. N. & Abraham, D. P. ; Theoretical examination of reference electrodes for lithium-ion cells. *J. Power Sources* **174,** 1001–1006 (2007).

96. Victoria, S. N. & Ramanathan, S. ; Effect of potential drifts and ac amplitude on the electrochemical impedance spectra. *Electrochim. Acta* **56,** 2606–2615 (2011).

97. Zhou, J. & Notten, P. H. L. ; Development of Reliable Lithium Microreference Electrodes for Long-Term In Situ Studies of Lithium-Based Battery Systems. *J. Electrochem. Soc.* **151,** A2173 (2004).

98. Abraham, D. P., Poppen, S. D., Jansen, A. N., Liu, J. & Dees, D. W. ; Application of a lithium-tin reference electrode to determine electrode contributions to impedance rise in high-power lithium-ion cells. *Electrochim. Acta* **49,** 4763–4775 (2004).

99. Solchenbach, S., Pritzl, D., Kong, E. J. Y., Landesfeind, J. & Gasteiger, H. A. ; A Gold Micro-Reference Electrode for Impedance and Potential Measurements in Lithium Ion Batteries. *J. Electrochem. Soc.* **163,** A2265–A2272 (2016).

100. Tsiouvaras, N., Meini, S., Buchberger, I. & Gasteiger, H. A. ; A Novel On-Line Mass Spectrometer Design for the Study of Multiple Charging Cycles of a Li-O_2 Battery. *J. Electrochem. Soc.* **160,** A471–A477 (2013).

101. Ma, L., Glazier, S. L., Petibon, R., Xia, J., Peters, J. M., Liu, Q., Allen, J., Doig, R. N. C. & Dahn, J. R. ; A Guide to Ethylene Carbonate-Free Electrolyte Making for Li-Ion Cells. *J. Electrochem. Soc.* **164,** A5008–A5018 (2017).

102. Bünzli, C., Kaiser, H. & Novák, P. ; Important Aspects for Reliable Electrochemical Impedance Spectroscopy Measurements of Li-Ion Battery Electrodes. *J. Electrochem. Soc.* **162,** A218–A222 (2014).

103. Gómez-Cámer, J. L. & Novák, P. ; Electrochemical impedance spectroscopy: Understanding the role of the reference electrode. *Electrochem. commun.* **34,** 208–210 (2013).

104. Klett, M., Gilbert, J. A., Trask, S. E., Polzin, B. J., Jansen, A. N., Dees, D. W. & Abraham, D. P. ; Electrode Behavior RE-Visited: Monitoring Potential Windows, Capacity Loss, and Impedance Changes in $Li_{1.03}(Ni_{0.5}Co_{0.2}Mn_{0.3})_{0.97}O_2$/Silicon-Graphite Full Cells. *J. Electrochem. Soc.* **163,** A875–A887 (2016).

105. Burns, J. C., Petibon, R., Nelson, K. J., Sinha, N. N., Kassam, A., Way, B. M. & Dahn, J. R. ; Studies of the Effect of Varying Vinylene Carbonate (VC) Content in Lithium Ion Cells on Cycling Performance and Cell Impedance. *J. Electrochem. Soc.* **160,** A1668–A1674 (2013).

106. Pritzl, D., Solchenbach, S., Wetjen, M. & Gasteiger, H. A. ; Analysis of Vinylene Carbonate (VC) as Additive in Graphite/$LiNi_{0.5}Mn_{1.5}O_4$ Cells. *J. Electrochem. Soc.* **164,** A2625–A2635 (2017).

107. El Ouatani, L., Dedryvère, R., Siret, C., Beinsan, P., reynod, S., Iratcabal, P. & Gonbeau, D. ; The Effect of Vinylene Carbonate Additive on Surface Film Formation on Both Electrodes in Li-Ion Batteries. *J. Electrochem. Soc.* **156,** A103 (2009).

108. Eom, J. Y., Jung, I. H. & Lee, J. H. ; Effects of vinylene carbonate on high temperature storage of high voltage Li-ion batteries. *J. Power Sources* **196,** 9810–9814 (2011).

109. Landesfeind, J., Pritzl, D. & Gasteiger, H. A. ; A novel analysis protocol for three electrode Li-Ion battery impedance spectra I. Analysis of a high-voltage positive electrode. *J. Electrochem. Soc.* **164,** A1773 – A1783 (2017).

110. Fievet, P., Mullet, M. & Pagetti, J. ; Impedance measurements for determination of pore texture of a carbon membrane. *J. Memb. Sci.* **149,** 143–150 (1998).

111. Landesfeind, J., Hattendorff, J., Ehrl, A., Wall, W. A. & Gasteiger, H. A. ; Tortuosity Determination of Battery Electrodes and Separators by Impedance Spectroscopy. *J. Electrochem. Soc.* **163,** A1373–A1387 (2016).

112. Pritzl, D., Landesfeind, J., Solchenbach, S. & Gasteiger, H. A. ; An Analysis Protocol for Three-Electrode Li-Ion Battery Impedance Spectra : Part II. Analysis of a Graphite Anode Cycled vs. LNMO. *J. Electrochem. Soc.* **165,** A2145–A2153 (2018).

113. Pritzl, D. Bumberger, A. E., Wetjen, M., Landesfeind, J., Solchenbach, S. & Gasteiger, H.A. ; Identifying Contact Resistances in High-Voltage Cathodes by Impedance Spectroscopy. *J. Electrochem. Soc.* **166,** A582–A590 (2019)

114. Xiong, X., Wang, Z., Yue, P., Guo, H., Wu, F., Wang, J. & Li, X. ; Washing effects on electrochemical performance and storage characteristics of $LiNi_{0.8}Co_{0.1}Mn_{0.1}O_2$ as cathode material for lithium-ion batteries. *J. Power Sources* **222,** 318–325 (2013).

Acknowledgements

The content of this thesis was accomplished between November 2015 and November 2018 at the Chair of Technical Electrochemistry at the Technical University of Munich (TUM).

I would like to express my deepest gratitude to my PhD supervisor

Prof. Dr. Hubert A. Gasteiger

for the invaluable and outstanding guidance throughout the last years. I admire the way you share your almost endless knowledge about electrochemistry and teach us how to become critical and honest researchers, driven by the curiosity about science, as you are one. Thank you also for creating an environment in the group which is one of the most inspirational I have ever experienced and which made it a real pleasure to work in. Furthermore, I am very thankful for your large support of my own scientific career. With being a person, who always gives way more than he takes, you made my PhD time a fascinating journey through the field of electrochemistry for which I will always be very grateful.

I especially want to say thank you to **Veronika Pichler** for the help with all the paperwork and for being very supportive towards every one of us.

The basis for the success of this thesis were set by my two master's thesis supervisors **Johannes Landesfeind** and **Sophie Solchenbach**. Especially, I have to thank Johannes for introducing me to the fundamentals of electrochemical impedance spectroscopy and being able to learn from your way how to obtain scientific results in a very efficient and precise manner. Sophie is greatly acknowledged for sharing the large knowledge about batteries in general and showing me how to write scientific publications.

This thesis was carried out in the "Network on Electrochemistry and Batteries" from BASF SE. I greatly acknowledge our BASF team at TUM with the former members **Michael Metzger**, **Hans Beyer** and **Sophie Solchenbach** and the current

members **Benjamin Strehle**, **Johannes Sicklinger**, **Michele Piana**, **Franziska Friedrich**, **Anna Freiberg** and **Stefan Oswald**. I have learned a lot from you and it was always very exciting to work with you.

Next, I have to thank **Tobias Teufl** who carried out his PhD at BASF in Ludwigshafen and with whom I could work together very closely. It was always great fun to work with you, especially on the last study of this thesis. I also have to acknowledge **BASF SE** for funding the work of this thesis and especially **Heino Sommer**, **Pascal Hartmann** and **Manuel Mendez** from BASF for the great collaboration and the close exchange during the last years. I also had the great pleasure to stay abroad in the US at the BASF R&D facility in Beachwood, Ohio. I have to thank **Jordan Lampert** for giving me the opportunity to stay in his group and supporting me throughout the stay. Next, I have to thank **Zhong Shi** for being my supervisor at that time and **Plousia Vassilaras**, **Young-Jin Kim** and **Leo Xiufeng** for the support. Also, I have to acknowledge the technicians, **Desirée Shultz** and **Anthony Tallerico** for the great time I had with you.

I am very grateful for the support from my bachelor and master students **Edmund Kong**, **Andreas Bumberger**, **Florian Petermichl**, **Wan Da Hao**, **Louis Hartmann**, **Stefan Oswald** and **Maxi Graf**.

I also want to say thank you to my office colleagues **Tanja Zünd**, **Fabian Linsenmann**, **Qi He** and **Anna Freiberg** for the great atmosphere and nice non-scientific discussions.

I would like to say thank you to my parents **Sonja** and **Josef** for your great support throughout the whole time. I also want to thank my two brothers **Tobias** and **Nico** for supporting me and critically following my personal development through my PhD time.

Last and very important I have to say thank you to my girlfriend **Vroni** for her continuous motivational support and for being a very important part of my life. I am very happy for the time we spent together and I am looking forward to all the exciting adventures which are still ahead of us.

Scientific Contributions

Articles

D. Pritzl, A. Bumberger, M. Wetjen, J. Landesfeind, S. Solchenbach and H. A. Gasteiger "Identifying Contact Resistances in High-Voltage Cathodes by Impedance Spectroscopy", *J. Electrochem. Soc.*, 166 (4), A582-A590 (**2019**)

D. Pritzl[=], J. Landesfeind[=], S. Solchenbach and H. A. Gasteiger, "An Analysis protocol for Three-Electrode Li-Ion Battery Impedance Spectra: Part II. Analysis of a Graphite Anode cycled vs. LNMO", *J. Electrochem. Soc.*, 165 (10), A2145-A2153 (**2018**) ([=] equal contribution)

M. Wetjen, S. Solchenbach, **D. Pritzl**, J. Hou, V. Tileli, H. A. Gasteiger, „Morphological Changes of Silicon Nanoparticles and the Influence of Cutoff Potentials in Silicon-Graphite Electrodes", *J. Electrochem. Soc.*, 165 (7), A1503-A1514 (**2018**)

S. Solchenbach, M. Wetjen, **D. Pritzl**, K. U. Schwenke and H. A. Gasteiger, "Lithium Oxalate as Capacity and Cycle-Life Enhancer in LNMO/Graphite and LNMO/SiG Full Cells", *J. Electrochem. Soc.*, 165 (3), A512-A524 (**2018**)

M. Wetjen, **D. Pritzl**, R. Jung, S. Solchenbach, R. Ghadimi, and H. A. Gasteiger, "Differentiating the Degradation Phenomena in Silicon/Graphite Electrodes for Lithium Ion Batteries", *J. Electrochem. Soc.*, 164 (12), A2840-A2852 (**2017**)

D. Pritzl, S. Solchenbach, M. Wetjen and H. A. Gasteiger, "Analysis of vinylene carbonate as additive in graphite/LNMO cells", *J. Electrochem. Soc.*, 164 (12), A2625-A2635 (**2017**)

J. Landesfeind[=], **D. Pritzl***[=], and H. A. Gasteiger, "An Analysis protocol for Three-Electrode Li-Ion Battery Impedance Spectra: Part I. Analysis of a High-Voltage Positive Electrode", *J. Electrochem. Soc.*, 164 (7), A1773-A1783 (**2017**) (* corresponding author, [=] equal contribution)

S. Solchenbach, **D. Pritzl**, E. J. Y. Kong, J. Landesfeind and H. A. Gasteiger "A Gold Micro-Reference Electrode for Potential and Impedance Measurements in Lithium Ion Batteries", *J. Electrochem. Soc.*, 163 (10), A2265-A2272 (**2016**)

Articles in preparation

D. Pritzl, T. Teufl, A.T.S. Freiberg, B. Strehle, J. Sicklinger, H. Sommer, P. Hartmann and H. A. Gasteiger "Washing of Ni-rich cathode materials for lithium-ion batteries – Towards a mechanistic understanding", *manuscript in preparation*

Oral presentations

Surface contaminants on Ni-rich Cathode Active Materials: Influence of the Storage Conditions, AiMES (September 30 – October 04, **2018**)**, Cancun** (Mexico)

Analysis of graphite/LNMO cells with a micro-reference electrode: Role of the graphite anode, 233rd Meeting of The Electrochemical Society (May 13th - 17th, **2018**), **Seattle** (USA)

Identifying Contact Resistances in High-Voltage Cathodes By Impedance Spectroscopy, 232nd Meeting of The Electrochemical Society (October 1st - 6th, **2017**), **National Harbor** (USA)

Analyzing High-Voltage Graphite/LNMO Cells with a Novel Impedance Procedure Utilizing a Micro-Reference Electrode, 231st Meeting of The Electrochemical Society (May 28th – June 1st, **2017**), **New Orleans** (USA)

Analysis of VC and FEC in High-Voltage Li-Ion Batteries with Impedance Spectroscopy, PRiME (October 02-07, **2016**), **Honolulu** (USA)